A Narrowband Multiple Frequency Simultaneous Drive EIT System Applied to a Linear Array.

by

JILL C. SIMPSON

A thesis presented for the Doctor of Philosophy, Department of Electronic and Electrical Engineering, University of Sheffield.

December 1995.

A Narrowband Multiple Frequency Simultaneous Drive EIT System Applied to a Linear Array

J.C.Simpson

Summary

A high speed, injected current, Electrical Impedance Tomography (EIT) system for producing images of electrical conductivity distributions is described. The measurements required to produce an image are acquired in a time of 2ms, allowing rapidly changing distributions to be imaged. To achieve this speed, the drive currents of different frequencies are applied simultaneously to the medium of interest. The system is applied to a linear array, although other electrode configurations could be used.

An introduction to the topic of Electrical Impedance Tomography (EIT) is presented detailing present applications of EIT and giving some theoretical background to the technique. Reasons for reducing the measurement time and applying the system to a linear array are given. The general specification for the system is derived and the parallel drive and measurement circuitry is described in detail. The filtering process used to determine the components of the measured data at each of the drive frequencies is described. The algorithm used to form images is explained and image filters are applied to images generated from analytic data in order to improve the image quality. Measurements made on conductivity distributions set up in a phantom and images generated from these measurements are presented including images of single and multiple objects of higher and lower conductivity than the background medium. Images of moving objects, including a sequence of images generated from measurements taken in consecutive 2ms intervals, are presented. Conclusions from the work are drawn and suggestions for further work are given.

Acknowledgements

I should like to express my sincere gratitude to Professor Ian Freeston and Dr Richard Tozer for their guidance and continual encouragement throughout the project. I should also like to thank Anthony McGaw for his assembly of the current sources and Wayne Frankish for his fabrication of the phantom and electrode array.

I would like to thank family, friends and postgraduate colleagues (especially Jamie, Darren, Amar and Chris) for their support and enthusiasm throughout the duration of the project.

I would like to take this opportunity to thank Mr James Bryant of Analog Devices for generously donating a significant quantity of components used in this project.

Finally, I would like to acknowledge the financial support of the Science and Engineering Research Council (now Engineering and Physical Sciences Research Council).

Contents

Chapter 1 Introduction

1.1 Introduction

This thesis describes the design and construction of a simultaneous drive Electrical Impedance Tomography (EIT) system and its application to a linear array of electrodes. EIT is a non-invasive technique by which an unknown conductivity distribution in a particular plane of a region of interest can be estimated. Electric current is introduced into the medium of interest through electrodes placed on the surface of the medium [1], or by magnetic induction [2]. The resulting potential differences are measured on the surface of the medium by other electrodes and used to determine the conductivity distribution.

Applications for EIT exist in medicine, industry, geology and archaeology. The principle of using electrical currents and measured potentials to determine unknown impedance distributions was used as early as 1920 in geophysical prospecting [3] and a similar method is still used today [4]. In 1978 Henderson and Webster produced an image of the thorax using electrical methods [5], and in 1982 Barber and Brown produced the first tomographic in-vivo image with the Applied Potential Tomography (APT) system [6]. This led to the development of an APT system which used 16 encircling electrodes and could take measurements at a rate of 24 frames a second [7]. Since then a number of working EIT systems for medical applications have been reported which use 16, 32, or 64 electrodes [7][8][9]. Typically these take 28ms or longer to gather the data and some produce images in real-time [10][11]. EIT has only been applied to industrial processes since about 1990 [12] and its most common area of application is in measuring the cross section of contents of pipes and mixing vessels [12].

It is difficult, using EIT, to produce an image of the absolute conductivity distribution of the medium of interest (sometimes called a static image). This is because a slight deviation in electrode positioning on the surface of the medium of interest, or a deformation of the surface shape gives rise to large errors in the measured potential differences. These errors are large compared to the potential differences caused by inhomogeneities to be determined, and so the conductivity distribution cannot be imaged accurately [13]. Consequently, images of changes in the conductivity distribution with time are usually imaged. This imaging process, called dynamic imaging [14], is performed by taking two sets of measurements, the reference set and data set, which are separated in

time, and using the difference between the two sets of data to produce the image. Any errors which are caused by electrode positioning or other 'static' errors will be present in both the reference and the data set. By subtracting the measurement sets, any coherent errors will be removed, leaving only the information about the change in conductivity. Griffiths [15] was the first to propose and demonstrate the use of two frequencies to generate a pseudo-static image (ie not a dynamic image due to changes of conductivity with time, but an image of changes of conductivity with frequency). This was performed by taking one set of measurements with the drive current at one frequency and then repeating the measurements with the drive current at another frequency (41kHz and 82kHz were the frequencies used by Griffiths). The data sets at the different frequencies were subtracted, so eliminating the coherent errors, and the conductivity differences due to the change in frequency were imaged [14].

Since temporal changes in conductivity are often of interest, the time required to perform the measurements is often an important parameter. The work described in this thesis uses an original technique to reduce the measurement time. There are a number of advantages to be gained by decreasing the measurement time. If consecutive measurements can be made at higher speeds, faster events can be monitored which may not be possible using other methods. Also, if a dynamic process is being imaged, the shorter the measurement time, the less the conductivity distribution will have changed during the measurement time. If the electrodes were mobile and the position of the electrodes was detected or known, a sequence of images could be taken which could be used as a basis for producing a 3D image. If the conductivity distribution is not changing rapidly, a number of measurements could be taken and averaged in order to increase the signal-to-noise ratio of the reference and data sets.

Most of the medical and industrial applications of EIT use an encircling array of electrodes, but for geological and archaeological applications, such an array is not feasible. It is also the case that encircling arrays cannot be used in some medical and industrial situations. Although the system reported here can be applied to any configuration of electrodes, the instrumentation in this thesis is applied to a linear array of electrodes, ie the electrodes are placed in a line on the surface of the region to be investigated. This electrode arrangement was chosen partly because it is the most demanding geometry from an instrumentation point of view.

This chapter gives the background information to the project. The next section reviews the present tomographic imaging methods used in medicine, industry and geology

and outlines the advantages of EIT over other imaging modalities and the particular applications for which it is used. The theoretical background of EIT is explained and an example of an image forming technique is given. A brief review of the measurement speeds of existing EIT systems is followed by a description of the electrode arrangements used in different applications. The proposed work is described and the chapter concludes with an outline of the rest of this thesis.

1.2 EIT and Other Tomographic Imaging Techniques

EIT has been used in medicine to image a number of conditions or bodily functions. Present medical applications of EIT include lung perfusion and cardiac output [16], where an encircling array of electrodes are used. Images have been produced in real-time allowing problems in the cardio-pulmonary system to be identified [10]. Lung ventilation has also been imaged in real-time and lung defects have been detected [17]. Gastric emptying has been imaged using EIT [18] and the monitoring of the movement of thoracic fluids in space (zero gravity) has been proposed using a specially built portable APT system [19]. The tissue temperature of patients undergoing hyperthermia treatment for tumours has also been imaged [20].

The main drawbacks of EIT as a medical imaging system are its poor spatial resolution and the limitations imposed by 3D effects. The resolution can be increased to some degree by an increase in the number of electrodes used to make the measurements [21], but the physical aspect of attaching a large number of electrodes to a patient is impractical in some applications. Considerable effort is being expended at present in understanding 3D effects in EIT [22][23][24], both in terms of compensating measurements and in the formation of 3D images.

EIT is a medical imaging technique with little or no hazard associated with repetitive use [9]. It can have good tissue contrast since the conductivity of one soft tissue can be markedly different from the conductivity of another soft tissue [25]. EIT systems are relatively cheap in comparison with other medical imaging systems. A number of other medical imaging techniques use x-rays or radioisotope radiation where repetitive use is not advisable due to the harmful nature of prolonged exposure of bodily tissue to the sources. These methods include planar x-radiography [26] where a projection image is formed of x-ray absorption through the body. This method is used to identify bone fractures and tumours but cannot easily distinguish between soft tissues. A modification to planar x-radiography is x-ray computerised tomography [26] where the x-ray source and detector are rotated around the

body and a number of projections are made. This allows a tomographic image to be produced, but the process involves a longer exposure to x-rays and so its use is restricted. Radiation techniques are used to image parts of the body where radioactive isotopes are introduced to the body intravenously or orally and the progress of the isotopes are tracked by gamma ray detectors [27]. These methods also have some risk associated with them and so are not used repetitively. In medical imaging applications of ultrasound [26], waves emitted from a source are detected after reflections from a tissue interface. This method is not known to be harmful and can be used repeatedly, but because very little reflection occurs at an interface between two relatively soft tissues, tissue contrast is generally poor in ultrasound images. Magnetic Resonance Imaging (MRI) [27] is an imaging process which applies a large magnetic field to the body. This aligns the protons in the atoms in the body and as the field is removed, the energy emitted by the relaxation of the protons is detected and from this an image of the body can be produced. Although the resolution and soft tissue contrast for an MRI image are excellent, the systems are very expensive - typically two orders of magnitude more expensive than an EIT system.

EIT and Electrical Capacitance Tomography (ECT) [28], a similar method to EIT, are both used in imaging industrial processes despite their relatively poor resolution. In ECT systems the discharge times of capacitances are measured (the capacitances consist of the electrodes on the surface of the medium and the dielectric is the medium being investigated) [29] rather than the transfer impedance (voltage difference measured divided by current injected into the medium) as in EIT.

Both EIT and ECT are used to measure the concentration and velocity profiles of mixtures of two components flowing in a pipe and imaging cross sections of mixing vessels [12][29]. Other applications of ECT are flow rate measurement [12] and combustion process imaging [30]. EIT has been used to image structured soil samples [31], hydrocyclone separator dynamics [32] and resistivity distribution of semiconductor wafers [33].

Other imaging techniques used to image industrial processes are similar to those used in medical imaging. However, radiation imaging techniques such as x-rays [28], gamma ray detection [28], microwave [34], PET (Positron Emission Tomography) [28] and PEPT (Positron Emission Particle Tracking) [35] suffer from stringent safety requirements and expensive components. MRI (Magnetic Resonance Imaging) is used in some processes [28], but is very expensive and temporally poor so it is not used for real time imaging. Ultrasound is used in some applications [36] but has poor resolution and optical tomography,

which uses light sources and sensors, can only be used where the medium being imaged is not opaque [28].

Electrical methods have been used in geophysical applications since Schlumberger first proposed their use in 1920 [3] and EIT has been used to map large scale structures of particular areas of geological interest [37][38]. EIT has been used to detect geophysical strata in a process called resistivity sounding [39][40] where two or three horizontal layers of material can be detected. EIT is also used for resistivity profiling [40] where the whole electrode array is moved laterally along the area to be profiled thus detecting changes of conductivity in the horizontal direction rather than the vertical. Preliminary investigations have also been performed on the possible use of EIT in archaeological surveying [41]. A similar process to ECT is also used in geophysics, called induced polarisation [4]. A pulse of current is applied to two of the electrodes in the ground and the resulting potential difference measured on the two other electrodes. When the current returns to zero, the voltage does not instantaneously return to zero, but decays in a manner characteristic of the rock (dependent upon the interaction between the electrolyte and the metallic minerals in the rock). If the decay shape is measured, the rock can be identified.

Other geophysical detection techniques used to detect rock formations include gravity meters which are spring based instruments used to detect local increases in gravity due to the presence of high density rock , but this method suffers from errors due to latitude, altitude, tides and terrain all of which have to be compensated for [39]. Proton magnetometers can be used to detect the presence of rock types that are magnetic [4], but since these are few, their use is limited. Scintillometers and other radiation detectors are used to measure the radiation emitted from naturally radioactive rock and materials and hence the quantity of the radioactive material present can be deduced [4]. A number of electromagnetic methods exist which are used to locate geological inhomogeneities by detecting the eddy currents generated within the inhomogeneity by the application of an external time varying magnetic field [4], but this can only be used for reasonably conductive inhomogeneities. Seismic methods are perhaps the most common geophysical technique for determining strata and work on the principle of creating a seismic wave and detecting the reflections and refractions of the wave from the strata [39]. However, unlike EIT, this technique cannot be used to detect inhomogeneities or vertical discontinuities.

1.3 The Theoretical Background of EIT

This section will explain the theoretical background of EIT and demonstrate how an image can be generated from the potential difference measurements made on the surface of the medium of interest.

Figure 1.1 shows a linear array of 16 electrodes on the surface of the medium of interest. The current is introduced into the medium via electrodes 1 and 2 and the potential differences between the remaining adjacent electrodes are measured ie between 3-4, 4-5, .., 15-16. The current drive is then moved to electrodes 2 and 3 and the measurements of potential differences between remaining adjacent electrodes made again. This process is repeated until all adjacent electrode pairs have been driven. In practice, some of these measurements are reciprocal, for example measuring the potential between electrodes 8-9 when driving current between electrodes 3-4 gives the same result as measuring the potential between electrodes 3-4 when driving current between electrodes 8-9. Therefore, only half the measurements are independent.

If the position of a pair of current injecting electrodes placed on the surface of a homogeneous region of interest is known accurately, the current distribution within the medium can be calculated theoretically and since the equipotential loci are perpendicular to the currents, these can also be determined. For a linear array, the potential at a point due to one current drive can be derived for a semi-infinite homogeneous 2D and 3D region as shown by Powell [42].

For a 3D region the potential, Φ, at a point is given by

$$\Phi(r_1, r_2) = \frac{I}{2\pi\sigma}\left(\frac{1}{r_1} - \frac{1}{r_2}\right) \qquad \{1.1\}$$

where I is the current amplitude, σ is the conductivity of the homogeneous medium, r_1 is the distance from the electrode used to source current to the point and r_2 is the distance from the electrode used to sink current to the point.

For a 2D region the potential is given by

$$\Phi(r_1, r_2) = \frac{I}{\pi\sigma_a}\ln\left(\frac{r_2}{r_1}\right) \qquad \{1.2\}$$

where the variables have the same meaning as in Eqn {1.1} except for σ_a which is the conductivity per unit length in the direction perpendicular to the plane of interest. Since σ_a is not really a meaningful parameter, the equation can be extended to a pseudo-2D situation

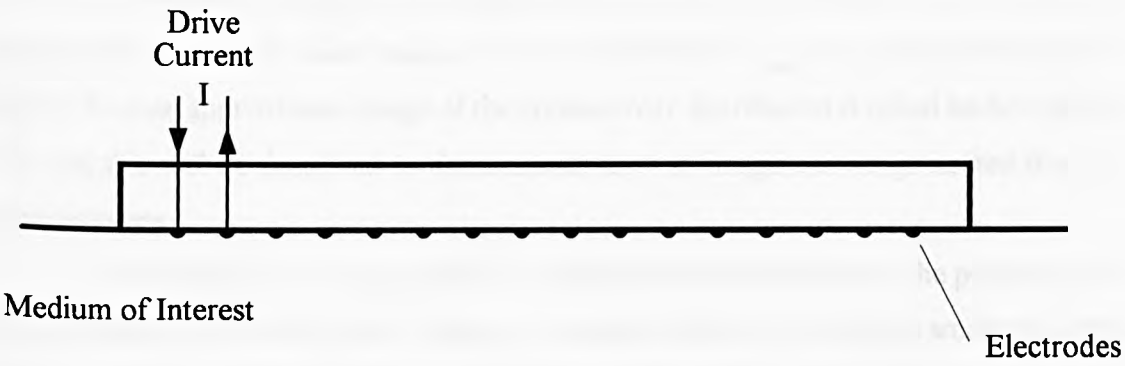

Figure 1.1 : A linear array of 16 electrodes applied to the surface of a medium of interest.

where the medium of interest has a finite depth but it is assumed that the currents flow in the same pattern as for a 2D situation and are constant in the z direction (depth). The pseudo-2D equation is

$$\Phi(r_1, r_2) = \frac{I}{\pi\sigma d} \ln\left(\frac{r_2}{r_1}\right) \qquad \{1.3\}$$

where the variables have the same meaning as in Eqn {1.1} and d is the depth.

The equipotential loci for a homogeneous region can be seen in Figure 1.2 for the drive pair 8-9. The potential differences which should be measured between the adjacent receive electrodes can be calculated and are denoted as V_{ref}. If the region were non-homogeneous and a small object of conductivity different from the background conductivity were to be introduced into the medium of interest as shown in Figure 1.3, the potential differences between the adjacent receive electrodes will be different from those for the homogeneous case and these measurements are denoted as V_m. One method which can be used to form an approximate image of the conductivity distribution is called backprojection [13] and this will be described to demonstrate how an image can be generated from the measurements.

The method of backprojection assumes that the perturbation to the position of the equipotential loci caused by the presence of a conductivity discontinuity is small and can be neglected. For a small object of lower conductivity than the background medium placed in the region to be imaged as shown in Figure 1.3 the measurement between the electrodes 2 and 3 will be the measurement most affected by the presence of the object ($(V_m - V_{ref})/V_{ref}$ will be the largest) for the drive pair shown. It can be inferred from the change in the measured voltage difference that the inhomogeneity lies partly or wholly within the equipotential band which terminates on the electrodes 2 and 3. In forming the image, the band bounded by the equipotential loci which terminate on each electrode pair is weighted by the value $(V_m - V_{ref})/V_{ref}$ for each receive pair for one drive. This process is repeated for all the drive pairs and the images generated are superimposed. The images will add to produce a region of low conductivity in the final image at the approximate position of the inhomogeneity and in this way small inhomogeneities can be imaged. Although the backprojection procedure is empirical, it has been widely used to produce useful images [13].

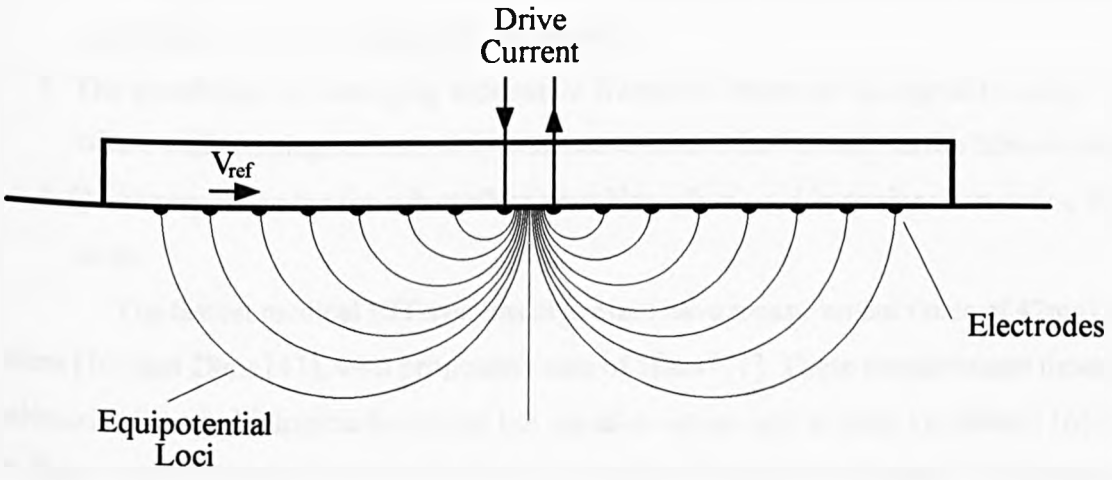

Figure 1.2 : Equipotential loci for a linear array caused by a central drive pair.

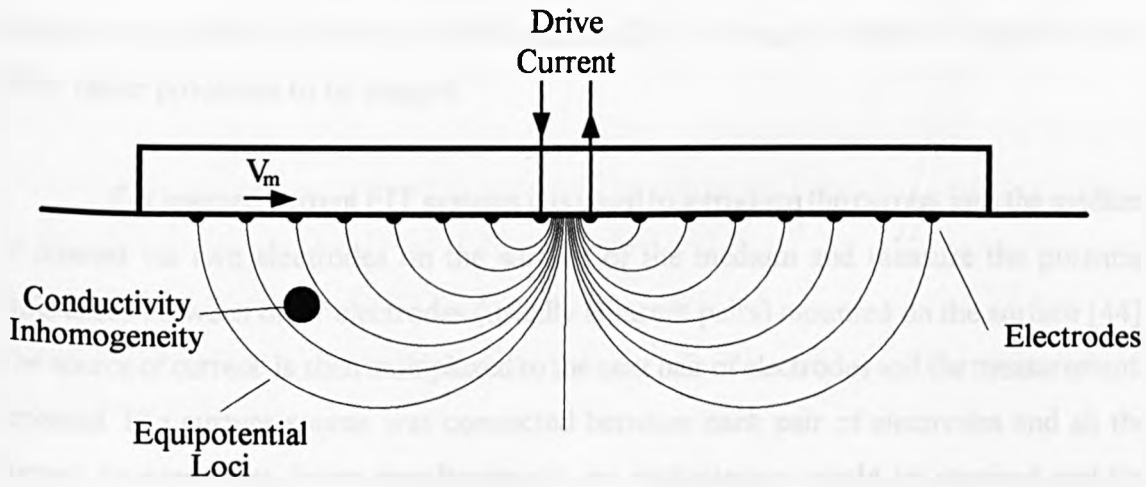

Figure 1.3 : Equipotential loci for a linear array caused by a central drive pair with a single inhomogeneity as shown.

1.4 Measurement Time

The advantages to be gained by a reduction in measurement time were given in section 1.1 and include

1. The possibility of imaging fast events.
2. The taking of snapshot measurements (ie the conductivity distribution does not change significantly over the measurement period).
3. The possibility of averaging successive frames to increase the signal-to-noise ratio where with existing systems only one measurement can be made in the time available.
4. Quick response time for sub-surface searching when used in conjunction with a linear array.

The fastest medical EIT systems at present have measurement times of 42ms [16], 40ms [10] and 28ms [43], with proposed times of 16ms [11]. These measurement times are adequate to image biological functions, but signal-to-noise ratio is often a problem [16][44]. A faster measurement time would allow averaging of successive frames to increase the signal-to-noise ratio.

In general, the systems used for geological applications are not optimised for speed since the objects being imaged are usually static (rock) or changing slowly (seepage) and so a decrease in measurement time would be of limited use.

Industrial EIT systems are often used to measure dynamic events eg flow rates, mixing processes, chemical processes and combustion events. The speeds of industrial EIT systems are currently similar to medical systems [23], although a faster EIT system would allow faster processes to be imaged.

For injected current EIT systems it is usual to introduce the current into the medium of interest via two electrodes on the surface of the medium and measure the potential differences between other electrodes (usually adjacent pairs) mounted on the surface [44]. The source of current is then multiplexed to the next pair of electrodes and the measurements repeated. If a current source was connected between each pair of electrodes and all the current sources were driven simultaneously, no multiplexing would be required and the time necessary to take a full set of measurements would be reduced by a factor of $1/n$, where n is the number of pairs of injection electrodes. The potential differences detected at the electrodes would be the sum of the potential differences due to each current source and so it must be possible to identify the contribution made to each potential difference by each of the sources. In order to measure the potential difference caused by each drive, the drive

waveforms must have a low cross-correlation, and suitable signals would be sinewaves at different frequencies.

The approach of using simultaneous currents to drive the medium of interest has been suggested by Murphy [45] and subsequently by Rosell [46] and by Hasekioglu [47]. Although methods of simultaneous drive have been proposed, no images appear to have been produced from measurements made in this way. One reason for this could be the technical difficulties of such a system, including system complexity and the requirements on matching of the component parts which lead to a demanding specification. In this work an EIT system using a simultaneous drive methodology and digital filtering to separate the measurements has been designed and constructed, and has been shown to produce a significant reduction in measurement time.

It should be noted that at present, many EIT groups are using wideband multiple frequency currents applied serially to the medium of interest in order to characterise tissue [48] (in biological applications) or material [49] (in industrial applications). This characterisation can be performed because the conductivity of some chemicals and cellular structures vary with frequency [48][50] in a manner characteristic of its tissue or material type, and is essentially an extension of the work by Griffiths [15]. By performing a series of measurements on the medium of interest over a wide band of frequencies, the frequency dependence of conductivity of each pixel in the image can be measured and hence the tissue or material type determined.

The object of the work described in this thesis is not tissue characterisation and does not use the frequency dependence of the conductivity of materials. Indeed, the frequencies used are chosen such that any change in conductivity within the range of frequencies is negligible. In this work multiple frequencies are being used purely so that the medium of interest can be interrogated quickly. This system will be referred to in the rest of this thesis as a narrowband multifrequency simultaneous drive EIT system. The possibility of combining tissue characterisation and parallel drive are discussed in Chapter 8 in the section on future work.

1.5 Electrode Arrangements

In principle, EIT can be used with any arrangement of electrodes. In medical applications, the region of interest is often approximately circular in cross section (eg thorax, head, leg, arm) and so the usual arrangement is to use a ring of electrodes to encircle the part of the body to be imaged [7][8][9] (see Figure 1.4(a)). The image generated from

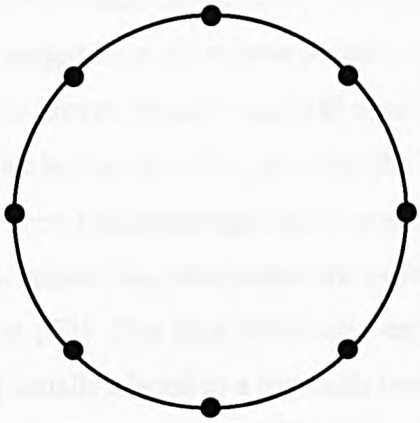

(a)

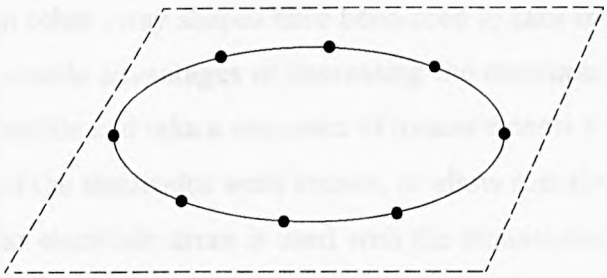

(b)

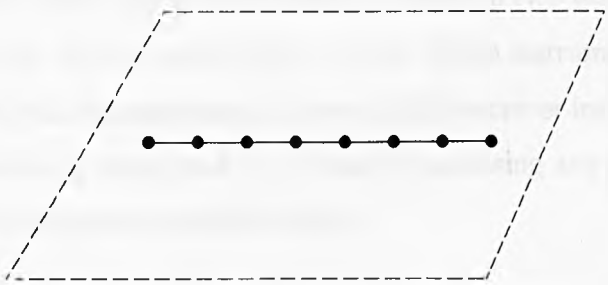

(c)

Figure 1.4 : Electrode Arrangements.

(a) Encircling Array.

(b) Rosette.

(c) Linear array.

these measurements represents a slice of the body through the plane of the electrodes. Other shapes have been investigated to determine possible advantages that can be gained from non-encircling electrode arrays. Smallwood [18] used a rosette, a ring of electrodes placed on the surface as shown in Figure 1.4(b), to image the stomach and Powell [51] used electrodes in a line (or linear array) to image regions close to the surface (see Figure 1.4(c)).

In geological applications four electrodes are usually used [39], although linear multi-electrode systems exist [52]. The four electrodes can be arranged in a number of configurations [39], but are usually placed in a line with two of the electrodes being used for the current source and sink, and the potential between the other two electrodes being measured. The electrodes are then moved, another measurement made and the process repeated until enough data has been gathered.

Industrial applications use the encircling electrode array to image circular cross sections [12], although other array shapes have been used to take measurements [53].

One of the possible advantages of decreasing the measurement time could be to make the array more mobile and take a sequence of measurements to produce either a 3D image, if the position of the electrodes were known, or allow real-time searching of a sub-surface region. A linear electrode array is used with the simultaneous drive EIT system, since it is difficult to achieve mobility using encircling electrodes unless the object is perfectly circular. In the context of an encircling array for medical purposes, mobility is impractical. In a linear array the electrodes would be in a fixed position on a rigid probe, and the probe could thus be swept across the surface of the medium of interest. The same is also true of a rosette although this would require the surface to be flat in two directions.

The linear array is very demanding in terms of the instrumentation required for making measurements (the dynamic range required of the receiver instrumentation is much larger than for an encircling array) and so is ideal for assessing any problems which may arise from the use of simultaneous parallel drives.

1.6 Outline of Thesis

The rest of this thesis describes the design of a simultaneous drive system applied to a linear electrode array.

In Chapter 2 the general specification for the narrowband multifrequency simultaneous drive system is developed and an overview of the component parts which will be required in the system is given. Chapter 3 is concerned with the drive circuitry, including waveform generators, current sources and common mode feedback circuitry. Detailed

specifications are generated and the important decisions leading to the final design are highlighted. The final circuitry used in the system is described in detail and its measured behaviour is compared with simulation and the specification and any shortfalls are stated. Chapter 4 details the receive circuitry used to measure the adjacent potential differences on the surface of the medium of interest and explains the filtering process used to separate the potential differences at each drive frequency. Again the circuitry is described in detail and predicted and measured performance compared against the specification. Chapter 5 describes the phantom used to test the system and the overall control of the system. This includes a description of the phantom and electrode array and their critical dimensions as well as a detailed description of the circuitry used to control the system and interface to the host computer. In Chapter 6 some common image forming algorithms and image filters are described. Images produced from data generated analytically are presented to demonstrate the limitations of the image forming algorithm and filters are applied to the image to improve the image quality. Chapter 7 presents measurements made on the phantom by the narrowband multifrequency simultaneous drive system and compares these with expected calculated values. Images of a number of conductivity distributions are shown including multiple objects and moving targets. In Chapter 8 conclusions are drawn from the work presented in this thesis and some suggestions for development and future work are given.

Chapter 2 System Configuration

2.1 Introduction

In this chapter the specification used as a basis for the design of the narrowband multiple frequency simultaneous drive EIT system is generated. Although a linear array is the specific subject of this work, the technical aspects considered here would apply equally to an encircling array. The major difference in the specification for the two array types is the increased receiver dynamic range required for a linear array of electrodes. It should be noted that although the requirements are discussed separately, in some cases they are highly inter-related and some degree of compromise is necessary.

Firstly, the physical arrangement of the electrode array is discussed and the drive type, measurement speed and the frequency and amplitude of the drive waveforms are considered. The expected dynamic range requirement, which is larger than for a single multiplexed source system, is calculated and an outline specification of the measurement system is developed. The chapter concludes with a summary of the specification of the system.

2.2 Electrode Arrangement

In early EIT systems, and some present systems, current is injected into the medium of interest via the same electrodes that are used to make the voltage difference measurements on the periphery of the medium [7][8]. This dual functionality of the electrodes means that the voltage buffers need to be disconnected when the electrode is being used to source or sink current and that the current source needs to be disconnected when the electrode is being used for voltage measurements. The electrode function switching is usually performed by analogue switches. The input capacitance of an analogue switch is typically 10pF [54], an impedance of approximately 800kΩ at 20kHz. This impedance is in parallel with the output impedance of the current source and the input impedance of the voltage buffer at the electrode, thus limiting the total impedance presented to the electrode to a maximum of 800kΩ. The lower the impedance to ground at the electrode, the more current will flow to ground through it, instead of flowing through the medium of interest. This distorts the equipotential loci and thus affects the image forming process which assumes no loss of

current. Since the electrodes perform the dual function of current injection and voltage measurement, the number of independent measurements is reduced since reciprocity can be applied as stated in section 1.7. Also, due to the presence of contact impedances between the medium of interest and the electrodes, the potential at the electrode being driven cannot be measured reliably and thus further reduces the number of measurements available.

These limitations can be overcome by using separate electrodes for current injection and peripheral voltage sensing [9] and this is the arrangement used in this system. The drive and receive electrodes are chosen to be equispaced and interleaved, although other configurations can be used (eg parallel arrays).

For an encircling array of electrodes, the electrode system is continuous and so there are equal numbers of drive and receive electrodes, giving an even number of electrodes. Most EIT systems which use an encircling array of electrodes have 16 or 32 electrodes [7][8][15]. To ensure symmetry for a linear array the electrodes at each end of the array must perform the same function ie they must both be either drive electrodes or receive electrodes, giving rise to an odd number of electrodes. The simultaneous drive system was chosen to have 16 drive electrodes and 17 receive electrodes making a total of 33 electrodes. The number of independent measurements that can be made for this arrangement is 15x16=240. A diagram showing the electrode arrangement can be seen in Figure 2.1.

A major concern in the design of injected current EIT systems is the common mode voltages that are generated in the medium of interest by mismatches in the system parameters. For example, a mismatch in the source and sink current of a drive will result in a net flow of current into, or out of, the medium of interest. This current will flow to or from ground through the output impedances of the current sources (and any other impedances to ground) causing a common mode voltage to be set up between the medium of interest and ground. This is particularly significant in this design because the parallel sources at different frequencies will all contribute to the common mode voltage. A facility to apply common mode feedback will be required to reduce the effects of these common mode voltages in the medium, (see Section 3.5 for more details), and so a further two electrodes placed at a distance from the array (in the 'far field') will be required for this purpose.

2.3 Speed of Measurement

The aim of this work was to evaluate a multiple frequency simultaneous drive system and identify the critical factors associated with the use of such a system to maximise measurement speed. A system described by Zhu quotes a measurement time of 16ms [11]

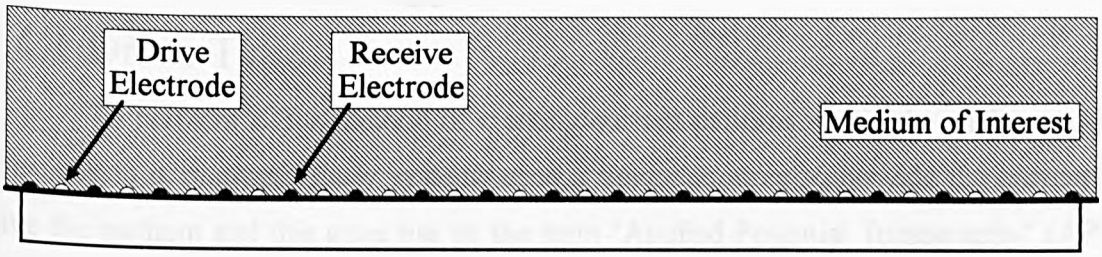

Figure 2.1 : The linear array of 16 drive electrodes and 17 receive electrodes.

and so a measurement time of less than 16ms was proposed.

Practically there is a limit to how fast measurements can be made and compromises have to be made. For example, a reduction in measurement time increases the bandwidth of the system and hence reduces the signal-to-noise ratio. A reduction in measurement time also corresponds to an increase in drive frequency separation, which will mean that the frequency dependence of the conductivity of particular materials can no longer be ignored.

After making appropriate compromises on the issues stated above, the system was designed to take the measurements as quickly as possible and the data was stored for off-line processing. For conductivity distribution changes which are imaged by existing slower systems, it would be possible to take a number of frames and average them in order to increase the signal-to-noise ratio of the measurements.

2.4 Drive Methodology

2.4.1 Drive Type

To perform EIT a method of creating current patterns within the medium under investigation is required. Early systems used a voltage source to provide the current to drive the medium and this gave rise to the term "Applied Potential Tomography" (APT) [1]. Since then, most groups have used a constant current drive strategy with one source to inject and another to extract a constant current [10][55]. The method of Adaptive Impedance Imaging is used by some [9][11] to create a range of current patterns in the medium under investigation which are different from the current patterns generated by a single source-sink pair. In Adaptive Impedance Imaging all drive electrodes are used simultaneously to inject a current of the same frequency, and the current patterns are determined by control of the amplitudes of these injected currents. In this way current patterns which are claimed to give the optimum information about the medium under investigation can be employed [56].

Some groups using the Adaptive Impedance Imaging technique have reverted to the voltage driven system and measure the current being injected into the medium [9]. Although it is easier to achieve the low output impedance required for a good voltage source than to achieve the high output impedance required for a good current source, this method has two major disadvantages. The first is a significant increase in the number of measurements that need to be taken and processed before imaging can be performed (the current at each electrode must be measured) and the second is that the amplitude of the current injected is dependent upon the load resistance and hence the conductivity of the medium being imaged.

A constant current source injection system does not suffer from the above disadvantages. Provided that the current source output impedance is large compared with the load impedance, the current delivered by the current source is defined without the need for measurement. For example, for a single multiplexed current drive system with a maximum load impedance of 3kΩ between the drive electrodes, an output impedance of 1.5MΩ will guarantee a 0.1% accuracy of the current flowing between the electrodes through the medium of interest (see section 3.4.2 for further details). The output impedances of the current sources used in various single multiplexed EIT systems are 830kΩ (at 10kHz) [55], 1.3MΩ (at 100kHz) [57] and 210kΩ (at 20kHz) [44].

A constant current source approach has been adopted in this system design since this approach does not require extra measurements to be performed and hence will minimise measurement time.

2.4.2 Drive Set

A drive set is defined as the set of independent measurements that can be made for a particular drive configuration. Figure 2.2 shows different drive sets for an encircling and linear array. The adjacent drive set is the set of measurements which are made when adjacent electrodes are used to source and sink current (shown in Figure 2.2(a) and (b) for the encircling and linear array). The polar drive set refers to an encircling array and is the set of measurements made when diametrically opposite electrodes are used to source and sink current. In circular geometries where the electrode array encircles the medium of interest, the most commonly used drive set uses adjacent drive pairs [7][10][58]. The non-adjacent drive sets have the advantage of increased signal size over the adjacent drive set, but in the case of dual function electrodes (electrodes which are used to drive and receive) it has the disadvantage of fewer independent measurements available (due to reciprocity) and four voltage differences, rather than three for the adjacent drive, are eliminated because the voltages cannot be measured at the drive electrodes. If measurements could be made at the drive electrodes, in principle it would be possible to calculate the data for one drive set from data measured for any other drive set using superposition. However, the signal-to-noise ratio of this calculated data would be reduced and in practice the voltages measured at the drive electrodes are unreliable.

In geophysical applications which use a linear geometry a four electrode approach is often used and the four electrodes are physically moved to take different measurements [59]. The positioning of the electrodes is dependent upon the application. For example

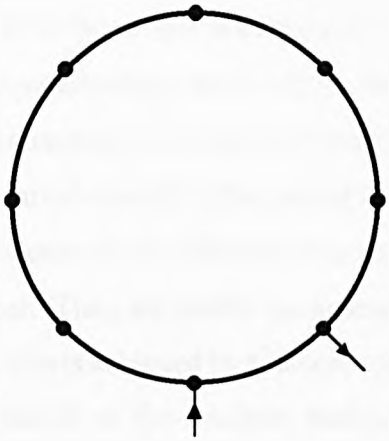

(a)

(b)

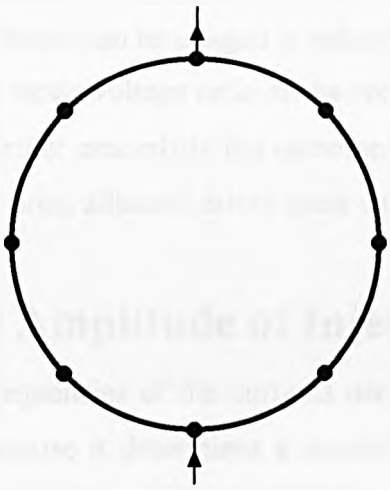

(c)

Figure 2.2 : Drive Sets.

(a) Adjacent drive set for an encircling array.

(b) Adjacent drive set for a linear array.

(c) Polar drive set for an encircling array.

when the depth of strata parallel to the surface is being measured, the current electrodes are placed between the two voltage measurement electrodes as shown in Figure 2.3(a). However, if the position of a vertical discontinuity is being measured as shown in Figure 2.3(b), the pair of current drive electrodes are distant from the pair of voltage measurement electrodes.

Powell [42] looked extensively at different drive sets for a linear geometry and the advantages to be gained by each. They are briefly summarised here :

1. Maximum depth of detection is achieved by adjacent source and sink drive electrodes.
2. The best y (depth) resolution of the resultant backprojected image is obtained by using adjacent source and sink drive electrodes.
3. The best x (array direction) resolution of the resultant backprojected image is obtained by using well spaced source and sink drive electrodes.
4. The smallest dynamic range of measurements is achieved by using well spaced source and sink drive electrodes.

The maximum depth at which a conductivity inhomogeneity can be imaged (using the backprojection method for the image formation) using a linear array is half the total length of the array if adjacent drives are used, the actual area of detection being almost semicircular with a diameter equal to the array length (see section 5.2.3). For any other drive set the depth at which objects can be imaged is reduced. Adjacent drives give rise to a low differential to common mode voltage ratio at the receive pairs in comparison with other drive sets, which will further exacerbate the common mode voltage problem, but in order to maximise the imaged area, adjacent drives were chosen.

2.5 Frequency and Amplitude of Injected Currents

The choice of the frequencies of the currents used simultaneously to drive the medium is very important because it determines a number of factors which define the specification of other parts of the system. For a single frequency EIT system the typical drive frequency is in the range 10 to 100kHz [1][8][10]. Lower frequencies have the following advantages :

1. The effect of stray capacitances is reduced since capacitive impedance is higher at lower frequencies.
2. A high common mode rejection ratio (CMRR) is more readily achieved in the subtractor circuitry, which is necessary to extract the difference in voltage between adjacent receive electrodes.
3. Sampling at a lower frequency allows a longer time for conversion and hence requires

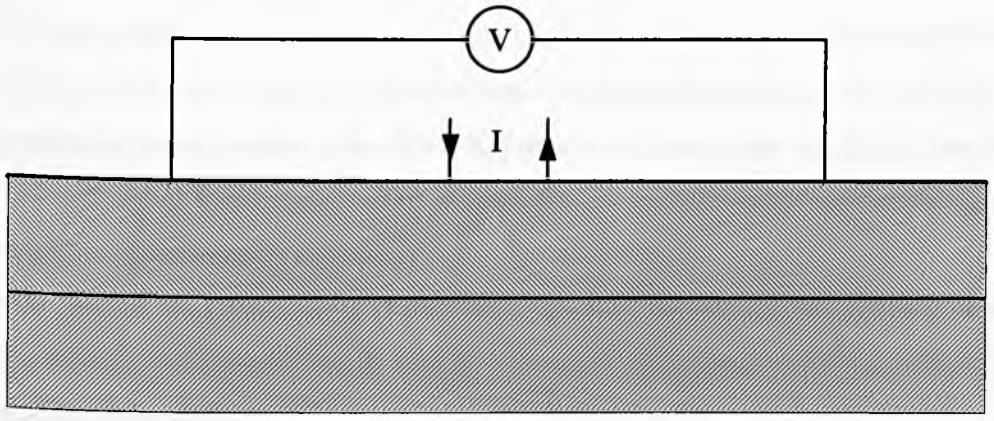

(a)

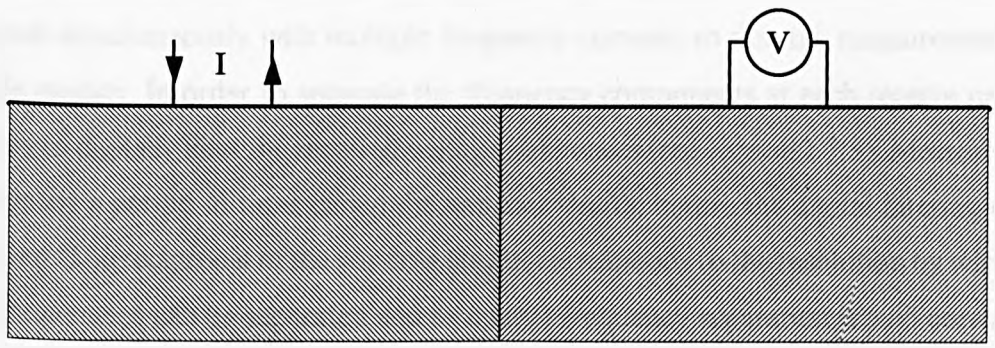

(b)

Figure 2.3 : Two drive sets used in geophysical applications.

(a) Drive set used for strata measurement.

(b) Drive set used for measurement of vertical discontinuity.

less expensive analogue-to-digital converters.

4. The errors introduced in sampling by aperture jitter are reduced since the maximum rate of change of voltage with time, dV/dt, is reduced.

Higher frequencies have the following advantages :

1. A higher amplitude of injected current is permitted for a medical system. BS5724, which specifies the upper limit of current that can be introduced into the body for a medically based system, permits a higher current amplitude at higher frequencies. Thus at higher frequencies the maximum signal size allowed is higher and hence the signal-to-noise ratio is increased.
2. The contact impedance seen at the electrodes will be reduced since the models used for contact impedance usually include a large series capacitor [60] and the effect of this will be reduced.

Since the majority of the advantages of using higher frequencies apply only to medical applications and the system is not being designed specifically for a medical situation, it was decided that lower frequencies would to be used in preference to higher frequencies.

As outlined in Chapter 1, the basic measurement philosophy is to drive the medium of interest simultaneously with multiple frequency currents so that the measurements can be made quickly. In order to separate the frequency components at each receive pair it is necessary to digitally filter the received voltage differences (see section 2.7.3). Measurements are made for a period of time, called the window length, before the digital filtering can be performed. The reciprocal of the window length corresponds to the resolution by which the signal frequencies can be separated and so a large frequency separation would correspond to a small window length and hence reduce the length of time for which measurements must be made. However, another consideration is the frequency dependence of conductivity; the frequencies used must be close enough together such that the variation of conductivity with frequency is small enough to be ignored.

Fifteen frequencies were required to drive the 16 drive electrodes. The available information on the frequency dependent characteristics of tissue and other materials over the range of 10-50kHz [61] suggested that a range of 10kHz or less would give only small resistivity changes. The drive signal frequencies were chosen to be $(20 + 0.5n)$ kHz for $0 \leq n \leq 14$, giving a range of 20 to 27kHz in steps of 500Hz.

Existing injected current systems used for medical applications are limited by the constraints of BS5724 to an injected current level of typically 2.5mA peak [10][23]. An amplitude of the same order (3mA) was chosen for each of the frequencies, since the experience of others has shown that currents of 2.5mA produce detectable voltage differences [10][42]. The sum of the total injected current will not satisfy BS5724 which imposes a limit of approximately 2.0mArms total at the frequencies of interest. Therefore the system could not be used in medical applications in its present form unless the current magnitude is reduced. However, the purpose of this work is to determine the feasibility of the method of simultaneous drive, and the value of 3mApeak (giving 8.3mArms total injection current) will ensure that adequate signal can be obtained.

2.6 Signal and Dynamic Range

Equations 1.1 and 1.3 are repeated here for convenience and can be used to calculate the potential at any point in a homogeneous region caused by a particular drive pair.

For 3D $$\Phi(r_1,r_2)=\frac{I}{2\pi\sigma}\left[\frac{1}{r_1}-\frac{1}{r_2}\right] \qquad \{1.1\}$$

For pseudo 2D $$\Phi(r_1,r_2)=\frac{I}{\pi\sigma d}\ln\left[\frac{r_2}{r_1}\right] \qquad \{1.3\}$$

where Φ is the potential generated at the point, σ is the conductivity of the homogeneous medium, r_1 is the distance from the current source, r_2 is the distance from the current sink and d is the depth of the medium of interest in the pseudo-2D case (the electrode array is placed at half the depth to maintain symmetry).

The table in Figure 2.4 lists the potentials generated at all the electrodes for a drive current between drive electrodes 1 and 2. Note that the potentials at the drive electrodes 1 and 2 have not been calculated using the above equations but have been calculated using Equation 5.1 in Chapter 5 which takes into account the finite area of the drive electrodes.

2.6.1 Single Frequency Signal Range

The signal range at each of the drive frequencies is given by the ratio of the maximum voltage difference to the minimum voltage difference at one frequency. This can be calculated by using the figures in the table in Figure 2.4 giving a single frequency signal range of 66dB for the 3D case and 47dB for the 2D case.

If a 25% change in the smallest potential difference is to be detected (Powell

Drive Electrode	Voltage in mV (3D)	Voltage in mV (2D)
1	4610.04	3763.94
2	-4610.04	-3763.94
3	-79.57	-165.48
4	-26.52	-96.79
5	-13.26	-68.68
6	-7.96	-53.27
7	-5.30	-43.52
8	-3.79	-36.80
9	-2.84	-31.88
10	-2.21	-28.12
11	-1.76	-25.15
12	-1.45	-22.51
13	-1.20	-20.77
14	-1.02	-19.10
15	-0.88	-17.69
16	-0.76	-16.48

Receive Electrode	Voltage in mV (3D)	Voltage in mV (2D)
1	212.21	262.27
2	0.00	0.00
3	-212.21	-262.27
4	-42.44	-121.96
5	-18.19	-80.33
6	-10.10	-60.00
7	-6.43	-47.90
8	-4.45	-39.88
9	-3.26	-34.16
10	-2.50	-29.88
11	-1.97	-26.56
12	-1.60	-23.89
13	-1.32	-21.72
14	-1.10	-19.91
15	-0.95	-18.37
16	-0.82	-17.06
17	-0.71	-15.92

Figure 2.4 : Expected potentials at electrodes for a 3D and pseudo-2D homogeneous medium caused by a 3mA peak drive current between drive electrodes 1 and 2 assuming a conductivity of $0.2Sm^{-1}$ and a receive-receive/drive-drive electrode spacing of 15mm.

quotes a maximum of 30% change in measurements between the reference and data set for an encircling array used in medical applications [42]) the signal range will be increased to 78dB for a 3D medium and 59dB for a pseudo-2D medium. The system resolution would have to be 78dB if the full range of 3D measurements were to be made. The smaller signals are associated with information about regions further from the array. There is less current passing through these regions and so not only are the measured voltage differences small, the resolution of the image forming algorithms in these regions is poor [21][62] (this is shown to be the case in section 6.3.1, when poor images are produced from analytically generated data for objects greater than a quarter of the array length from the array). Experience with single frequency injected current systems suggest that in practice, 60dB is a reasonable value [10] for the signal range. By choosing 60dB as the signal range for this system, a 25% change can only be detected for up to 7 receive electrode pairs from the drive, instead of the full array length, for a 3D medium. This reduces the depth of detection for the 3D case by approximately a factor of 2.

2.6.2 Dynamic Range

The dynamic range is defined as the ratio of the maximum instantaneous potential difference at any receive electrode pair divided by the minimum potential difference to be measured at any pair. The maximum instantaneous potential difference was calculated computationally and the worst case value of 0.6Vpeak between adjacent electrodes was obtained for the 2D case. Therefore the dynamic range is approximately 67dB (600/(1.14x0.25)).

2.6.3 ADC Resolution

The ADC resolution is defined by the expected dynamic range of the signals which is 67dB, corresponding to an ADC of resolution of 12 bits.

2.6.4 Noise

To be able to measure the signal range of 60dB stated in section 2.6.1, the noise should be at least 60dB down on the maximum signal amplitude at one frequency (or at least 67dB down on the maximum instantaneous signal). There are a number of possible sources of noise in an EIT system. There will be electronic noise (thermal, shot and flicker noise) generated by the drive and receive electronics and noise generated by the medium of interest itself (based on the thermal movement of ions). The noise at high frequencies

generated by these sources will be reduced by the use of an anti-alias filter which will also prevent the aliassed noise increasing the noise floor of the measurements. There will also be quantisation noise will be introduced at the point of analogue-to-digital conversion of the signals. Smith [44] concluded that the most significant source of noise in an EIT system is that due to the receiver circuitry and so efforts should be made to keep this noise at least 67dB below the maximum signal amplitude level.

2.7 Receiver Circuitry

2.7.1 Receiver Organisation

Since the system was being designed with a view to maximising the speed at which measurements could be taken, a parallel approach was taken to receiver design. To increase the speed for a serial system in which a single receive channel is multiplexed to each receive pair in turn, fast components must be used, often leading to the need for expensive hybrid components, especially the ADC. The time available for each measurement is also reduced which causes a degradation in signal-to-noise ratio. In a parallel system each receive pair, or channel, has its own associated receive circuitry. This increases the number of components required for the system, and hence its cost, but it simplifies system organisation and is a necessary strategy for achieving the fastest possible measuring system.

2.7.2 Gain Stage

For any drive configuration, the potentials generated at the receive electrodes, and hence the potential difference between the receive electrodes for a homogeneous medium, can be calculated. In conventional single frequency EIT systems the small potential differences which occur furthest from the drive are amplified to approximately fill the full input range of the ADC before being converted. This practice is called programmable gain amplification (PGA) and ensures that each measurement is made with the same signal-to-noise ratio (this is only true if the noise in the system after amplification is less than the quantisation noise of the converter, so the quantisation noise is the limiting noise of the system).

For a simultaneous multiple frequency drive system the potential difference at a single receive pair will have components at each of the drive frequencies and these will be of different amplitudes. In order to measure the voltage differences at each frequency to the same accuracy, a frequency dependent gain would need to be applied to the voltage difference before sampling. In practise it is very difficult to realise such frequency dependent circuitry with sufficient selectivity without also introducing serious problems of channel matching.

For the reasons given in section 2.7.3, the filtering of the received voltage differences is performed digitally and so frequency dependent gain cannot be applied and the option of programmable gain amplification is unavailable. The maximum gain that can be applied to the voltage difference is frequency independent and is defined by the largest instantaneous value of the difference voltage, which, when multiplied by the gain, must be within the input range of the ADC.

2.7.3 Filtering

The potential difference waveform at each receive pair of electrodes will have components at each of the drive frequencies. The waveform must therefore be filtered so that the magnitude (and phase) at each of the frequency components can be measured.

In general, filtering can be performed in the analogue or digital domain but, in this particular system, analogue filtering of the signals is not feasible. Firstly, the number of analogue filters that would be required (15 bandpass filters per channel) is considerable. Each filter output waveform would need to be sampled, hence increasing the number of waveforms to be sampled from 16 to (16x15). Secondly, each filter would require a high order to ensure the necessary attenuation at the other signal frequencies. This is a problem because the centre frequencies of the filters are subject to component tolerances, and if the centre frequency of the filter did not coincide exactly with the signal frequency, the gain at the signal frequency may be much smaller than expected.

Digital filtering does not have any of these problems. Only 16 signals will need to be sampled and no extra circuitry is required. Furthermore, by choosing the sampling frequency appropriately, it is possible to eliminate the errors due to windowing effects, as explained in the next section. The digital filtering used is discussed further in section 4.7.

2.8 Sampling and Windows

The amplitude of the potential differences between the receive electrodes must be measured for each frequency component. This is performed by sampling and digitising the voltage difference waveform prior to digital filtering.

The duration for which samples of the signal waveforms are taken is an important parameter and is called the window length, τ. When a Discrete Fourier Transform is performed on a sampled time waveform, the frequency spectrum from dc to half the sampling frequency is calculated for particular values of frequency, these values being multiples of the reciprocal of the window length (called the frequency resolution). It is important for

this application that the frequencies to be filtered correspond with an exact multiple of $1/\tau$. This is equivalent to the window length containing a whole number of cycles of each signal frequency [63]. In practice, by using a finite number of samples, a rectangular window is being applied to the sampled data and the frequency spectrum of the waveform is convolved with the Fourier Transform of the rectangular window function, which is a function of the form $\sin x/x$. These $\sin x/x$ functions, where $x=\omega\tau/2$, (which have nulls at $1/\tau$, $2/\tau$, $3/\tau$, .. as shown in Figure 2.5) are modulated at each signal frequency and will overlap with the $\sin x/x$ functions modulated at the other signal frequencies. By ensuring that the signals are all multiples of $1/\tau$, it has been ensured that each signal frequency will coincide with the nulls of all the other signal frequency modulated $\sin x/x$ functions as shown in Figure 2.6.

The drive frequencies used are (20 + 0.5n) kHz where $0 \leq n \leq 14$ and so the smallest window length which will contain an integer number of cycles of each signal frequency is 2ms (40 cycles at 20kHz and 54 cycles at 27kHz) giving a frequency resolution of 500Hz (1/2ms). If measurements are made for one window only, the measurement time will be 2ms and the measurement frame rate will be 500Hz which is 20 times faster than the real-time system reported by Smith [10].

2.8.1 Sampling Frequency

The sampling frequency must not be less than twice the highest frequency component in the signal to be detected (ie the sampling frequency must exceed 54kHz). By using a sampling frequency close to this value, more time is allowed for conversion which eases the time constraints and allows cheaper components to be used. However by using a lower sampling frequency, the likelihood of errors due to aliasing is increased, although this can be controlled by appropriate anti-alias filtering. For a converter with infinite resolution the amplitude of a sinewave can be accurately determined from just over two samples per cycle. However, for real converters, effects due to quantisation and other noise are introduced and these can be reduced by having as large a number of samples as possible in the fixed window length, τ. By choosing a sampling frequency which gives a number of samples in the window which can be expressed as a power of two, the possibility of using a Fast Fourier Transform to perform the digital filtering process is available (see section 4.7 for more details). This would correspond to sampling frequencies of 64kHz, 128kHz, 256kHz ... A sampling frequency of 64kHz would only give 2.4 samples per cycle at the highest frequency and was too close to the Nyquist frequency for convenient design of closely matched anti-alias filters. The higher sampling frequency of 128kHz was chosen for the

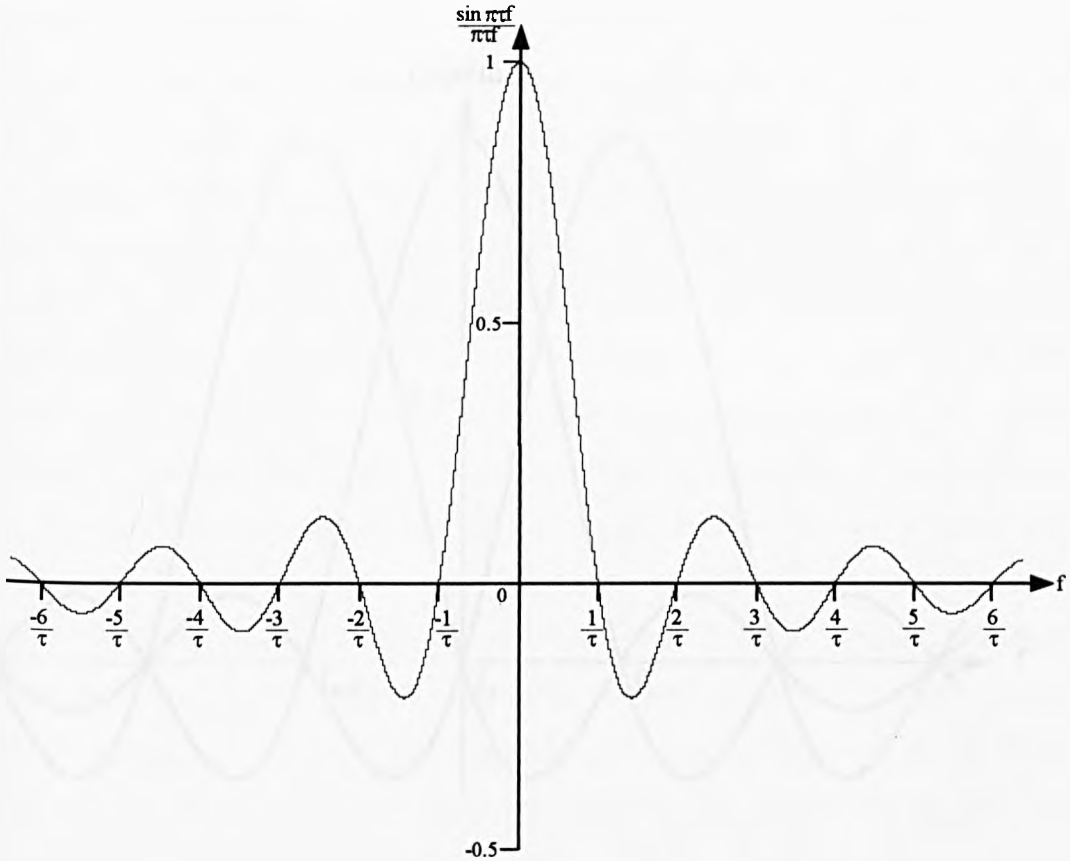

Figure 2.5 : The Fourier Transform of the rectangular window time function of duration τ.

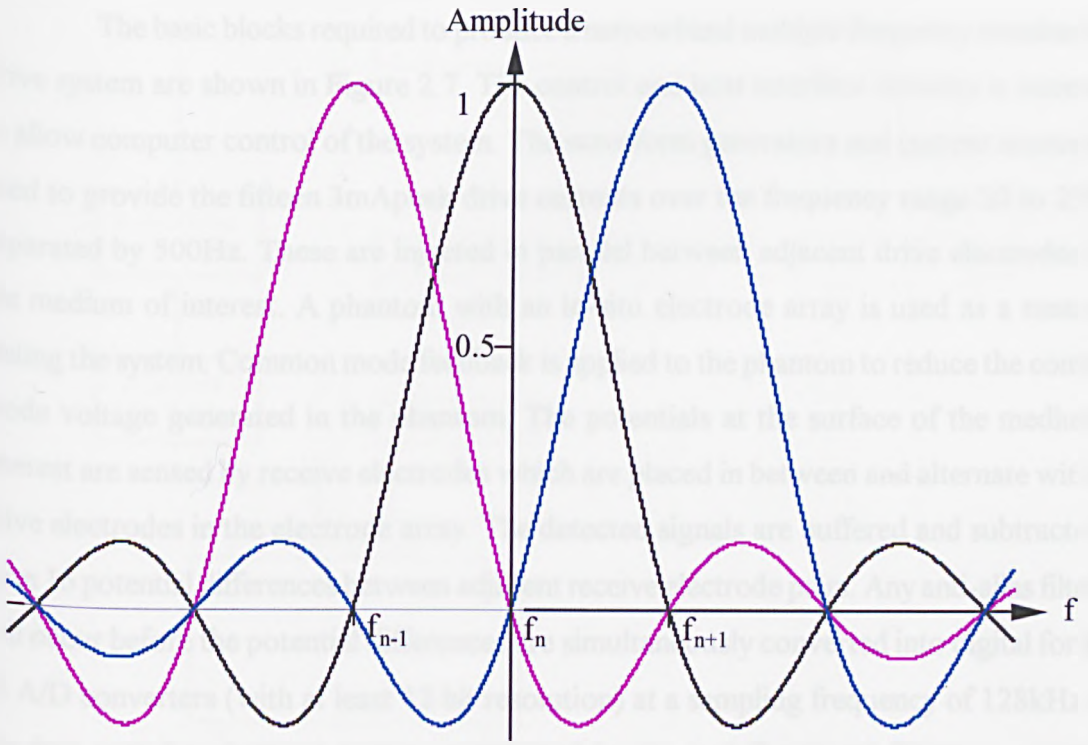

Figure 2.6 : Three signal frequencies and their sin*x*/*x* modulated functions.

sampling frequency giving 4.7 samples per cycle at the highest signal frequency and 6.4 samples per cycle at the lowest signal frequency. At higher sampling frequencies the ADCs become more expensive and fast memory would be required to store the data at the throughput rate of the conversion. A sampling frequency of 128kHz gives 256 samples per window.

2.9 Summary

The system requirements have been defined in the previous sections and are summarised here.

The basic blocks required to produce a narrowband multiple frequency simultaneous drive system are shown in Figure 2.7. The control and host interface circuitry is necessary to allow computer control of the system. The waveform generators and current sources are used to provide the fifteen 3mApeak drive currents over the frequency range 20 to 27kHz separated by 500Hz. These are injected in parallel between adjacent drive electrodes into the medium of interest. A phantom with an in-situ electrode array is used as a means of testing the system. Common mode feedback is applied to the phantom to reduce the common mode voltage generated in the phantom. The potentials at the surface of the medium of interest are sensed by receive electrodes which are placed in between and alternate with the drive electrodes in the electrode array. The detected signals are buffered and subtracted to form 16 potential differences between adjacent receive electrode pairs. Any anti-alias filtering will occur before the potential differences are simultaneously converted into digital form by 16 A/D converters (with at least 12 bit resolution) at a sampling frequency of 128kHz and the data stored in memory prior to transferral to the host for digital filtering and image forming.

The table in Figure 2.8 details the general specification and features of the system.

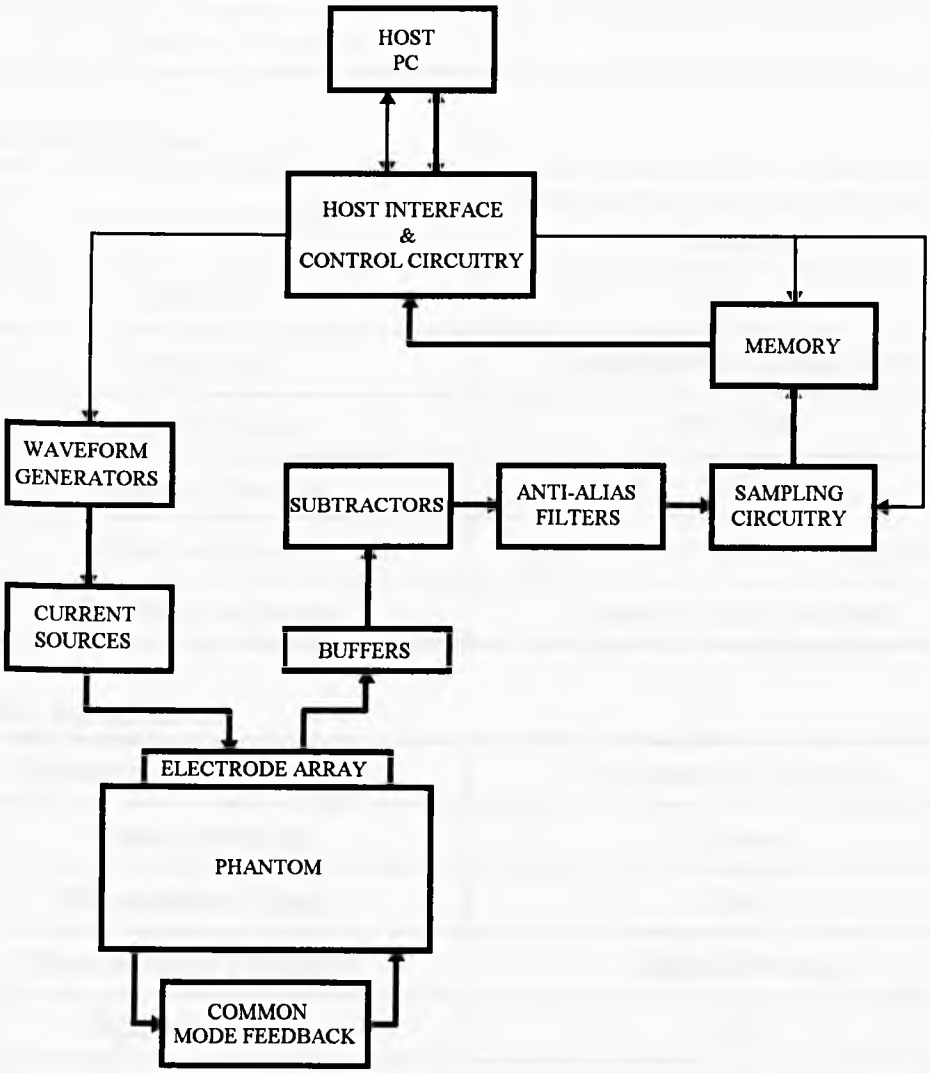

Figure 2.7 : Block diagram of component parts in the Narrowband Multiple Frequency Simultaneous Drive EIT System.

Physical Specification

Array Type	Linear
Electrode Arrangement	Equispaced Alternate Drive & Receive
No. of drive electrodes	16
No. of receive electrodes	17

Drive Specification

Drive Arrangement	Simultaneous Narrowband Multiple Frequency
Drive set	Adjacent
Drive type	Deterministic Current Drive
Frequency Range	20-27kHz
Frequency Spacing	500Hz
Drive Amplitude	Approx. 3mA peak per frequency
Miscellaneous Drives	Common mode feedback

Receive Specification

Measurement Arrangement	Simultaneous Detection
Measurement set	Adjacent
Measurement Speed	2ms
Demodulation Technique	Digital Filtering
Dynamic Range	67dB
Single Frequency Signal Range	60dB
ADC Resolution	12 bits
Noise Level	-67dB
Sampling Frequency	128kHz
No. of samples per measurement	256

Figure 2.8 : Table showing the features and general specification of the system.

Chapter 3 Current Drives & Common Mode Feedback Circuitry

3.1 Introduction

This chapter describes in detail the requirements and specification of the circuitry used to generate the injected currents and to apply common mode feedback to the medium of interest. In each section the general principle is discussed, the specification for the circuitry is generated, the design is presented and the measured performance compared with the expected performance. The important aspects of the design for the simultaneous drive system are that the signal sources should be defined in terms of frequency and amplitude to ensure accurate filtering and minimisation of common mode voltages.

3.2 Choice of Current Drive Topology

The drive methodology discussed in Section 2.4 requires each drive electrode, except for the two end electrodes, to be a source of current at one frequency and a sink of current at another frequency : a sink being defined as a current extractor (ie a source of current 180° out of phase with the corresponding current injector). Thus at a typical drive electrode there is a current containing two frequencies as shown in Fig. 3.1. Three possible configurations of hardware which could be used to achieve an alternating current containing the two frequency components are described below.

In deciding which method is best suited to a multiple frequency simultaneous drive system, the characteristics which are most desirable are a high output impedance at each drive electrode to minimise the loading on the medium, matched source and sink currents to minimise the common mode voltage and the minimum number of components per channel to minimise cost and pcb space. The most important of these considerations is maximising the output impedance of the current sources, since this will compromise the performance of the system such that compensation would be difficult. The common mode voltages generated by mismatches, however, can in principle be reduced by the application of common mode feedback.

Figure 3.2 depicts a system in which each waveform generator produces single frequency sinewaves. These are fed directly to the current sources which produce antiphase

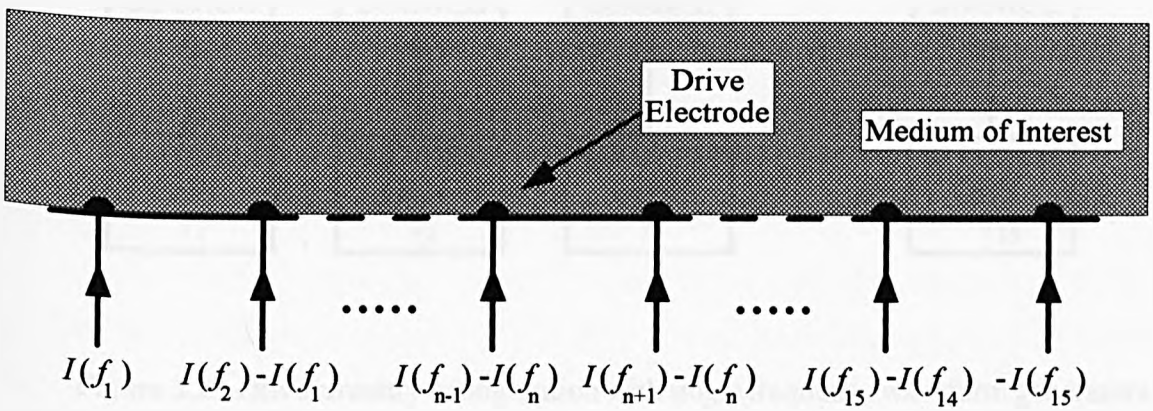

Figure 3.1 : Diagram showing the frequency components of the drive currents. (Only drive electrodes are shown).

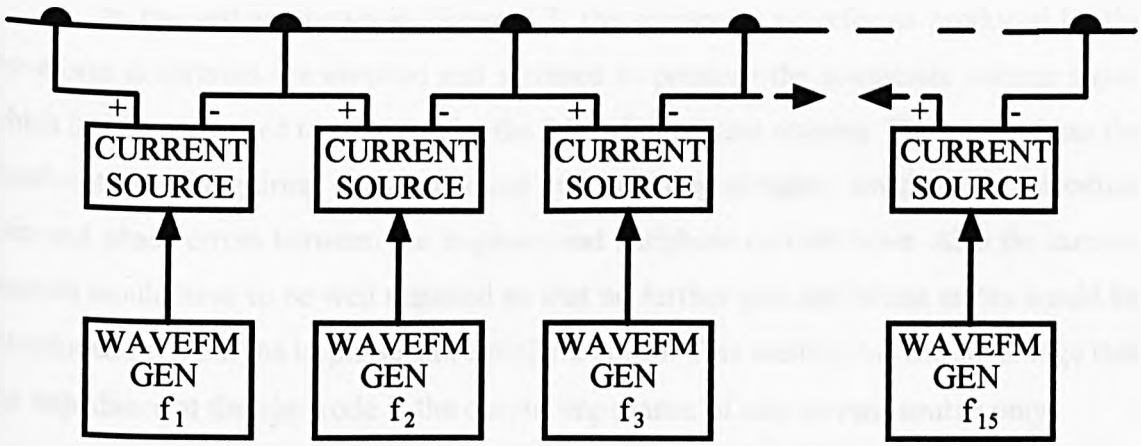

Figure 3.2 : Drive circuitry configuration with single frequency waveform generators. The current sources produce the antiphase currents.

current sinewaves of the single frequency. The outputs of the current sources are then connected together at the electrodes and the sum of the two currents injected into the body. The disadvantage of this method is the reduced impedance at the drive electrode which occurs as a result of the output impedances of the two current sources being connected in parallel. This method has the advantage that since the two signals (source and sink) of each frequency are generated by the current source, and not at an earlier stage, there are fewer possibilities for gain and phase mismatches to be introduced between the in-phase and antiphase signals before injection into the medium of interest.

In the system shown in Figure 3.3, the sinusoidal waveforms produced by the waveform generators are inverted and summed to produce the composite voltage signal which is then converted to a current by the following current sources. This method has the disadvantage of requiring extra summing and inverting circuitry which could introduce gain and phase errors between the in-phase and antiphase current drive. Also the current sources would have to be well matched so that no further gain and phase errors would be introduced between the in-phase and antiphase signal. This method has the advantage that the impedance at the electrode is the output impedance of one current source only.

Figure 3.4 shows the third method of connection in which the waveform generators produce the composite frequency signal containing two frequency signals which is then converted to a current by the current sources. This method requires the current sources and the waveform generators to be well matched so as not to introduce gain and phase mismatches between the in-phase and antiphase signals, but offers flexibility in the choice of the drive configuration. No summing and inverting circuitry is required and the impedance at the electrode is the output impedance of one current source.

The method shown in Figure 3.4 was chosen for the final design because of the high output impedance and the reduced number of components. Any difficulty arising from mismatching the channels will give rise to common mode voltages, but these will be reduced significantly by the use of common mode feedback. The flexibility to employ different drive configurations, which may be useful in the future development of the system, also made it attractive.

In the next section the design of the waveform generators is discussed and in section 3.4, the current sources.

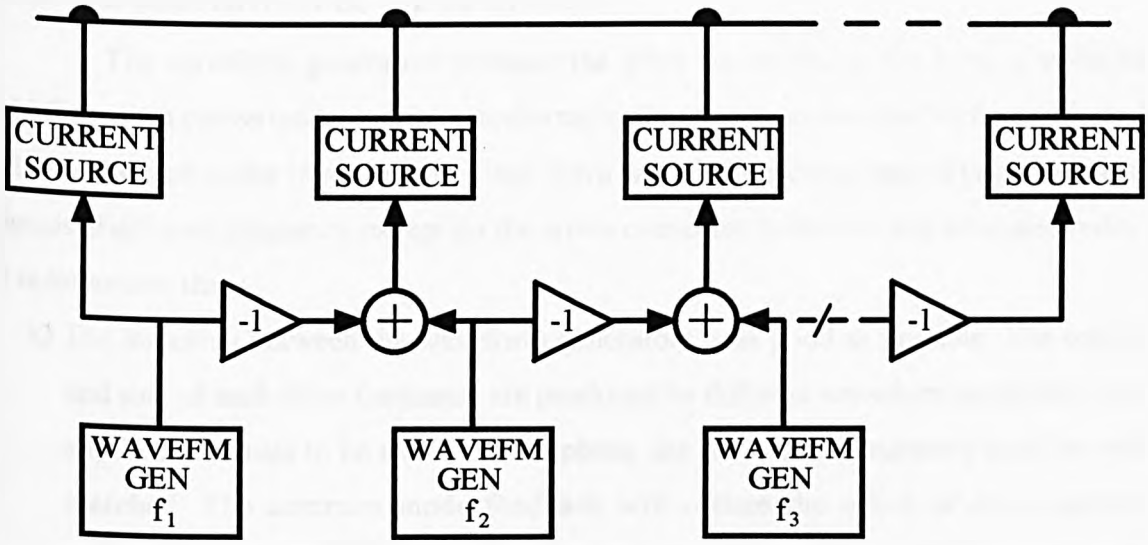

Figure 3.3 : Drive circuitry configuration with single frequency waveform generators. The dual frequency signals are produced prior to voltage to current conversion.

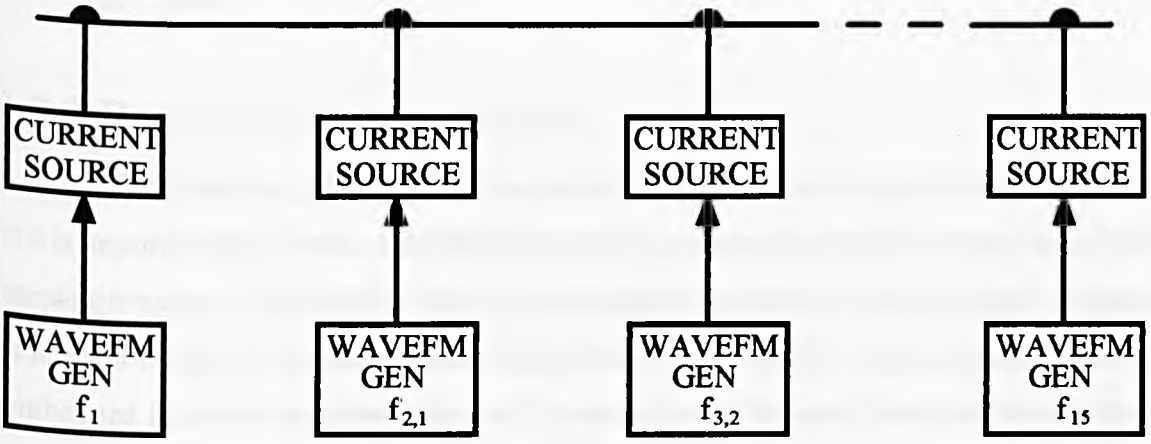

Figure 3.4 : Drive circuitry configuration where the waveform generators produce the dual frequency signals.

3.3 Waveform Generators

3.3.1 Description & Specification

The waveform generators produce the drive waveforms in the form of voltages which are then converted to current waveforms by the current sources before being injected into the medium under investigation. Each drive waveform is composed of two sinusoidal signals of different frequency, except for the drives connected to the two end drive electrodes. It is important that :

a) The matching between the waveform generators is as good as possible. The source and sink of each drive frequency are produced by different waveform generators and so, for the signals to be exactly in antiphase, the waveform generators must be well matched. The common mode feedback will reduce the effect of drive current mismatches, but only by a limited amount and so the mismatches should be minimised.

b) Any unwanted signals at the output of the waveform generators (eg harmonics, subharmonics, noise), particularly at the drive current frequencies, are made as small as possible. For the signal range stated in section 2.6.1 the amplitude of such signals should be at least -60dB in comparison with the signal frequency components. (Frequency components at higher frequencies will be attenuated by the anti-alias filter described in section 4.4 and should be such that the attenuated amplitude is less than -60dB).

3.3.2 Possible Implementations

The detection process outlined in section 2.8 is essentially a synchronous receiver so it is important that there is a definite relationship between the signal frequencies and the sampling frequency. The time for which measurements are made (the window length) contains an integral number of cycles at each of the drive frequencies. For these reasons, digitally synthesised frequency sources were used. A single clock frequency was used as the time base for both the frequency sources and the sampling signal, thus ensuring that any frequency drift of this clock signal would affect all sources and the sampling signal equally. Since it is necessary to derive all the waveforms from one clock frequency source no two drive signal frequencies will have the same number of samples per cycle. It is not possible to choose a clock frequency which gives an integer number of samples per cycle for each drive frequency and so more than one sinusoidal cycle must be stored. The shortest time within which there is an integer number of cycles for all the frequencies used is 2ms and so 2ms of data must be stored for each of the signal sources.

The digitally synthesised frequency source is shown in block diagram form in Figure 3.5. It consists of a clocked counter used to address memory which contains a look-up table for each waveform required. This produces a sequence of samples which constitute a complete window of the desired waveform. Data from the look-up tables are latched into Digital-to-Analogue Converters (DACs). The current outputs of the DACs are then converted to voltages and deglitched using a sample-and-hold amplifier, before being fed to the current sources via RG174A/U 50Ω coaxial cables.

The spectral purity of the waveforms generated will depend upon :

1. The waveform generator clock frequency - the more samples per window of data, the smaller the components at frequencies other than the signal frequencies.
2. The resolution of the DAC - an increase in the number of bits will reduce components at frequencies other than the signal frequencies and increase the signal to noise ratio.
3. The parameters of the DAC and its associated circuitry. For example, the current to voltage converter at the DAC output has a finite slew rate which, if too low, has a non-linear effect and will generate harmonics.

The spectra resulting from varying the clock frequency and the DAC resolution were calculated numerically using the procedure outlined in Appendix A and the results are shown in Figures 3.6 to 3.8. A line has been drawn at -60dB to indicate the maximum level allowed for any frequency components other than the signal. In these Figures, the frequency spectra have been calculated at multiples of 500Hz, which is the cycling frequency of the look-up tables. It can be seen that as the resolution of the DAC is increased or the clock frequency of the waveform generators is increased, the frequency components at frequencies other than the signal frequency decrease. The frequency components at frequencies which exceed the sampling frequency, including the harmonics of the signal frequencies, are not shown in Figures 3.6 to 3.8. These components will be filtered out by the anti-alias filter used in the receive circuitry and consequently will be prevented from causing aliasing problems.

An 8 bit DAC and a sampling frequency of 1.024MHz were chosen because this combination met the spectral specification that the unwanted frequency components are at least -60dB with respect to the fundamental. This solution has the advantage over the 12 bit DAC of reducing the look-up table size and hence the space required on the pcb, and the lower sampling frequency of 1.024MHz requires half the storage space of a sampling frequency of 2.048MHz. Eight-bit DACs are also readily available at low cost. The lower

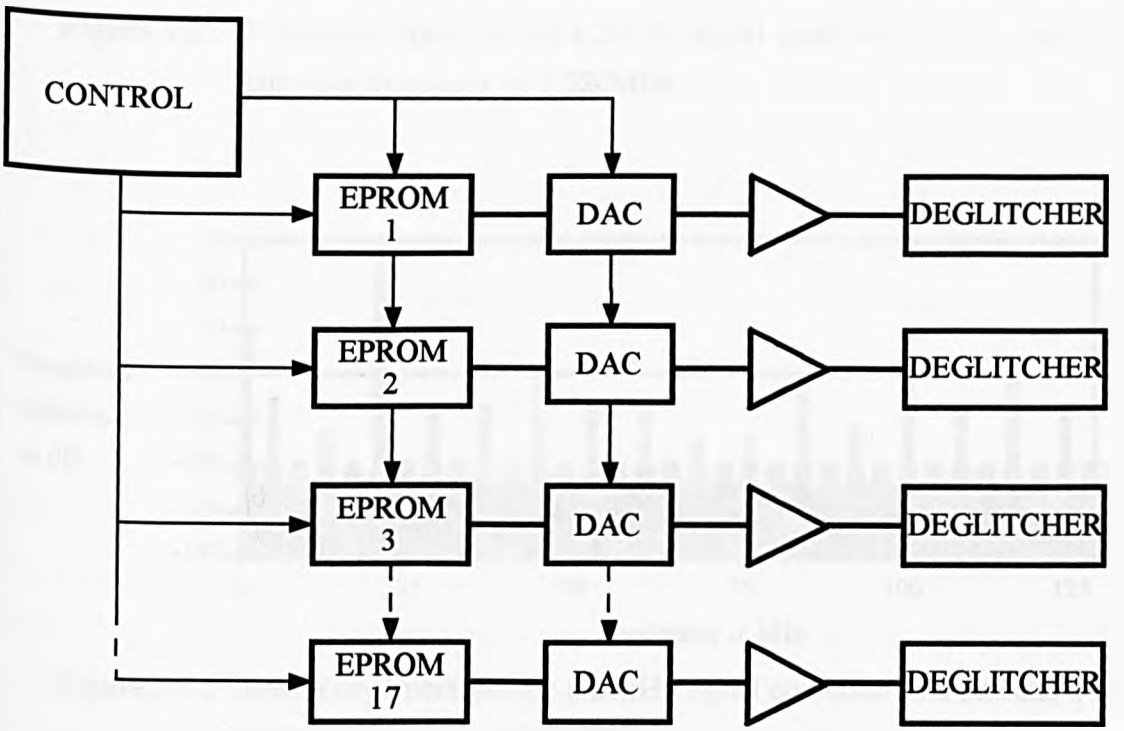

Figure 3.5 : Block diagram of Waveform Generators.

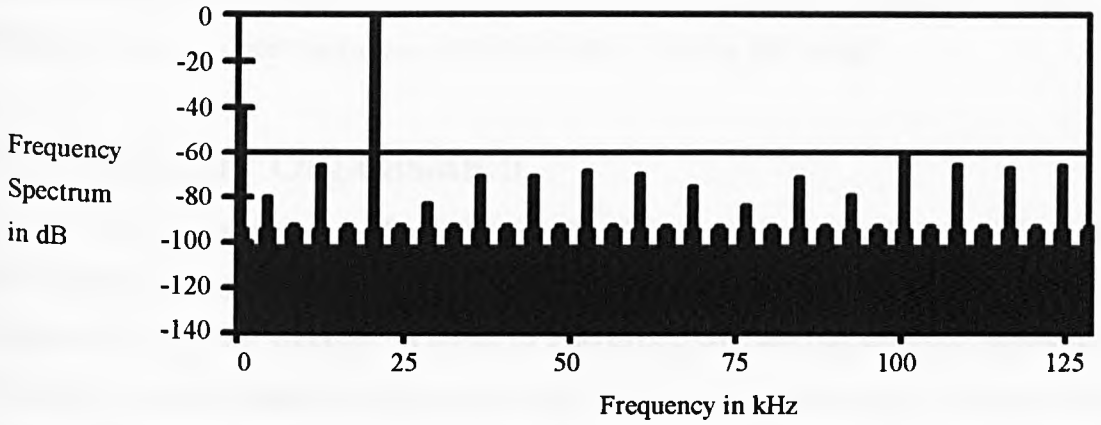

Figure 3.6 : Frequency Spectrum for a 20kHz signal quantised to 8 bits and a sampling frequency of 1.024MHz.

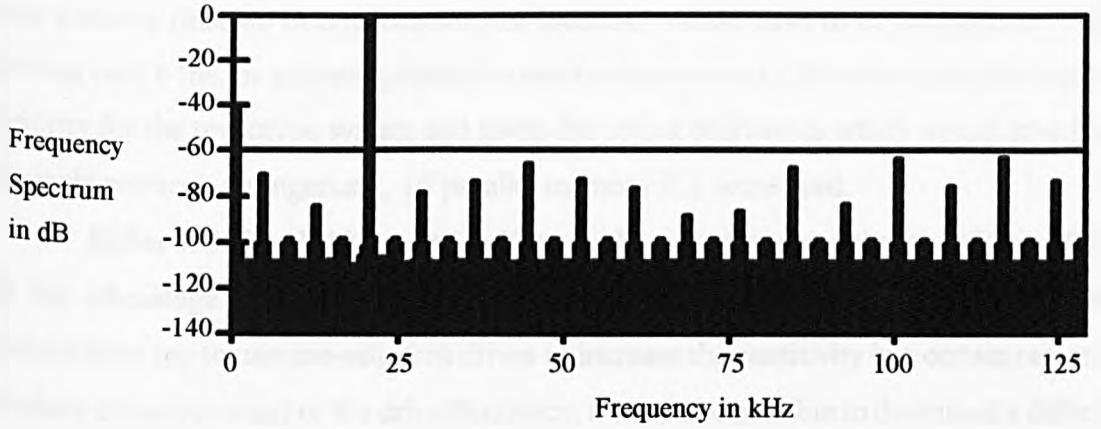

Figure 3.7 : Frequency Spectrum for a 20kHz signal quantised to 8 bits and a sampling frequency of 2.048MHz.

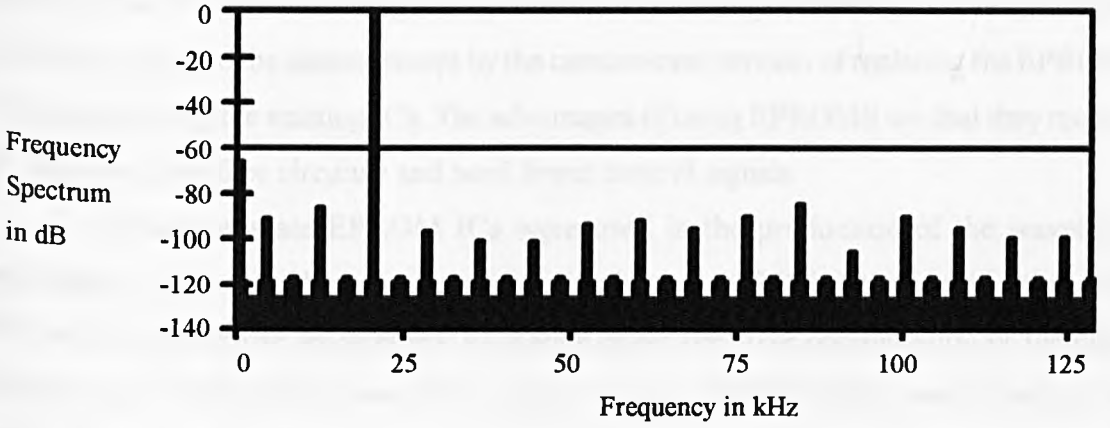

Figure 3.8 : Frequency Spectrum for a 20kHz signal quantised to 12 bits and a sampling frequency of 1.024MHz.

clock speed also allows more time for conversion, settling and switching of the deglitcher making the timing constraints less restrictive and so easing the design.

3.3.3 Memory Organisation

For the combination of an 8 bit DAC and a waveform generator clock frequency of 1.024MHz described in the previous section, each waveform requires 2048 bytes of storage. The simplest solution, in terms of control signals and the speed of components required, is to use 16 separate 2kbyte memory ICs, each storing the data for one waveform, with all the channels clocked in parallel.

If pcb size is important, it would, in principle, be possible to use a single memory IC to store the data for all the waveforms and multiplex the data lines to each DAC. However, this method would require more complex control signals, address generation and much faster memory (instead of one location, 16 locations would have to be accessed in 976ns, allowing only 61ns for address generation and memory access). However pcb size was not a priority for the prototype system and given the timing difficulties which would arise from the single memory arrangement, 16 parallel memory ICs were used.

Either ROM or RAM memory ICs could be used to store the waveforms. RAM has the advantage of flexibility. For example, if it was required to change the drive configuration (eg to use non-adjacent drives to increase the sensitivity in a certain region or to reduce dynamic range) or the drive frequency, it would be possible to download a different set of drive waveforms into the RAM. However, the use of RAM would increase the complexity of the host-system interface and the number of control signals, since the buffered host data bus, address bus and control lines would need to be connected to the waveform generator board for downloading the waveforms. Conversely, if EPROM is used, the drive waveforms could not be altered except by the cumbersome process of replacing the EPROMs or reprogramming the existing ICs. The advantages of using EPROMS are that they require no extra host interface circuitry and need fewer control signals.

Sixteen separate EPROM ICs were used in the production of the waveform generators since it was the easier option to implement, it fulfilled the specification, and there was no immediate requirement to change either the drive configuration or the drive frequencies. If other drive waveforms were required, the EPROMs would have to be reprogrammed or replaced.

3.3.4 Digital-to-Analogue Converter Circuitry

The requirements of the DACs used in the waveform generators are : 8-bit resolution, a linearity of at least 1LSB, a quick settling time (a time of 350ns would leave 600ns for sample-and-hold acquisition time) and a buffered input which would eliminate the need for external latches between the EPROMs and the DACs. In principle, it would have been possible to multiplex a single DAC to each of the drive channels, which would have the advantage that all the signals were produced by the same DAC and so would be matched in amplitude. However, this option requires a much higher operating speed and would significantly complicate the control requirements and so 16 parallel DACs with a clock speed of 1.024MHz were used. The DAC chosen, which fulfilled these requirements, was the PM7524, whose output current had to be converted to a voltage before being fed to the current sources. Voltage output DACs tend to have long settling times and so were unsuitable for this application. The current output from the DAC could not be used directly as the drive current for the system because of its unipolar nature, its inappropriate amplitude and the relatively low DAC output impedance levels. The circuit used to convert the DAC output current into the voltage signal, which is used to drive the current sources is shown in Figure 3.9. The amplifier A_1 is used to provide a dc offset current into the output node of the DAC so that the average current out is 0mA, effectively making the DAC into a bipolar source. The amplifier A_2 is an LM6361 and is used to convert the current signal into a voltage signal which is fed to the input of the unity gain track-and-hold amplifier, A_3, used to deglitch the voltage output. The capacitor, C, connected around A_2 is recommended by the manufacturer [54] to maintain stability and the variable resistor, R_v, allows adjustment of gain so that gain matching between the channels can be achieved.

3.3.5 Measurements

The waveform generators were constructed on a single pcb and measurements made to quantify the behaviour of the generators.

The crosstalk between the channels was measured on a spectrum analyser at less than -61dB in comparison with the fundamental which is within the specification of -60dB.

The harmonics of the waveform generators were measured with a spectrum analyser and in all cases the second harmonic was less than -68dB with respect to the fundamental. The third harmonics were measured at less than -57dB. This value is higher than the -60dB suggested in section 3.3.1. However, these third harmonics will alias into the frequency range 47-68kHz, which does not coincide with the frequency range of interest, and so

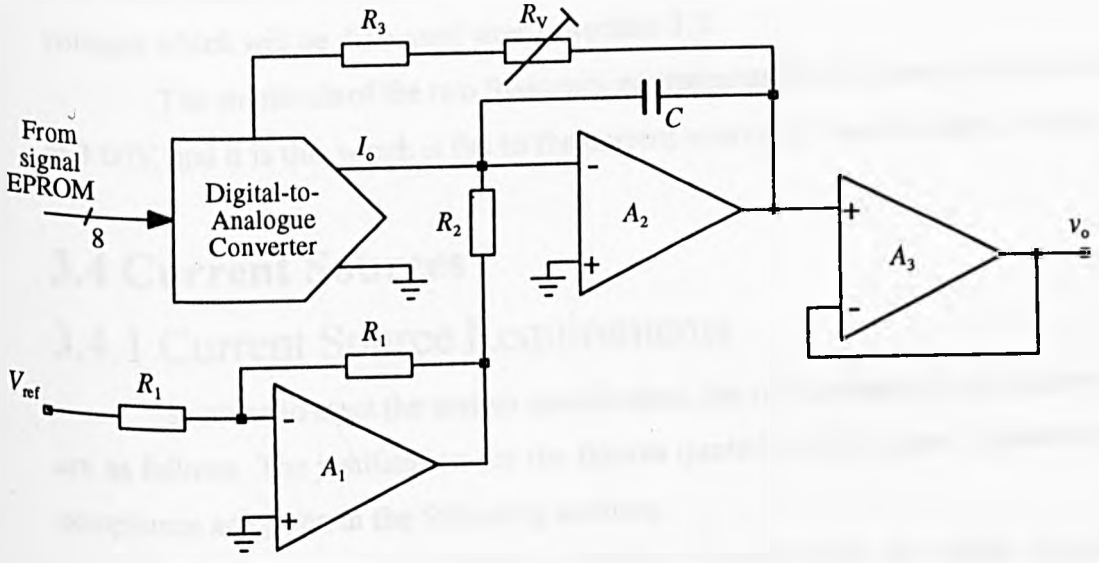

Figure 3.9 : The DAC and its associated circuitry.

should not affect the measurements.

The gains of each waveform generator channel were set using the variable resistor R_v, and the gains of channels carrying the same frequency were matched. This matching was performed by placing two EPROMs programmed with exactly the same waveform into the EPROM sockets of the channels to be matched. The two voltage outputs were fed to the input of a subtractor. The output of the subtractor was monitored using a spectrum analyser while the resistor value was varied, until the minimum output voltage was achieved. All the channels were matched to an amplitude difference of less then -60dB except for the channels 2-3 (20.5kHz source) and 15-16 (27kHz source) which could only be matched to values of -58dB and -56dB respectively. These mismatches will give rise to common mode voltages which will be discussed later in section 3.5.

The amplitude of the two frequency components for all the sources were measured at 3.00V, and it is this which is fed to the current source for conversion to current.

3.4 Current Sources

3.4.1 Current Source Requirements

In order to meet the system specification, the requirements for the current sources are as follows. The justification for the figures quoted for the output impedance and the compliance are given in the following sections.

1. Output impedance : >1.6MΩ at 27kHz (corresponding to a shunt capacitance of 3.7pF).
2. Output current : >6mA peak (there are two frequency components each at nominally 3mA peak).
3. Output voltage compliance : >6.1V peak.
4. Source type : Bipolar - able to source and sink current.
5. Matching in transconductance between current sources is to be as good as possible in order to minimise the common mode voltage.

3.4.2 Output Impedance

The amplitudes of the currents injected into the medium of interest at each of the frequencies used must be matched as closely as possible. Any mismatch will generate common mode voltages. Mismatches in the output impedances of the current source and sink used to generate a single drive frequency current will lead to common mode voltages. Assuming that the currents in the output stage of each current source are matched, the amplitude of

the current passed between the two sources can be determined to a particular accuracy by either measuring the output impedance of all the current sources so that the percentage of the injected current lost through the output impedance to ground and the percentage of the extracted current drawn from ground through the output impedance of the sources can be calculated, or by making the output impedance so large that the current flowing to ground through the output impedance in each channel is sufficiently small that the specified accuracy can be maintained.

Figure 3.10 shows the equivalent circuit for a single frequency drive connected to the medium of interest. I is the current generated by the current sources with output impedances Z_{out1} and Z_{out2} , R_{c1} and R_{c2} are contact resistances at electrodes e_1 and e_2 respectively and R_m is the resistance of the medium of interest. It can be shown that the current, i, flowing through the medium of interest is given by

$$i = \frac{(Z_{o1} + Z_{o2})I}{Z_{o1} + Z_{o2} + R_{c1} + R_{c2} + r_m} \qquad \{3.1\}$$

A typical value for the total inter-electrode resistance (R_{c1}+R_{c2}+r_m) is 3kΩ and so if the current i is to be defined to an accuracy of 0.1%, for example, of the current generated, I, then the output impedance of each current source must be greater than 1.5MΩ. (A 0.1% mismatch in current amplitude would generate a common mode voltage of 4.5V through 1.5MΩ - see section 3.5.2 for more details). However, in practice, sixteen current sources are connected to the medium of interest and an estimate of the magnitude of the current which is lost through the output impedances of these other current source output impedances to ground is required. The input impedances of the buffers are much larger than the output impedances of the current sources (see section 4.2) and so can be ignored.

The table in Figure 2.4 shows the potentials expected at all the electrodes caused by a current between drive electrodes 1 and 2 with a homogeneous medium of conductivity 0.2Sm^{-1} and drive-drive/receive-receive electrode spacing of 15mm. It can be seen that, for the 3D case, the potentials at the electrodes are less than 10mV from drive electrode 6 to drive electrode 16. By considering the currents flowing to ground at the drive electrodes, calculated by dividing the potential at the electrode by the output impedance of the current source at that electrode, an approximate value of the current lost can be obtained. This value is only approximate because the calculation of the potentials at the electrodes has assumed no loading at the electrodes. By loading the electrodes at these points with the output impedances of the current sources, this assumption is violated and the calculation of potential at the electrodes is only approximate. However, since the current flowing through

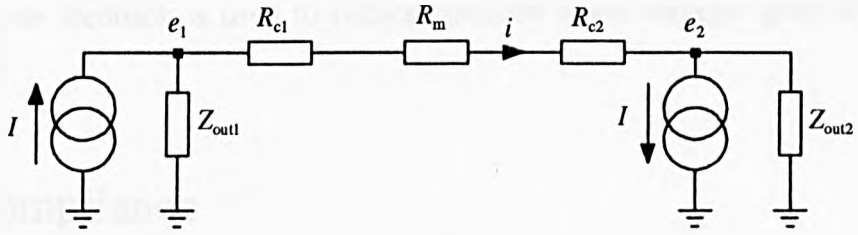

Figure 3.10 : The equivalent circuit used to estimate the effect of a mismatch between current source output impedances on the current flowing in the medium.

the output impedances is very small compared with the currents in the medium of interest the error in the calculated potential will be small and it is reasonable to assume that current lost through each output impedance is approximately given by the ideal potential at each electrode divided by the output impedance of the current source driving that electrode. Assuming the current sources have an output impedance of 1.6MΩ, a current of 2.88μA is lost through the output impedance of the drive source and a current of approximately 0.09μA is lost through the output impedances of the other current sources giving a total loss of 2.97μA (for the 2D case the current lost is 2.75μA). This corresponds to a total error of just under 0.1%. The effect of such mismatches in each channel would be to cause a maximum common mode voltage of 4.8V (see section 3.5.2). The effects of common mode voltage of this order on the behaviour of the system is discussed in section 3.5 and the process of common mode feedback is used to reduce common mode voltages generated by these mismatches.

3.4.3 Compliance

The compliance of a current source is the maximum output voltage that the source can support while still behaving as a current source. The worst case potential at a drive electrode will occur at the centre of the array (drive electrode 8 or 9), since all the potentials will add. Equation {1.1} can be used to estimate the compliance required of the current sources in a 3D medium. The magnitude of the potential at drive electrode 8, V_8, generated by the current injected at other drive electrodes is given by

$$V_8 = \frac{I}{2\pi\sigma a}\left[\left|\frac{1}{7}-\frac{1}{6}\right|+\left|\frac{1}{6}-\frac{1}{5}\right|+\ldots+\left|\frac{1}{2}-1\right|+\left|1-\frac{1}{2}\right|+\ldots+\left|\frac{1}{7}-\frac{1}{8}\right|\right]+V_{d8} \qquad \{3.2\}$$

$$V_8 = 4.9\mathrm{V}$$

where I is the amplitude of the injected current, σ is the conductivity of the medium, a is the drive-drive/receive-receive electrode spacing and V_{d8} is the potential at drive electrode 8 generated by its own injection current (this is calculated as shown in section 5.2.2 using Equation 5.1).

Performing a similar calculation for a pseudo-2D medium gives V_8=4.7V, so the compliance of each source must be greater than 4.9V peak for a homogeneous medium. If a maximum of 25% change in measurements is expected when a target is introduced into the homogeneous medium (section 2.6.1), this value is increased to 6.1Vpeak.

3.4.4 Possible Current Source Implementations

Various types of current sources have been used by EIT groups in the past and some of these are outlined below.

Smith et al [10] used a transformer as a current source in their real-time EIT system. There are a number of advantages of using a transformer for this purpose. For example, it is easy to make the source floating, the output is inherently bipolar and few components are required. However the use of transformers does have some drawbacks. Unless the flux in the core is kept to a very low level, the non-linearities of the magnetic material will give rise to significant odd harmonics. In order to keep the magnetic flux density low, a relatively large core is required making the size of the transformer significant. There is also a load dependent phase shift across the transformer which would need to be measured for each source every time a set of measurements was made. This would increase the time required to take each measurement set and increase the amount of data to be processed. Another problem associated with using a transformer as a current source is that of achieving a high output impedance.

A simplified mid frequency equivalent circuit of a transformer is shown in Figure 3.11(a) where the components R_1 , R_2 are the primary and secondary winding resistances, L_{l1} , L_{l2} are the primary and secondary leakage inductances, R_l is the load resistance, R_m' models the core losses, L_m' is the magnetising inductance and the transformer T is ideal with turns ratio n (primary turns to secondary turns). This equivalent circuit can be modified so that all the components are referred to the primary as shown in Figure 3.11(b), where ' represents referred values ($R_2' = n^2R_2$, $L_{l2}' = n^2L_{l2}$, $R_l' = n^2R_l$ and $I_2' = I_2/n$). It can be seen that the magnetising arm of the transformer, $R_m'//L_m'$, is in parallel with the part of the circuit containing the load resistance, R_l' . In order to ensure that most of the current I_1 flows into the load, the parallel combination of R_m' and L_m' must have a much larger impedance than the $L_{l2}'R_2'R_l'$ series combination. To achieve this $1/n$ (ie N_2/N_1) must be high. Also, to reduce distortion the magnetic flux density in the core must be kept low and this can be achieved by having a large number of primary, and hence secondary, turns. However, a transformer has interwinding and static capacitances as shown, in a simplified form, in Figure 3.11(c) and these tend to increase as the number of turns increases. These capacitances will reduce the output impedance of the source.

A number of experimental transformers using different ferrite cores were constructed and were found to have capacitances of greater than 20pF at their output nodes. This would limit the output impedance of the current source to 295kΩ at 27kHz.

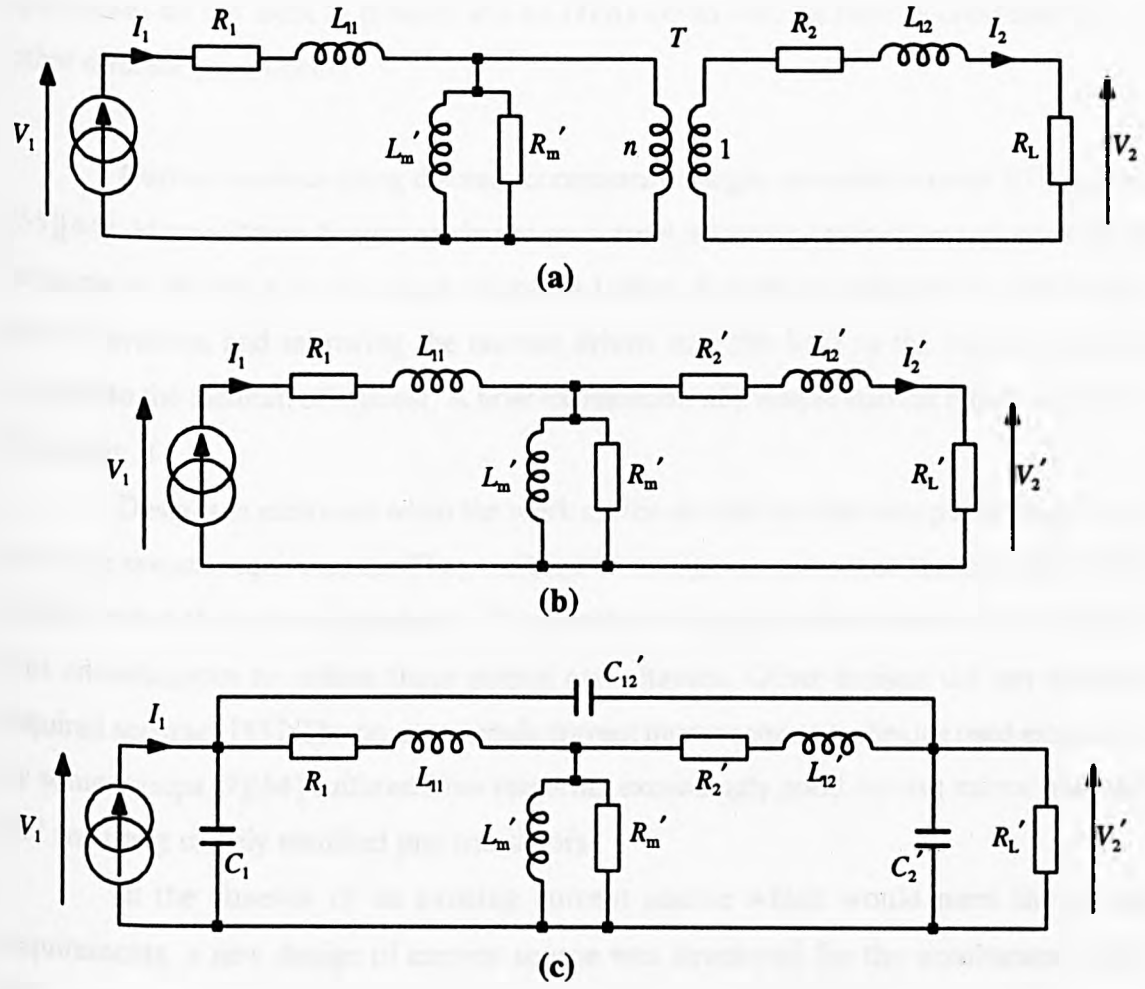

Figure 3.11 : The equivalent circuit of a transformer.

(a) Equivalent circuit.

(b) Equivalent circuit referred to primary.

(c) Equivalent circuit referred to primary with parasitic capacitance included.

Operational Transconductance Amplifiers (OTAs) are op-amps which behave as voltage-to-current converters. They have the advantage of being fabricated on one IC and so component matching is good and pcb space required is small. However, OTAs which have an appropriate combination of bandwidth and peak current capability required for this application do not exist at present and so OTAs could only be used in combination with other discrete components.

Current sources using discrete component designs are used in some EIT systems [55][64]. Most of these designs are based on current mirroring techniques and work on the principle of driving a known load resistance (either directly or indirectly) by the voltage input waveform and mirroring the current driven into this load to the output node and hence into the medium of interest. A brief explanation of a simple current mirror is given in Appendix B.

Designs in existence when the work on the current sources was performed did not meet the system requirements. They suffered from high output capacitances [66][67][68] which limited the output impedance. Since real and imaginary data was to be collected it was advantageous to reduce these output capacitances. Other designs did not meet the required accuracy [55]. The op-amp supply current mirror sensing technique used extensively by some groups [9][64] suffered from requiring exceedingly good current mirror matching and requiring closely matched pnp transistors.

In the absence of an existing current source which would meet the system requirements, a new design of current source was developed for the simultaneous drive EIT system.

(Since the completion of this work, however, much effort has been expended on designing wideband current sources for EIT applications and these have subsequently been published [65][69]. The circuit by Bragos [69] has a similar topology to the discrete design used in this work).

3.4.5 Current Source Circuit and Description

Figure 3.12 shows a very simple current source. The voltage source v_{in} creates currents I_1 and I_2 in the circuit as shown which are related to the input voltage. The transistor pairs T_1T_3 and T_2T_4 are connected as current mirrors which mirror the currents I_1 and I_2 to the right hand section of the circuit. The output current, I_o, flows out of the output node and is defined by the difference between the currents I_1 and I_2. The problem with this circuit

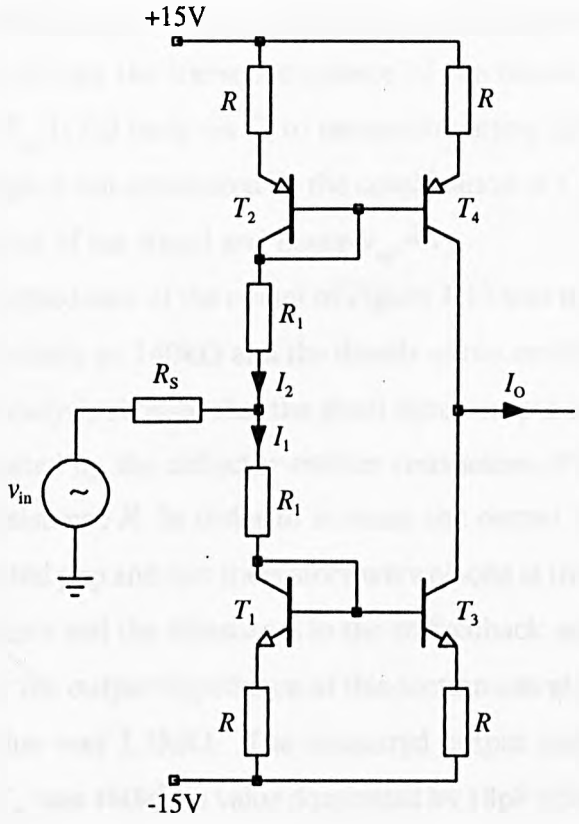

Figure 3.12 : A simple bipolar current source.

is that there is no feedback and so the dc voltage at the output node will be undefined if the dc current gains of the transistors are not perfectly matched. To overcome this problem, dc feedback is applied as shown in Figure 3.13, where the output voltage is buffered by a FET input op-amp A_2 and low pass filtered by R_{f1} C_2 and the filtered signal applied to the non-inverting input of A_1 . In order for the transconductance of this circuit to be defined by feedback, another pair of current mirrors, T_5T_6, and a reference resistor is added as shown in Figure 3.13. This defines the transconductance of the circuit as $I_o/v_i = 1/R_{ref}$. The ac voltage, v_{ref}, across R_{ref} is fed back via C_1 to the non-inverting input of A_1 . R_{f2} is added so the ac feedback voltage is not attenuated by the combination of C_1 and C_2 and is chosen so that $R_{f2}C_1$ >> the period of the signal and hence $v_{ref} = v_i$.

The output impedance of the circuit of Figure 3.13 was measured at 150kΩ. It had been calculated analytically as 140kΩ and the details of the small signal analysis are given in Appendix C. This analysis showed that the small signal output resistance of the circuit of Figure 3.13 is dominated by the collector emitter resistances of the output transistors T_3 and T_4, and by the resistance R. In order to increase the output impedance of the circuit, common-base connected pnp and npn transistors were placed at the collectors of the current mirror output transistors and the transistors in the ac feedback section as shown in Figure 3.14. The analysis for the output impedance of this section can also be seen in Appendix C and the predicted value was 2.5MΩ. The measured output impedance of the circuit of Figure 3.14 without C_{fb} was 480kΩ, a value dominated by 18pF of stray capacitance between the output node and ground. This value of parasitic capacitance comprised of 2xC_{cb}(5pF each) + C_{inFET}(5pF) + C_{probe}(2.5pF). The effects of the parasitic capacitance were reduced by adding a capacitor C_{fb}, which injected a current into the output node equal to the current lost through the parasitic capacitance. A value of 16.6pF was used for C_{fb} which increased the measured output impedance of the circuit to 1.47MΩ. Any further increase in C_{fb} caused instability. The effects of increasing C_{fb} on the value of output impedance predicted by SPICE can be seen on the graphs in Figures 3.15 and 3.16.

The circuit of Figure 3.14 had the disadvantage that the upper half of the circuit needed well matched pnp transistors (T_4 and T_6) which are not readily available. The circuit was therefore modified so that the transistors T_2 , T_4 and T_6 were connected to mirror only a bias current and so did not need to be well matched. The bottom half of the circuit remained the same except that the output of A_1 was connected only to the bottom half of the circuit. The transistors T_5 and T_3 were replaced with a super-matched BJT pair [70] to ensure good matching between the output arm and the reference arm of the mirror and the

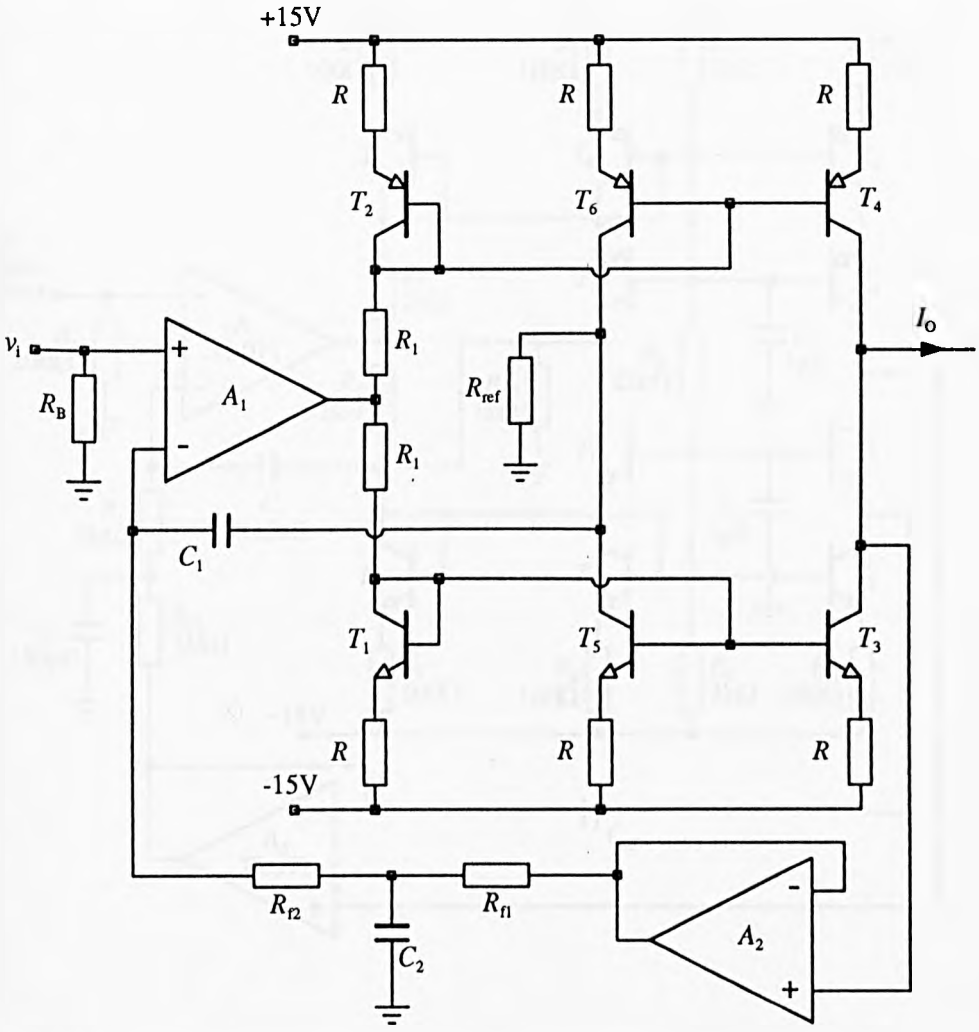

Figure 3.13 : An extension of the circuit of Figure 3.12 to include both dc and ac negative feedback.

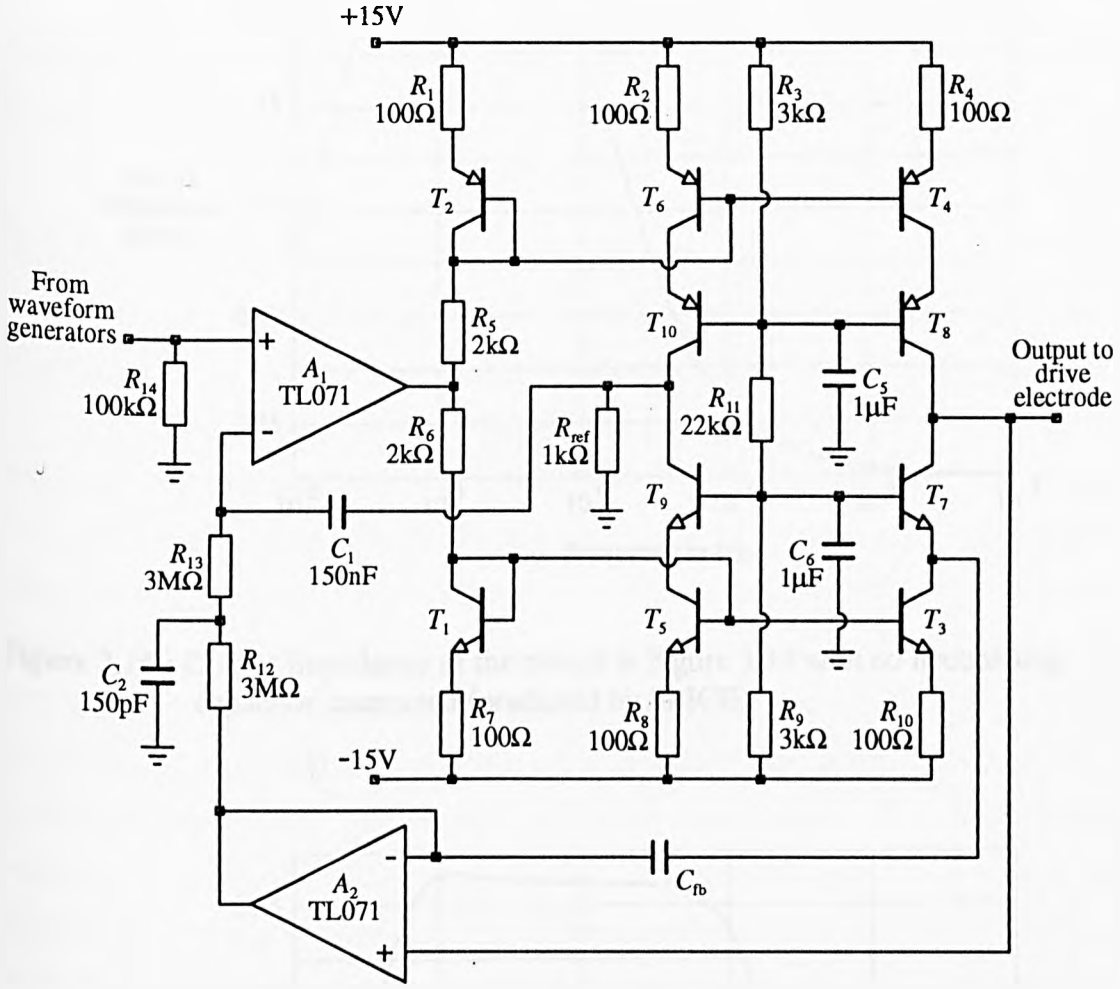

Figure 3.14 : The basic current source design including cascode transistors to increase output impedance.
Transistors T_1, T_3, T_5, T_7, and T_9 are BC184L.
Transistors T_2, T_4, T_6, T_8, and T_{10} are BC559.

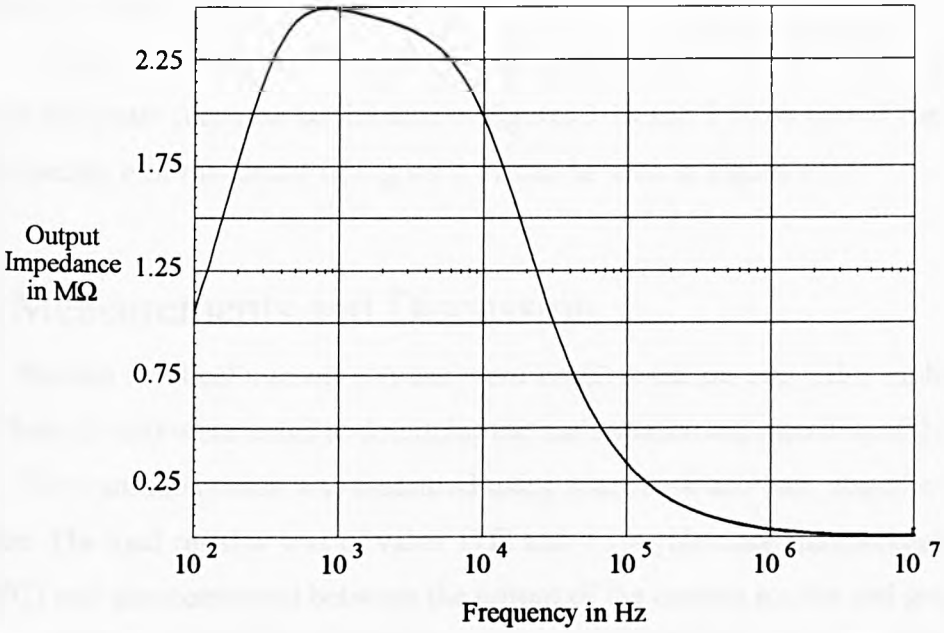

Figure 3.15 : Output Impedance of the circuit in Figure 3.14 with no neutralising capacitor connected (predicted by SPICE).

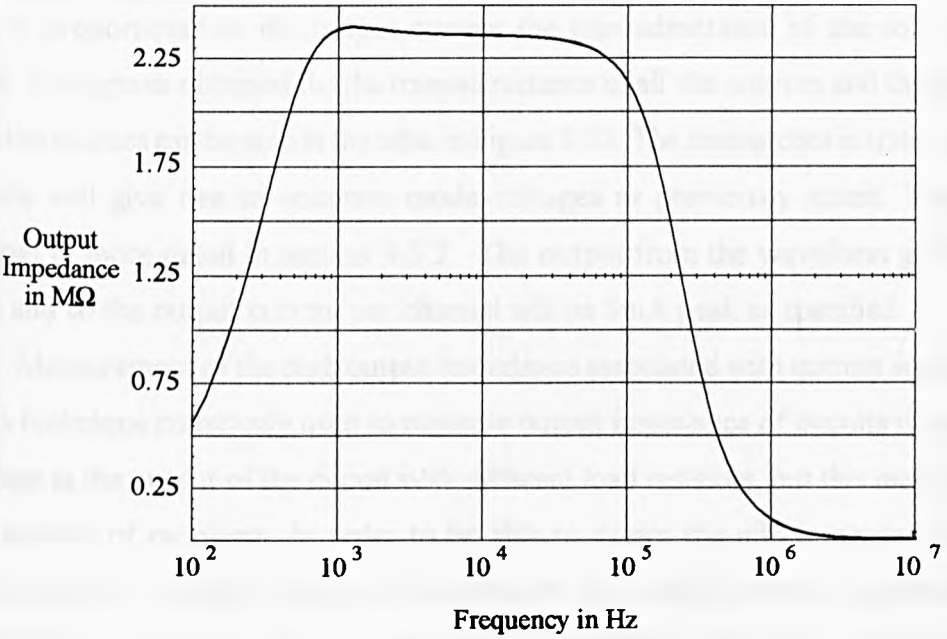

Figure 3.16 : Output Impedance of the circuit in Figure 3.14 with a neutralising capacitor of 5pF connected (predicted by SPICE).

common base connected transistors, T_7 and T_9 were replaced by n-channel DMOSFETs to ensure that the signal current lost in the gate was negligible. The modified circuit diagram can be seen in Figure 3.17.

The circuit shown in Figure 3.17 was simulated on a SPICE package and the frequency and phase response can be seen in Figures 3.18 and 3.19. A plot of the predicted output impedance of the circuit of Figure 3.17 can be seen in Figure 3.20.

3.4.6 Measurements and Discussion

Sixteen identical current sources were constructed on two pcbs; eight on each board. These circuits were tested to determine the performance and matching of the sources.

The transadmittance was measured using a network analyser, amplifier and load resistance. The load resistor was of value 1kΩ and 0.1% tolerance (temperature stability 15ppm/°C) and was connected between the output of the current source and ground. The same resistor was used to test all the current sources to allow comparison between the channels. The swept frequency output of the network analyser was amplified to a suitable level (approximately the same amplitude as the output of the waveform generators) and fed to the voltage input of the current source. The ratio of the output voltage to the input voltage was then plotted and a typical plot can be seen in Figure 3.21. Since the output voltage is proportional to the output current the transadmittance of the source can be deduced. The figures obtained for the transadmittance of all the sources and the phase shift through the sources can be seen in the table in Figure 3.22. The mismatches in transadmittance and phase will give rise to common mode voltages as previously stated. This will be considered in more detail in section 3.5.2. The output from the waveform generators is 3Vpeak and so the output current per channel will be 3mA peak as specified.

Measurement of the high output impedance associated with current sources is not trivial. A technique commonly used to measure output impedance of circuits is to measure the voltage at the output of the circuit with different load resistors, but this method suffers from a number of problems. In order to be able to detect the effects caused by a finite output impedance, the load resistance used must be of a similar order of magnitude to the output impedance. However, for a load resistance of 1MΩ say, the input voltage must be approximately 10mV in order to avoid saturation at the output. With such small signals, the noise in the system becomes significant and measurement is more difficult. If the load resistance is reduced so that a large input voltage can be used, the resulting change in output amplitude by connecting loads is smaller and so more difficult to measure. Also the

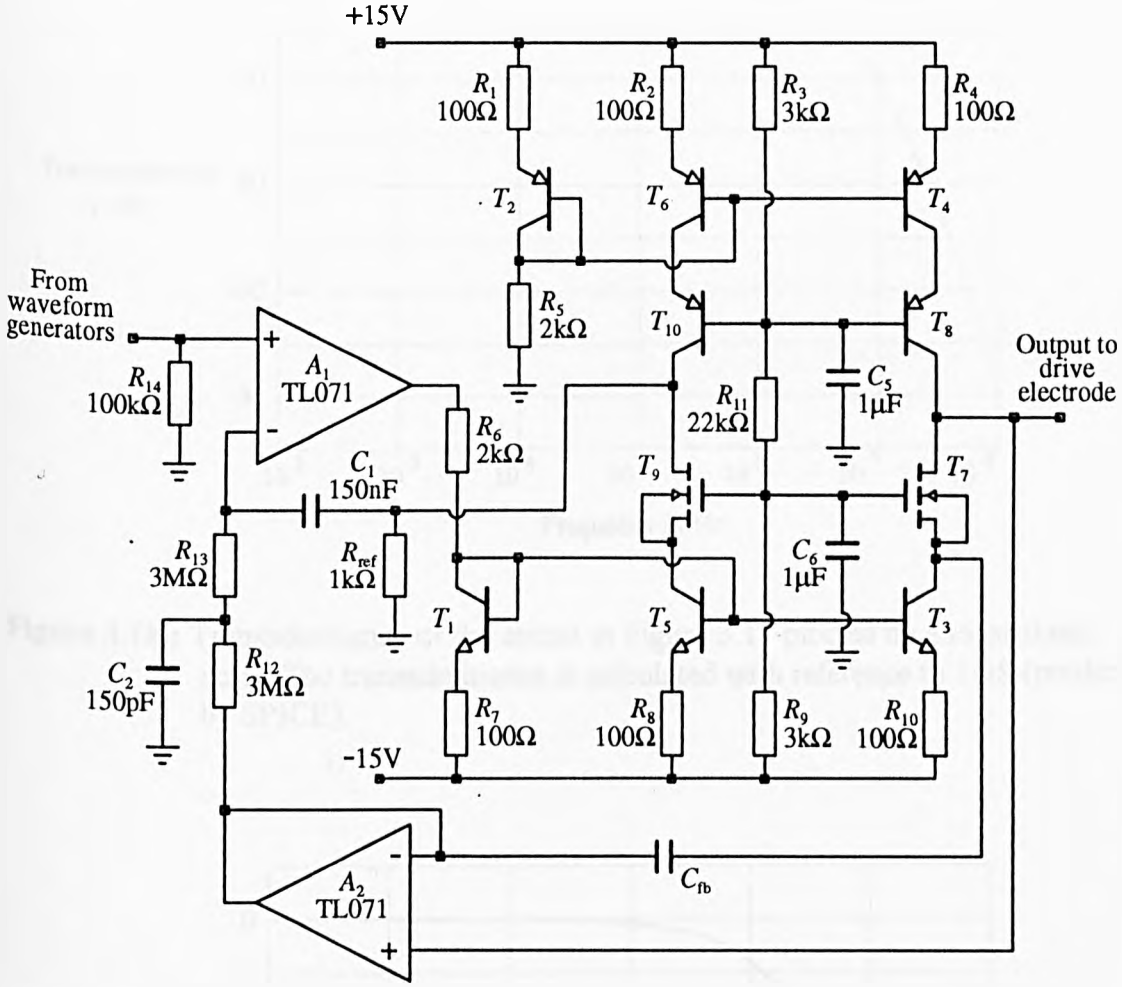

Figure 3.17 : The final current source design.
Transistor T_1 is BC184L.
Transistors T_2, T_4, T_6, T_8, and T_{10} are BC559.
Transistors T_3 and T_5 are an LM394 supermatched pair.
Transistors T_7 and T_9 are SD215 MOSFETs.

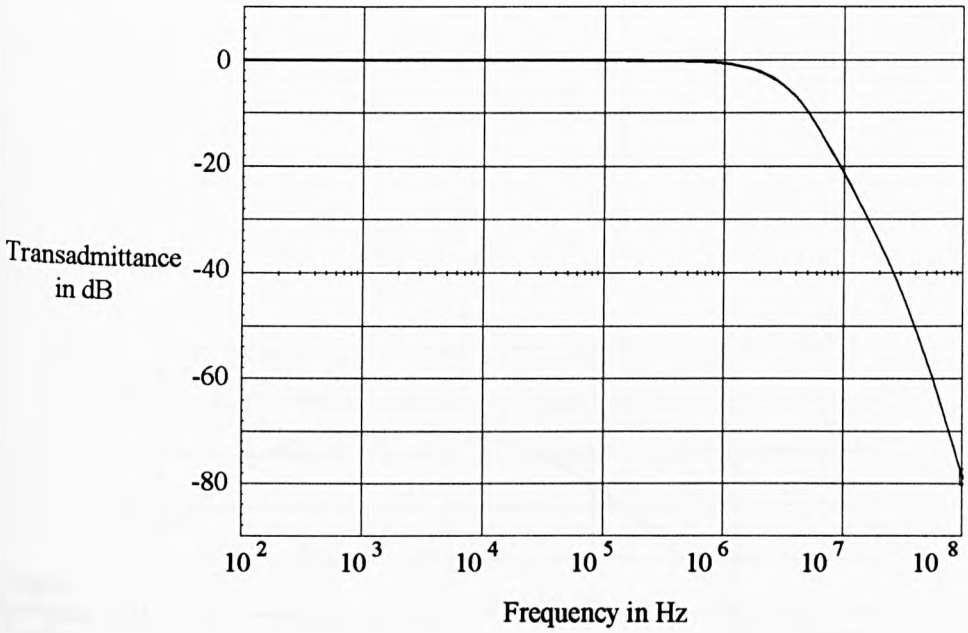

Figure 3.18 : Transadmittance of the circuit in Figure 3.17 plotted on a logarithmic scale. The transadmittance is calculated with reference to 1mS (predicted by SPICE).

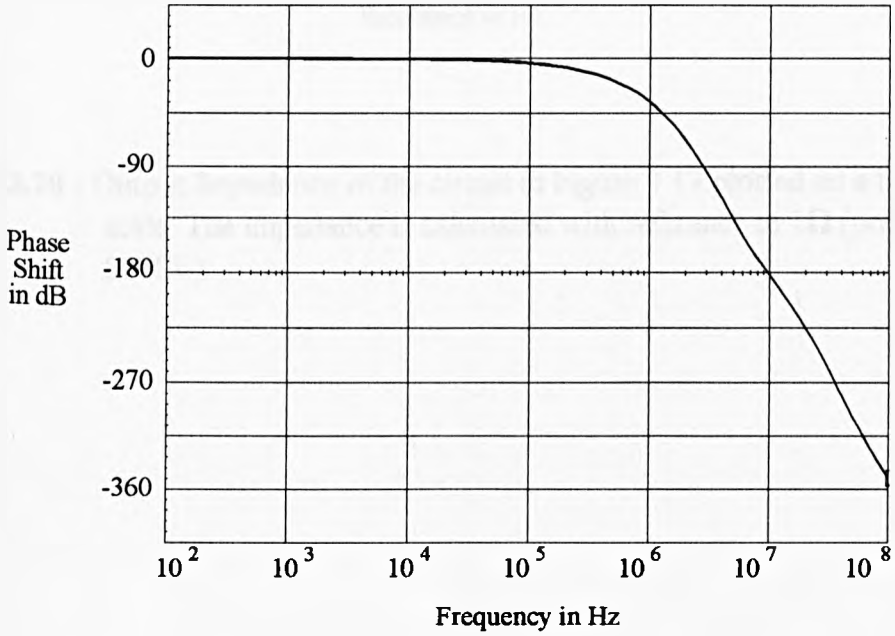

Figure 3.19 : Phase shift through the circuit in Figure 3.17 (predicted by SPICE).

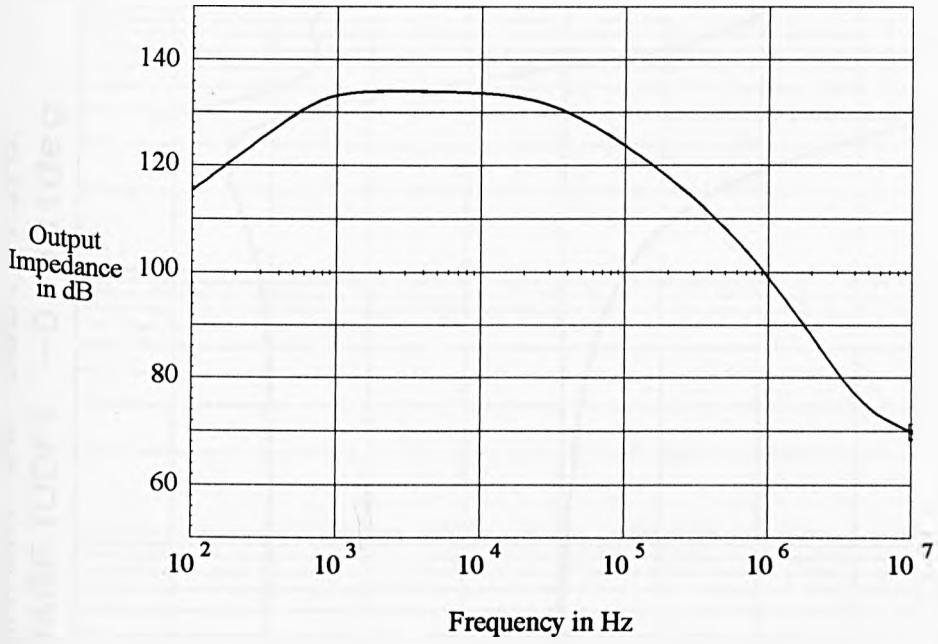

Figure 3.20 : Output Impedance of the circuit in Figure 3.17 plotted on a logarithmic scale. The impedance is calculated with reference to 1Ω (predicted by SPICE).

Figure 3.21 : Measured transadmittance of the current source against frequency. (Plotted in dB with 0dB = 1mS).

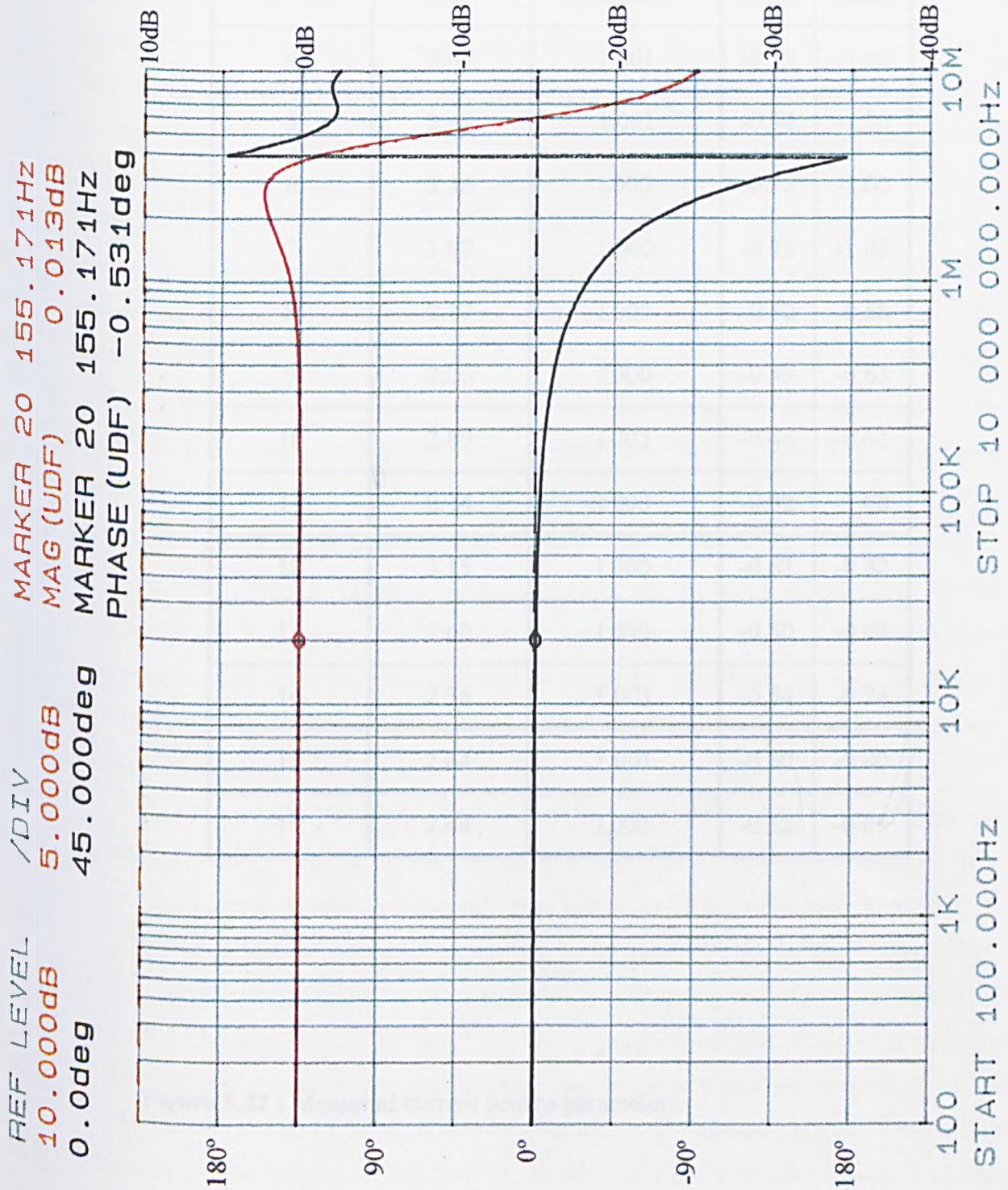

Current Source Number	Output Impedance in MΩ	Transadmittance over 20-30kHz	Phase (deg)	
			20kHz	27kHz
1	1.87	1.002	-0.46	-0.62
2	2.82	1.001	-0.49	-0.64
3	2.26	1.000	-0.47	-0.66
4	3.07	1.001	-0.79	-1.06
5	2.49	1.001	-0.74	-1.00
6	2.36	1.000	-0.75	-1.00
7	3.07	1.002	-0.75	-1.03
8	2.17	1.000	-0.52	-0.68
9	2.20	1.000	-0.49	-0.63
10	2.80	1.002	-0.46	-0.61
11	2.14	1.000	-0.82	-1.08
12	3.15	1.000	-0.63	-0.82
13	2.60	1.000	-0.50	-0.68
14	2.36	1.001	-0.54	-0.74
15	2.44	1.001	-0.60	-0.80
16	2.48	1.000	-0.52	-0.69

Figure 3.22 : Measured current source parameters.

probe used to measure the voltage change is in parallel with the output impedance of the current source and so will affect the measurements. This would have to be compensated.

Given these problems with this approach of measuring the output impedance an alternative method of driving the current source output with a voltage source and measuring the current drawn was used. The voltage input to the current source, v_{in}, was grounded and the output was driven by the swept frequency voltage source of an HP3577 network analyser. Using a swept frequency source has the added advantage that the output impedance can be readily observed over the frequency range of interest. The current driven into the output impedance was measured using a Tektronix CT2 current probe [71] with a wideband amplifier to increase the signal level at the output of the probe. The current probe and amplifier were calibrated as shown in Figure 3.23(a). A 10kΩ 0.1% resistor was driven by the HP3577 source, and the current through it was sensed by the current probe. The voltage at the output of the amplifier was recorded by the analyser and used as the basis of a normalisation measurement. Subsequent measurements would then automatically be referenced to a 10kΩ resistor. The voltage at the output of the swept frequency source was measured using a 10MΩ probe and the ratio of the voltage measured to the current measured was plotted, from which the frequency dependent output impedance could be deduced. (With reference to Figure 3.23 the value $(V_m/V_{ref})/(V_{Im}/V_{Iref})$ was plotted which is equivalent to Z_{out}/R_L) A typical plot of the output impedance produced by this method can be seen in Figure 3.24. Comparison of Figure 3.24 and Figure 3.20 show the similarity of behaviour between measured and predicted output impedances as a function of frequency. The output impedances of all the current sources were measured by this method and the impedances at the frequencies of interest are given in the table in Figure 3.22. All the output impedances are greater than the 1.6MΩ specified in section 3.4.1.

The compliance of the current sources were measured by increasing the load resistance with a 3V peak, 20kHz sinusoidal input voltage waveform connected to the input. The point at which saturation occurred was at an output voltage of 12.4V peak.

The crosstalk between channels was measured at <-82dB, which is acceptable.

The linearity of the circuits was tested by measuring intermodulation products of two input frequencies of 300Hz and 10kHz on a spectrum analyser. These were measured at ≤-59dB with respect to the amplitude of one of the fundamental components, which implies that harmonics of this level may be generated by the current sources. These will not cause a problem so long as they are not aliassed into the frequency range of interest. Harmonics greater than the third harmonic will be attenuated by the anti-alias filter thus

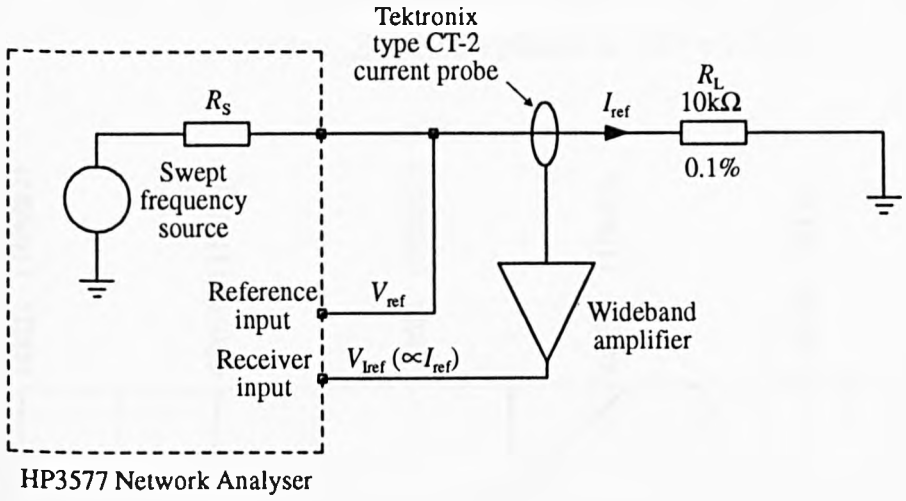

(a) Calibration circuit

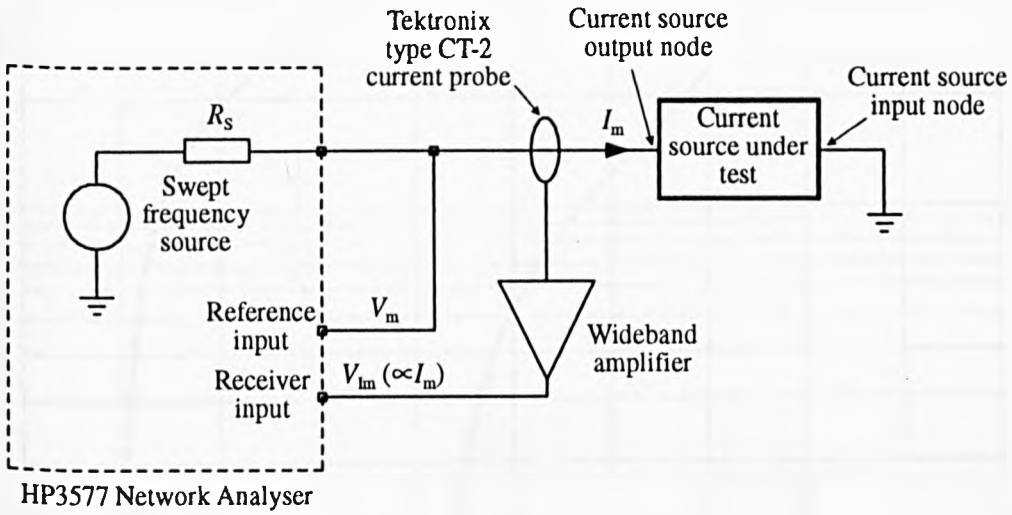

(b) Measurement circuit

Figure 3.23 : Current source output impedance measurement configuration.

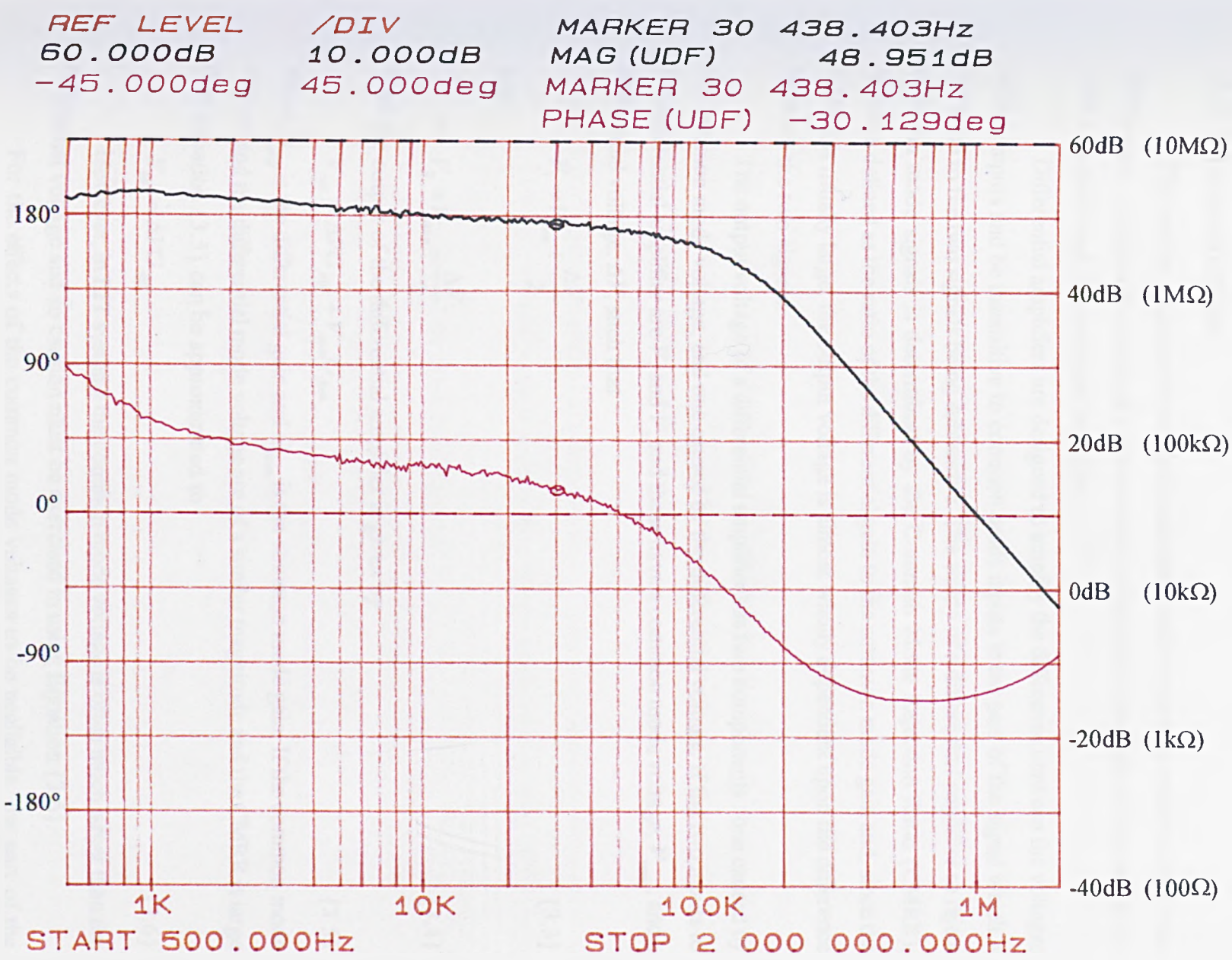

Figure 3.24 : Measured output impedance of the current source. ($20\log_{10}Z_{out}/10k\Omega$ plotted ie 0dB = 10kΩ).

reducing their amplitude to less than -60dB with respect to the fundamental. The second harmonics will be aliassed into the 74-88kHz range of frequencies and the third harmonic into the 47-68 kHz range and so will be rejected by the digital filters.

3.5 Common Mode Feedback

3.5.1 Introduction

This section explains the problems associated with a common mode voltage in an EIT system, discusses the causes of common mode voltage and concludes with a description of the method used to counteract its effects.

Differential amplifiers are designed to amplify the difference between the voltages at their inputs and be insensitive to common mode inputs ie the part of the signal which is common to the two signals being subtracted. The ability of a differential amplifier to reject common mode signals is determined by the Common Mode Rejection Ratio (CMRR), which is defined as the ratio of the differential gain to the common mode gain and, since the CMRR is usually large, the output voltage is almost wholly dependent upon the difference between the two signals.

The output voltage of a differential amplifier has two components : one caused by the common mode voltage, and one caused by the differential voltage. If the two inputs to the differential amplifier are V_1 and V_2 and these have a common mode voltage, V_{com}, and a differential voltage, ΔV, such that

$$V_1 = V_{com} + \frac{\Delta V}{2} \qquad \{3.3\}$$

and

$$V_2 = V_{com} - \frac{\Delta V}{2} \qquad \{3.4\}$$

Then the output of the differential amplifier is given by

$$V_{out} = \Delta V G_{diff} + V_{com} G_{com} \qquad \{3.5\}$$

where G_{diff} is the differential gain and G_{com} is the common mode gain. If the common mode voltage and the differential mode voltage are of a similar magnitude and the CMRR is large then Equation {3.5} can be approximated to

$$V_{out} = \Delta V G_{diff} \qquad \{3.6\}$$

However, in EIT systems the common mode voltage is often much larger than the differential voltage and so caution must be exercised in using Equation {3.6}.

For the effects of the common mode voltages to be negligible, the part of the

output voltage of the subtractor which is due to the common mode voltage must be less than half of the least significant bit of the following analogue-to-digital converter as stated in Equation {3.8}

$$V_{com}G_{com} < \frac{1}{2}LSB \qquad \{3.7\}$$

or

$$V_{com}\frac{G_{diff}}{CMRR} < \frac{1}{2}LSB \qquad \{3.8\}$$

Therefore, it is advantageous to minimise the common mode voltage so that the CMRR required of the subtractor can be reduced. The common mode voltage can be reduced by the application of common mode feedback circuitry [72][73]. The circuitry provides a low impedance path to ground for any mismatches in current which are injected into the medium of interest, detects the common mode voltage of the medium (generated by the mismatch current flowing through the contact impedance of the common mode feedback electrode), inverts this voltage and drives the medium with this inverted signal, thus reducing the common mode voltage.

The possible sources of common mode voltage are described in the next section and calculations are performed to estimate the magnitude of the resultant common mode voltage before common mode feedback is applied.

3.5.2 Current Source Drives.

There are several possible sources of common mode voltage in an EIT system and these include :

- (i) Geometry of the drive configuration.
- (ii) Mismatches in the transadmittance of the current sources.
- (iii) Mismatches in phase between the current sources.
- (iv) Mismatches in output impedance of the current sources.
- (v) Mismatches in contact impedances.

The expected amplitude of the common mode voltage caused by each of the sources will now be estimated.

(i) There will be a common mode voltage caused by the current sources, which is inherent to the geometry of the drive configuration and hence does not reflect any deficiencies in the circuitry used to realise the system. In Figure 3.25, the desired measurement is the difference

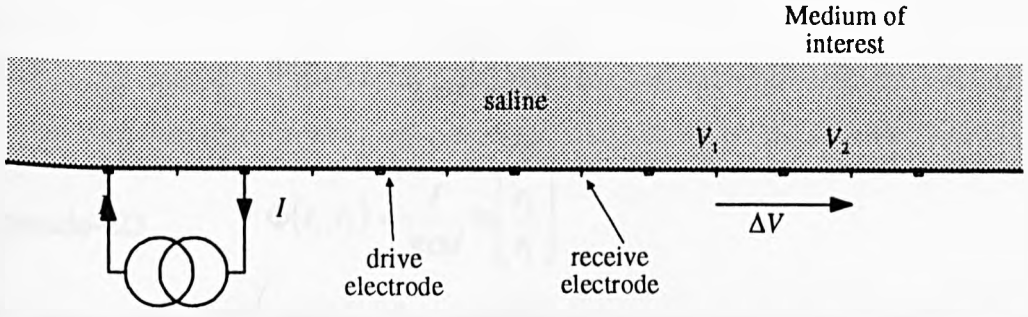

Figure 3.25 : A section of the electrode array showing a common mode voltage caused by a current drive.

voltage, $\Delta V = V_1 - V_2$ and the common mode voltage at that point due to the drive , I, will be $(V_1+V_2)/2$. As the distance from the drive increases the component of the common mode voltage at that drive frequency will decrease. This type of common mode voltage cannot be compensated because it is different at each point along the array; only a common mode voltage which is independent of position and applies to the whole medium of interest can be compensated. The total common mode voltage at any one point is the sum of the common mode voltages due to each drive frequency. Thus, the worst case instantaneous common mode voltage will occur at the central receive pairs ie at receive electrodes 8 and 9 and receive electrodes 9 and 10 when all the potential difference waveforms are in phase. An approximate value for this maximum common mode voltage can be calculated using Equations {1.1} for 3D regions and {1.3} for 2D regions which are repeated here for convenience.

For 3D
$$\Phi(r_1, r_2) = \frac{I}{2\pi\sigma}\left[\frac{1}{r_1} - \frac{1}{r_2}\right] \qquad \{1.1\}$$

For pseudo-2D
$$\Phi(r_1, r_2) = \frac{I}{\pi\sigma d}\ln\left[\frac{r_2}{r_1}\right] \qquad \{1.3\}$$

For a homogeneous 3D medium the potentials at receive electrodes 8 and 9, V_{r8} and V_{r9} respectively, caused by all the drives are given by

$$V_{r8} = \frac{I}{2\pi\sigma a}\left[\left|\frac{1}{6.5} - \frac{1}{5.5}\right| + \left|\frac{1}{5.5} - \frac{1}{4.5}\right| + \ldots + \left|\frac{1}{1.5} - \frac{1}{0.5}\right| + 0 + \left|\frac{1}{0.5} - \frac{1}{1.5}\right| + \ldots + \left|\frac{1}{7.5} - \frac{1}{8.5}\right|\right] \qquad \{3.9\}$$

$$V_{r9} = \frac{I}{2\pi\sigma a}\left[\left|\frac{1}{7.5} - \frac{1}{6.5}\right| + \left|\frac{1}{6.5} - \frac{1}{5.5}\right| + \ldots + \left|\frac{1}{1.5} - \frac{1}{0.5}\right| + 0 + \left|\frac{1}{0.5} - \frac{1}{1.5}\right| + \ldots + \left|\frac{1}{6.5} - \frac{1}{7.5}\right|\right] \qquad \{3.10\}$$

where a is the distance between electrodes performing the same function (ie drive-drive/ receive-receive electrode spacing). The common mode voltage, V_{cm}, is given by

$$V_{cm} = \frac{V_{r8} + V_{r9}}{2} \qquad \{3.11\}$$

Substituting parameter values I=3mA, a=15mm and σ=0.2Sm^{-1}, the common mode voltage is 0.59V peak. Performing a similar calculation for 2D gives the value 1.29V for the common mode voltage. If a maximum of 25% change in measured amplitude is assumed to arise due to a change in conductivity in the region of interest (section 2.6.1), the maximum common mode voltage will be given by the 2D case and will be 1.6Vpeak.

Unlike the common mode voltage caused by the geometry of the drive configuration which is inherent to EIT, all other common mode voltages are generated by mismatches in the components of the system, and so if the components were perfectly matched no other common mode voltage would be generated. In reality there will be mismatches between channels and the effects of these mismatches are now considered.

(ii) Mismatches in the transadmittances of the current sources lead to a net flow of current into or out of the medium of interest. A simplified diagram showing the impedances for a single drive pair and a single receive pair can be seen in Figure 3.26 where I_1 and I_2 are the mismatched source and sink currents respectively, Z_{out1} and Z_{out2} are the output impedances of the current sources, R_{c1} to R_{c4} are the contact impedances, the combination of R_{m1}, R_{m2} and R_{m3} is the load resistance and Z_{in1} and Z_{in2} are the input impedances of the voltage sensing buffers. If the source and sink currents I_1 and I_2 are not matched then the difference in current, δI, will flow to ground through the parallel combination of all the output impedances of the current sources (Z_{out1} , Z_{out2} ,.., Z_{out16}) and all the input impedances of the buffers (Z_{in1} , Z_{in2} ,.., Z_{in17}), thus generating a voltage which appears as a common mode voltage.

The buffer input impedances are greater than 9MΩ (R_{in}>150MΩ, C_{in}<0.6pF, section 4.2.2) which is large compared with the output impedances of the current sources (Z_{out} >1.8MΩ, see section 3.4) and so are ignored in this calculation. The current sources and buffers are mounted at the electrodes to reduce any stray capacitance at the electrode due to cabling which would also appear as a path to ground for a mismatch in current. The contact impedances R_{c1-4} (typically 500-1500Ω) and load impedances R_{m1} , R_{m2} and R_{m3} (typically 30Ω) are both small in comparison with the output impedances of the current sources and so will be neglected. Therefore, the total impedance to ground seen by any mismatch in drive currents will approximate to the parallel combination of all the output impedances of the current sources. This is calculated as 197kΩ using the measured output impedances of the current sources given in section 3.4.

The mismatches in transadmittance of the current sources give rise to amplitude and phase errors between the source-sink currents. As an example, consider a drive current amplitude mismatch of 0.1% in one of the source-sink pairs. The common mode voltage generated would be 0.001 x 3×10^{-3} x 197k = 0.59Vpk which would be the potential of the whole medium of interest (neglecting the impedance of the medium itself) on which the potential gradients would be superimposed.

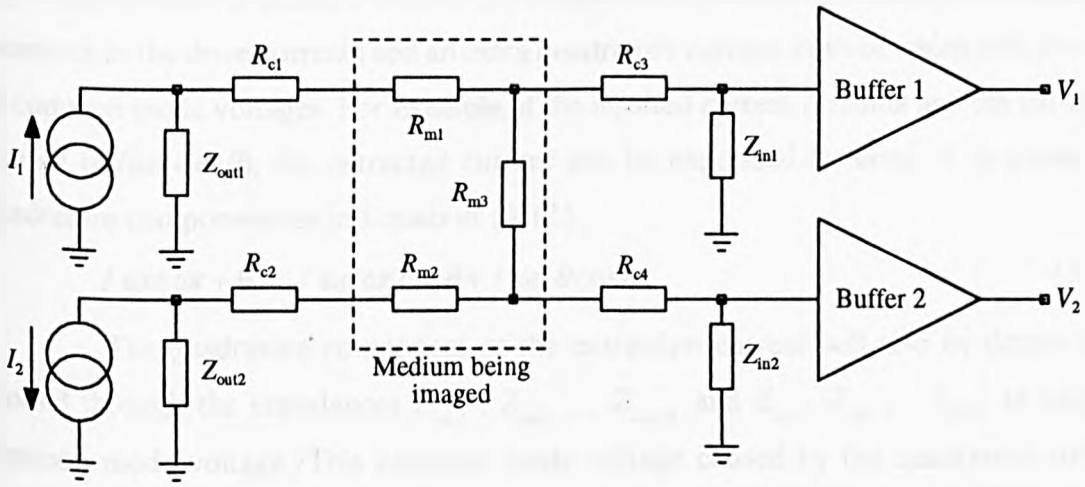

Figure 3.26 : The impedances associated with a single drive pair and a single receive pair.

The measured mismatches in transadmittance through the current sources tabulated in Figure 3.22 can be used to calculate the common mode voltage caused by this effect. The table in Figure 3.27 shows the percentage mismatch in transadmittance between the two sources used for each frequency. If this is combined with the information about the waveform generator gain mismatches given in section 3.3.5, the sum of the current errors due to amplitude current mismatches is 36μA through a resistance of 197kΩ which corresponds to a common mode voltage of 7.1V.

(iii) Mismatches in phase between the sources is equivalent to having an amplitude mismatch in the drive currents and an extra quadrature current, both of which will give rise to common mode voltages. For example, if the injected current is $I\sin\omega t$ and the extracted current is $I\sin(\omega t+\theta)$, the extracted current can be expressed in terms of in phase and quadrature components as in Equation {3.12}.

$$I\sin(\omega t+\theta) = I\sin\omega t\cos\theta + I\sin\theta\cos\omega t \qquad \{3.12\}$$

The quadrature component of the extraction current will also be drawn from ground through the impedances Z_{out1} , Z_{out2} ,.., Z_{out16} and Z_{in1} , Z_{in2} ,.., Z_{in17} to cause a common mode voltage. This common mode voltage caused by the quadrature current component will be much larger than the in-phase component.

From Figure 3.22 the measured phase shift between each source and sink drive can be calculated and so the maximum expected common mode voltage due to phase mismatch can be found. As the current sources are mounted on two boards and the outputs are interleaved along the array, the current source pairs which correspond to each drive frequency are shown in the table in Figure 3.27. The in-phase and quadrature current mismatch which occurs because of the phase mismatches can be calculated by summing the mismatches for each drive frequency as before. This will give the worst case current by assuming that all the in-phase errors add and all the quadrature phase errors add. The sum of all the currents caused by the phase mismatch at 27kHz is 304nA in-phase and 134μA quadrature, which flowing through 197kΩ give a common mode voltage of 0.1Vpk in-phase and 26.3Vpk quadrature.

(iv) Mismatches in output impedances of the current source and current sink will generate a common mode voltage. A simplified equivalent circuit of the current sources and the medium of interest is shown in Figure 3.28 where I is the matched source-sink current, R is the combined contact and medium resistance and V_1 and V_2 are the voltages at the outputs

Freq. in kHz	Current Source Drive Number	Percentage error in trans-admittance	Average phase in degrees		Phase Mismatch in degrees		Output Impedance Mismatch in MΩ	Average Output Impedance in MΩ
			20kHz	27kHz	20kHz	27kHz		
20	9,8	0	-0.51	-0.66	0.03	0.05	0.03	2.19
20.5	8,10	0.2	-0.49	-0.65	0.06	0.07	0.63	2.49
21	10,7	0	-0.61	-0.82	0.29	0.42	0.27	2.94
21.5	7,11	0.2	-0.79	-1.06	0.07	0.05	0.93	2.61
22	11,6	0	-0.79	-1.04	0.07	0.08	0.22	2.25
22.5	6,12	0	-0.69	-0.91	0.12	0.18	0.79	2.76
23	12,5	0.1	-0.69	-0.91	0.11	0.18	0.66	2.82
23.5	5,13	0.1	-0.62	-0.84	0.24	0.32	0.11	2.55
24	13,4	0.1	-0.65	-0.87	0.29	0.38	0.47	2.84
24.5	4,14	0	-0.67	-0.90	0.25	0.32	0.71	2.72
25	14,3	0.1	-0.51	-0.70	0.07	0.08	0.10	2.31
25.5	3,15	0.1	-0.54	-0.73	0.13	0.14	0.18	2.35
26	15,2	0	-0.55	-0.72	0.11	0.16	0.38	2.63
26.5	2,16	0.1	-0.51	-0.67	0.03	0.05	0.34	2.65
27	16,1	0.2	-0.49	-0.66	0.06	0.07	0.61	2.18

Figure 3.27 : Table showing the mismatches in the current sources leading to common mode voltages.

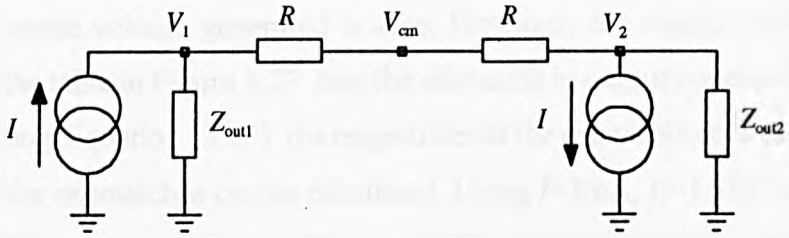

Figure 3.28 : An equivalent circuit to show the effects of mismatches in current source output impedance on common mode voltage.

of the current sources. V_1 and V_2 are given by

$$V_1 = \frac{2IRZ_{out1}}{Z_{out1} + Z_{out2} + 2R} \quad \{3.13\}$$

$$V_2 = \frac{-2IRZ_{out2}}{Z_{out1} + Z_{out2} + 2R} \quad \{3.14\}$$

and the common mode voltage, V_{cm}, is given by

$$V_{cm} = \frac{V_1 + V_2}{2}$$

$$= \frac{IR_m(Z_{out1} - Z_{out2})}{Z_{out1} + Z_{out2} + 2R} \quad \{3.15\}$$

It can be seen that if the output impedances of the two current sources are matched, the common mode voltage generated is zero. However, the output impedances are not matched and the table in Figure 3.27 lists the mismatch in output impedance of the current sources. By using Equation {3.15} the magnitudes of the equivalent common mode voltages generated by the mismatches can be calculated. Using I=3mA, R=1.5kΩ and the values of output impedances given in the table, the sum of the errors is calculated to be 4.0V peak.

(v) Mismatches in contact impedance at the electrodes can cause significant common mode voltages. If, for any drive pair, the drive contact impedances are equal (and there are no other mismatches in the system), the voltages set up by the drive current at the junction of the contact impedance and medium of interest impedance are of the same magnitude but of opposite sign and so the common mode voltage applied to the region is said to be zero. If the contact impedances are dissimilar, then the potentials at the contact impedance - medium interface will not be equal and opposite. Their average value will be the common mode voltage. Figure 3.29 shows an equivalent circuit incorporating contact impedances, R_{c1} and R_{c2}, for matched sources of amplitude I and output impedances Z_o with a medium resistance of R_m. Assuming everything except the contact impedances are matched, it can be shown that the common mode voltage is given by

$$V_{cm} = \frac{I(R_{c2} - R_{c1})Z_o}{2Z_o + R_{c1} + R_{c2} + 2R_m} \quad \{3.16\}$$

A mismatch of 500Ω in contact impedance (a typical value in medical applications) and using the values of R_{c1}=1.5kΩ and R_{c2}=1kΩ, R_m=500Ω, I=3.0mA and Z_o=2MΩ yields a common mode voltage caused by one source of 0.75V, giving a total common mode

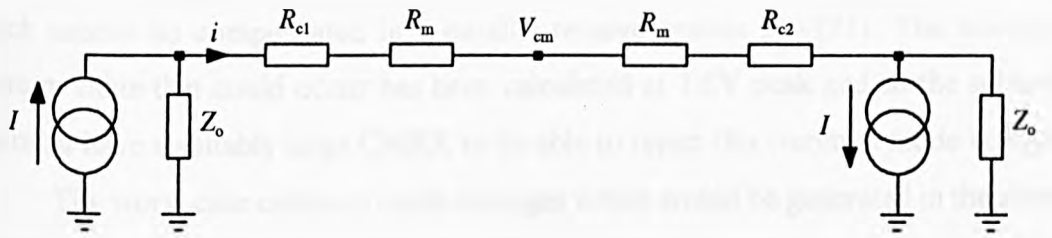

Figure 3.29 : The equivalent circuit used to show the effect of mismatches in contact impedances.

voltage of 11.25V for a similar mismatch in each pair of drive electrodes.

It is not known how large the errors in contact impedance will be for the phantom used to test this system. The load resistance consists mainly of the spreading resistance at the electrode and this is heavily dependent upon area of contact and shape of contact. It is expected that the errors in contact resistance are unlikely to be greater than the 33% suggested above and so this value is used to estimate the common mode voltages caused by contact impedance mismatch.

3.5.3 Summary of sources of Common Mode Voltage

There are common mode voltages generated in the medium of interest by the geometry of the drive configuration, current mismatches and impedance mismatches. The common mode voltage due to the drive configuration is inherent to the principle of EIT and as such cannot be compensated in a parallel receive system [10][21]. The worst case maximum value that could occur has been calculated at 1.6V peak and so the subtractor stage must have a suitably large CMRR to be able to reject this common mode voltage.

The worst case common mode voltages which would be generated in the absence of common mode feedback by the drive current mismatches in amplitude and phase have been calculated at 7.1Vpk and 0.1Vpk (quadrature voltage is 26.3Vpk). The common mode voltages generated by impedance mismatches are expected to be less than 15.25Vpk. It would be difficult to design a system which could measure the small voltage differences expected in the presence of such a large common mode voltage. The common mode feedback applied to the phantom to reduce the common mode voltages is described in the next section.

3.5.4 Common Mode Feedback Circuitry.

The easiest method which can be used to combat common mode voltages caused by mismatches is to earth the medium of interest at a point remote from the array. This provides a low impedance path to ground for the mismatched currents without distorting the current paths near the electrode array. However, the contact resistance of the electrode does not allow the elimination of all the common mode voltage in this way, since the current mismatches flowing through the contact resistance to ground generate a voltage, which is applied to the medium.

The phantom to be used in testing the system is a rectangular tank and is described fully in Chapter 5. The phantom was connected to the drive and receive circuitry and the

medium of interest (saline of conductivity 0.2Sm^{-1}) was grounded at a remote electrode. The common mode voltage of the saline was measured in a remote corner of the phantom. The voltage contained components at all frequencies and had a maximum instantaneous voltage of 5.3V peak. This would mean that for the dynamic range stated in section 2.6.2 to be achieved using a 13 bit ADC of input range 10V (see section 4.5), a minimum CMRR of 80dB (if the differential gain was unity) would be required of the subtractor. Since it is likely that the subtracted signal will be amplified, the CMRR required will be even higher and so common mode feedback was applied to reduce the common mode voltage.

The basic principle of common mode feedback is to detect the voltage of the medium of interest at a remote point, invert this signal and then drive the medium of interest with this inverted signal and so, ideally, reducing the common mode voltage to zero. The inverted signal is often also amplified to increase the effectiveness of the feedback. Figure 3.30 shows the feedback circuit in control terms, where V_{cm} is the common mode voltage, V_d is the driven voltage and V_{eff} is the effective voltage of the medium of interest. It can be shown that

$$\frac{V_{eff}}{V_{cm}} = \frac{1}{1+G} \qquad \{3.17\}$$

where G is the forward loop gain of the circuit, hence as $G \rightarrow \infty$, $V_{eff} \rightarrow 0$.

The common mode voltage has frequency components at each of the drive frequencies and so common mode feedback must be applied across the frequency range 20-27kHz. The simplest circuit to use for a common mode feedback circuit is a wideband inverting amplifier. This could be connected with a reasonable gain and small phase shifts at the drive frequencies. In practice, however, wideband amplifiers are not used since they tend to be unstable when used in this application [44][58] and so a bandpass filter was used to limit the application of gain to the frequencies of interest. Bandpass filtering has the disadvantage of introducing significant phase shifts at the frequencies in the passband but ensures system stability, provided the gain is limited to a modest value, in this case approximately 10.

The circuit used to achieve the common mode feedback is shown in Figure 3.31. It is a unity gain buffer followed by a bandpass filter. The input is decoupled by the 330nF capacitor so that bias current is not drawn from the medium and the buffer is connected with a bootstrapped input resistance to ground so that the detected voltage is not significantly reduced by the contact impedance of the electrode. The output of the buffer is used to drive the screen of the coaxial cable which carries the signal to reduce the effective input

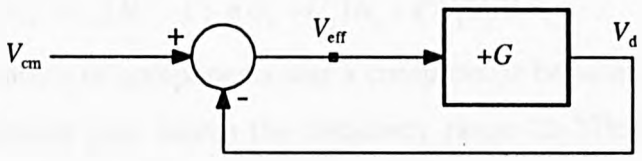

Figure 3.30 : The common mode feedback principle.

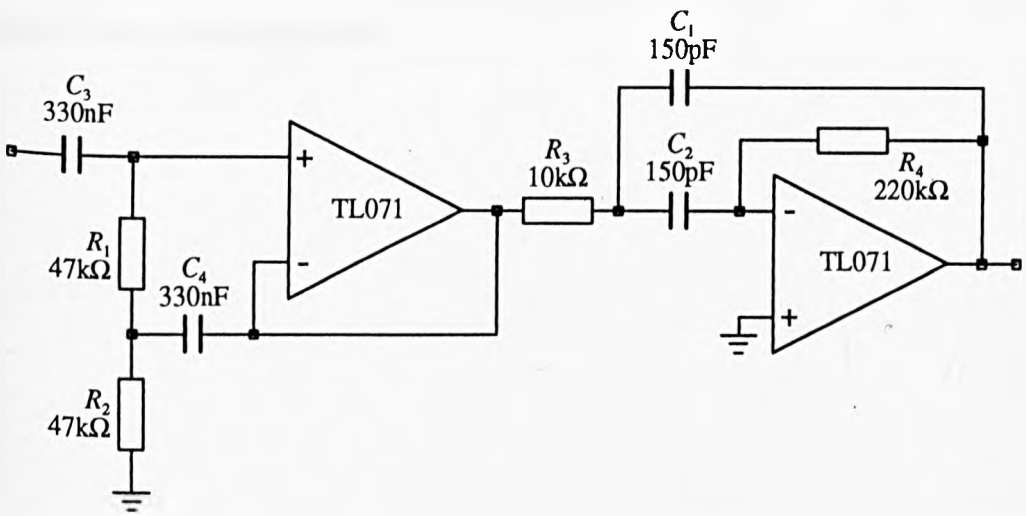

Figure 3.31 : The common mode feedback circuit.

capacitance of the buffer. The signal is then fed to a 'Friend circuit' [74] second order bandpass filter which has the transfer function

$$\frac{V_o}{V_i} = \frac{-C_2 R_2}{(C_1 + C_2)R_1} \cdot \frac{s(C_1 + C_2)R_1}{1 + s(C_1 + C_2)R_1 + s^2 C_1 C_2 R_1 R_2} \qquad \{3.18\}$$

The choice of components was a compromise between wanting a high pass band gain and a constant gain across the frequency range 20-27kHz. The components were chosen as R_1=10kΩ, R_2=220kΩ, C_1=C_2=150pF which centred the response on 22.6kHz with a Q of 2.34 and a bandwidth, f_0/Q of 9.6kHz. The predicted circuit response shown in Figure 3.32 (gain) and Figure 3.33 (phase) is in good agreement with the measured circuit response shown in Figure 3.34.

The maximum instantaneous common mode voltage at the input of the common mode feedback circuit when connected to the phantom was measured at approximately 0.6Vpk. The circuit should have reduced the common mode voltage by approximately one tenth at the drive frequencies.

The subtractors in the receive channels should be designed to cope with a common mode voltage of 1.3Vpk (due to position) plus 0.6Vpk due to mismatches giving a total of 1.9V. This value should be increased to 2.4V to allow for a maximum potential variation of 25%. This value of common mode voltage will be used in Chapter 4 when calculating the required CMRR of the subtractors.

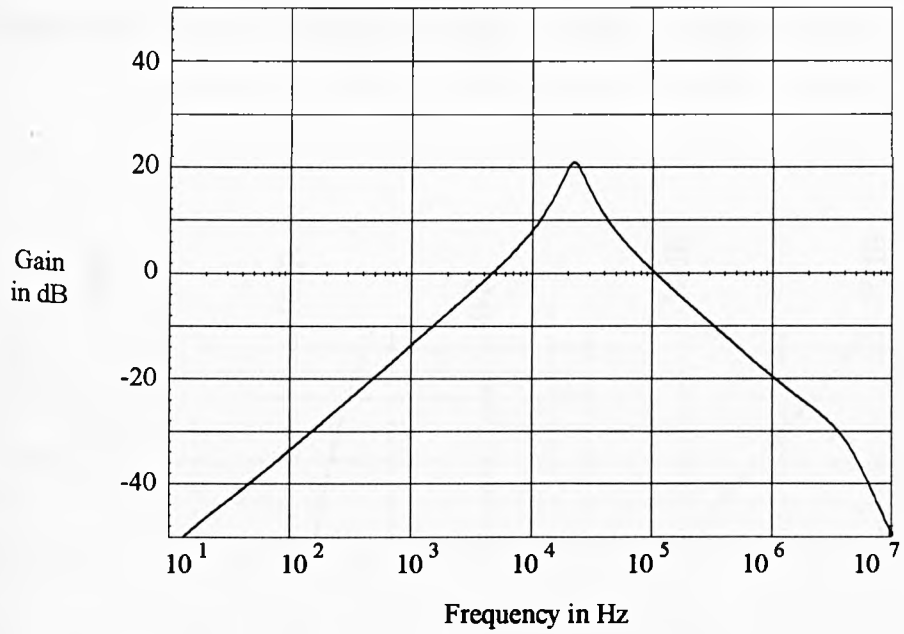

Figure 3.32 : Gain of Common Mode Feedback Circuitry (predicted by SPICE).

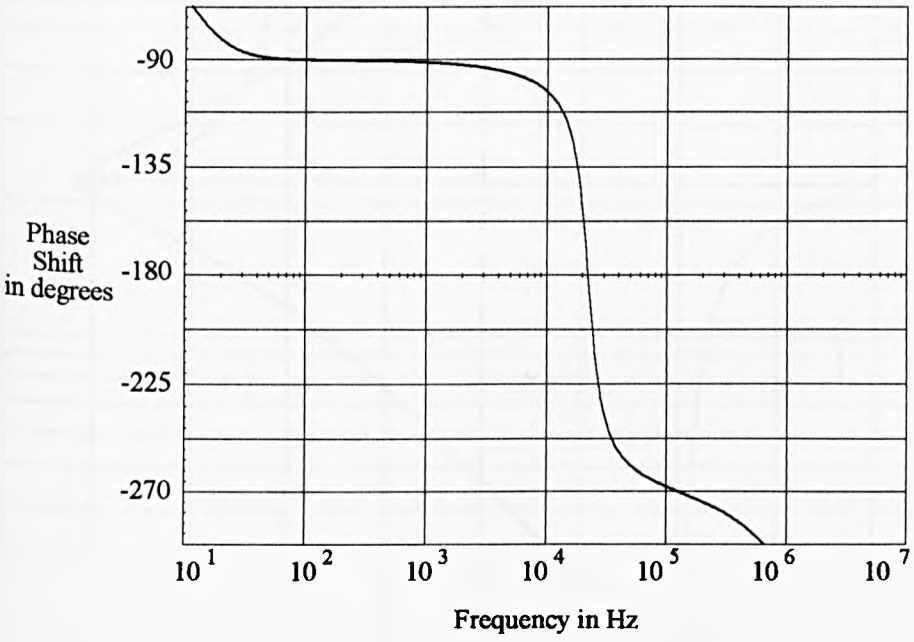

Figure 3.33 : Phase shift through Common Mode Feedback Circuitry (predicted by SPICE).

Figure 3.34 : Measured frequency response of the common mode feedback circuitry.

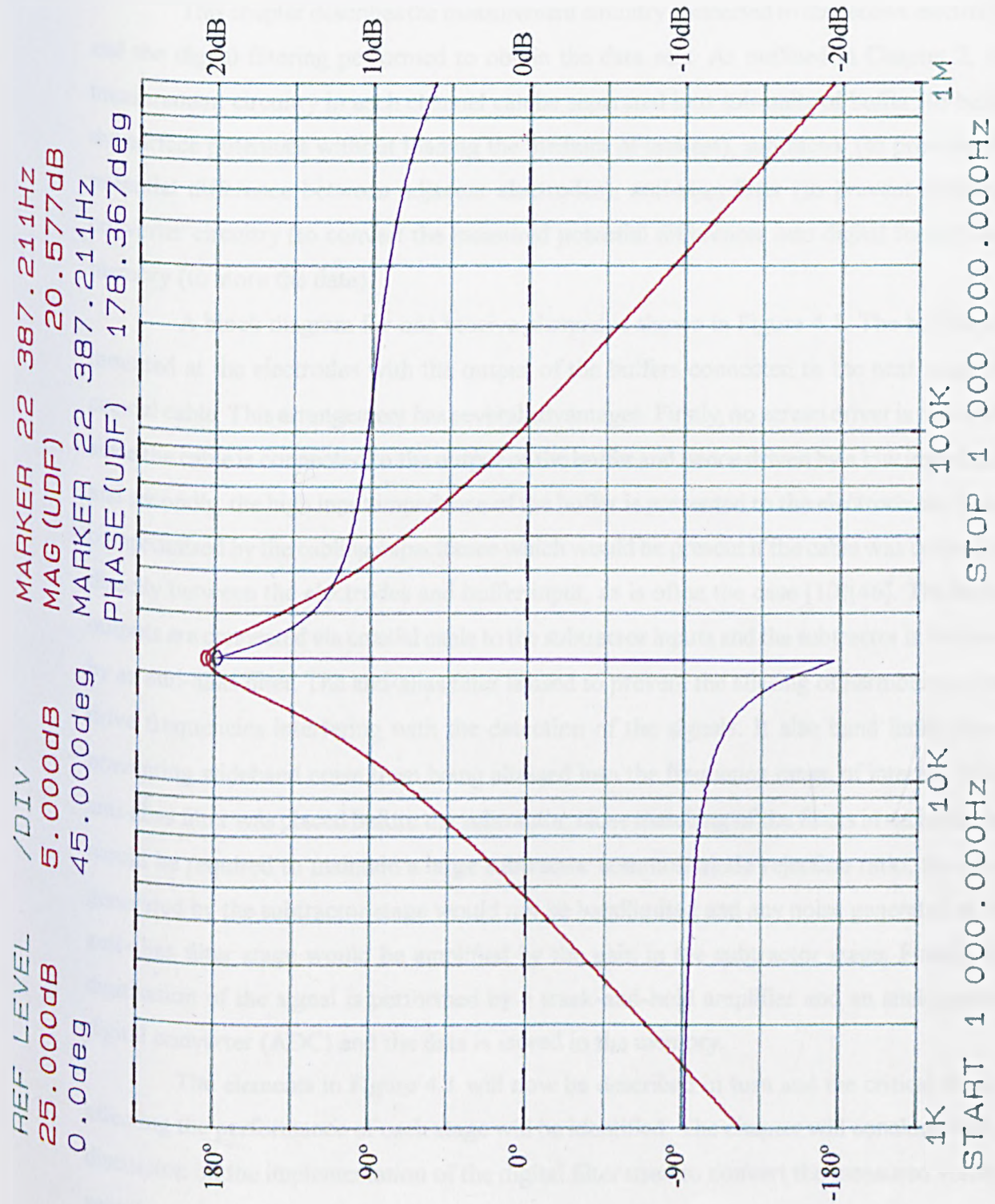

Chapter 4 Receiver Circuitry

4.1 Introduction

This chapter describes the measurement circuitry connected to the receive electrodes and the digital filtering performed to obtain the data sets. As outlined in Chapter 2, the measurement circuitry in each channel can be separated into sub-units of buffer (to buffer the surface potentials without loading the medium of interest), subtractor (to produce the potential difference between adjacent electrodes), anti-alias filter (to prevent aliasing), converter circuitry (to convert the measured potential differences into digital format) and memory (to store the data).

A block diagram for one receive channel is shown in Figure 4.1. The buffers are mounted at the electrodes with the output of the buffers connected to the next stage via coaxial cable. This arrangement has several advantages. Firstly, no screen driver is necessary since the cable is connected to the output of the buffer and hence driven by a low impedance and secondly, the high input impedance of the buffer is presented to the electrode and is not compromised by the cabling capacitance which would be present if the cable was connected directly between the electrodes and buffer input, as is often the case [10][46]. The buffer outputs are connected via coaxial cable to the subtractor inputs and the subtractor is followed by an anti-alias filter. The anti-alias filter is used to prevent the aliasing of harmonics of the drive frequencies interfering with the detection of the signals. It also band limits noise, preventing wideband noise from being aliassed into the frequency range of interest. If the anti-alias filter was placed before the subtractor, close matching of the filters in each channel would be required to maintain a large subtractor common mode rejection ratio, the noise generated by the subtractor stage would not be bandlimited and any noise generated in the anti-alias filter stage would be amplified by the gain in the subtractor stage. Finally, the digitisation of the signal is performed by a track-and-hold amplifier and an analogue-to-digital converter (ADC) and the data is stored in the memory.

The elements in Figure 4.1 will now be described in turn and the critical factors affecting the performance of each stage will be identified. The chapter will conclude with a discussion on the implementation of the digital filter used to convert the measured voltage samples into the reference and data set.

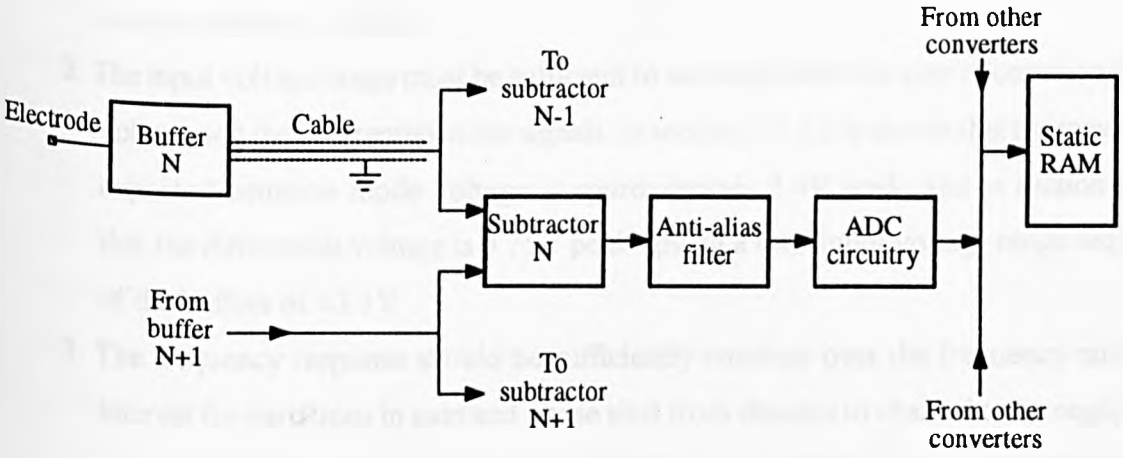

Figure 4.1 : Receive channel organisation.

4.2 Buffers

The purpose of the buffers is to detect the potential on the surface of the medium under investigation at the receive electrodes, without loading the medium.

4.2.1. Specification

The performance required of the buffers is listed below.

1. The input impedance must be high so as not to disturb the equipotential patterns set up in the medium of interest. To be consistent with the current source requirements, the input impedance of the buffers must be greater than the output impedance of the current sources (1.8MΩ).
2. The input voltage range must be sufficient to accommodate the sum of common mode voltage and the differential mode signals. In section 3.5.4 it is shown that the maximum expected common mode voltage is approximately 2.4V peak, and in section 4.3.1 that the differential voltage is 0.75V peak giving a total input voltage range required of the buffers of ±3.1V.
3. The frequency response should be sufficiently constant over the frequency range of interest for variations in gain and phase shift from channel to channel to be negligible. A gain error between buffers in each channel will generate, from a common mode voltage input, a differential voltage at the inputs of the subtractor stage which will be indistinguishable from the difference signal of interest. The gain error between channels that can be tolerated is therefore defined by the CMRR required of the following subtractor stage. This is given as 65dB in section 4.3.1 which means that the gain error should be less than 0.06%. The phase error between channels must be less than 0.67°. This figure is obtained by determining that the in-phase differential voltage generated by this error should not cause a voltage at the output of the subtractor which is detectable (ie the error is less than 0.5LSB of the ADC). It can be shown that

$$G_{diff}V_{cm}(1-\cos\phi) < \frac{1}{2}LSB \qquad \{4.1\}$$

By using the largest expected common mode voltage of 1.8V (see section 3.5.4), a subtractor differential gain of 5 (see section 4.3.3) and a 13 bit converter with a ±5V input range (see section 4.5) that ϕ <0.67°.

4.2.2 The Buffer Circuit and its Performance

A number of groups working within EIT use a simple unity gain connected FET input op-amp as a buffer [75]. Such op-amps have a typical parasitic input capacitance of 5-10pF [54], a reactance of 1.2MΩ at 27kHz which will limit the input impedance of the buffer. To avoid the problem posed by the parasitic input capacitance of op-amp inputs, a discrete buffer based on the circuit used by Tozer [76] was used. The discrete circuit of Tozer was slightly modified by the removal of the screen driver circuitry which was not necessary in this application, and the insertion of a wideband op-amp at the output to drive the coaxial cable. The buffer circuit is shown in Figure 4.2. The circuit was modelled using a SPICE package and the predicted gain and phase frequency response are shown in Figure 4.3 and Figure 4.4 respectively. The predicted input impedance as a function of frequency is shown in Figure 4.5. The input impedance is predicted as greater than 150MΩ and the amplitude response is flat at 0.9950 across the frequency range of interest. The phase was predicted as varying from 0.023° to 0.033° across the frequency range of interest. By varying the current gain, β, of the transistor in the output stage from 250 to 800, variations from 0.9950 to 0.9945 in gain were obtained (0.05%). The input range of the buffer was predicted to be approximately ±7V.

Seventeen identical buffer circuits were built on one pcb and the transfer function of each was measured on an HP3557A Network Analyser. A typical measured amplitude response is shown in Figure 4.6. The gain peaking occurs at a lower frequency in the measured response than in the predicted one and the measured peak is larger in amplitude. The difference between the measured and predicted response is likely to be caused by the inaccuracies in modelling the parasitic elements, particularly capacitance, which occurs in a real circuit layout. Since the peaking occurs at frequencies of greater than 3MHz it will not affect the performance of the buffer at the frequencies of interest. The gain and phase shift from input to output of the buffers at the frequencies of interest were measured for each buffer. The measurements were averaged to ensure some degree of accuracy. The transfer functions were flat across the frequency range of interest for each buffer and the gains varied from 0.9936V/V to 0.9951V/V corresponding to a matching of 0.15%. The maximum error in gain between adjacent buffers was measured as 0.08%. This is not within the gain matching specification of the channels and hence will give rise to small differential voltages from a common mode voltage input. However, it is difficult to measure such small variations in gain and the instrument used to measure the gain is quoted as having a temperature stability of 0.02dB/°C and a temporal stability of 0.05dB/hour, so caution should be used in

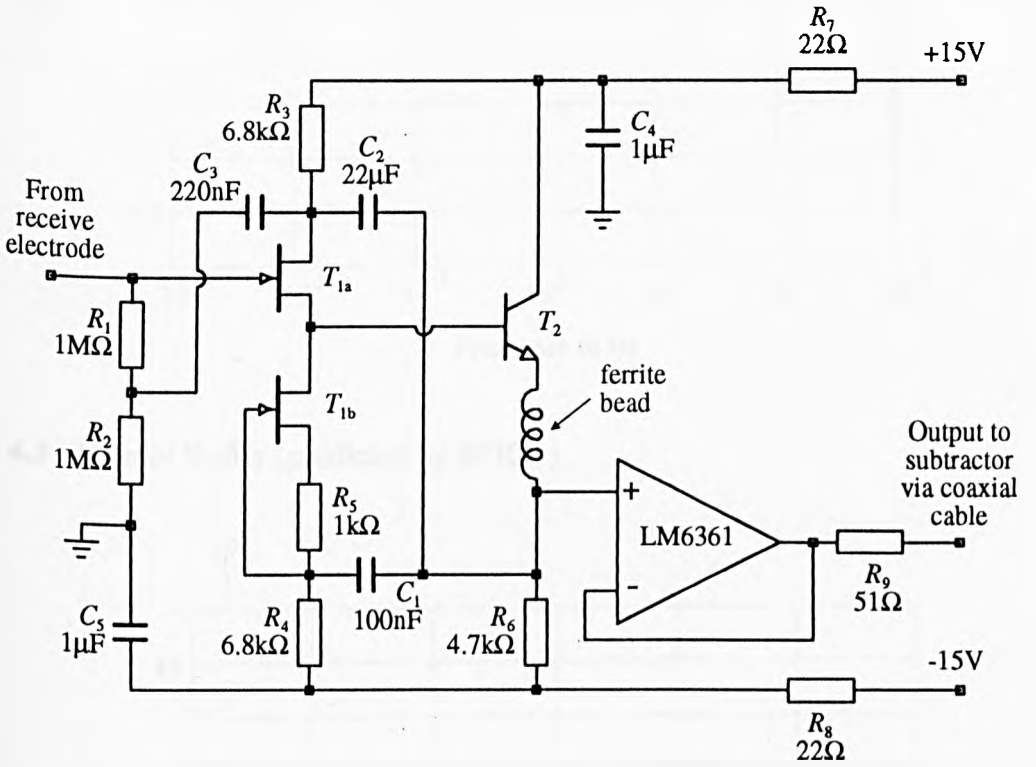

Figure 4.2 : Buffer circuitry used to sense the voltages on the surface of the medium.
Transistor T1 is a 2N3958 dual JFET.
Transistor T2 is a BC184LC.

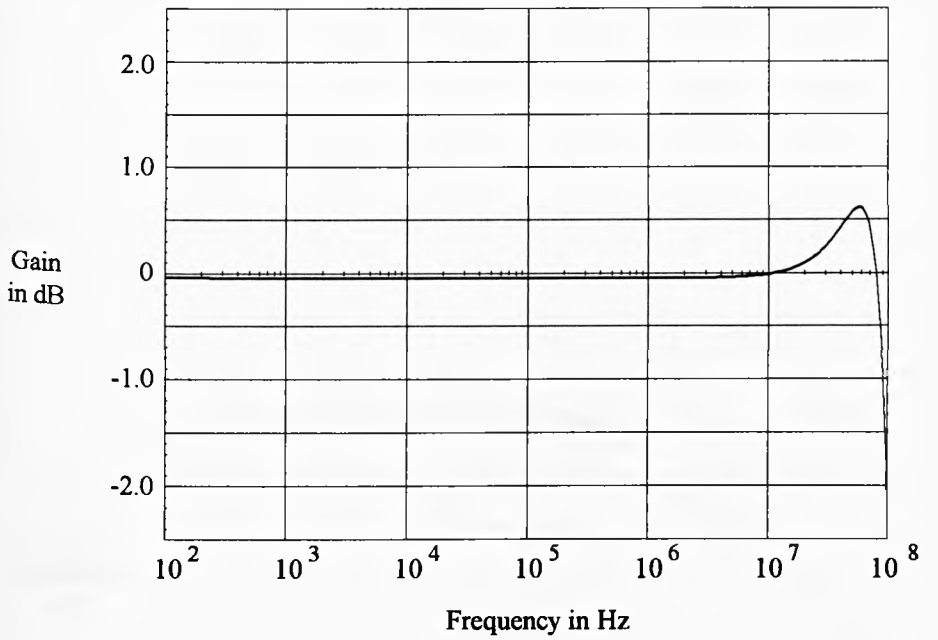

Figure 4.3 : Gain of Buffer (predicted by SPICE).

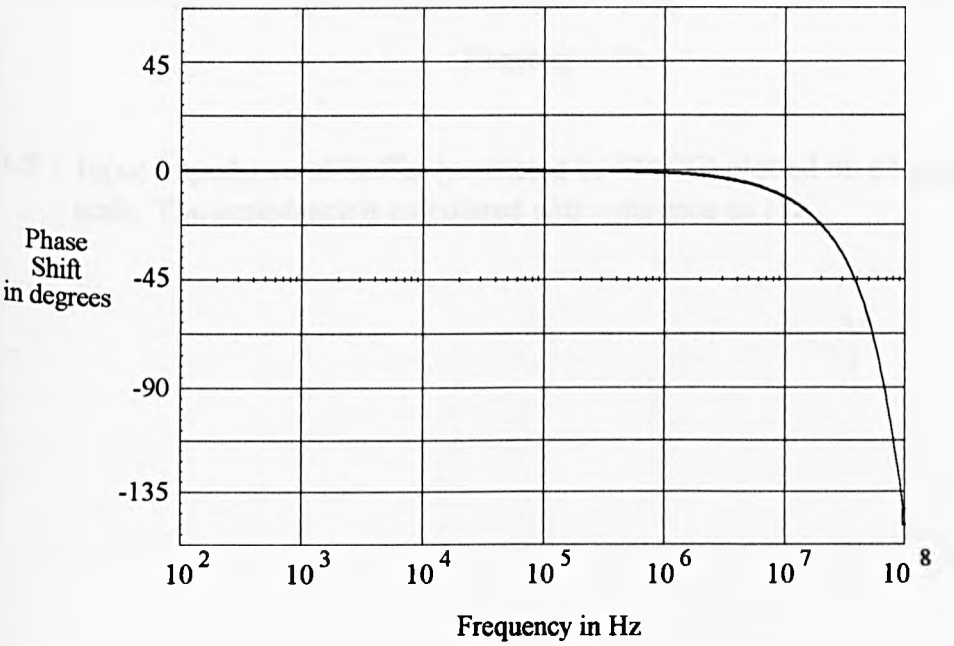

Figure 4.4 : Phase shift through Buffer (predicted by SPICE).

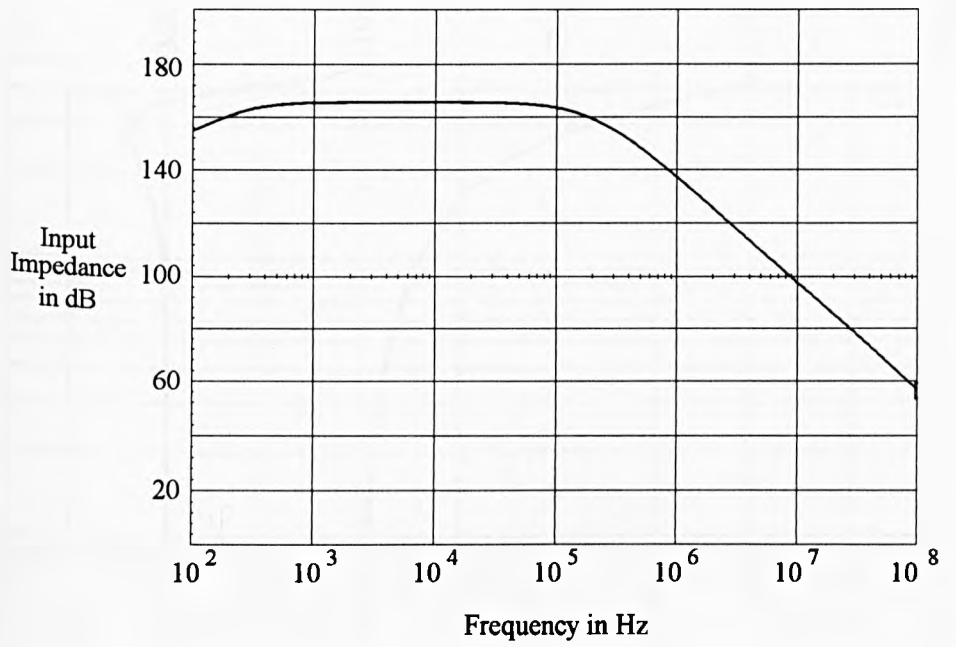

Figure 4.5 : Input Impedance of Buffer (predicted by SPICE) plotted on a logarithmic scale. The impedance is calculated with reference to 1Ω.

Figure 4.6 : Measured frequency response of the buffer.

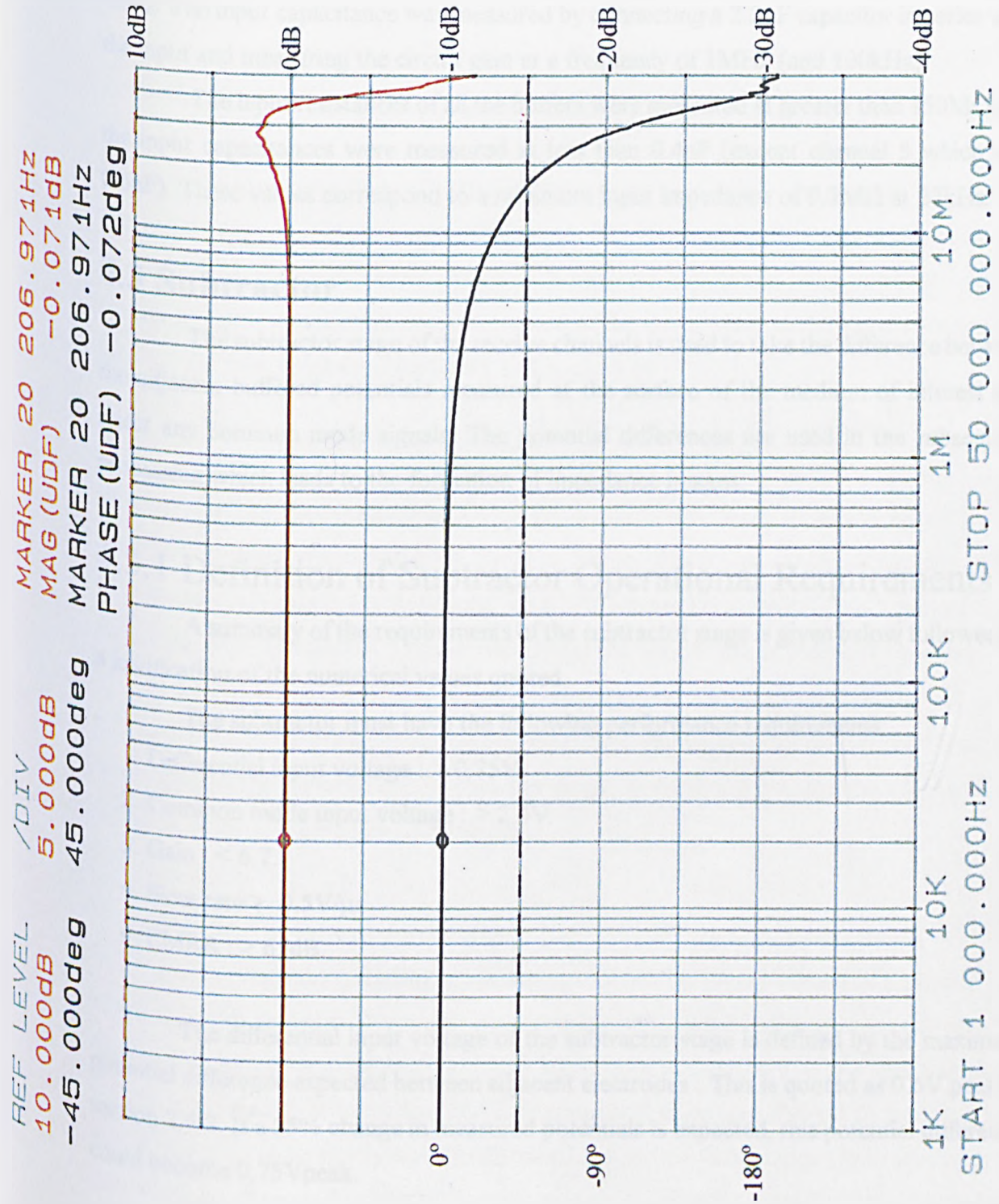

the interpretation of the above figures. Although the measured gain matching of the buffers is not within the specification, experiments performed later to measure the effects of the mismatch on the common mode rejection ratio of the following subtractor stages suggest that the matching is better than these measurements indicate. The phase shifts through all the buffers at the frequencies of interest were measured to be less than 0.1°.

The input impedance was measured by driving the buffer through a number of series resistances (820kΩ, 1.5MΩ, 2.2MΩ) and measuring the circuit gain at a frequency of 1kHz. The input capacitance was measured by connecting a 2.2pF capacitor in series with the input and measuring the circuit gain at a frequency of 1MHz (and 100kHz).

The input resistances of all the buffers were measured at greater than 150MΩ and the input capacitances were measured at less than 0.4pF (except channel 5 which was 0.6pF). These values correspond to a minimum input impedance of 9.2MΩ at 27kHz.

4.3 Subtractor

The subtractor stage of the receive channels is used to take the difference between the adjacent buffered potentials measured at the surface of the medium of interest and reject any common mode signals. The potential differences are used in the subsequent processing which leads to the formation of impedance images.

4.3.1 Definition of Subtractor Operational Requirements

A summary of the requirements of the subtractor stage is given below followed by a justification of the numerical values quoted.

The subtractor must have the following performance requirements:

1. Differential input voltage : > 0.75V.
2. Common mode input voltage : > 2.4V.
3. Gain : < 6.7.
4. Slew rate > 0.5V/μs.
4. CMRR : > 65dB.

The differential input voltage of the subtractor stage is defined by the maximum potential difference expected between adjacent electrodes : This is quoted as 0.6V peak in section 2.6.2. If a 25% change in measured potentials is expected, this potential difference could become 0.75Vpeak.

The maximum common mode voltage expected is 2.4V peak as stated in section

3.5.4, so the inputs of the subtractor should be able to cope with this range.

Any gain required to amplify the signal such that the maximum signal occupies the full range of the ADC input range may be applied at the subtraction stage. The input range of the ADC is ±5V (see section 4.5) and so the maximum possible instantaneous voltage difference should be amplified to fill this range in order to maintain the maximum receiver dynamic range. The maximum expected potential difference is 0.75Vpk (see above), so the gain required to make full use of the ADC input range is 5/0.75 = 6.7. However, it is important that the input of the ADC does not saturate under any circumstances, since this will not necessarily be obvious from the filtered data. In order to avoid saturation, a gain of approximately 5 was used and, so that resolution was not lost, a 13 bit ADC was used.

The slew rate required by the subtractor can be calculated by considering the slew rates of the signals at the separate frequencies. The received signal at any receive pair will consist of the 15 drive frequencies all with different amplitudes. The maximum rate of change of signal voltage will occur at the end of the array, when all the signals are passing through the zero point simultaneously and is given by

$$\left.\frac{dV}{dt}\right|_{\max} = A_1\omega_1 + A_2\omega_2 + \ldots + A_{15}\omega_{15} \qquad \{4.2\}$$

Where $A_1..A_{15}$ are the magnitudes of the voltage differences caused at an end pair of receive electrodes by each of the frequency drives at frequencies ω_1 , ω_2 ,.., ω_{15}. Using the values of potentials in Figure 2.4 and allowing for a 25% increase in amplitude and a gain of 5, the maximum dV/dt is 0.5V/μs, a figure well within the capabilities of standard op-amps.

The CMRR of a subtractor is defined at each frequency as the ratio of the differential mode gain to the common mode gain. As stated in section 3.5.1, for the effects of the common mode voltage to be undetected,

$$CMRR > \frac{V_{com}G_{diff}}{0.5LSB} \qquad \{4.3\}$$

The maximum common mode voltage at one frequency occurs at a receive pair which straddles the drive electrodes. By averaging the potential calculated at each of these receive electrodes, the maximum common mode voltage is 131mV. If the common mode voltage generated by mismatches (which was reported as being 0.6Vpeak in section 3.5.4) can be assumed to be composed equally of all the source frequencies , then the common mode voltage generated by one of the sources would be 0.6/16 = 38mV. This would give a

total common mode voltage at one of the source frequencies of approximately 170mV. If this is subject to a variation of 25%, the maximum common mode voltage at one frequency could reach 213mV. This gives a CMRR requirement of 65dB across the signal frequency range for the 13 bit ADC and a differential gain of 5 as stated above.

4.3.2 Possible Subtractor Implementations

There are a number of ways of subtracting the signals between adjacent electrodes; some of these are listed below.

A switched capacitor can be used to extract the potential difference between two potentials. In this method the capacitor would be connected via analogue switches between two adjacent receive electrodes and would therefore be charged to the potential difference between the electrodes as shown in Figure 4.7. The capacitor would then be switched to the input of an amplifier with appropriate gain, followed by the analogue-to-digital converter. A sample-and-hold amplifier is not required in this method since the switched capacitor is effectively performing a sample and hold process. However, because the sampling of the signal is occurring at the capacitor stage, the anti-alias filters must precede this stage.

Figure 4.7 shows the connection of the circuitry where B_1 to B_{17} are the buffers connected to the receive electrodes on the surface of the medium of interest, AAF_1 to AAF_{16} are the anti-alias filters, S_1 and S_2 are analogue switches, A_1 to A_{16} are amplifiers and ADC_1 to ADC_{16} are the ADCs.

When S_1 is closed and S_2 is open the capacitor is charged through the on resistance, R_{on}, of the analogue switches S_1 and S_2. The capacitor between each channel, denoted as C_h, should be chosen such that the product $2R_{on}C_h$ is much less than the time period of the signal, so that the potential on the capacitor will be the voltage difference between the two potentials at the electrodes to an acceptable accuracy. Also, for the capacitor, C_h, to charge to the maximum potential difference expected of 0.75V to within 1/2 least significant bit of the following 13 bit ADC and a gain of 5 of the subtractor stage is assumed, then the ratio of the sampling time to $2R_{on}C_h$ must be less than 8.7. Assuming a typical value of 100Ω for R_{on}, the 'on' resistance of the switch S_1, and assuming that the system is sampling for half the duration of the switching period, then C_h must be less than 2.3nF.

The droop in voltage caused by bias current flowing into A_1 must be less than 1/2 least significant bit of the ADC over the time for which any settling and conversion occurs.

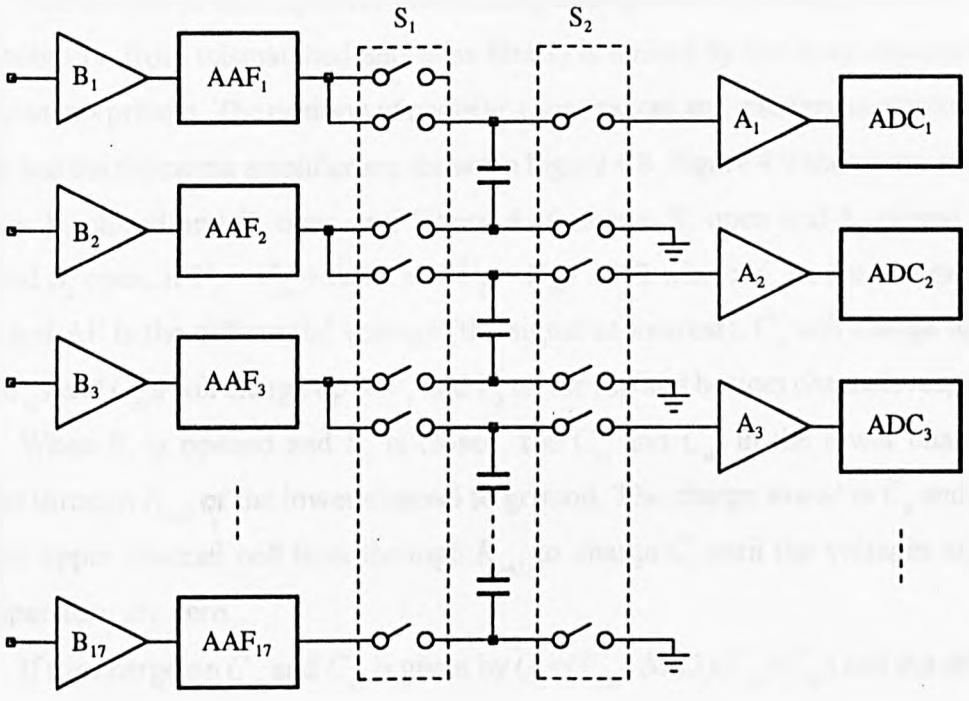

Figure 4.7 : Subtraction using switched capacitors.

For example, for a hold capacitor of 2.2nF, and a hold time of half the switching period, the bias current must be less than 340nA which is easily realisable using FET input op-amps.

The positioning of the anti-alias filters before the subtraction stage means that the anti-alias filters have to be well matched or extra processing will be required to take into account the different transfer functions of the AAFs (see Appendix D). Furthermore, any mismatch will also cause a reduction in the common mode rejection ratio of the subtraction stage (see section 4.3.3 and Appendix E.3 for more details).

The CMRR of this capacitor differencing arrangement (ignoring, for the moment, any contribution from mismatched anti-alias filters) is limited by the stray capacitances of the components present. The position of parasitic capacitances and resistances of the analogue switches and the following amplifier are shown in Figure 4.8. Figure 4.9 shows the equivalent circuit for S_1 closed and S_2 open and Figure 4.10 shows S_1 open and S_2 closed. For S_1 closed and S_2 open, if $V_1 = V_{cm} + \Delta V/2$ and $V_2 = V_{cm} - \Delta V/2$ where V_{cm} is the common mode voltage and ΔV is the differential voltage (the signal of interest), C_h will charge up to ΔV and the C_{s1}s and C_{d2}s will charge up to V_1 and V_2 on the top and bottom channels respectively.

When S_1 is opened and S_2 is closed, the C_{s1} and C_{d2} in the lower channel will discharge through R_{on2} of the lower channel to ground. The charge stored in C_h and C_{s1} and C_{d2} in the upper channel will flow through R_{on2} to charge C_f until the voltages across all other capacitors are zero.

If the charge on C_{s1} and C_{d2} is given by $Q_1=(V_{cm}+\Delta V/2)(C_{s1}+C_{d2})$ and the charge on C_h is given by $Q_2=\Delta V C_h$,and assuming that the amplifier A_1 takes no bias current, the conservation of charge can be applied and the voltage across the capacitor C_f as $t\rightarrow\infty$ is

$$V_o = \frac{Q_{tot}}{C_{tot}} = \frac{\left(V_{cm} + \frac{\Delta V}{2}\right)(C_{s1} + C_{d2}) + \Delta V C_h}{C_f} \qquad \{4.4\}$$

The CMRR is defined as the ratio of the differential mode gain to common mode gain which in this case is

$$CMRR = \frac{C_h + \left(\frac{C_{s1} + C_{d2}}{2}\right)}{C_{s1} + C_{d2}} = -61\text{dB} \quad \text{for } C_h\text{=10nF and } C_{s1} = C_{d2} = 5\text{pF.} \qquad \{4.5\}$$

Although this technique is commonly used in switched capacitor filters and has recently been successfully used in EIT applications at low frequencies [77] it was not used as the subtraction stage in this system. The expected CMRR is too low and although on ICs

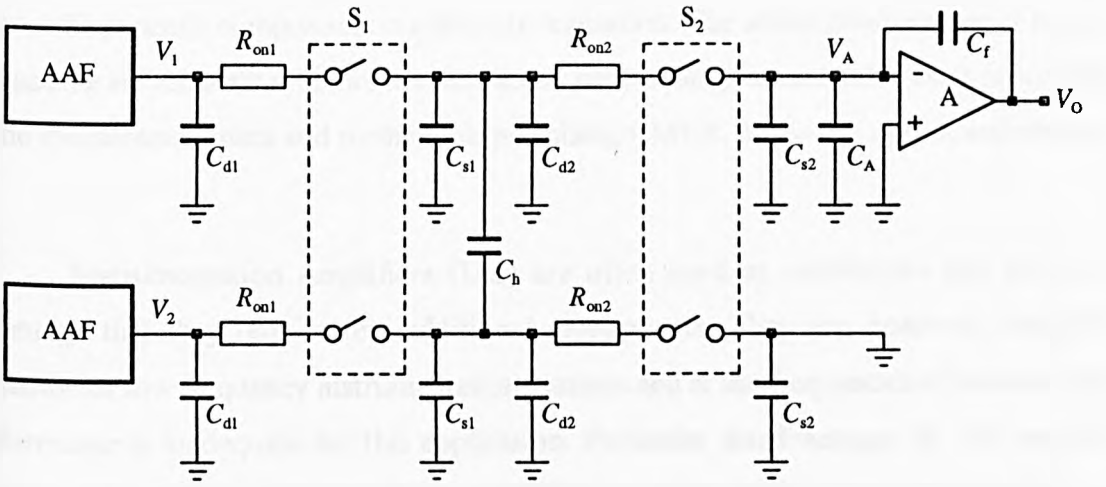

Figure 4.8 : An equivalent circuit showing the parasitic elements in a switched capacitor subtractor.

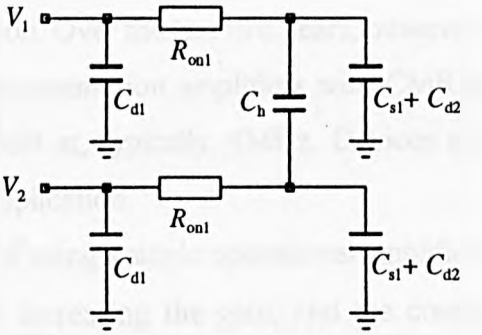

Figure 4.9 : Reduced form of Figure 4.8 for S_1 closed and S_2 open.

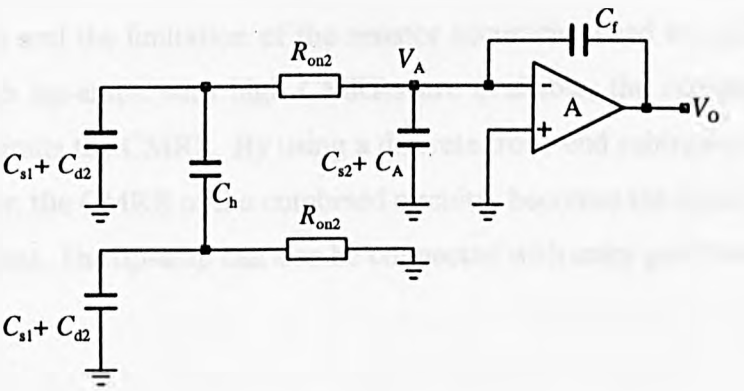

Figure 4.10 : Reduced form of Figure 4.8 for S_1 open and S_2 closed.

used in switched capacitor filters the parasitics are fairly well matched, it is difficult to control the parasitic components in a discrete realisation. The added disadvantage of having to place the anti-alias filter before the subtractor, necessitating considerable extra processing of the measurement data and further compromising CMRR, made this option undesirable.

Instrumentation Amplifiers (IAs) are often used as subtractors and have the advantage that they require few additional components. They are, however, designed primarily for low frequency instrumentation systems and at the frequencies of interest their performance is inadequate for this application. Particular disadvantages of IAs are that some have fixed gain which would mean that the signals would have to be amplified at a later stage, their CMRR is low at the frequencies of interest and their bandwidths are poor, hence introducing phase errors at the signal frequencies.

A number of IAs which satisfied the >65dB CMRR specification were investigated but none of these were capable of satisfying all of the requirements listed in section 4.3.1 at the time of this investigation. Over the last two years, however, a number of manufacturers have produced video instrumentation amplifiers with CMRRs in excess of 80dB at low frequencies, falling to 70dB at, typically, 4MHz. Devices such as these [54][78] would have been ideal for this application.

The drawbacks of using a single operational amplifier subtractor circuit is that the bandwidth is reduced by increasing the gain, and the common mode rejection ratio is dependent upon resistor accuracy. Three op-amp subtractors are often used to imitate instrumentation amplifier topologies [79]. Two of the op-amps are used to buffer the input voltages so that the previous circuitry does not affect the behaviour of the third op-amp which is used as a subtractor. This still has the disadvantage of reduced bandwidth for gains greater than unity and the limitation of the resistor accuracies used to set the gain on the CMRR. Although op-amps with high CMRRs are available, the component tolerance dependency still limits the CMRR. By using a discrete front-end subtractor to precede the op-amp subtractor, the CMRR of the combined circuitry becomes the sum of the CMRR of the two components. The op-amp can also be connected with unity gain thus increasing the bandwidth.

Due to the failings of other possible subtractor implementations the subtractor chosen was a discrete differential input pair with a current source tail followed by a unity gain op-amp subtractor. This arrangement has the advantage just mentioned that both the

differential input pair and the op-amp are subtracting the signal and so the CMRR of the whole circuit is the sum of the CMRRs of the two separate stages.

4.3.3 Subtractor Circuit Description

The circuit of the subtractor is shown in Figure 4.11. The discrete differential input pair are biassed by a current source tail and their collectors are connected to a standard subtractor connected op-amp. The gain of the circuit is calculated in Appendix E.1 and is given approximately by

$$Gain = \frac{RR_C}{(R_E + r_e)(R + R_C)} \qquad \{4.6\}$$

where r_e is the incremental resistance of T_1 and T_2, $R=R_4=R_5=R_6=R_7$, $R_E=R_{E1}=R_{E2}$ and $R_C=R_{C1}=R_{C2}$ as shown in the figure. The current source is set up to draw a total current of 4mA (making $r_e \approx 13\Omega$). The value of gain given by the circuit for the components shown is 4.9 which is within the maximum allowable gain of 6.7. The components R_{C1}, R_{C2}, R_{E1}, R_{E2}, and $R_{4\text{-}7}$ are all matched to 0.1% (temperature stability 15ppm) so that the op-amp subtraction stage CMRR is as high as possible. The slew rate of a TL071 op-amp (the amplifier in Figure 4.11) is greater than 5V/μs and thus satisfies the required value of 0.5V/μs.

Equation {4.6} which expresses the gain of the subtractor was derived by assuming matched components as shown in Appendix E.1. The circuit was simulated using a SPICE package and the gain and phase responses of the transfer function $V_o/(V_1\text{-}V_2)$ are given in Figure 4.12 and Figure 4.13 respectively for perfectly matched components. When the components are mismatched by the tolerance of the components and using transistors of current gains of 230 and 210, variations in gain from 4.8226 to 4.8216 (0.02%) are obtained. This shows that any gain mismatch between the channels should be less than approximately -74dB down on the normal figure for differential gain.

The common mode voltage input range that can be tolerated by the circuit of Figure 4.11 for a maximum differential input voltage of 0.7V, can be calculated using large signal considerations. This analysis is given in Appendix E.2 and gives the range of common mode input voltage as $-7.4\text{V} < V_{cm} < 6.8\text{V}$.

The maximum CMRR that can be obtained from any subtractor circuitry is heavily dependent upon component matching. Figure 4.14 shows the predicted CMRR for all components exactly matched. When components were mismatched on the SPICE simulation, it was found that only mismatches in the base bias resistors, R_{b1} , R_{b2} , the ac coupling capacitors C_1 , C_2, and the transistor current gains, β_1 , β_2, had a serious effect on the

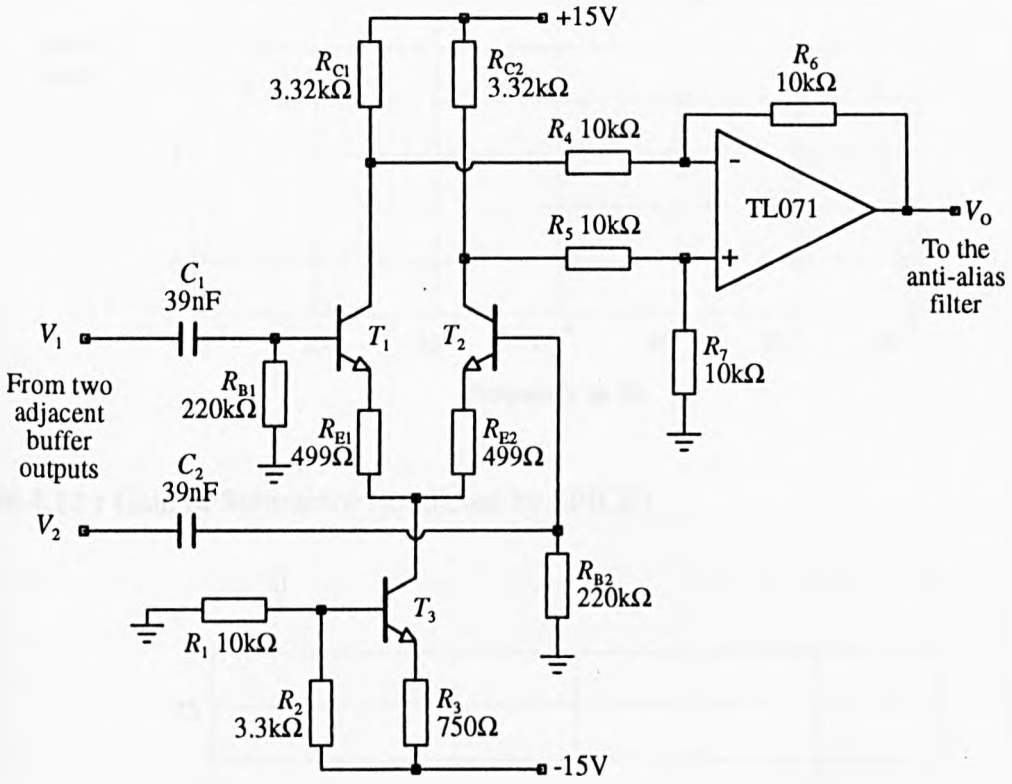

Figure 4.11 : The subtractor circuit.
Transistors T_1, T_2 and T_3 are BC184LC.
Resistors R_{E1}, R_{E2}, R_{C1}, R_{C2}, R_4, R_5, R_6 and R_7 are 0.1%.

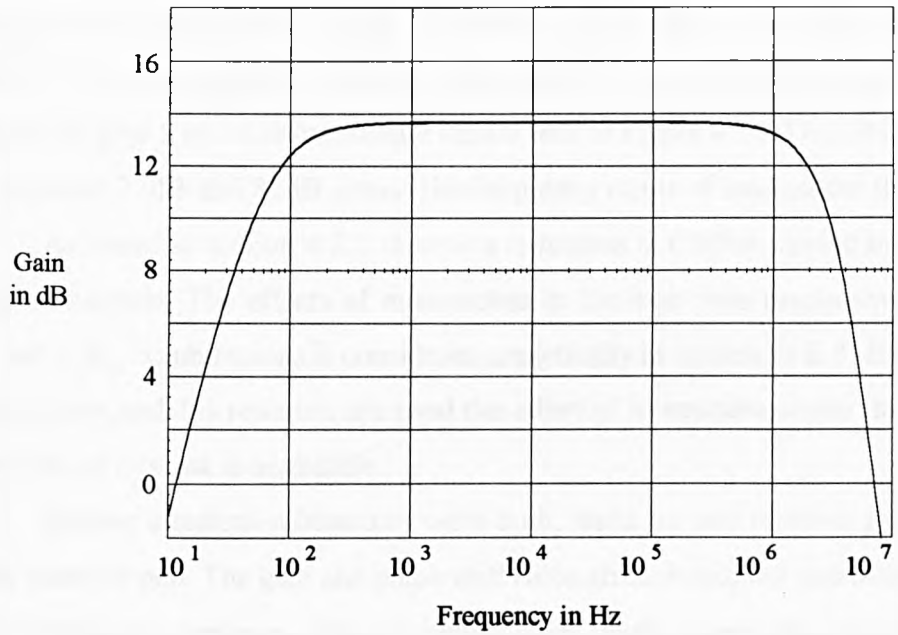

Figure 4.12 : Gain of Subtractor (predicted by SPICE).

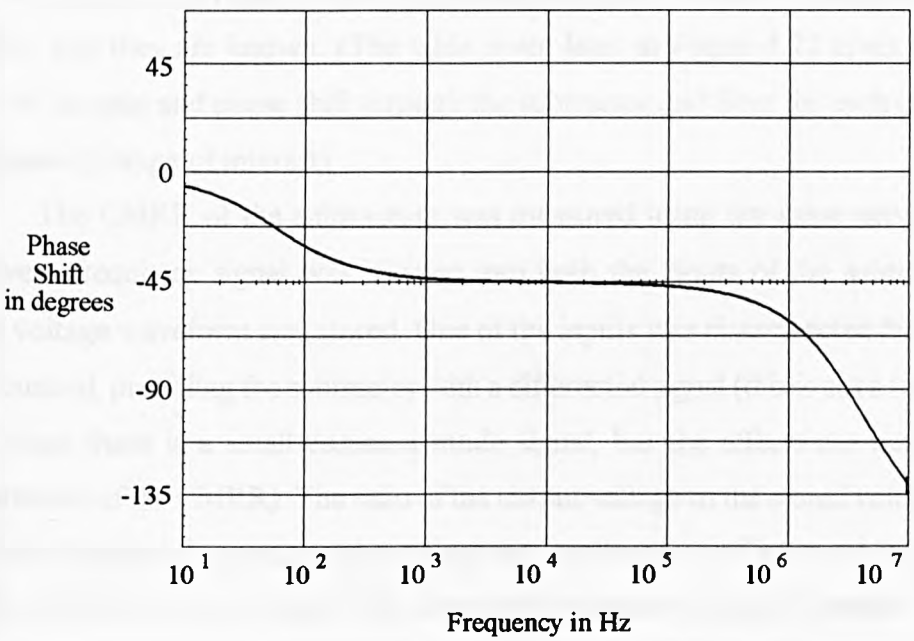

Figure 4.13 : Phase shift through Subtractor (predicted by SPICE).

CMRR. This is because mismatches in these parameters convert a common mode voltage into an effective differential voltage before subtraction has occurred and hence cannot be distinguished from the signal voltage difference. The CMRR of the circuit for the base bias resistors, the input capacitors and the current gains of the transistors mismatched by their tolerances to give a worst case estimate can be seen in Figure 4.15. The CMRR is predicted to be between 77dB and 81dB across the frequency range of interest for this case.

As stated in section 4.2.1 there is a reduction in CMRR caused by mismatches in the input channels. The effects of mismatches in the high pass responses created by the C_1R_{b1} and C_2R_{b2} combinations is considered analytically in Appendix E.3. It is shown that if 1% capacitors and 1% resistors are used the effect of mismatches upon the CMRR at the frequencies of interest is negligible.

Sixteen identical subtractors were built, eight on one receiver pcb and eight on another receiver pcb. The gain and phase shift through each channel was measured using an HP3557 Network Analyser with one input driven by the swept frequency source of the network analyser and the other input of the subtractor grounded. A typical plot can be seen in Figure 4.16. The gain is 4.85 across the frequency range of interest as predicted by simulation, and the phase shift is approximately -0.7°. The variation in gain and phase between channels can readily be compensated, along with the anti-alias filter mismatches, provided that they are known. (The table given later in Figure 4.22 gives the measured values of the gain and phase shift through the subtractor and filter for each channel across the frequency range of interest).

The CMRR of the subtractors was measured using the same network analyser. The swept frequency signal was injected into both the inputs of the subtractor and the output voltage waveform was stored. One of the inputs was disconnected from the source and grounded, providing the subtractor with a differential signal (this is not a true differential signal since there is a small common mode signal, but the effects are negligible in the measurement of the CMRR). The ratio of the output voltage to the stored voltage waveform was plotted against frequency and a typical plot can be seen in Figure 4.17. It can be seen that the CMRR is greater than 72dB across the frequency range of interest. The CMRR was measured for all channels and did not fall below 72dB for any channel.

Since mismatches in input channel transfer functions give rise to differential mode voltages, it is expected that because the adjacent buffer gains were only matched to 0.08%, the CMRR will be below the values measured for the subtractor only. However, the measurement process was repeated using the worst gain matched pair of buffers with the input signals connected to the buffer inputs rather than directly into the subtractor inputs.

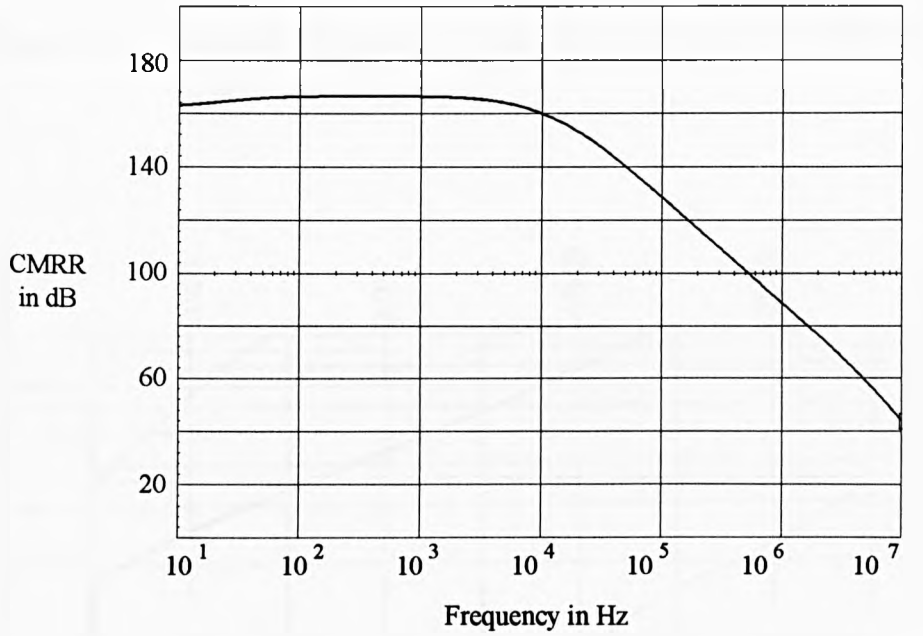

Figure 4.14 : Common Mode Rejection Ratio of Subtractor with matched components (predicted by SPICE).

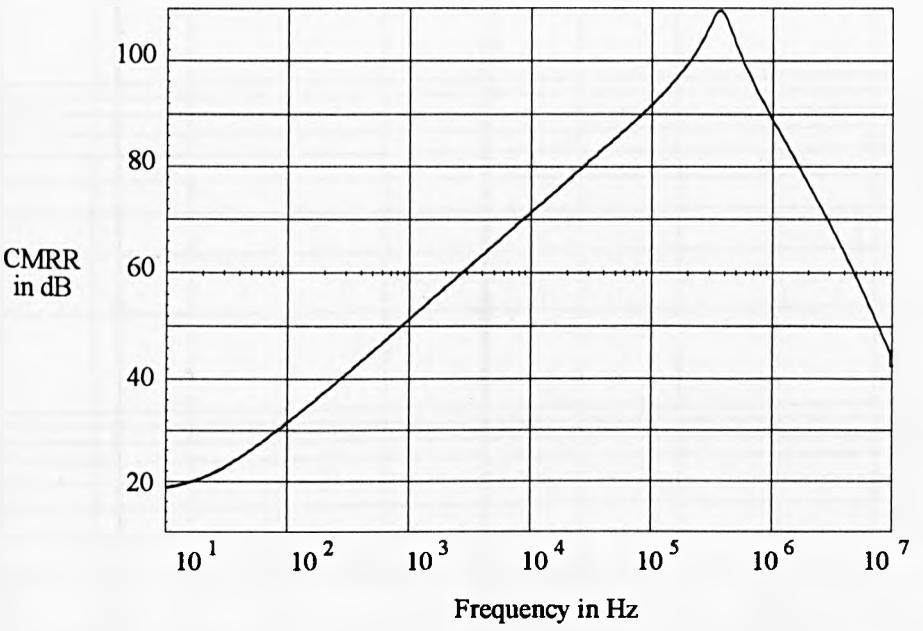

Figure 4.15 : Common Mode Rejection Ratio of Subtractor with mismatched components (predicted by SPICE).

Figure 4.16 : Measured frequency response of the subtractor for a differential voltage input.

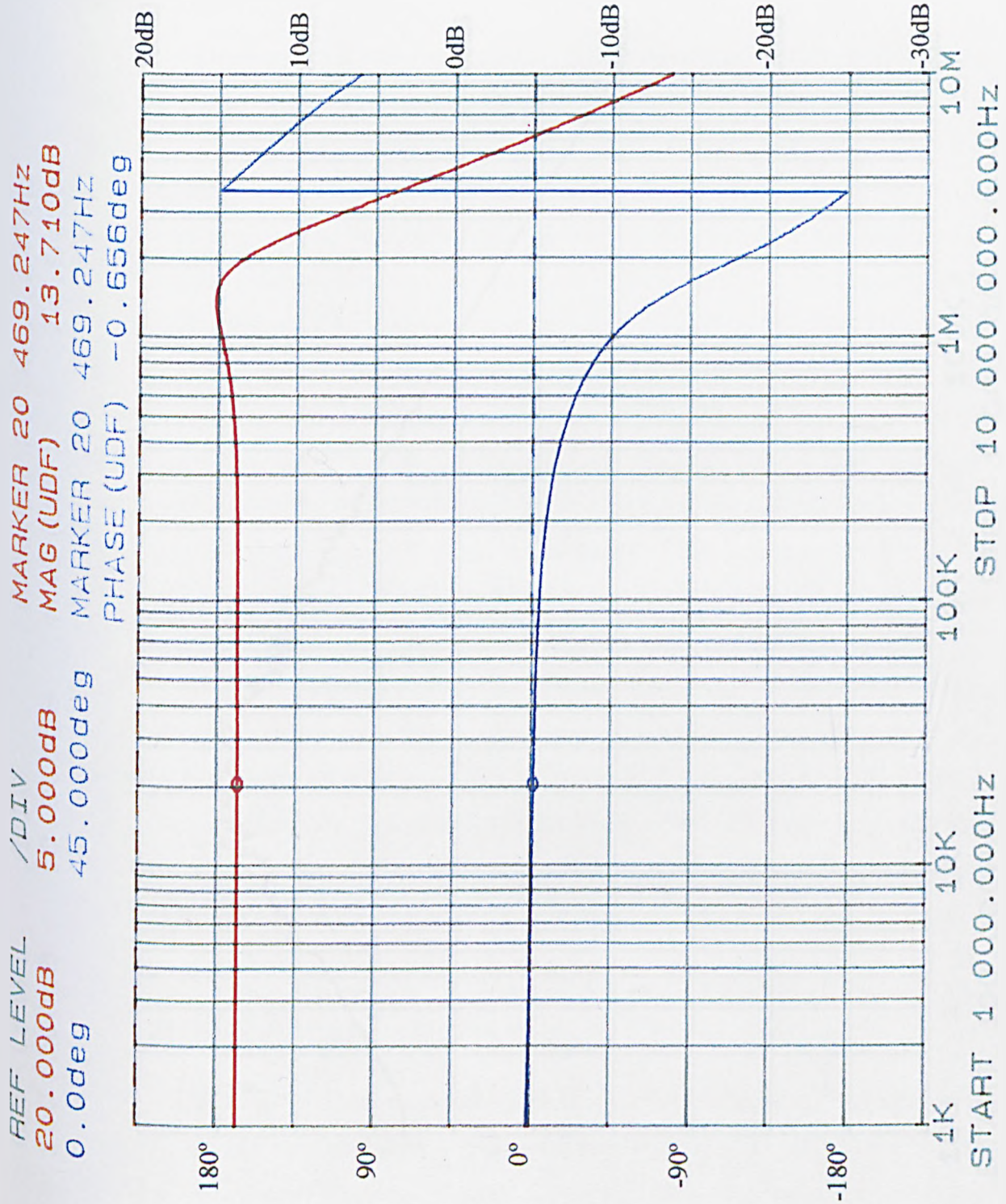

Figure 4.17 : Measured common mode rejection ratio of the subtractor.

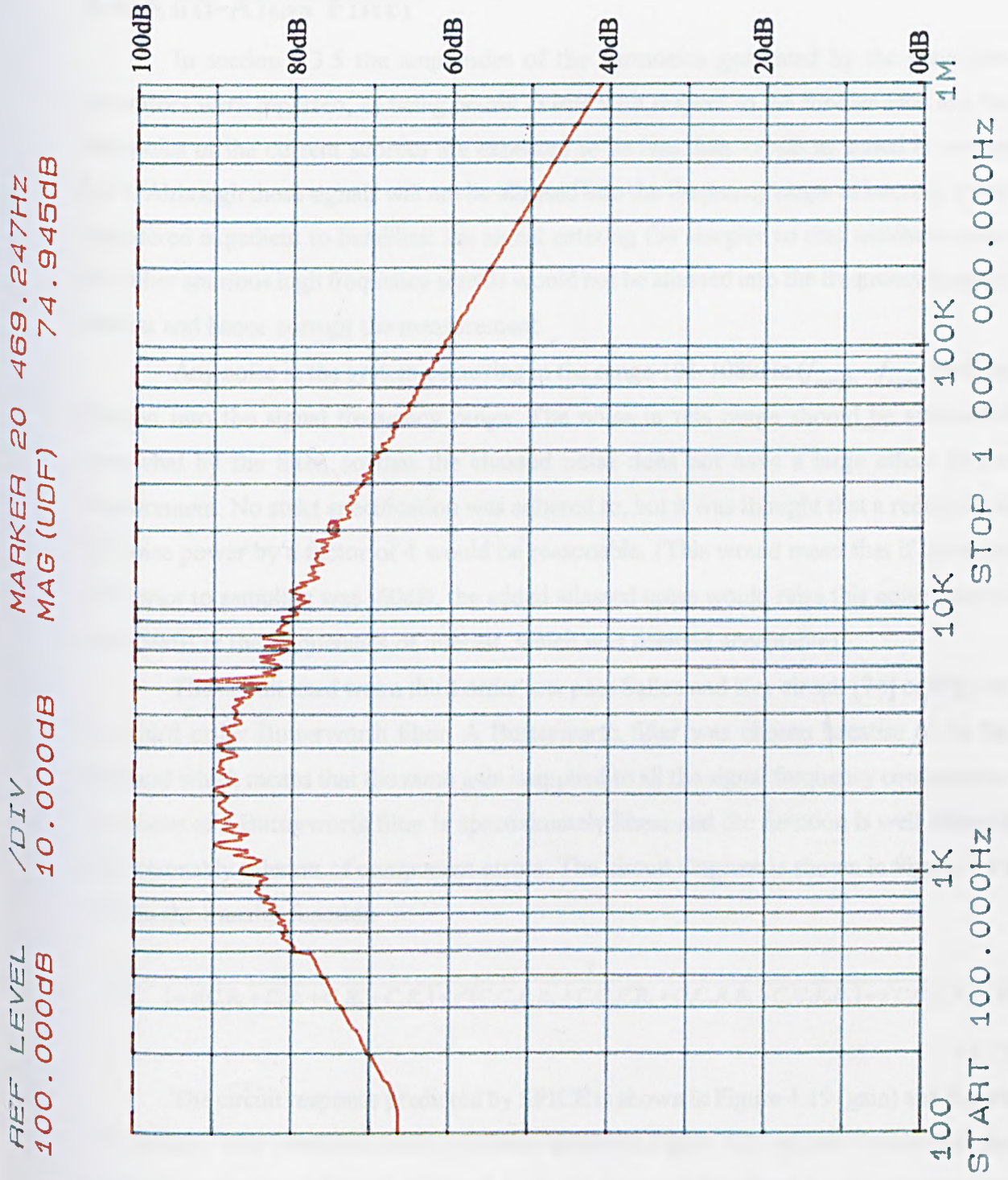

The CMRR of the channel was measured and was only 0.4dB down on the subtractor CMRR. This implies that the buffers must be matched more closely than could be measured in section 4.2.2 and highlights the problems of making measurements to such an accuracy. In fact it appears that CMRR measurement is a much more sensitive method of determining the gain matching of the channels prior to subtraction than direct gain measurement.

4.4 Anti-Alias Filter

In section 3.3.5 the amplitudes of the harmonics generated by the waveform generators were reported, as being below -57dB with respect to the fundamental and the harmonics of the current sources are expected to be less than -59dB as stated in section 3.4.7. Although these signals will not be aliassed into the frequency range of interest, it was considered expedient to bandlimit the signal entering the sampler so that wideband noise and other spurious high frequency signals would not be aliassed into the frequency range of interest and hence corrupt the measurement.

Any noise in the system occurring in the range 101-108kHz (f_{sample} - f_{signal}) will be aliassed into the signal frequency range. The noise in this range should be attenuated somewhat by the filter, so that the aliassed noise does not have a large effect on the measurement. No strict specification was adhered to, but it was thought that a reduction in the noise power by a factor of 4 would be reasonable. (This would mean that if the noise level prior to sampling was -60dB, the added aliassed noise would raise this noise floor to only -59dB at the frequencies of interest, which was deemed acceptable).

The circuit used was a third order low pass Sallen and Key circuit [74] configured as a third order Butterworth filter. A Butterworth filter was chosen because of its flat passband which means that the same gain is applied to all the signal frequency components. The phase of a Butterworth filter is approximately linear and the function is well behaved and reasonably tolerant of component errors. The circuit diagram is shown in Figure 4.18 and has the transfer function

$$\frac{V_o}{V_{in}} = \frac{1}{1+s(C_1R_1+C_3R_1+C_3R_2+C_3R_3)+s^2(C_1C_3R_1R_2+C_1C_3R_1R_3+C_2C_3R_1R_3+C_2C_3R_1R_3)+s^3C_1C_2C_3R_1R_2R_3} \quad \{4.7\}$$

The circuit response predicted by SPICE is shown in Figure 4.19 (gain) and Figure 4.20 (phase). The measured circuit response shown in Figure 4.21 agrees closely with the predicted responses of figures 4.19 and 4.20. As expected the phase is not constant over the frequency range of interest, but since the anti-alias filter is placed after the subtractor,

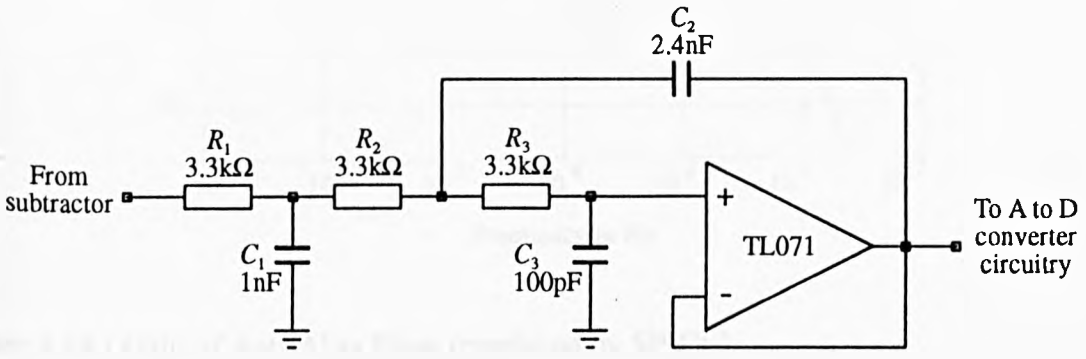

Figure 4.18 : The third order anti-alias filter.

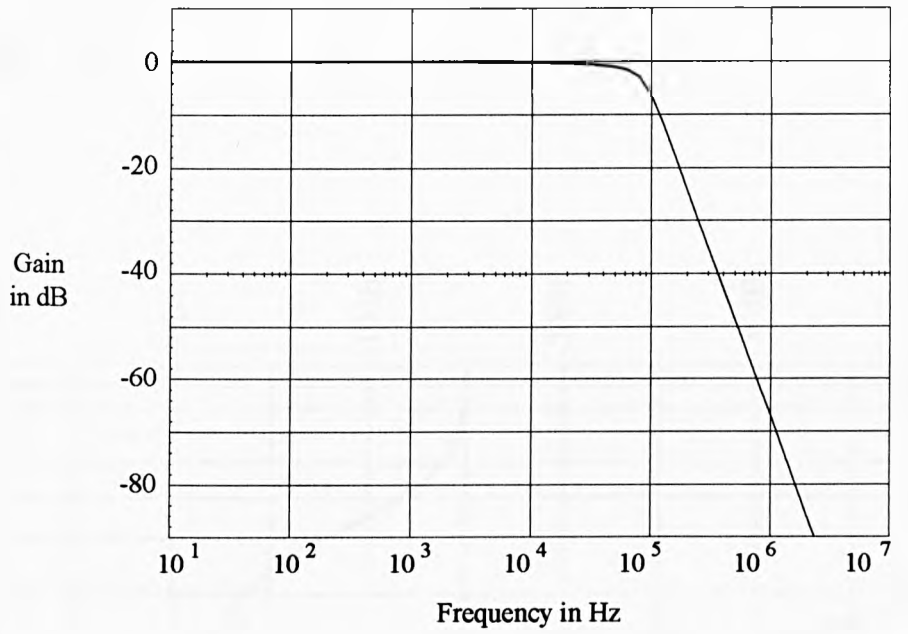

Figure 4.19 : Gain of Anti-Alias Filter (predicted by SPICE).

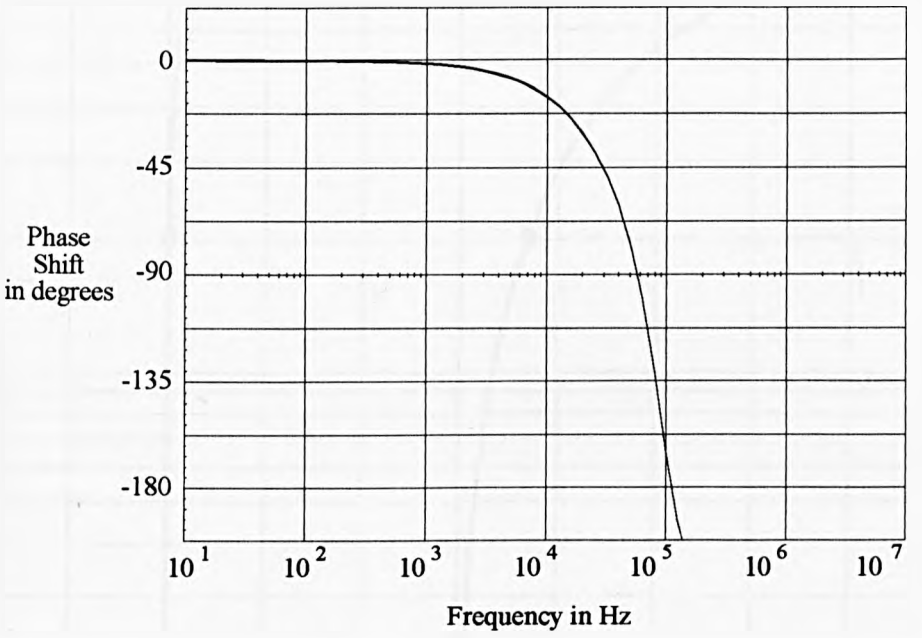

Figure 4.20 : Phase shift through Anti-Alias Filter (predicted by SPICE).

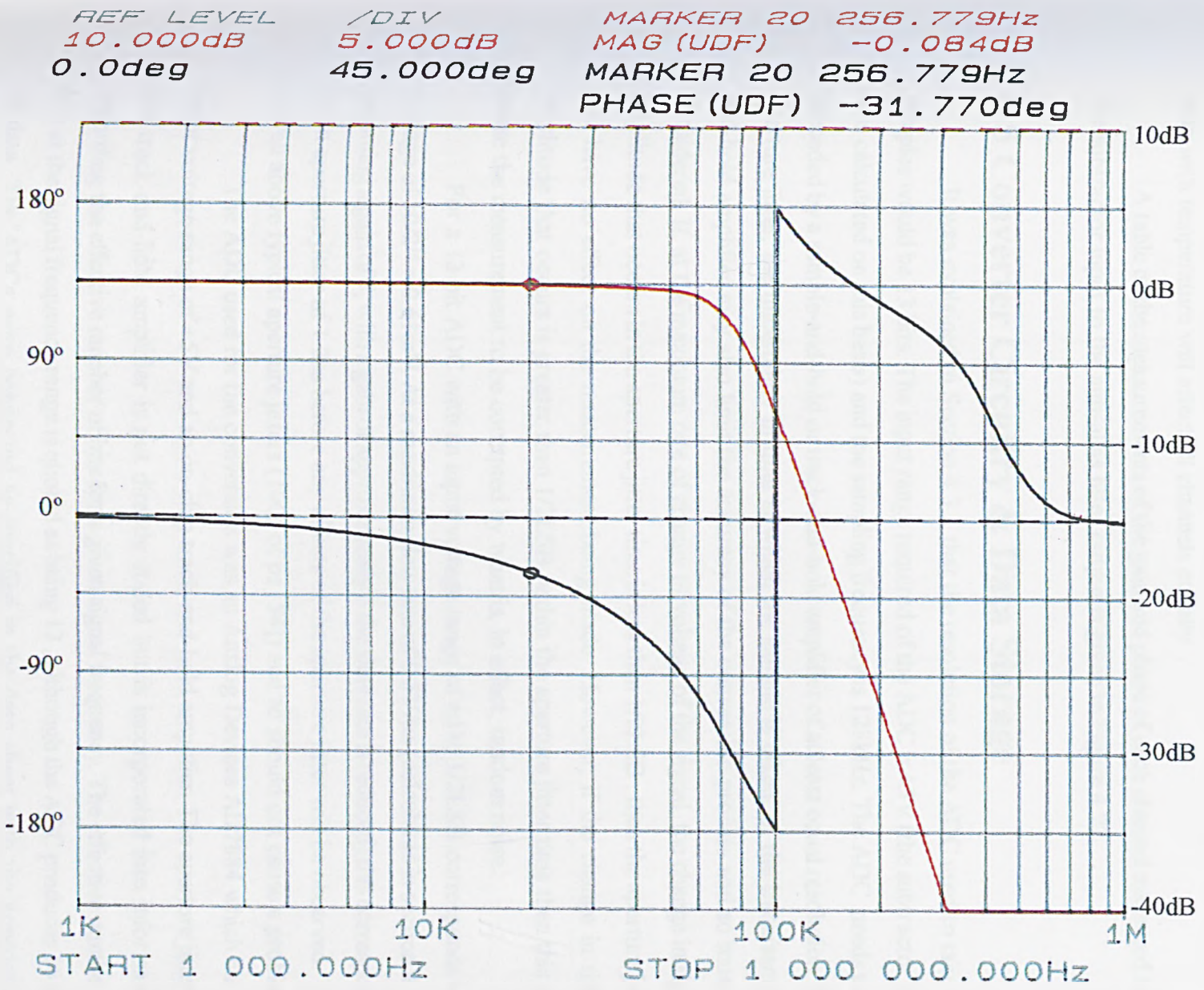

Figure 4.21 : Measured frequency response of the anti-alias filter.

this problem can be overcome by measuring the phase shift through each anti-alias filter and taking these measurements into account prior to the image formation. If the anti-alias filters had been placed before the subtractors, the gain and phase matching between the filters in each channel would have been critical in ensuring that a useful CMRR was achieved. The phase shift variation between channels at the same frequencies was 0.59°. It is expected that the receive channels will be at the same temperature, since the two boards containing the receiver circuitry are in close proximity to one another and so any drift of phase and gain with temperature will affect all channels equally.

A table of the measurements of the gain and phase of each channel measured from the subtractor input to the anti-alias filter output is given in Figure 4.22.

4.5 Converter Circuitry & Data Storage

It was explained in Section 4.3.1 that the resolution of the ADC used to take the samples would be 13 bits. The input range required of the ADC is ±5V (the subtractor gain was calculated on this basis) and the sampling frequency is 128kHz. The ADC needs to be preceded by a sample-and-hold or track-and-hold amplifier of at least equal resolution. The aperture jitter, the uncertainty in time at which the sample is taken, of the track/sample-and-hold amplifier may also limit the accuracy of the conversion process and so must be considered. If, at the maximum rate of change of voltage of the signal, the change in signal amplitude that occurs in the aperture jitter time is less than 1/2LSB , then the aperture jitter will have no effect on the measurement being made. However, if the change in signal amplitude that occurs is greater than 1/2LSB within the aperture jitter time then this will cause the measurement to be corrupted by what is, in effect, random noise.

For a 13 bit ADC with an input voltage range of ±5V, 1/2LSB corresponds to a voltage of $10/2^{14} = 0.61$mV. At a maximum slew rate of 0.5V/µs (calculated in section 4.3.1 assuming a gain of 7, with a gain of approximately 5 the slew rate is reduced) this corresponds to an aperture jitter of 1.2ns before any effects of the aperture jitter will be observed. This is well above typical aperture jitters (100s of ps [54]) and so should not cause a problem.

The ADC used for the conversion was an Analog Devices AD7884 which has an input voltage range of ±5V and an on-chip track-and-hold amplifier. The aperture jitter of the track-and-hold amplifier is not directly stated but is incorporated into information regarding the effective number of bits for a given signal frequency. The effective number of bits at the signal frequency range is quoted as being 13 , although the ADC produces 16 bits of data. The ADCs were connected as specified in the data sheet with the appropriate

Receive Channel Number	20kHz		30kHz	
	Gain in dB	Phase in degrees	Gain in dB	Phase in degrees
1	4.794	-32.40	4.751	-48.90
2	4.796	-32.39	4.756	-48.83
3	4.792	-32.37	4.748	-48.82
4	4.792	-32.56	4.747	-49.14
5	4.790	-32.36	4.746	-48.80
6	4.793	-32.59	4.752	-49.19
7	4.794	-32.52	4.756	-49.06
8	4.781	-32.26	4.723	-48.60
9	4.786	-32.38	4.741	-48.82
10	4.787	-32.40	4.747	-48.92
11	4.787	-32.35	4.734	-48.76
12	4.789	-32.30	4.747	-48.80
13	4.785	-32.41	4.745	-48.88
14	4.799	-32.46	4.753	-48.97
15	4.788	-32.54	4.745	-49.10
16	4.786	-32.37	4.737	-48.82

Figure 4.22 : Table showing the gain and phase shift through each receive channel.

associated circuitry and protected by Shottky Barrier Diodes. The data output lines were connected to buffers which were used to latch the measurements and output data onto a bus for storage. The circuit diagram of the converter and associated circuitry is shown in Figure 4.23.

Memory ICs are used to store the data while measurements are being taken. Once the measurements have been completed, the data is transferred to the host computer for digital filtering and image forming to be performed. In order to simplify the control of the memory ICs, two 32kbyte static RAM ICs were used to store all the data. Static RAM has the advantages over dynamic RAM that it requires no refresh signal and has faster access times. FIFO buffers have fast access times but are more expensive than static RAM. Dual port RAM was considered so that the reading and writing actions could be performed independently, but it is very expensive and only readily available for small memory blocks. One of the 8 bit SRAMs stored the least significant bits of the measured data and the other SRAM stored the most significant bits of the data. All 16 samples from each receive channel were written to the memory in one sampling period, allowing 480ns (7.8μs/16) per channel for the enabling of the buffers, write process and disabling. This meant that reasonably fast memory had to be used and the ICs chosen had an access time of 85ns. The memory capacity of 32kbytes was used to store a maximum of 6 frames of data.

4.6 Physical Organisation of the Receiver Channels

Seventeen identical buffers were built on one pcb which was mounted at the phantom. The buffers were connected via coaxial cable to the two receiver boards which contained eight receiver channels each. Each channel on the receiver board consisted of subtractors, anti-alias filters, converter circuitry and data buffers. Both the receiver boards plug into a backplane on which the memory is mounted. This backplane is connected via data, address and control lines to the control/interface board.

Photographs of the system circuitry can be seen in Figure 4.24.

4.7 Digital Filtering

After being transferred to the host PC, the measurements which have been stored in the external memory on the backplane must be digitally filtered to separate the various frequency components measured between each receive electrode pair, and hence enable the determination of the potential differences at each drive signal frequency. This section describes

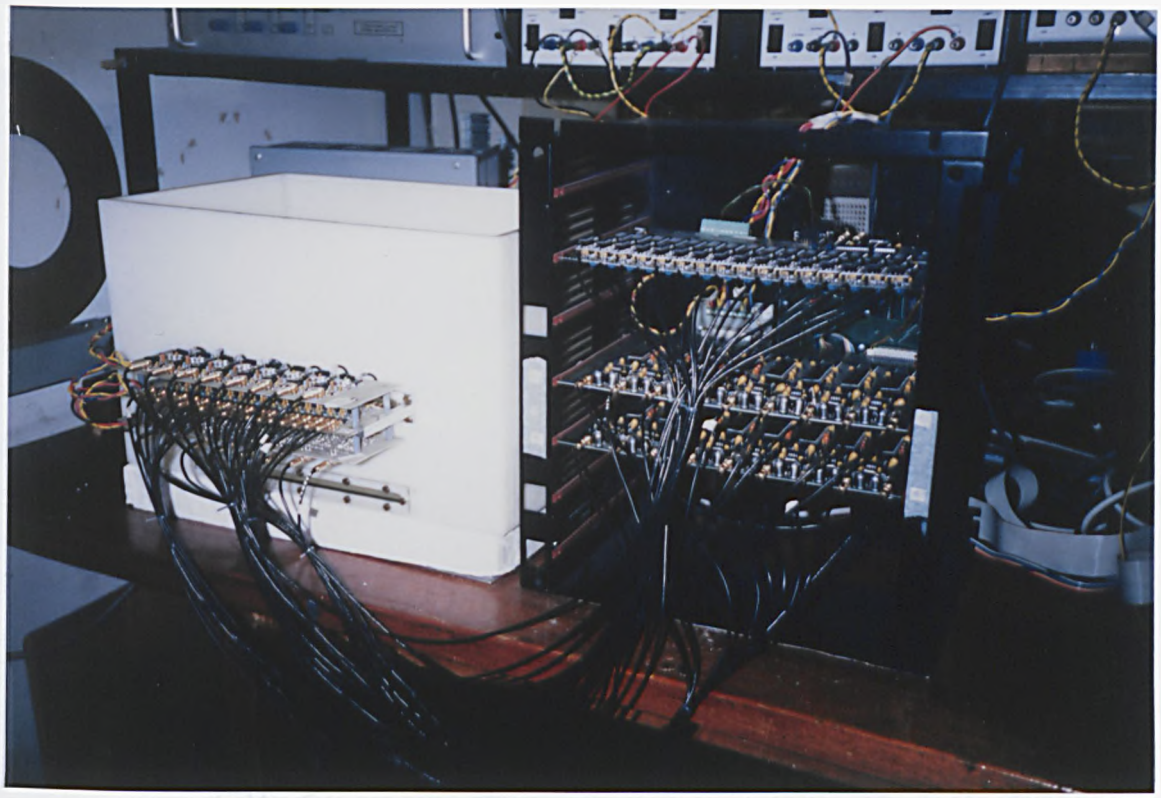

(a)

(b)

Figure 4.24 : Photographs of the system.

(a) Photograph of the phantom and the current sources and buffers mounted on the phantom wall. The waveform generator board (top) and the two receiver boards (middle and bottom) can be seen to the right of the phantom.

(b) Close up of the circuitry mounted on the phantom wall. The current sources are on the top and bottom boards, the buffers are on the middle board.

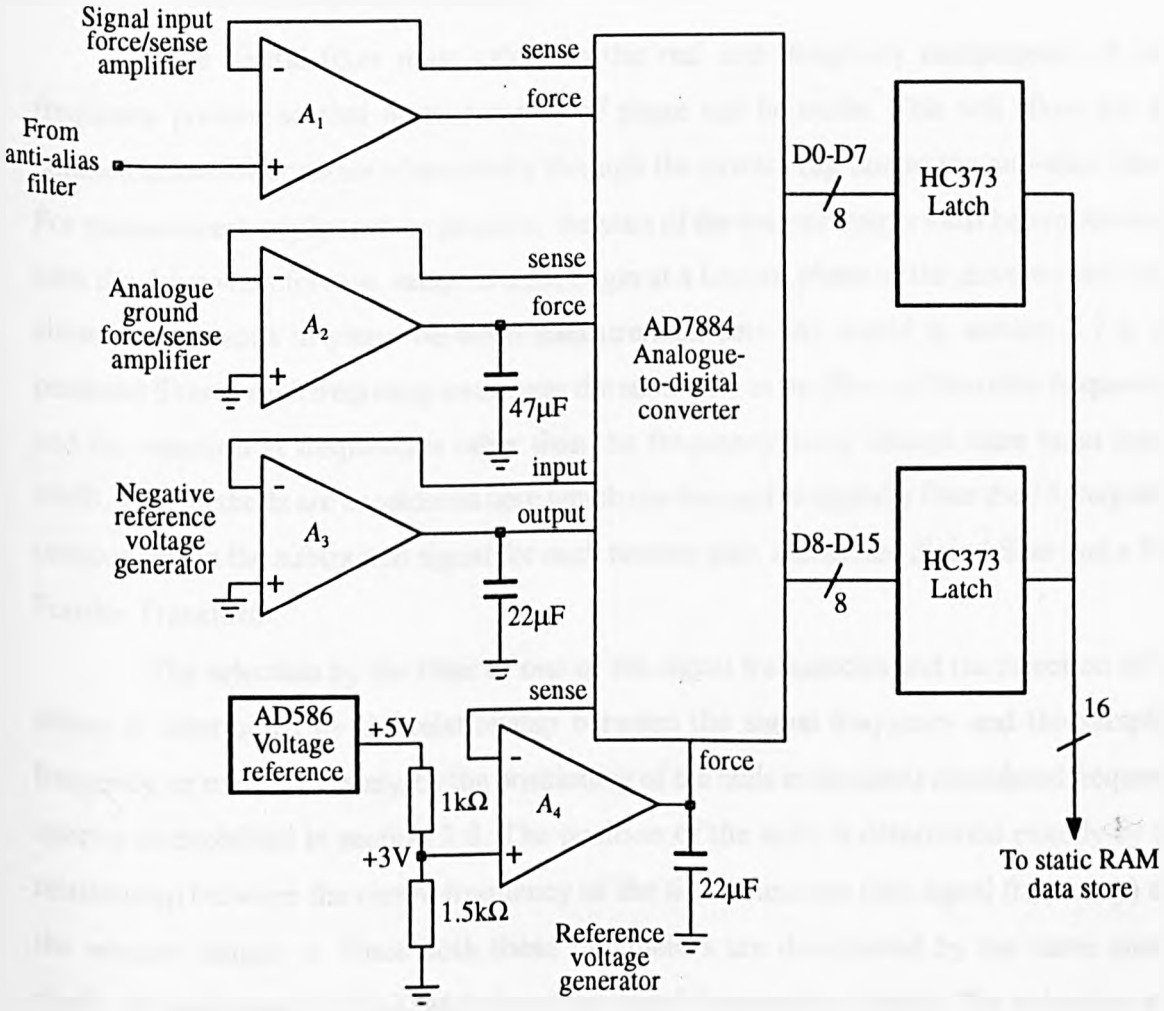

Figure 4.23 : The Analogue-to-Digital converter circuitry recommended by the manufacturer. Each input was protected by shottky barrier diode clamps to both the +5V and -5V supplies.
The amplifiers used were:

A_1	AD711,
A_2 and A_3	AD708,
A_4	OP07.

firstly the requirements of the filter and secondly, two possible implementations of the filter, the matched digital filter and the Discrete Fourier Transform.

4.7.1 Filter Requirements

The digital filter must calculate the real and imaginary components of each frequency present so that measurements of phase can be made. This will allow for any compensation for constant phase shifts through the system (eg due to the anti-alias filter). For measurement of phase to be possible, the start of the measurements must be synchronised with the drive waveform ie. samples must begin at a known phase of the drive waveform to allow comparisons in phase between measurement sets. As stated in section 2.7.3, the passband filter at each frequency must have the same gain as the filters of the other frequencies and the rejection at frequencies other than the frequency being filtered must be at least -60dB. Two methods are considered here which can be used to digitally filter the 15 frequency components in the subtracted signal for each receive pair, a matched digital filter and a Fast Fourier Transform.

The selection by the filter of one of the signal frequencies and the rejection of the others is determined by the relationship between the signal frequency and the sampling frequency, or more accurately, by the positioning of the nulls in the $\sin x/x$ modulated frequency spectra as explained in section 2.8. The position of the nulls is determined exactly by the relationship between the centre frequency of the $\sin x/x$ function (the signal frequency) and the window length, τ. Since both these parameters are determined by the same master clock, the nulls must coincide with the other signal frequencies exactly. The only source of possible errors could be in the aperture jitter of the ADC, but since this is random, it will appear as noise on the signal and will not shift the null position.

The effective phase shift through the filter will be defined by the time delay between the drive waveform circuitry generating the signal and the sample actually being taken. This is calculated to be approximately 540ns giving a phase shift of 3.9° at 20kHz and 5.2° at 27kHz. These phase shifts can be compensated and so do not present a problem.

4.7.2 Digital Filter Implementations

Both digital filter implementations are based on the calculation of the Discrete Fourier Transform (DFT) of the measured data for each receive pair. The DFT is defined as [80]

$$F[m] = \frac{1}{NT}\sum_{n=0}^{N-1} f[n]\, e^{-\frac{j2\pi mn}{N}}$$

$$= \frac{1}{NT}\sum_{n=0}^{N-1} f[n]\cdot\left(\cos\frac{2\pi mn}{N} - j\sin\frac{2\pi mn}{N}\right) \qquad \{4.8\}$$

where

m = number of frequency sample (frequency sample m corresponds to m/NT Hz.)

n = number of time sample

N = total number of samples

T = period of sampling frequency = $1/f_s$

The matched digital filter used by Smith [81] utilises a simple delay line and multiplication by a set of weights that is dependent upon the frequency to be filtered. If the samples of the signal to be filtered are $f[n]$ then the real part of the amplitude of the frequency component at frequency f_1 is

$$F[f_1] = \frac{2f_s}{N}\sum_{n=0}^{N-1} f[n]\cdot h[n] \qquad \{4.9\}$$

where

$$h[n] = \sin\left(\frac{2\pi f_1 n}{f_s}\right) \qquad \{4.10\}$$

and n is the sample number, f_s is the sampling frequency and N is the total number of samples per window.

The quadrature component of $F[f_1]$ can be calculated in a similar manner where $h[n]$ is given by cosine rather than sine. For the narrowband multiple frequency system described here, thirty waveforms would have to be stored (two for each frequency) and the matched filtering process would have to be performed on all 16 receive pairs for each of the 15 frequencies - equivalent to performing a partial DFT on the potential difference at each receive pair (ie for one value of m in Equation {4.8}).

If a dedicated processor (eg DSP chip) were to be used to perform the filtering operations in real time, the processor would have to perform 15(freqs) x 2(real and imag) x 16(channels) multiply-accumulate (MAC) operations in the sampling period, $1/f_s$. For the given sampling frequency a time of 16ns would be available for each MAC instruction. This is faster than existing DSP chips and so unless a heavily parallel system was to be used, real time filtering could not be performed. (eg Texas Instrument TMS320C30 has a MAC instruction time of 60ns, and so the time required to perform the MACs only would be

7.4ms, and therefore at least 4 DSPs would be required).

The second method of filtering considered here is to perform a Fast Fourier Transform (FFT) on the sequence of measurements. The sampling frequency and the number of samples in the window, N, must be chosen carefully such that the resultant frequency samples coincide with the drive frequencies. The FFT is a method commonly used to perform the DFT and can only be used when the number of samples is a power of two, but gives an increase in the speed of calculation (number of multiplications) from N^2 (for a direct DFT calculation) to $2N\log_2 N$ (to calculate the FFT). The time required for the calculation of a 256 point FFT is 16 times less than that required to calculate a DFT directly. The advantage of using an FFT over a matched digital filter is that only two sets of weightings need to be stored (N samples of a sine and cosine wave).

In using the FFT to find the filtered waveform amplitudes time is wasted in the calculation of the frequency samples which are not required. However, very little execution time of an FFT is saved by attempting to customise the FFT algorithm since information about which parts of the calculation do not have to be performed have to be stored and read.

The times quoted by manufacturers for some specific DSP chips to perform a 256 bit, complex FFT are shown below

Texas Instruments TMS320C30	0.8ms
Texas Instruments TMS320C20	4.5ms
Texas Instruments TMS320C25	2.2ms
Motorola DSP56001	0.65ms

None of these would be quick enough to process the data at the measurement frame rate as 16 FFTs (one per receive channel) would need to be performed per frame (2ms). In order to filter the signals in real-time, 16 parallel fast DSP chips would be required (or 8 if multiplexing was feasible).

As explained in section 2.3, the image processing was to be performed off-line and so there was no advantage to be gained from the significant increase in system complexity necessary for filtering in real-time.

The measuring system was designed to meet the 2ms measurement time specification with the measurements being stored in memory on the backplane. The backplane memory was to be interfaced directly to the host PC (486) which was to be used to perform all the processing, including the off-line filtering. The memory had the capacity to store 6

frames of data which could be measured in a variety of modes which are outlined in Chapter 5.

FFTs were used to perform the filtering since procedures are readily available for this and information about other frequency components (eg harmonics and noise measurements) is available. The host PC was required to perform all 16 FFTs, one for each receive channel. A radix-2, decimation in frequency, complex FFT algorithm was performed on the data once transferred from the RAM storage to the host PC.

4.7.3 Demodulation Breakthrough and Noise

Demodulation breakthrough is a very important parameter in a simultaneous drive EIT system receiver. It is a measure of the ability of the digital filter at one signal frequency to reject the signals at the other frequencies. An experiment was performed to measure the demodulation breakthrough of the filters. A voltage waveform of a single frequency sinewave was connected to one of the inputs of a subtractors and the other input of the subtractor was grounded. The amplitude of the input waveform was chosen such that, after amplification, the full range of the ADC was used. The output of the filter at the frequency of the signal was 4659mV. The largest output at the other frequencies was 1.1mV. This corresponds to a breakthrough of at least -72dB, which is better than the specified -60dB.

As explained in section 2.6.3 the dominant source of noise will be the receiver circuitry. The noise at the input to the ADC was measured on a spectrum analyser by comparison with a single frequency source of known amplitude. The noise measured at the frequencies of interest was approximately $0.3\mu V/\sqrt{Hz}$.

The noise in the system can also be estimated by considering the values calculated by the FFT when there is no signal present at the input of the receive channels. The amplitude calculated by performing the FFT at each of the filtered frequencies should be zero if the inputs are grounded. Any non-zero output value will be caused by the presence of noise. If the noise can be assumed to be white and have a power density spectrum of P^2 V^2/Hz then the output value of each filter will be an estimate of $P/\sqrt{\tau}$ Vrms ($1/\tau$ is the effective bandwidth of the filter). The inputs of two buffers were connected together and grounded and a measurement was performed. The mean square average of the 127 frequency values generated by the FFT (500Hz to 63.5kHz in 500Hz steps) was calculated and this process was repeated a number of times and the mean found. The average was approximately

140μV in the 500Hz bandwidth corresponding to an approximate noise level of 6μV/√Hz. This value of noise includes the effects of aperture jitter, noise in the ADC and quantisation noise, which is why it is larger than the noise measured at the ADC input using the spectrum analyser.

This measured value of noise is less than the noise expected from the ADC and demonstrates the increase in signal-to-noise ratio that can be achieved by using this particular filtering method. The FFT used to calculate the signal amplitudes at each frequency performs an averaging process and, as such, could increase the signal-to-noise ratio by a factor of up to √256 (256 is the number of samples used).

The ADC is quoted as having a particular number of 'effective bits' at the frequencies of interest and this is defined by the signal-to-noise ratio measured by the manufacturer. Thirteen bits corresponds to 352μV/√Hz for the 5V input range of the ADC. This could be reduced to 22μV/√Hz by the averaging of the FFT. This value is still higher than the measured value and so it is expected that the signal-to-noise ratio is better than the value quoted by the manufacturer, approximately 15 effective bits rather than 13.

4.8 Conclusions

This chapter has presented the details leading to the construction of two receiver boards. The circuitry presented is capable of making the measurements to the required accuracy making it possible to form an image of a conductivity distribution of a medium of interest. The digital filtering used to demodulate the signals has been described and has been used to show that the noise of the system is below the specified level. The phantom required to test the system and control circuitry necessary to run the system are described in the next chapter

Chapter 5 Phantom & System Control

5.1 Introduction

This chapter is in two sections. The first section describes the phantom and electrode array used to test the system. The required characteristics of the phantom and electrode array are specified and the choice of electrode spacing, size and shape is given, followed by the dimensions of the phantom.

The second section describes the control circuitry used to control the drive and measuring system described in Chapters 3 and 4.

5.2 Phantom and Electrode Array

In order to test the system, a laboratory phantom was required as it was necessary to have a facility which allowed controlled conductivity distributions to be set up. This section describes the phantom constructed to facilitate measurements using a linear array.

The important issues affecting the design of the phantom are :

1. Different conductivity distributions must be readily attainable.
2. The size of the phantom should be such that any boundary effects are negligible and so the current patterns set up in the region of interest are as expected.
3. The phantom must be configurable for pseudo-2D and 3D measurements.
4. Electrodes must be available for the application of common mode feedback.
5. The array of electrodes must be linear and contain 16 drive electrodes and 17 receive electrodes, which are to be equispaced and interleaved.

5.2.1 Inter-electrode Spacing

As stated in section 2.2, the linear array of electrodes was to contain 33 identical electrodes consisting of 16 drive electrodes and 17 receive electrodes. The drive and receive electrodes were equispaced and positioned alternately along the array as shown in Figure 5.1.

The array must to be large enough to enable the connection of appropriate drive and receive circuitry to the electrodes. A larger electrode spacing (of the order of a centimetre) makes it easier to set up particular conductivity distributions with reasonable

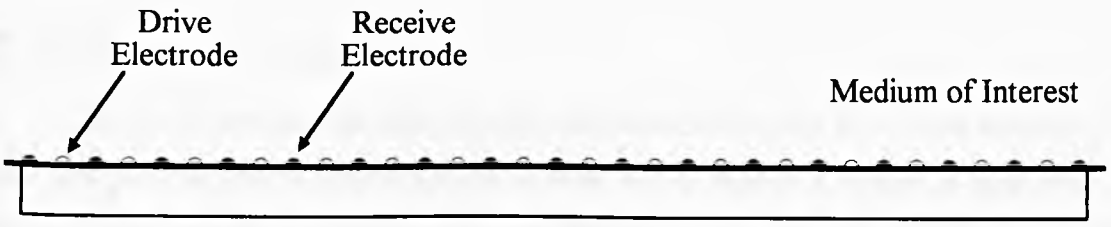

Figure 5.1 : Diagram showing the electrode array.

relative accuracy. However, as the inter-electrode spacing is increased, the dimensions of the phantom necessary for the current paths to be unaffected by the phantom boundaries become prohibitively large. Large phantoms also require considerable volumes of saline (or other conducting medium) and the cost of the materials required for fabrication becomes significant.

An electrode spacing of 7.5mm was chosen as a reasonable compromise, giving a total array length of 240mm. This determined the drive-drive/receive-receive electrode spacing as 15mm, thus allowing particular conductivity distributions to be set up accurately without the use of precise measuring equipment to locate the objects. The electrode separation affects both the absolute resolution of the system [21] and the effective impedance between any two electrodes.

5.2.2 Electrode Size

The electrodes must be small enough such that they appear to be point sources of current and point receive electrodes as far as most of the region of interest is concerned. The use of finite area drive electrodes makes it difficult to calculate analytically the shape of the current patterns. For large area receive electrodes, the electrode distorts the current paths by short circuiting part of the surface of the conducting medium. The electrodes must be sufficiently large, however, to ensure that the current density at the interface between the drive electrode and the medium of interest will not cause problems such as heating or, for medical applications, sensations of burning at the surface. The receive electrodes must also be sufficiently large that the contact impedance at the electrode is small in comparison with the input impedance of the buffer.

The electrodes were chosen to be hemispheres of 1mm diameter which was a reasonable compromise for ensuring a relatively low current density at the drive electrodes ($1.9mA/mm^2$) and an approximate point contact for the receive electrodes. Fabrication of electrodes less than this diameter becomes difficult and this electrode size is consistent with other EIT laboratory phantom electrode sizes [42]. The electrodes were chosen to be hemispherical in order to reduce the distortion of the equipotential loci at the electrodes and were made of gold plated brass to ensure a degree of corrosion resistance and hence reliable electrical contact with the medium under investigation.

The effective resistance between the electrodes can be estimated by dividing the potential difference between adjacent drive electrodes by the current injected through the electrodes. The potential on the surface of a single point current injecting electrode is

undefined, since there is an infinite current density at that point. For a hemispherical electrode of finite size, the equipotentials close to the electrode are approximately hemispherical, as for a point electrode, and so there should be no difference between the current paths in the two cases. Since the potential generated at some distance from the source should be the same, independent of whether point or hemispherical drive electrodes are used, an estimate of the potential on the surface of the electrodes due to the injection current passing through it is given by calculating the value of the equipotential generated by a point electrode source at a distance equal to the radius of the hemispherical electrode. Figure 5.2 shows a point electrode and hemispherical electrode with resultant potentials to demonstrate this principle.

By using Equation {1.1}, the effective load resistance between two drive electrodes can be estimated. For a homogeneous 3D medium the potential Φ at a point of interest is given by

$$\Phi(r_1, r_2) = \frac{I}{2\pi\sigma}\left(\frac{1}{r_1} - \frac{1}{r_2}\right) \qquad \{1.1\}$$

where σ is the conductivity, I is the injected current amplitude and r_1 and r_2 are the distances from the source and sink drive electrodes respectively. The voltage at the surface of the source drive electrode, $V_{surface}$, caused by the source and sink injection currents is given by

$$V_{surface} = \frac{I}{2\pi\sigma}\left(\frac{1}{R} - \frac{1}{a-R}\right) \qquad \{5.1\}$$

where R is the radius of the electrode and a is the distance between electrodes performing the same function ie drive-drive/receive-receive electrode spacing. The potential at the surface of the sink electrode will be equal in magnitude to $V_{surface}$, but opposite in sign. Thus the effective resistance between the two drive electrodes is given by

$$R_{eff} = \frac{2V_{surface}}{I} \qquad \{5.2\}$$

Substituting a=15mm, R=0.5mm and σ=0.2Sm^{-1}, the effective resistance between the two drive electrodes is 3.1kΩ. Equation {1.3} can be used to estimate the potential at the source electrode due to the sink current and hence the effective resistance for a pseudo-2D situation can be calculated. This effective resistance is 2.5kΩ. Both these values are typical load values encountered in a medical systems [9].

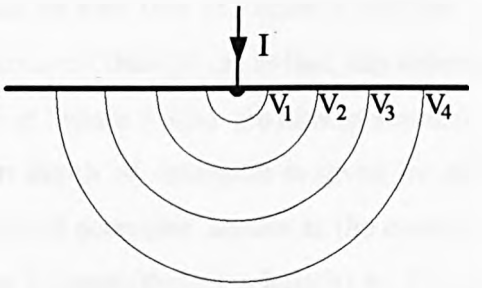

(a)

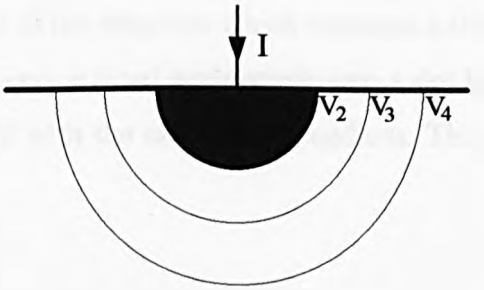

(b)

Figure 5.2 : Equipotential loci generated by electrodes.

(a) Equipotentials generated by a single current injecting point electrode.

(b) Equipotentials generated by a single current injecting hemispherical electrode.

5.2.3 The Phantom

The depth of sensitivity for a linear array using adjacent drives for backprojected images is approximately half the array length [51]. This can be demonstrated by considering the depth of detection for each drive-receive pair combination. Figure 5.3 shows two drive-receive pair combinations and the equipotential bands along which backprojection occurs for each combination. It can be seen that in Figure 5.3(b) the equipotential loci penetrate deeper into the medium of interest than (a) or, in fact, any other drive-receive combination. Since the equipotential loci in Figure 5.3(b) are almost semicircular with a diameter of the array length, the maximum depth of detection is given by approximately half the array length. This maximum depth of detection occurs at the centre of the array. Consequently the phantom must be of size 240mm (the array length) by 120mm (half the array length) at least. The actual size of the tank was chosen to be 300x500mm, approximately double these figures. The tank walls are sufficiently far away from the region of interest to have a negligible effect upon the current paths and hence the equipotential patterns in the region of interest. The height of the phantom was 300mm which allowed both pseudo-2D and 3D measurements to be made. For pseudo-2D measurements the array is fitted horizontally into a slot close to the base of the phantom which contains a shallow conducting medium. For 3D measurements the array is fitted horizontally into a slot halfway up the front wall of the phantom which is filled with the conducting medium. This arrangement is shown in Figure 5.4.

5.2.4 Common Mode Feedback Electrodes

Two extra electrodes are fitted at points remote from the array ie at the corners of the phantom on the wall opposite to the electrode array (see Figure 5.4). These are used to sense the common mode potential of the medium and drive the medium with an inverted amplified version of the detected potential using the circuitry described in section 3.5.

Drawings of the component parts used to make the phantom and electrode array can be seen in Appendix F.

5.3 Measurement System Control Circuitry

This section describes the circuitry used to control the measurement process. The entire system behaviour is governed by a digital control board which is situated in the host

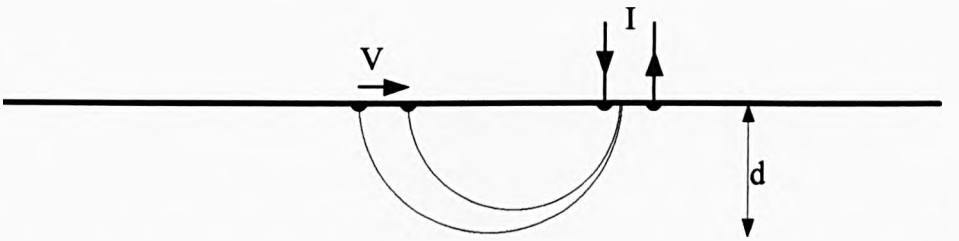

(a)

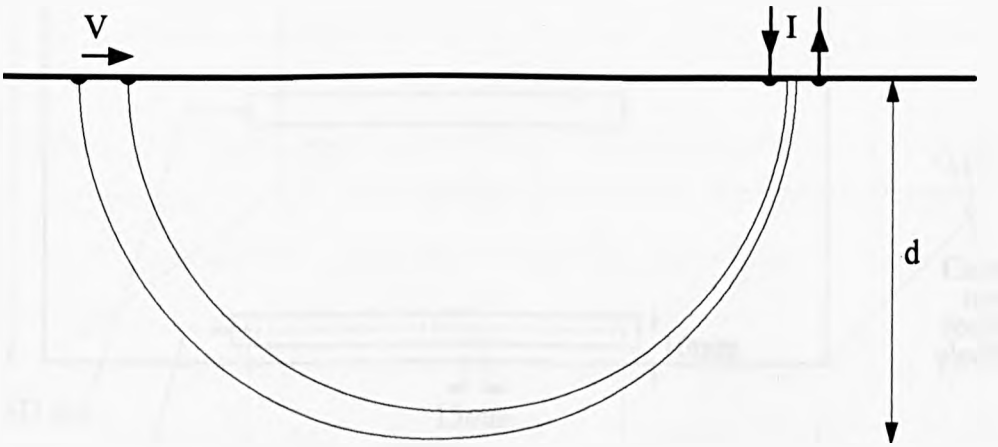

(b)

Figure 5.3 : Diagram to show the depth of penetration for each drive-receive pair combination

(a) Drive-receive pair with moderate penetration into the medium of interest.

(b) Drive-receive pair with the maximum penetration into the medium of interest.

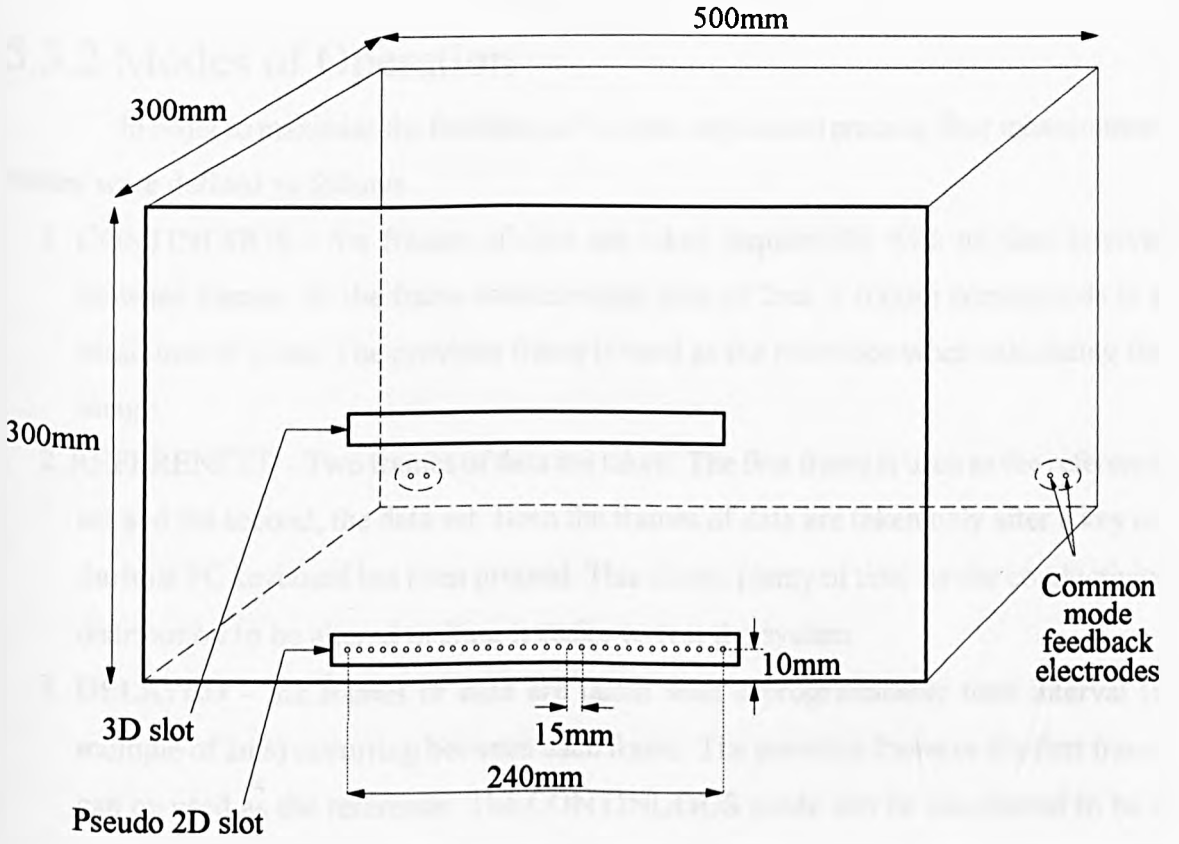

Figure 5.4 : Sketch of the laboratory phantom.

PC. This control board provides the interface between the host PC and the measurement circuitry and converts software commands into the control signals necessary to operate the measurement system.

5.3.1 Nomenclature

In this section a strict convention will be adhered to in order to avoid possible confusion. Control signals will be printed in *ITALIC CAPITALS* and an active low signal will be indicated by a '/' symbol preceding the signal name. Modes of operation of the system are printed in CAPITALS and states of the system are printed in **BOLD CAPITALS**.

5.3.2 Modes of Operation

In order to maximise the flexibility of the data acquisition process, four measurement modes were defined as follows.

1. CONTINUOUS - Six frames of data are taken sequentially with no time interval between frames. At the frame measurement time of 2ms, 6 frames corresponds to a total time of 12ms. The previous frame is used as the reference when calculating the image.
2. REFERENCED - Two frames of data are taken. The first frame is used as the reference set and the second, the data set. Both the frames of data are taken only after a key on the host PC keyboard has been pressed. This allows plenty of time for the conductivity distribution to be altered making it easier to test the system.
3. DELAYED - Six frames of data are taken with a programmable time interval (a multiple of 2ms) occurring between each frame. The previous frame or the first frame can be used as the reference. The CONTINUOUS mode can be considered to be a special case of this mode with a time interval between frames of zero. This mode is useful when monitoring conductivity changes which are occurring at a rate much slower than the maximum measurement frame rate of the system.
4. AVERAGED REFERENCED - This is similar to the REFERENCED mode, but three frames are taken consecutively and then averaged to find the reference set. Three more frames are taken and averaged to find the data set. These averaged measurements are then used by the host PC in the image forming process. This mode was included to increase the noise performance over the single REFERENCED mode.

The quantity of data stored by the system in these four modes is limited by the quantity of memory available, which in this case allows storage of 6 frames. Clearly, more frames could be stored for a particular application by simply using larger memory. In the AVERAGED REFERENCED mode this could be used to enhance the signal-to-noise ratio of the measurements by averaging if necessary.

5.3.3 Control States

The order and timing of the control signals necessary to control the measurement circuitry depends upon which mode is being used. The circuitry has five different states, or conditions, in which it can be operated and these are listed below.

1. **RESET** - Used to reset all the registers and counters to a known state after power up.
2. **IDLE** - The system is powered up but is not running.
3. **MEASURE** - Measurements are being made. The waveform generators are running and the receiver circuitry is taking measurements and storing them.
4. **WAIT** - Used when a time interval between measurements is required. The waveform generators are running but no measurement data is stored.
5. **READ** - The data is being downloaded from the memory to the host PC for processing.

The flow diagrams corresponding to each mode of operation showing the progression through the required sequence of control states are shown in Figure 5.5.

The circuitry required to control the system can be split into five main categories; drive control, measurement control, host interface, central control and the host PC. A block diagram showing these parts can be seen in Figure 5.6 and each of these parts will now be discussed separately.

5.3.4 Drive Control

This is the part of the control board which governs the behaviour of the drive circuitry. Of the drive component parts, only the waveform generators require digital control since the current sources are analogue voltage-to-current converters. The control required for the waveform generators can be split into two levels.

One level of control should provide the signals necessary to produce each output from the DAC in the waveform generators (see section 3.3) and these signals should be repeated every 976ns (the period of the waveform generator clock). The easiest way to

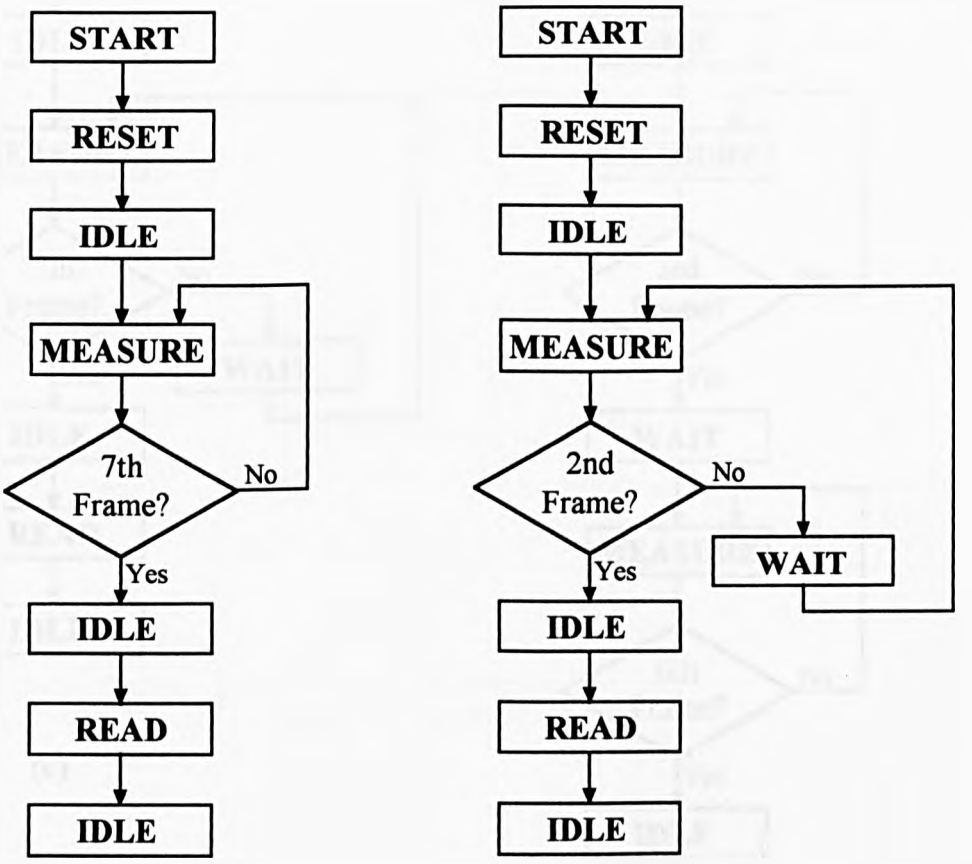

(a) **(b)**

Figure 5.5 : Flow Charts of the Modes of Operation of the System.

(a) CONTINUOUS mode.

(b) REFERENCED mode.

(c) and **(d)** continued on the next page ...

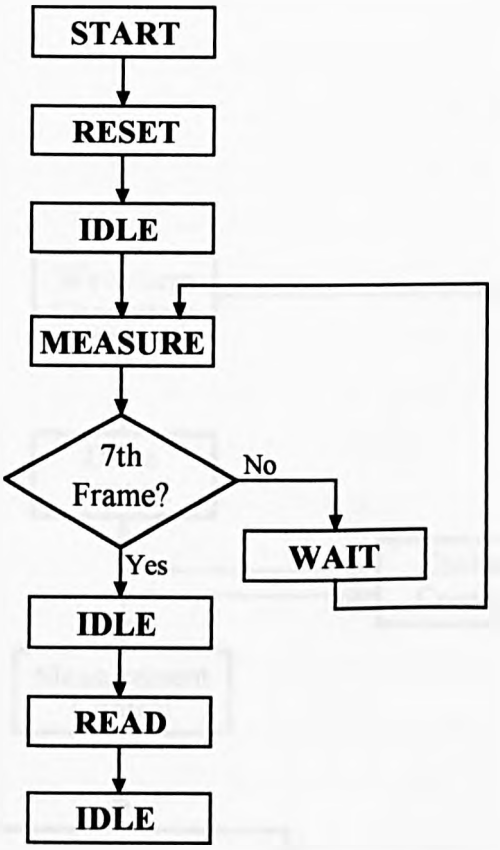

(c)

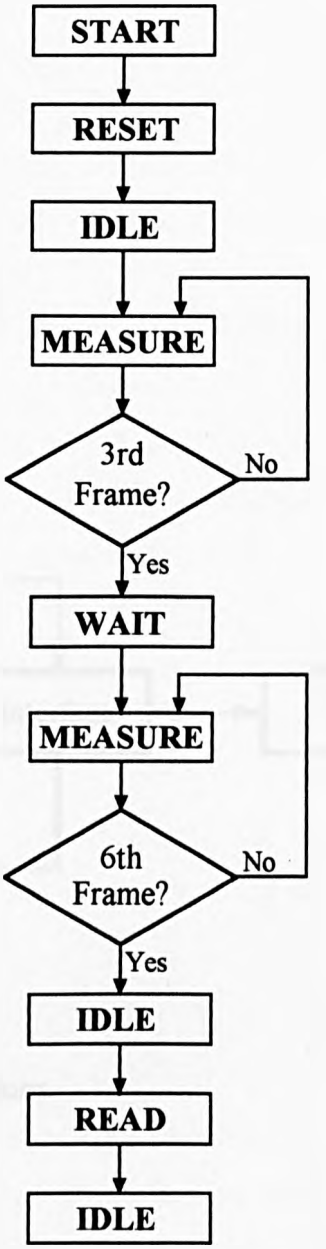

(d)

Figure 5.5 continued : Flow Charts of the Modes of Operation of the System.

(c) DELAYED mode.

(d) AVERAGED REFERENCED mode.

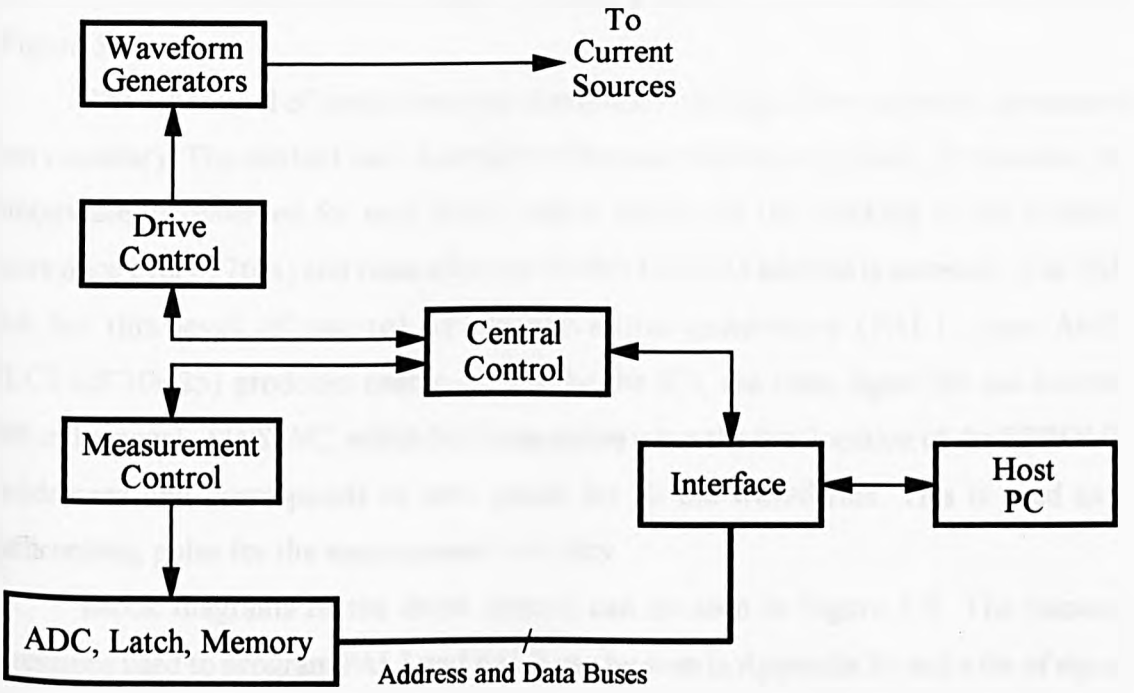

Figure 5.6 : Block Diagram of the Control Sections.

produce repetitive digital signals of this nature is to use a counter clocked with a fast clock (period <976ns) which is reset once every 976ns. The output of the counter can be decoded by a Programmable Logic Array Device to produce suitable signals. These repetitive control signals required for the waveform generators are the hold signal, */TRACKHOLD*, for the deglitching track-and-hold amplifier, the DAC write signal, */DACWR*, the clock to increment the address generator counters (the addresses for the EPROMs are generated by counters which are reset every 2ms) and the reset signal for the counter itself. These signals are produced by PAL2 (an AMD PALCE16V8H15) which decodes the output of a 4 bit counter clocked by the 16.384MHz clock signal. The timing diagrams of these signals can be seen in Figure 5.7.

The other level of control ensures continuous running of the waveform generators when necessary. The method used is similar to that described above where, in this case, the counters are incremented for each DAC output sample (ie the clocking of the counters occurs once every 976ns) and reset after the 2048th EPROM address is accessed. The PAL used for this level of control of the waveform generators (PAL1; type AMD PALCE22C10H25) produces enable signals for the ICs, the reset signal for the counter itself and a signal , *SINSYNC*, which becomes active when the first location of the EPROMS is addressed and corresponds to zero phase for all the waveforms. This is used as a synchronising pulse for the measurement circuitry.

Block diagrams of the drive control can be seen in Figure 5.8. The boolean expressions used to program PAL1 and PAL2 can be seen in Appendix M and a list of signal descriptions in Appendix G.

5.3.5 Measurement Control

The measurement control circuit provides the control signals for the receiver circuitry and data storage, namely the ADCs, data latches and for the loading of measurement data into memory. The signals required are the convert signal for the ADCs, the latch in, latch out and chip select for the data latches and the chip select and write enable for the memory. The conversion in the ADCs in all the channels occurs in parallel. Each ADC contains an output buffer making it possible, in principle, to connect these buffers directly onto the memory data lines, with the outputs controlled by the ADCs' read signal. However, it is advantageous to use external buffers for two reasons. Firstly, the timing constraints are much less demanding when external buffers are used since the whole sampling period is available for writing the data to the memory. Secondly, there is less likelihood of damaging

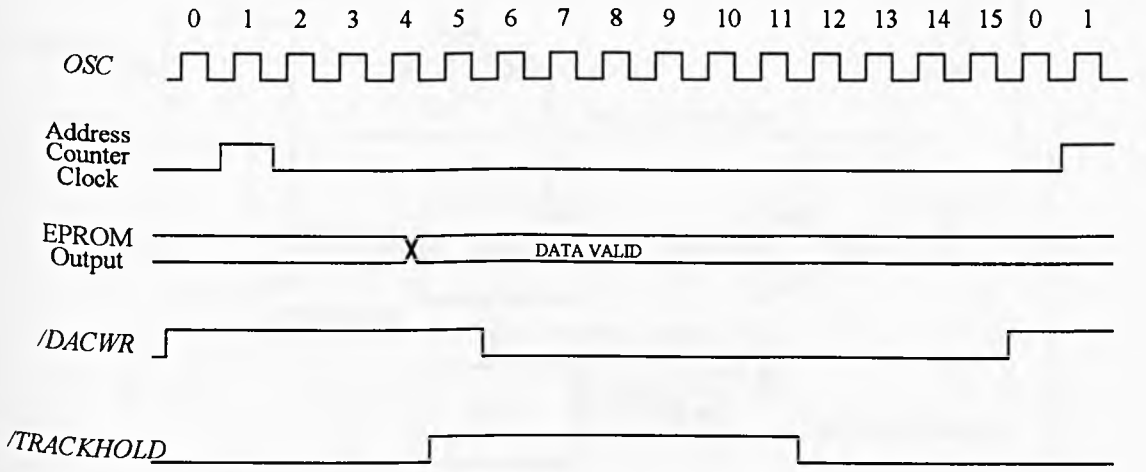

Figure 5.7 : Timing Diagram of the Drive Control signals for the DAC output.

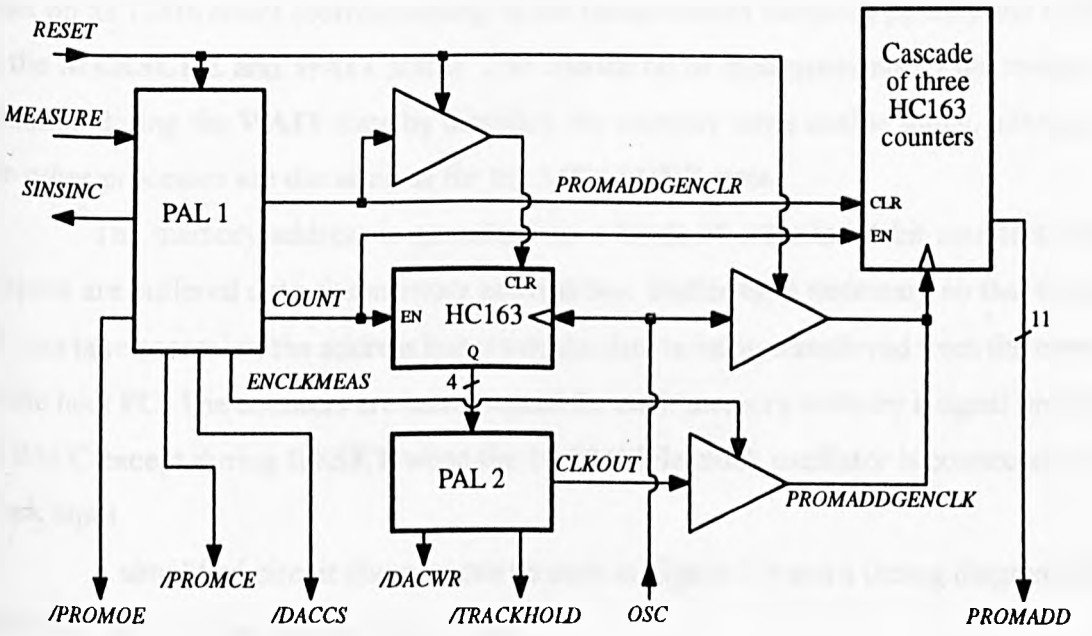

Figure 5.8 : The drive control.

the ADCs' outputs either by enabling the output buffers of each ADC at the same time or by static induced failure caused by repeated reconnection of the receiver boards to the backplane.

The measurement data is latched in parallel into the external buffers, HC373 latches, from the ADCs' output data lines. During the conversion of the subsequent measurement the data is loaded sequentially into the two temporary data storage memories - one holding the most significant bytes and the other the least significant bytes of the measurements.

A further PAL decoded counter produces the */OCx* (output control signals, where *x*=1..16) and *LATCHIN* for the latches, */CONVST* (the conversion signal for the ADC) and memory */MEMWE* (write enable) signals. This counter is clocked by the 16.384MHz clock, reset on its 128th count (corresponding to the measurement sampling period) and enabled in the **MEASURE** and **WAIT** states. The transferral of measurements to the memory is inhibited during the **WAIT** state by disabling the memory write enable signal, although all the other processes are the same as for the **MEASURE** state.

The memory address is generated by a block of cascaded 4-bit counters whose outputs are buffered onto the memory address bus. Buffering is necessary so that the host PC can take control of the address bus when the data is being transferred from the memory to the host PC. The counters are incremented for each memory write by a signal produced by PALC except during **RESET** when the 16.384MHz clock oscillator is connected to the clock input.

A simplified circuit diagram can be seen in Figure 5.9 and a timing diagram of the control signals can be seen in Figure 5.10.

5.3.6 Host Interface

An interface between the measurement system and the host PC is necessary for the system to be computer controlled and for the measurements to be passed from the system memory to the host for image forming.

The possibilities for interfacing to a PC are to use either a dedicated port or to design a circuit board which will plug into one of the PCs I/O channel card slots. The latter method allows direct access to the PC's address and data buses which are required for the data transferral and so this method was used.

The signals required to support the modes of operation and control states described previously were generated by decoding the contents of a control register into which the host PC writes control words. Two registers were placed on the control/interface board mounted in the PC; one was a write only port to which the PC could write control words

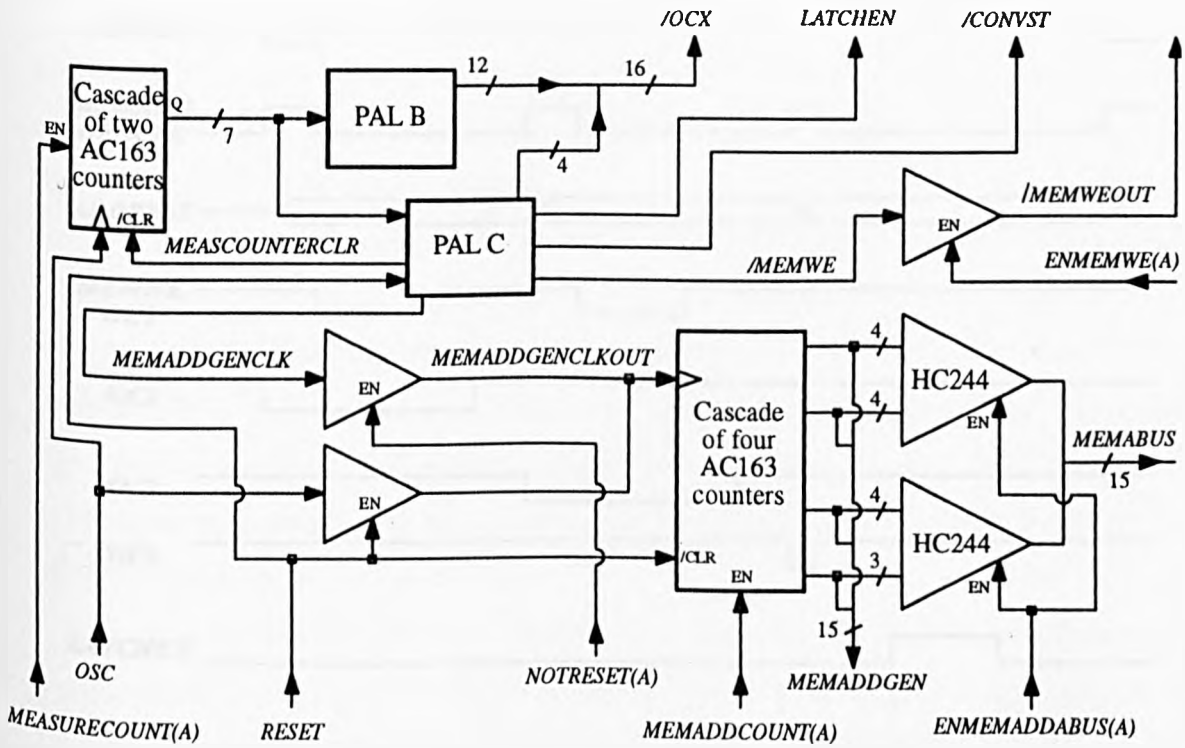

Figure 5.9 : The measurement control.

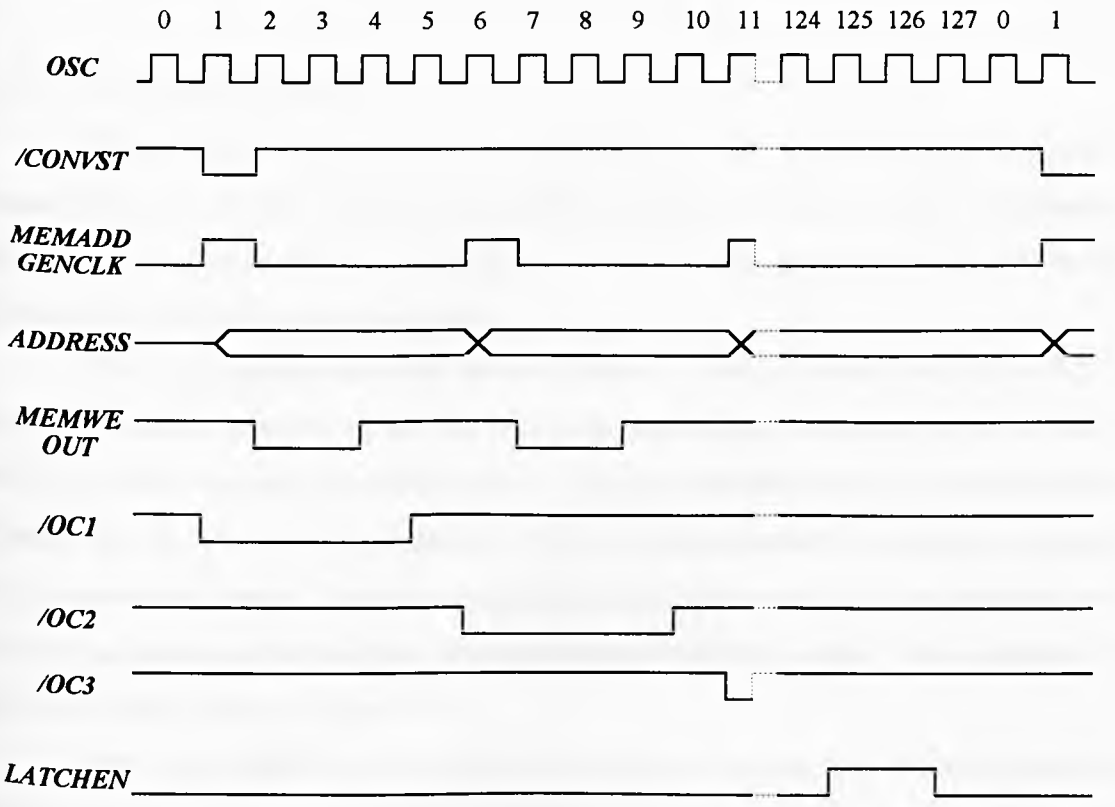

Figure 5.10 : Timing Diagram of the Measurement Control signals.

and the other was a read only port to which the system could write a status word to be read by the PC informing it of the state of the system.

This two way information flow was achieved by using a bidirectional buffer on the data lines of the PC and decoding certain PC control signals using PALH to produce the necessary clock signals. A simplified circuit diagram can be seen in Figure 5.11 and the PAL information in Appendix M.

5.3.7 Central Control

The central control decodes the control registers and provides the necessary control signals for the rest of the control circuitry. For example it will produce the signals which enable the activation of the counters that generate the measurement control signals and for the memory address generator counters.

The main component of the central control is a PALA (AMD PALCE16V8Q15) which performs the control register decoding and the writing. This is supported by PALD and PALE which are used to decode the end of memory address causing the measurements to cease, and some 74 series logic devices which are used to restart the measurements after a time interval has elapsed. The measurements for each frame must begin at the same point on the drive sinewaves for the phase between frames to be comparable. This is achieved by using the circuit shown in Figure 5.12.

The signal *WAITING* is set high to show that a measurement frame is complete and the system is waiting for the *ENDOFTIME* signal to be set high to indicate the end of the time interval. When *ENDOFTIME* is high, the next time *SINSYNC* is high, the data (high) will be clocked to the output of the D-type flip-flop thus restarting the measurements. When the measurements have begun (strictly when the address generator counter has incremented) the *WAITING* signal is made low therefore clearing the flip-flop ready for the next restart.

5.3.8 Host PC

The host used for the control and processing of the data was a 50MHz IBM compatible 486 with 180Mbytes hard disc and 8Mbytes RAM. The measurement program used to read and write to the control registers in the different modes was written in C and can be seen in Appendix H.

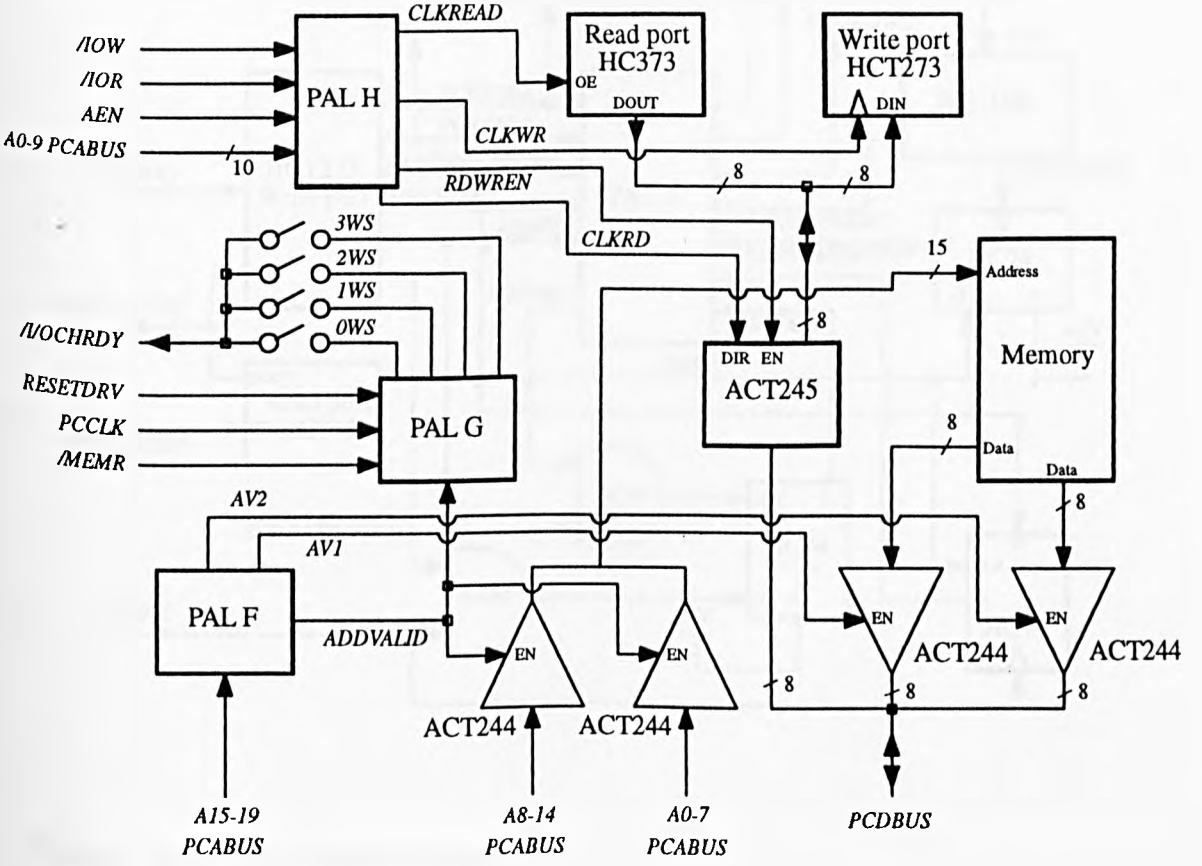

Figure 5.11 : The interface control.

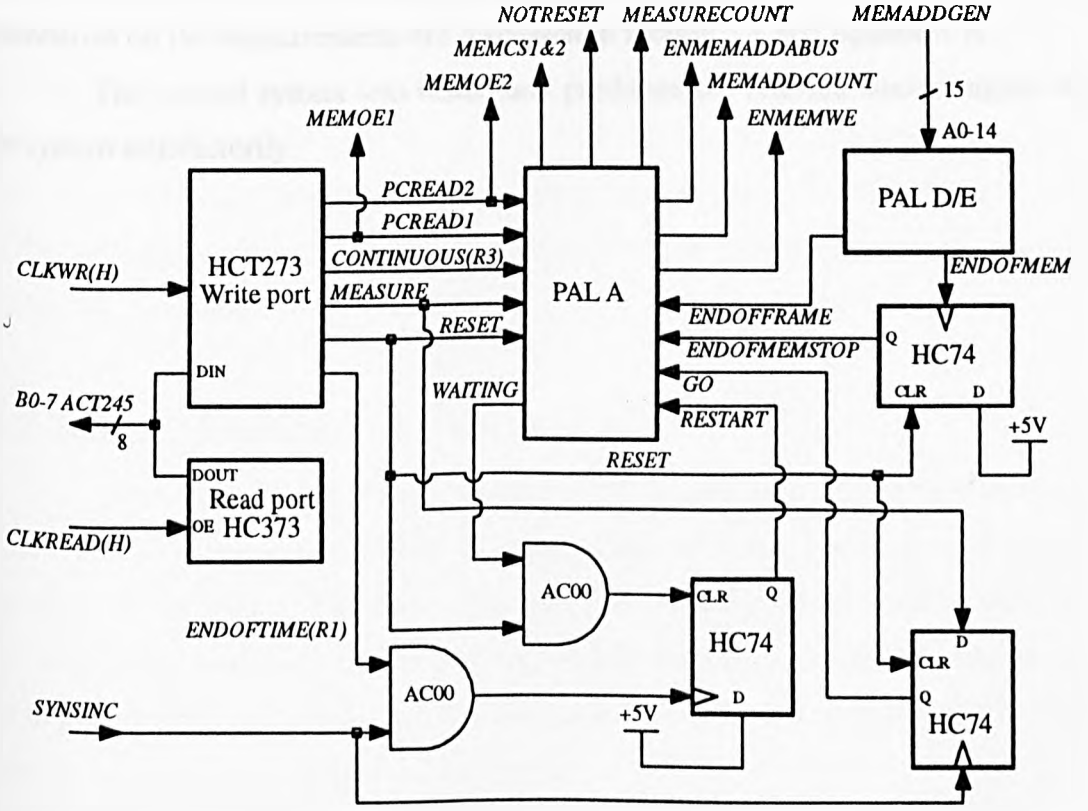

Figure 5.12 : The central control.

The information regarding all the PALs used in the control circuitry is given in Appendix M and an explanation of all the control signals is given in Appendix G.

5.4 Conclusions

No problems were encountered which were associated with the phantom and electrode array when used for testing the system. The possible effects of the finite phantom boundaries on the measurements are discussed in section 7.1 and Appendix K.

The control system was tested and produced the relevant control signals to run the system satisfactorily.

Chapter 6 Image Forming

6.1 Introduction

This chapter describes some of the methods which can be used to form images from measurements made using a linear array. These methods are evaluated, and the method used to produce the images for the system is described. Images produced from simulated data using this image forming algorithm are presented. Image filters commonly used on EIT images are applied in an attempt to improve image quality and the resulting filtered images are discussed.

6.2 Image Forming Processes

There are a number of methods used in EIT to produce an image from the measured data. A detailed comparison of image forming techniques was not undertaken and is beyond the scope of this project. However, commonly used methods are reviewed in Webster [26] and include the sensitivity matrix method, backprojection, weighted backprojection and the modified Newton-Raphson method and these are briefly described below followed by a detailed explanation of the approach adopted.

All these image forming algorithms operate on the two sets of measurement data, the reference set and the data set, as stated in Chapter 1. These measurement sets consist of the potential differences between adjacent receive electrodes prior to the conductivity change (reference set) and after the conductivity change (data set) has occurred.

6.2.1 Common Image Forming Techniques

The Sensitivity Matrix Inversion method involves solving the forward problem ie calculating the expected change in the potential difference measurements for a known conductivity distribution change. This calculation is performed with each pixel in the region to be imaged taken in turn as the only inhomogeneity and a matrix is created (often denoted by S) representing the sensitivity of the system to an inhomogeneity at each pixel location. This produces a matrix of dimensions (the number of pixels in the image) x (the number of independent measurements made) which is then inverted to produce the image forming matrix (S^{-1}). However, S is not always a square matrix and so often only an approximate

inverse of **S** can be found. The calculation of **S** is also subject to rounding errors in the calculation which can lead to poor results. The voltage difference information, formed by subtracting the reference set from the data set, is put into matrix form and is denoted here by **V**. When the inverse of the sensitivity matrix is multiplied by the voltage difference data ($\mathbf{S^{-1}V}$), the result is a matrix which describes the conductivity at each pixel.

The backprojection method does not involve calculating the forward problem and so is simpler than the sensitivity matrix method, but it does involve making a number of assumptions which are only approximately true. However, the range of conditions for which these approximations are reasonable is large and consequently, the method of backprojection has proved to be a remarkably robust image forming process [13].

Backprojection uses the equipotential patterns set up in a homogeneous medium by each drive pair and assumes that any inhomogeneity in conductivity does not significantly alter the shape of these equipotentials. Figure 6.1 shows a single conductivity inhomogeneity in an otherwise homogeneous medium of interest. A single drive pair is shown and some of the equipotential loci for this drive are drawn. The potential difference measured between the adjacent receive electrodes is assumed to be dependent upon the conductivity of the equipotential band which terminates on these receive electrodes. If the conductivity of this band is altered by the presence of an inhomogeneity this will be reflected by a change in measured potential difference. The percentage change of potential difference that occurs at the receive pair is used to weight all the pixels in the equipotential band. This process is performed for each drive-receive combination and the resultant images are superimposed to give the final image. The image formed often tends to be blurred along the equipotential paths, which is not surprising since there is no discrimination in position along the equipotential bands for each drive-receive pair.

Weighted backprojection is an extension of the backprojection process but rather than applying the same value to the whole of the equipotential band, it applies a value dependent upon the position of the pixel of interest with respect to the drive position. The justification for this modification is that since the current does not pass through each pixel in the band in the same direction it will have a different effect upon the change in measurements that occurs [82]. This modified backprojection matrix, **W**, is used by many EIT groups [16][33] since it gives better results than the simple backprojection method.

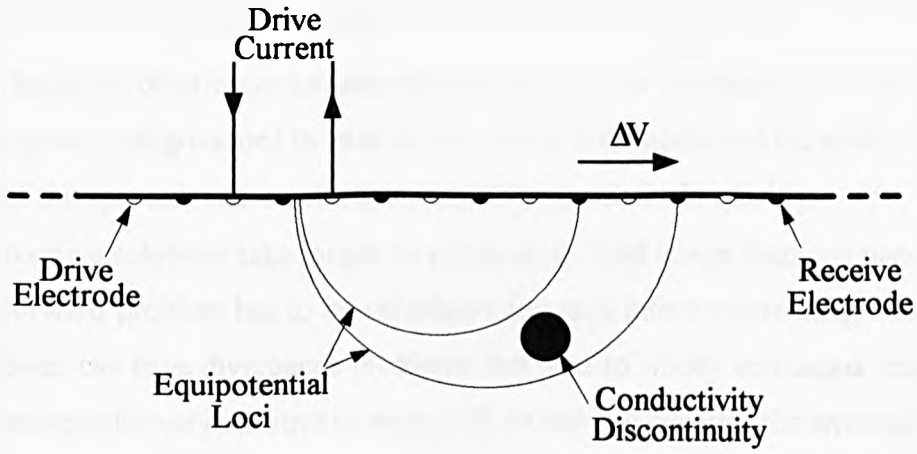

Figure 6.1 : Diagram showing a single drive pair and the equipotential loci bounding a conductivity discontinuity.

The Modified Newton-Raphson method is iterative and is principally aimed at minimising the errors between the measured voltage differences and the voltage differences expected by calculation of the forward problem for the reconstructed image. A uniform distribution or an approximate image produced by one of the other methods is used as the first image, and a solution to the forward problem for this image is calculated. The calculated voltage differences and the measured voltage differences are compared. Each pixel conductivity value is modified by a value dependent upon the difference between predicted and measured voltage differences to create a new image. The forward problem is solved for the new image and the iteration continues until the errors between the voltages are within a specified tolerance. The final image is taken to represent the conductivity distribution.

6.2.2 Choice of an Image Forming Algorithm

The choice of an image forming algorithm to validate the simultaneous drive multiple frequency system was governed by ease of calculation, robustness and the ability to produce an image of the approximate conductivity distribution relatively quickly.

Iterative solutions take longer to produce the final image than one pass solutions since the forward problem has to be calculated for each intermediate image. In addition, these solutions can have divergence problems that lead to wholly erroneous images being produced and are also very sensitive to noise [13]. In order to generate the inverted sensitivity matrix the forward problem has to be performed for each pixel and then the matrix inverted. Backprojection and weighted backprojection require only simple calculations in generating the image forming matrix and the methods are known to be relatively robust. Because of this robustness and relatively simple calculations required, the image forming process used in this work was based on the weighted backprojection approach.

6.2.3 Calculation of the weightings

If a pixel in the image is to be backprojected to form a circular point spread function (ie a single pixel inhomogeneity would produce a circularly symmetric image), the projections through the pixel must be of constant angular density [82]. For this reason, the weighting used for each pixel in the weighted backprojection algorithm is defined by the rate of change of angle of the current through a pixel with the change in drive position [82]. In a circular geometry as shown in Figure 6.2, this is denoted by $d\alpha/d\theta$ where $d\theta$ is the incremental change in drive position and $d\alpha$ is the resultant change in current direction through the pixel caused by the movement of the drive. For the case of a linear array, the weighting can

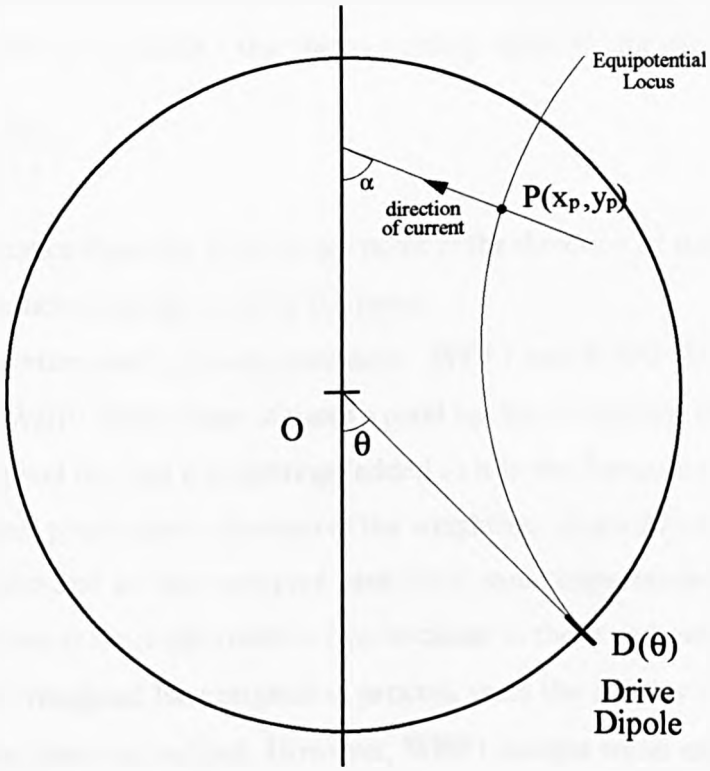

Figure 6.2 : Diagram showing the derivation of the weighting, $d\alpha/d\theta$, for an encircling array of electrodes.

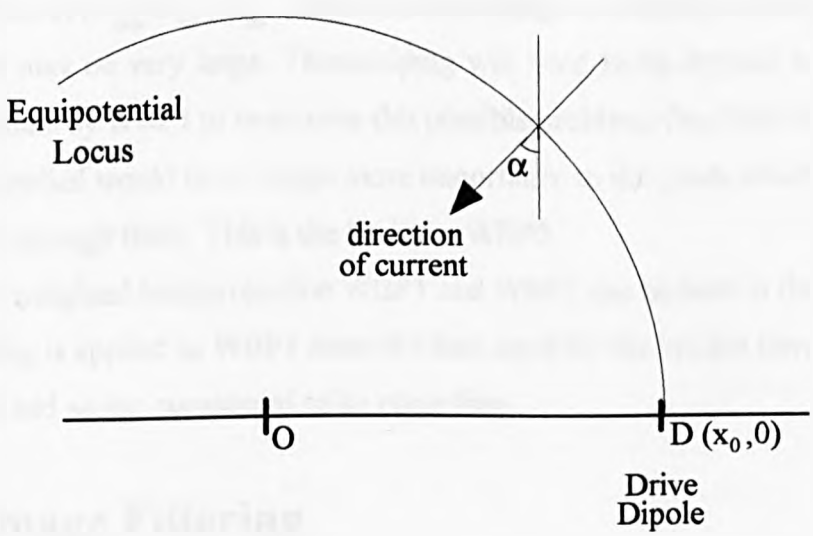

Figure 6.3 : Diagram showing the derivation of the weighting, $d\alpha/dx$, for a linear array of electrodes.

be denoted as $d\alpha/dx$ as shown in Figure 6.3 where dx is the incremental change in drive position. It is shown in Appendix J that this weighting value, W, for each pixel is given by

$$W = \frac{-2y}{x^2 + y^2} \qquad \{6.1\}$$

Where x is the distance from the drive to the point in the direction of the array and y is the perpendicular distance from the array to the point.

Two weighting matrices were produced : WBP1 and WBP2. They differ in that in the calculation of WBP1 the number of times a pixel has been weighted has been taken into account (ie if the pixel has had n weightings added to it in the formation of the weightings matrix, then the final pixel value is the sum of the weightings divided by n). WBP2 does not perform this division and so does not give each pixel equal importance but weights those pixels for which there is more information (those closer to the array) more than the others. WBP1 is the 'true' weighted backprojection process since the number of backprojections through a pixel has been normalised. However, WBP1 assigns equal importance to every pixel, independent of the number of backprojections through it. A pixel which has one or two backprojections through it will be on the boundary of the area of detection and consequently the measured potential differences caused by a target located here will be small. For these measurements the noise level could be of the order of the voltage difference being detected. Since fractional change in voltage is being used in the weighted backprojection algorithm (given by the values of $(V_{data}-V_{ref})/V_{ref}$), the fractional change in a small potential difference caused by noise may be very large. Thresholding will need to be applied to images produced from real data by WBP1 to overcome this possible problem. One form of weighting which could be applied would be to assign more importance to the pixels which have more backprojections through them. This is the basis for WBP2.

Images formed by weighted backprojection WBP1 and WBP2 can be seen in the next section. No thresholding is applied to WBP1 since the data used for the images have been generated analytically and so are considered to be noise free.

6.3 Images and Image Filtering

In order to demonstrate the limitations of the weighted backprojection algorithm some images will be presented here from data produced by simulation and some simple image filters will be applied to the images in an attempt to improve image quality. Images produced from measured data are presented in the next chapter.

The coordinate system referred to in conjunction with images and conductivity

distributions is a Cartesian system shown in Figure 6.4, where the x-axis is the axis of the electrode array and the y-axis is perpendicular to the axis of the array and perpendicular to the surface on which the array lies. The z-axis is perpendicular to the axis of the array and parallel to the plane of the surface on which the array lies. The units are the drive-drive/ receive-receive electrode spacing (henceforth referred to as 'like' electrode spacing) of 15mm and the coordinate (0,0,0) corresponds to the position of receive electrode zero, the leftmost electrode on all the images shown. The x and y coordinates given for all the 2D simulations and measurements and correspond to the plane z =0.

The simulated data used to demonstrate the image forming algorithm has been generated analytically using the approach devised by Anderson [83]. This predicts the voltage differences that would be measured by an ideal system for a single circular conductivity inhomogeneity in a 2D medium. All objects considered in this section are circular and have a conductivity of zero.

6.3.1 Unfiltered Images

Figures 6.5 to 6.8 are images produced from analytically generated data. In each of these figures, (a) is the conductivity distribution, (b) is the image produced using WBP1 and (c) is the image produced using WBP2. All the images are normalised to span the full colour scale, independent of the signal size. To give an indication of the signal size, the maximum voltage difference which occurs (V_{data}-V_{ref}) for each conductivity distribution, normalised to the maximum potential difference in the reference set between adjacent electrodes, is given in the caption.

Figure 6.5 shows a small circular object positioned in the phantom as shown in 6.5(a). The rectangle represents the imaged area (as described in Chapter 5, the phantom extends beyond the length of the array, but only the region defined by the array length and half the array length in depth is imaged) and the vertical lines beneath the rectangle represent the receive electrode positions. These are spaced at the 'like' electrode spacing (15mm in the phantom) and correspond to a coordinate unit of 1. The horizontal markings which are seen up the sides of the rectangle are present for scaling only and correspond to the coordinate positions.

It can be seen from the images in (b) and (c), generated by WBP1 and WBP2 respectively, that the centre of the object has been located accurately. However, neither of the images depict a circular object. This is because the object is placed near the end of the

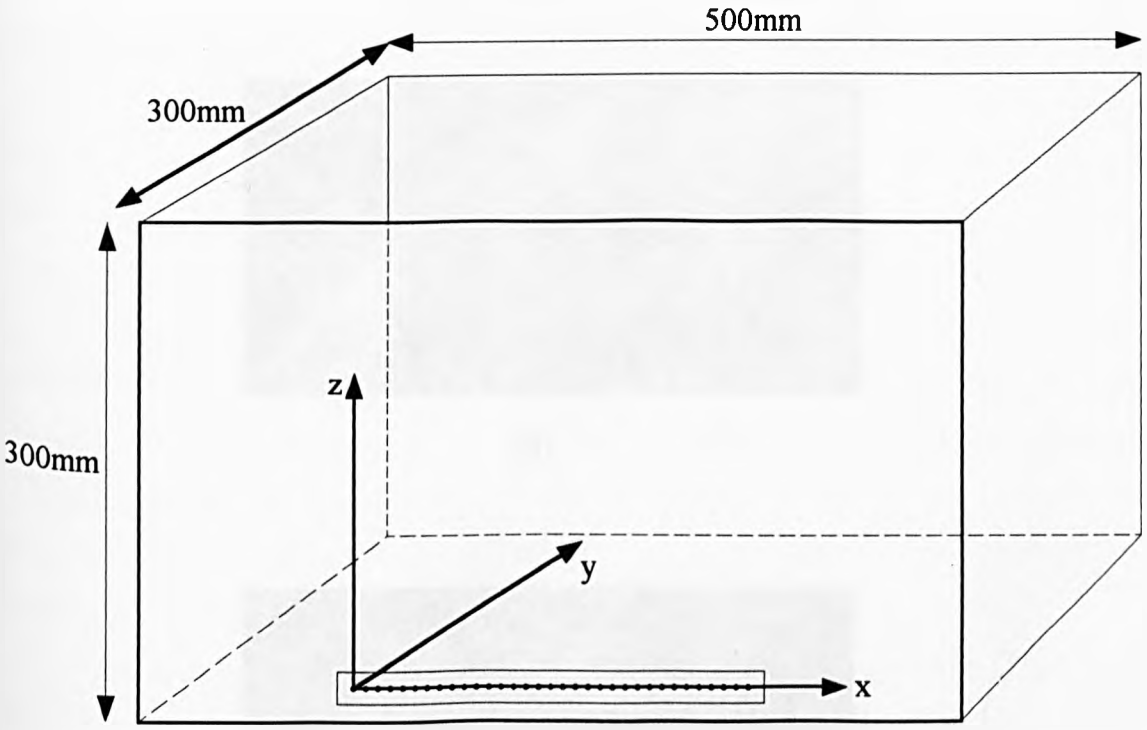

Figure 6.4 : Diagram showing the Cartesian co-ordinate system associated with the phantom.

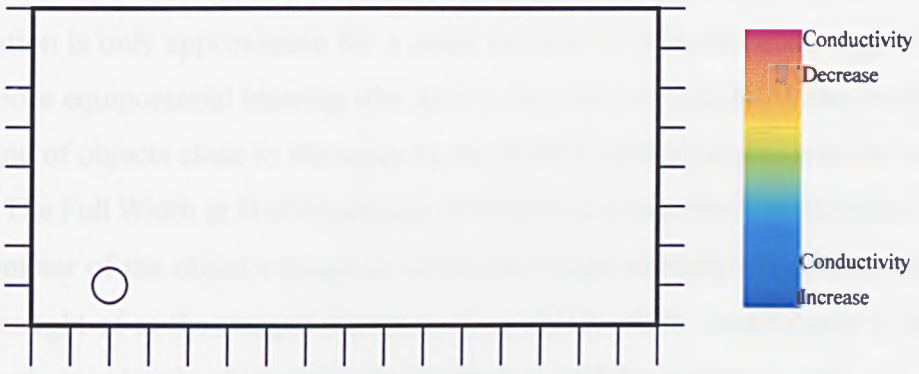

(a)

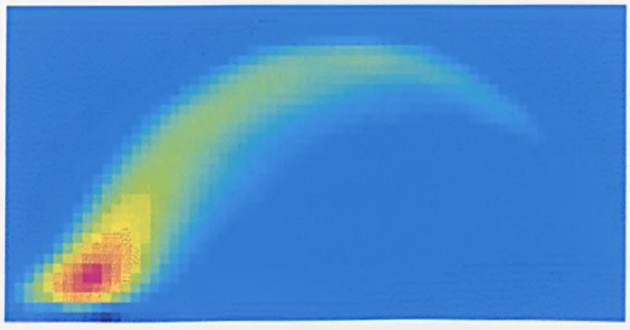

(b)

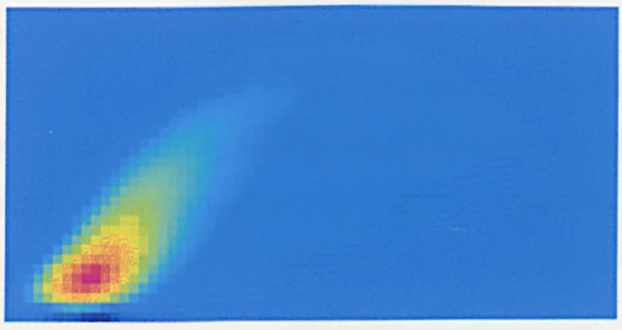

(c)

Figure 6.5 : Images formed from a simulated conductivity distribution.

(a) The conductivity distribution with an object of σ=0 of radius 0.433 units centred at position (2,1) in a background of σ=0.2Sm^{-1}.

(b) The image formed by WBP1.

(c) The image formed by WBP2.

(Max V_{data} -V_{ref} = 0.1678 normalised to the maximum potential difference in the reference set).

array and so the system is not symmetrical (by using weighted backprojection, the images are more circular than for backprojection because of the angular density weighting factors, but the compensation is only approximate for a small number of projections through the point). There is more equipotential blurring (the arc) in (b) than (c) and this is due to the preferential imaging of objects close to the array by the WBP2 method as discussed in the previous section. The Full Width at Half Maximum (FWHM) of a circular imaged object is defined as the diameter of the object's image at which the image intensity is half the peak value. It can be thought of as the imaged diameter of an object which would occur if the image contained only two levels of intensity thresholded at half the maximum value. Any FWHM figures given in this section and the following chapter refer to the average of the FWHM in the x-direction and the FWHM in the y-direction. The FWHM measured for the images in Figure 6.6(b) and (c) are 2.0 and 1.9 respectively, measured in units of 'like' electrode spacing as explained earlier in the chapter. (The dark lines directly beneath the object which can be seen in the images in (b) and (c) are produced by the high weighting values close to the array and should be ignored).

Figure 6.6 shows a larger object placed further from the array, but closer to the centre than in the previous figure. The peak of the image has been located accurately in the x-direction, but the image in (c) is marginally closer to the array than that in (b). This is due to the preferential imaging of the objects closer to the array for WBP2. The objects of the images are still non-circular due to the lack of symmetry and the equipotential 'tail' is more pronounced in (b) as before. The FWHMs are 3.3 for (b) and 3.2 for (c).

Figure 6.7 shows images produced from an object of the same size as in the previous figure, but placed in the centre of the area imaged. The shapes of the images of the object are non-circular, but are symmetrical about the line x=8 (midpoint). The x-centre has been located accurately in each case, but the y-centres are both a little low - the centre in (b) is approximately 0.4 units ('like' electrode spacing) too low and (c) is 0.6 units too low. However, with so much blurring the peak is quite flat and the FWHM of the image lies symmetrically about what should be the centre of the image in (b). The FWHM is measured as 7.1 and 5.9 in (b) and (c) respectively. The considerable blurring of the image is caused by the positioning of the object. With the object being positioned centrally and at a reasonable depth, most of the equipotentials passing through the object will tend to be parallel to the array. Coupled with the fact that no one measurement is strongly affected by the presence of the object as in the previous two Figures (note the absence of an equipotential 'tail'), the images generated are very blurred, especially in the x-direction.

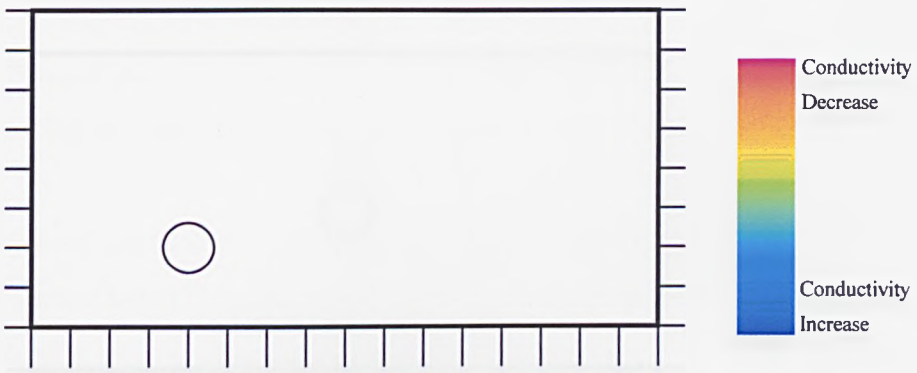

(a)

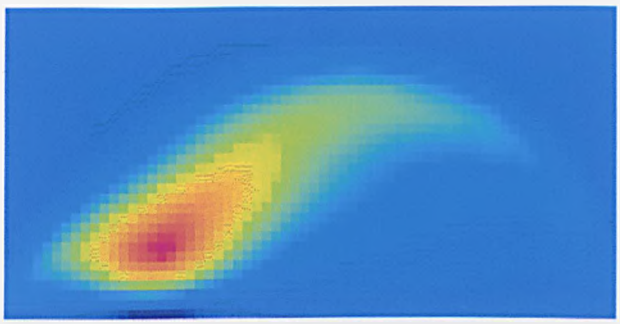

(b)

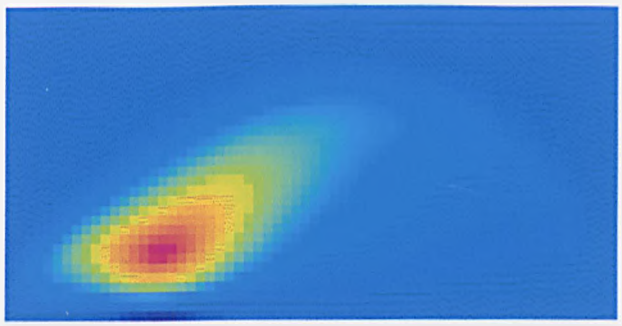

(c)

Figure 6.6 : Images formed from a simulated conductivity distribution.

(a) The conductivity distribution with an object of σ=0 of radius 0.633 units centred at position (4,2) in a background of σ=0.2Sm^{-1}.

(b) The image formed by WBP1.

(c) The image formed by WBP2.

(Max V_{data} -V_{ref} = 0.0413 normalised to the maximum potential difference in the reference set).

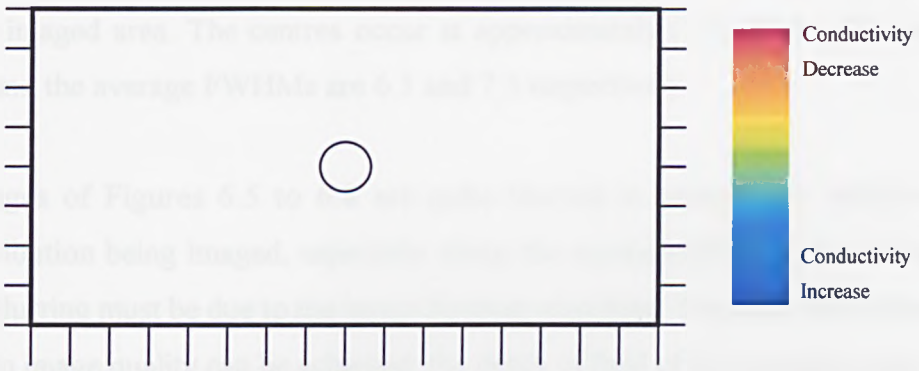

(a)

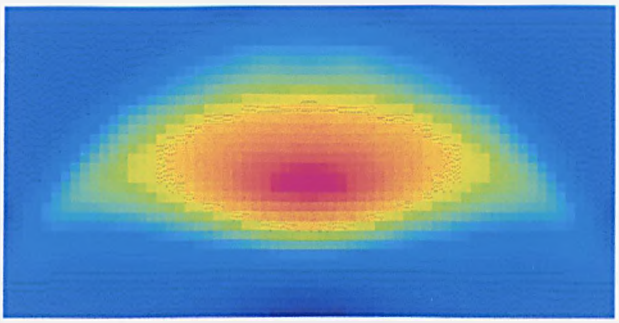

(b)

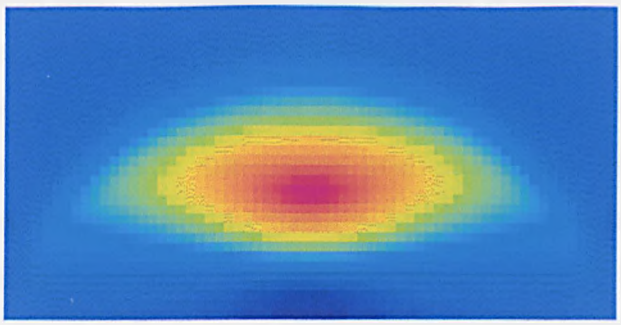

(c)

Figure 6.7 : Images formed from a simulated conductivity distribution.

(a) The conductivity distribution with an object of $\sigma=0$ of radius 0.633 units centred at position (8,4) in a background of $\sigma=0.2 Sm^{-1}$.

(b) The image formed by WBP1.

(c) The image formed by WBP2.

(Max V_{data} -V_{ref} = 0.0028 normalised to the maximum potential difference in the reference set).

Figure 6.8 shows the same object placed at the edge of the area of detection and the images produced from the simulated data. The images do not represent the object distribution, although there is a tilt to both images suggesting that the object is to the left of the centre of the imaged area. The centres occur at approximately (7.5,6.6) for (b) and (6.2,5.0) for (c) and the average FWHMs are 6.1 and 7.3 respectively.

The images of Figures 6.5 to 6.8 are quite blurred in comparison with the conductivity distribution being imaged, especially along the equipotential loci. Since the data is ideal, the blurring must be due to the image forming algorithm. It is clear that unless an improvement in image quality can be achieved, the depth of field of the imaging system could be limited by the image forming algorithm alone and not by the noise present on the real data. In an effort to improve the image quality some filters were applied to the images and these are discussed below.

6.3.2 Filtered Images

Three filtering techniques commonly applied to images generated by EIT systems have been considered. These are the Gaussian filter [84], the ramp filter [42] and filtered backprojection [85]. These three filtering methods will be briefly described and applied to the images of Figures 6.5 to 6.8. The resulting filtered images will be discussed.

The Gaussian filter proposed by Barber [84], is used on data gathered from a system which uses encircling electrodes. It is essentially based on the fact that an object at the centre of a circular region appears as an approximate Gaussian distribution in the image when backprojected. Objects at non-central positions appear as conformally mapped Gaussian distributions around the object position. The filtering process is similar to a process called unsharp masking [86] used in image processing, where a blurred version of the original image is produced and a fraction of this image is subtracted from the original image to produce the filtered image. In the application of the Gaussian filter, the intermediate 'blurred' image is produced by applying a conformally mapped Gaussian distribution to each pixel in turn and modifying the values of the pixels surrounding this pixel. A fraction of the blurred image is subtracted to produce the filtered image. This filter has been applied to data gathered from encircling arrays of electrodes and produced good results [84]. The same process can be applied to an image formed from data using a linear array of electrodes. The region to be imaged using the linear array must first be conformally mapped to a

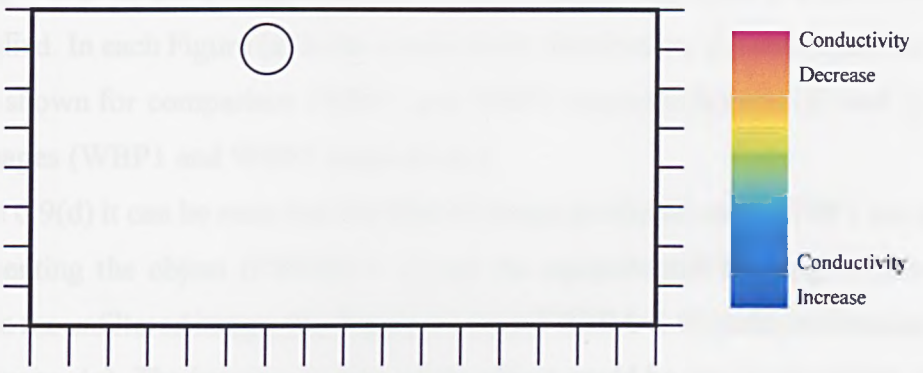

(a)

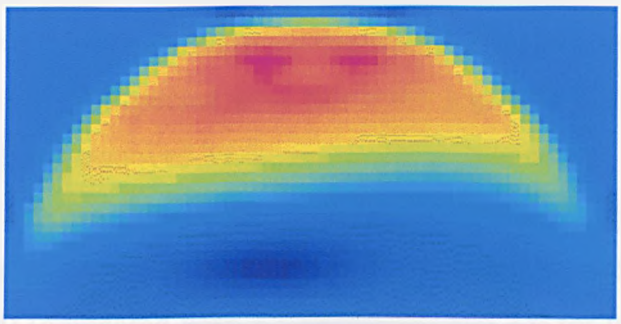

(b)

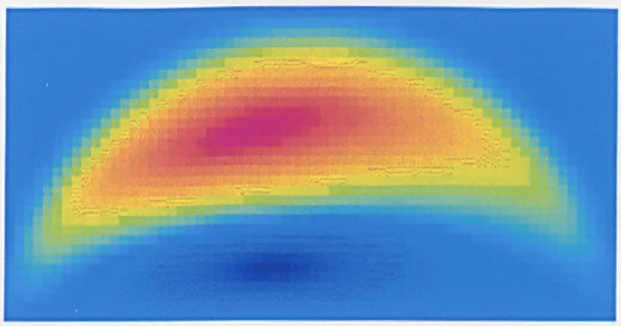

(c)

Figure 6.8 : Images formed from a simulated conductivity distribution.

(a) The conductivity distribution with an object of σ=0 of radius 0.633 units centred at position (6,7) in a background of σ=0.2Sm^{-1}.

(b) The image formed by WBP1.

(c) The image formed by WBP2.

(Max V_{data} -V_{ref} = 0.0003 normalised to the maximum potential difference in the reference set).

circular region corresponding to the image region of the circular array, so that the filter can then be applied.

Figures 6.9 to 6.12 show images produced from analytic data after the Gaussian filter has been applied. In each Figure (a) is the conductivity distribution, (b) and (c) are the unfiltered images shown for comparison (WBP1 and WBP2 respectively) and (d) and (e) are the filtered images (WBP1 and WBP2 respectively).

In Figure 6.9(d) it can be seen that the filtered image produced using WBP1 has a larger area representing the object (FWHM=3.1) and the equipotential blurring is more pronounced than in the unfiltered image, (b). Figure 6.10(e) (FWHM=1.9) is almost identical to the unfiltered image, (c). The increase in area of the object could be due to the radius of the Gaussian distribution used in the filtering process being incorrect for this particular object distribution (for the best filtering of the image, each object size and position requires a different radius, but this is impractical to implement). The increase in blurring along the equipotential lines is to be expected since this is not a general blurring around the object and so, rather than being removed by the filter, will be enhanced.

Figure 6.10 shows a similar set of images for a different object distribution. Again the equipotential 'tail' is more pronounced in the filtered images. The FWHM of the filtered images is 3.3 for (d) (compared with 3.3 unfiltered) and 3.0 for (e) (compared with 3.2 unfiltered) showing a reduction in object area for the filtered WBP2 image.

Figure 6.11 shows the filtered images of an object placed in the centre of the area of detection. It can be seen that both the filtered images are distorted versions of the unfiltered images. The odd shape can be explained by the conformal mapping procedure. The distribution (which was circular in the centre of the circle) becomes distorted when conformally mapped to near the edge of a circle. The distortion is strongly radial ie the shape is elongated in the radial direction. The linear array can be considered to be an infinitely narrow portion of the circumference of a circle, and so the mapped gaussian distribution will be longer in the y-direction than in the x-direction. However, the unfiltered images in Figure 6.11 are both elongated in the x-direction rather than the y-direction. Hence, the filtering process will reduce the y-direction blurring, but actually increase the x-direction blurring and this can be seen to be the case. The position of the centres is closer to the array than in the unfiltered images in both cases.

Similarly the filtered images in Figure 6.12 are distorted by the same process described above. The position of the object is not calculable and, given the extent of the distortion, the FWHM is meaningless.

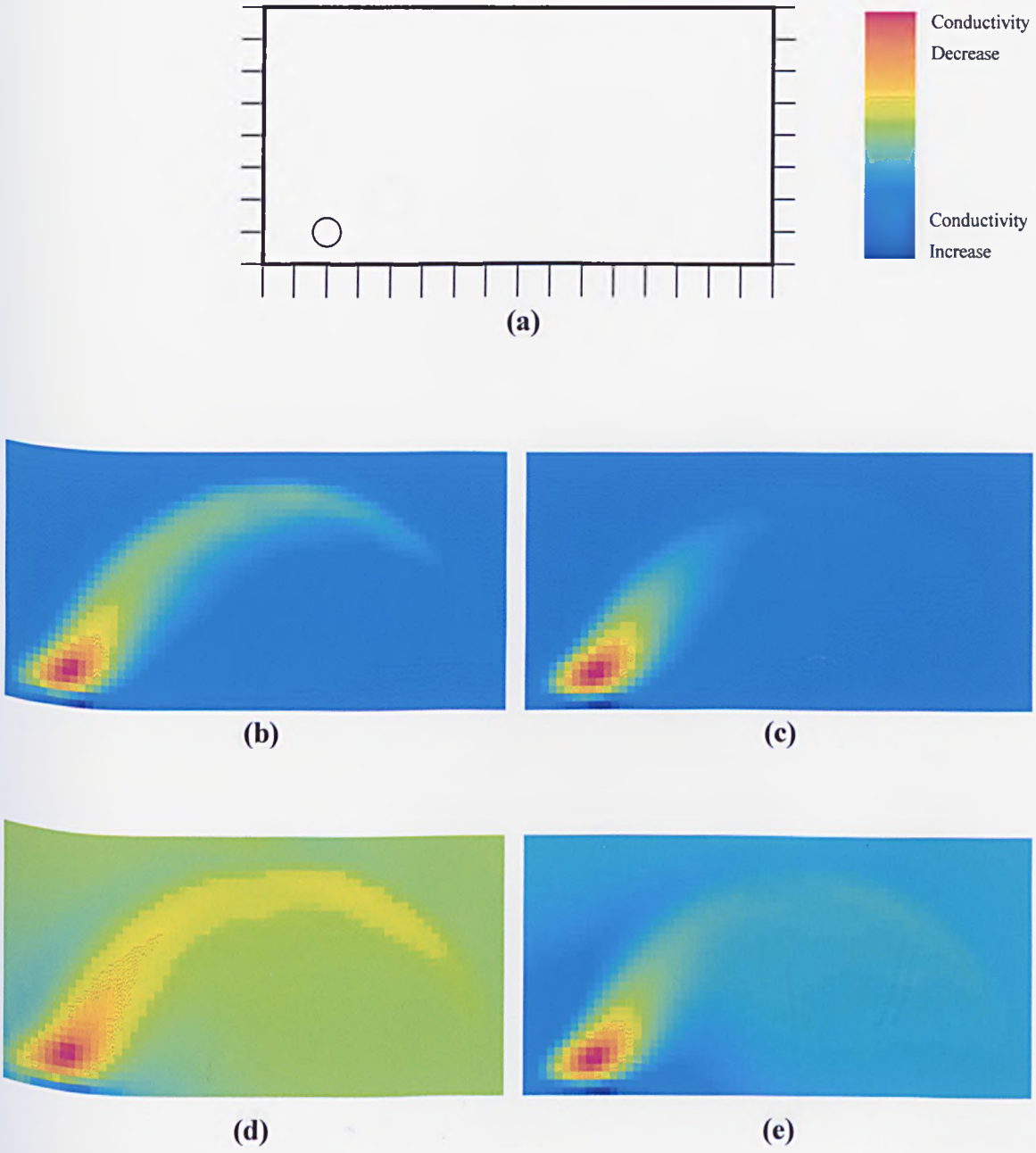

Figure 6.9 : Images formed from a simulated conductivity distribution.

- **(a)** The conductivity distribution with an object of $\sigma=0$ of radius 0.433 units centred at position (2,1) in a background of $\sigma=0.2Sm^{-1}$.
- **(b)** The image formed by WBP1.
- **(c)** The image formed by WBP2 .
- **(d)** A gaussian filtered version of image (b).
- **(e)** A gaussian filtered version of image (c).

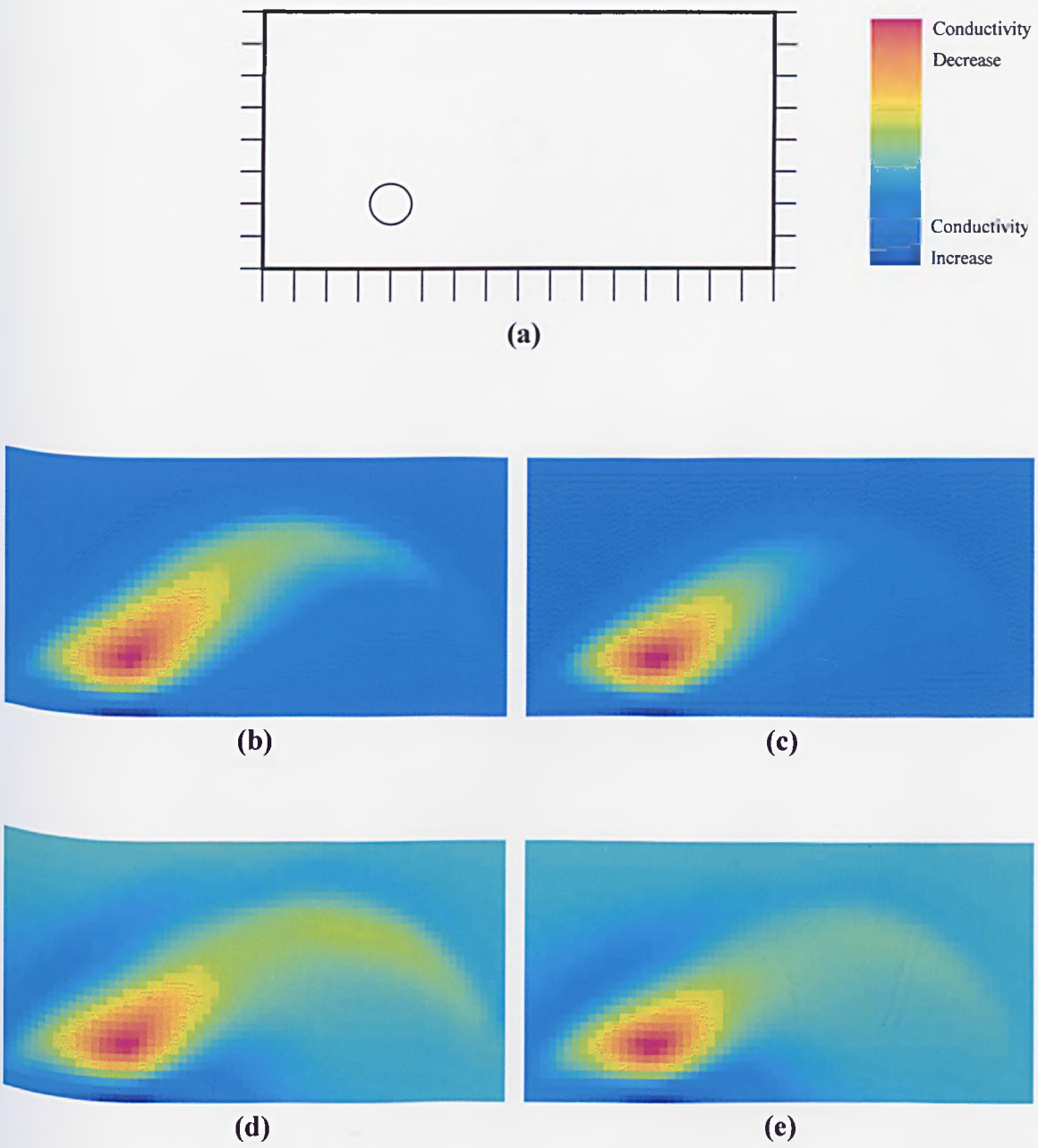

Figure 6.10 : Images formed from a simulated conductivity distribution.

- **(a)** The conductivity distribution with an object of $\sigma=0$ of radius 0.633 units centred at position (4,2) in a background of $\sigma=0.2Sm^{-1}$.
- **(b)** The image formed by WBP1.
- **(c)** The image formed by WBP2 .
- **(d)** A gaussian filtered version of image (b).
- **(e)** A gaussian filtered version of image (c).

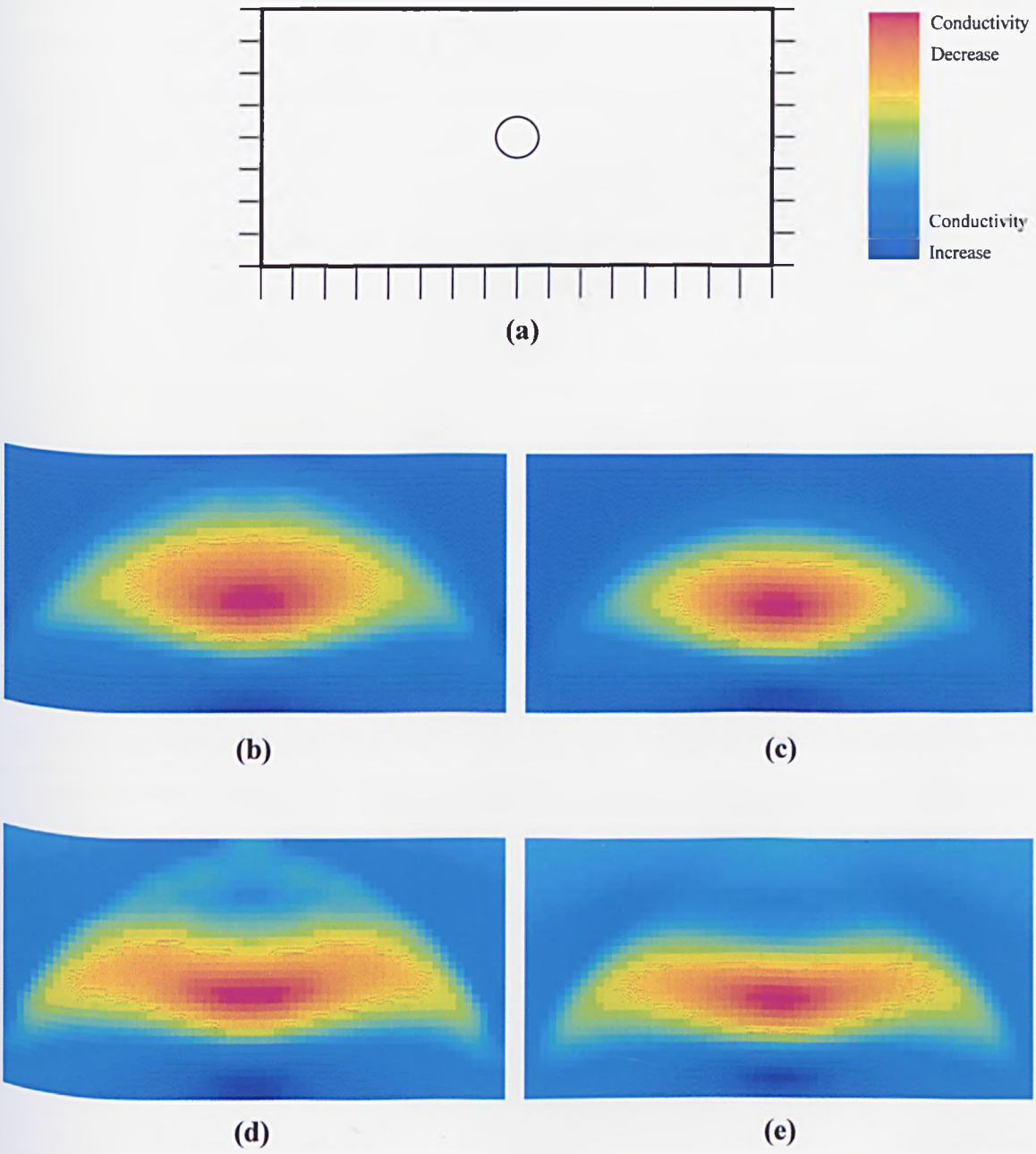

Figure 6.11 : Images formed from a simulated conductivity distribution.

- **(a)** The conductivity distribution with an object of $\sigma=0$ of radius 0.633 units centred at position (8,4) in a background of $\sigma=0.2Sm^{-1}$.
- **(b)** The image formed by WBP1.
- **(c)** The image formed by WBP2 .
- **(d)** A gaussian filtered version of image (b).
- **(e)** A gaussian filtered version of image (c).

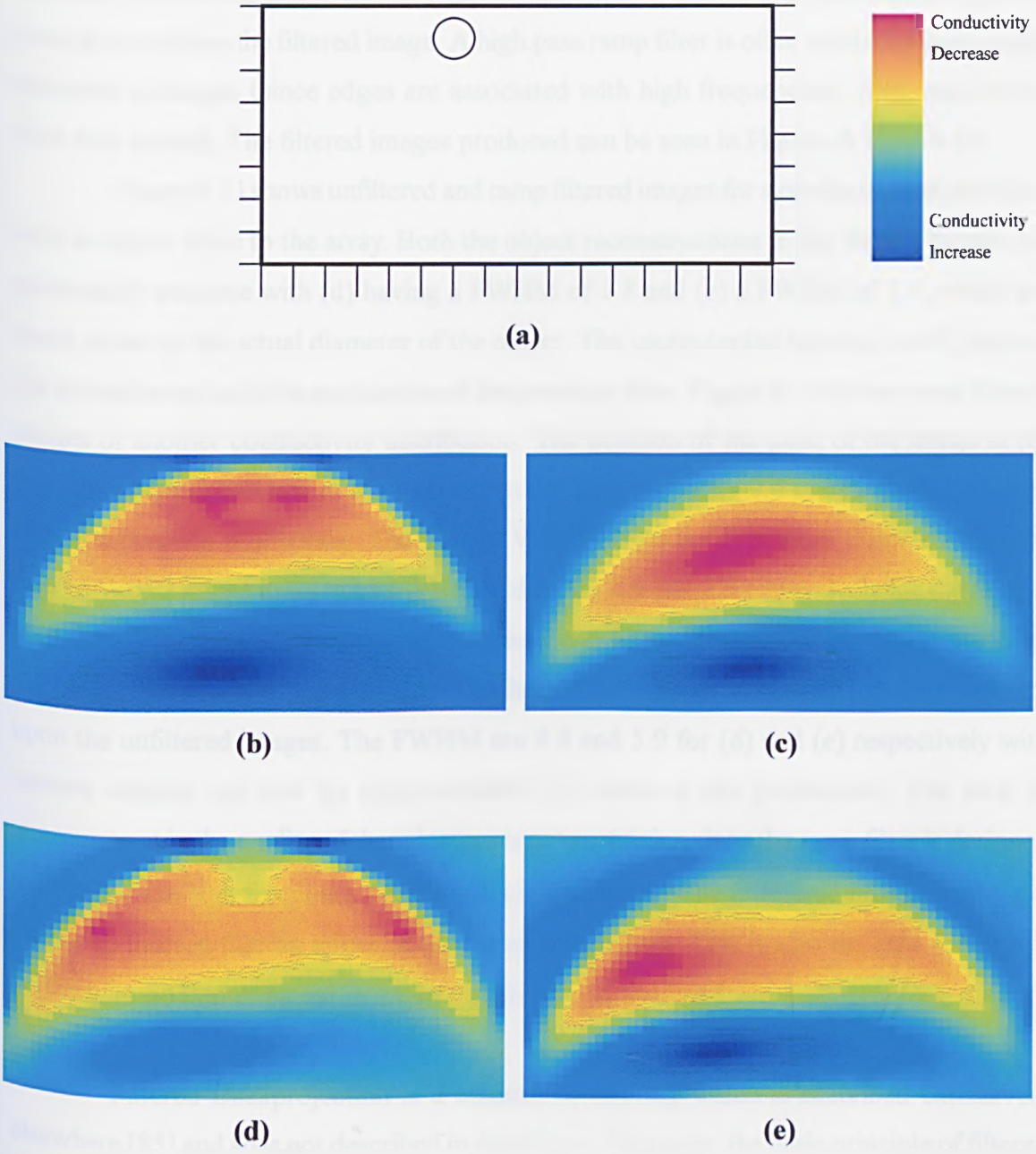

Figure 6.12 : Images formed from a simulated conductivity distribution.

- **(a)** The conductivity distribution with an object of $\sigma=0$ of radius 0.633 units centred at position (6,7) in a background of $\sigma=0.2Sm^{-1}$.
- **(b)** The image formed by WBP1.
- **(c)** The image formed by WBP2 .
- **(d)** A gaussian filtered version of image (b).
- **(e)** A gaussian filtered version of image (c).

Two-dimensional spatial frequency filters are sometimes used to filter images [86]. These involve calculating the 2D Fourier Transform of the image, applying a filter to the frequency spectra and then calculating the Inverse Fourier Transform of the filtered frequency spectra to produce the filtered image. A high pass ramp filter is often used to improve edge detection in images (since edges are associated with high frequencies) [86], and so this filter was applied. The filtered images produced can be seen in Figures 6.13 to 6.16.

Figure 6.13 shows unfiltered and ramp filtered images for a conductivity distribution with an object close to the array. Both the object reconstructions in the filtered images are positionally accurate with (d) having a FWHM of 1.8 and (e) a FWHM of 1.4, which are much closer to the actual diameter of the object. The equipotential blurring is still present, but not enhanced as in the application of the previous filter. Figure 6.14 shows ramp filtered images of another conductivity distribution. The position of the peak of the image in (d) and (e) is slightly too low in the y-direction (by approximately 0.4 units), although the x-direction position is accurate. The filtered WBP1 image in (d) is more distorted than the filtered WBP2 image in (e). The FWHM widths are 2.8 and 2.5 respectively for the images in (d) and (e). Figure 6.15 shows the unfiltered and filtered images for the object placed in the centre of the region of detection. Neither of the filtered images are an improvement upon the unfiltered images. The FWHM are 8.8 and 5.9 for (d) and (e) respectively with centres slightly too low by approximately 0.2 units in the y-direction. The lack of improvement in the quality of these images is not surprising since the ramp filter is designed to enhance the high frequency components in the image. The unfiltered images in (b) and (c) are so blurred that no edges of the object are evident. This is also the case for Figure 6.16 where no improvement in image quality can be observed.

Filtered Backprojection is a method of filtering which is described extensively elsewhere [85] and so is not described in detail here. However, the basic principle of filtered backprojection is to solve the forward problem for an inhomogeneity placed at each pixel in turn, as in the calculation of the sensitivity matrix. This matrix is denoted by **F**. **F** is then multiplied by the matrix of backprojection weights, usually called **B** in this context, to produce a square matrix **FB**. The matrix **FB** contains information about errors in the image forming algorithm, since ideally **B** should be the inverse of **F** and so **FB** should be the identity matrix. This matrix of errors is then inverted $(\mathbf{FB})^{-1}$ and multiplied by **B** to give a matrix $\mathbf{B}(\mathbf{FB})^{-1}$ which forms **B'**, the modified backprojection matrix to be used for the image forming. The image forming matrix $\mathbf{B}(\mathbf{FB})^{-1}$ was calculated for a linear array and

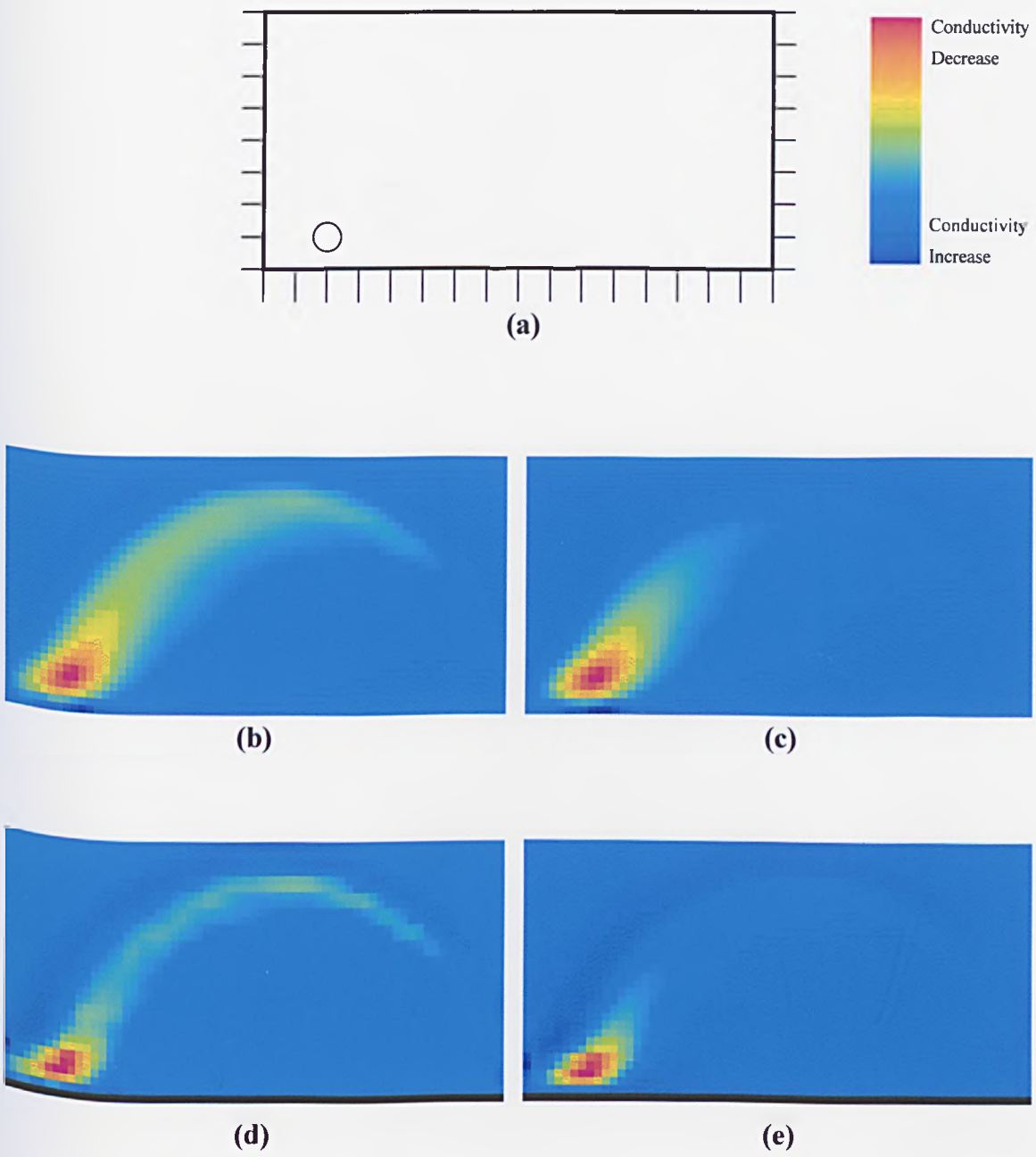

Figure 6.13 : Images formed from a simulated conductivity distribution.

- **(a)** The conductivity distribution with an object of $\sigma=0$ of radius 0.433 units centred at position (2,1) in a background of $\sigma=0.2Sm^{-1}$.
- **(b)** The image formed by WBP1.
- **(c)** The image formed by WBP2 .
- **(d)** A ramp filtered version of image (b).
- **(e)** A ramp filtered version of image (c).

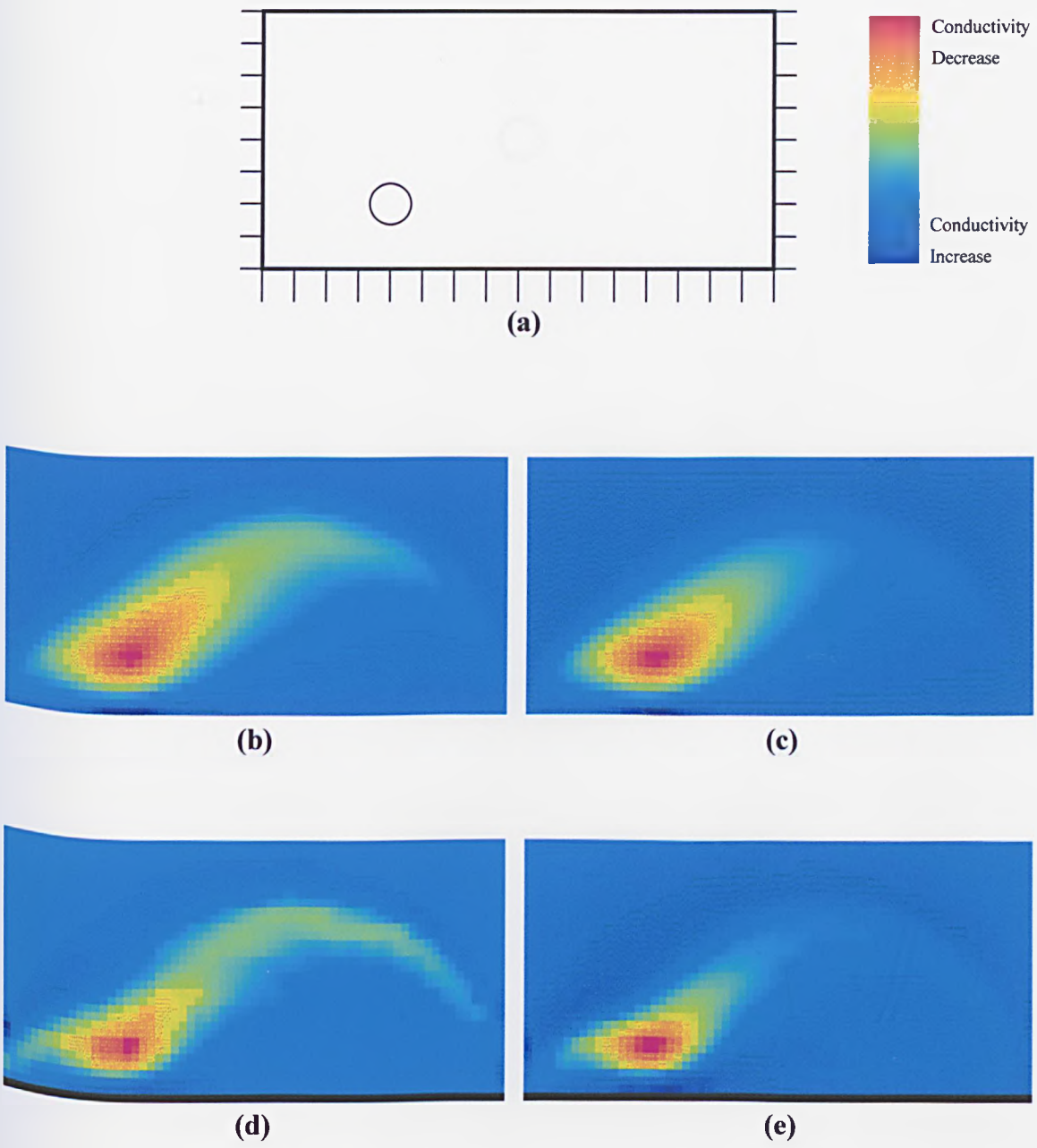

Figure 6.14 : Images formed from a simulated conductivity distribution.

- **(a)** The conductivity distribution with an object of $\sigma=0$ of radius 0.633 units centred at position (4,2) in a background of $\sigma=0.2Sm^{-1}$.
- **(b)** The image formed by WBP1.
- **(c)** The image formed by WBP2.
- **(d)** A ramp filtered version of image (b).
- **(e)** A ramp filtered version of image (c).

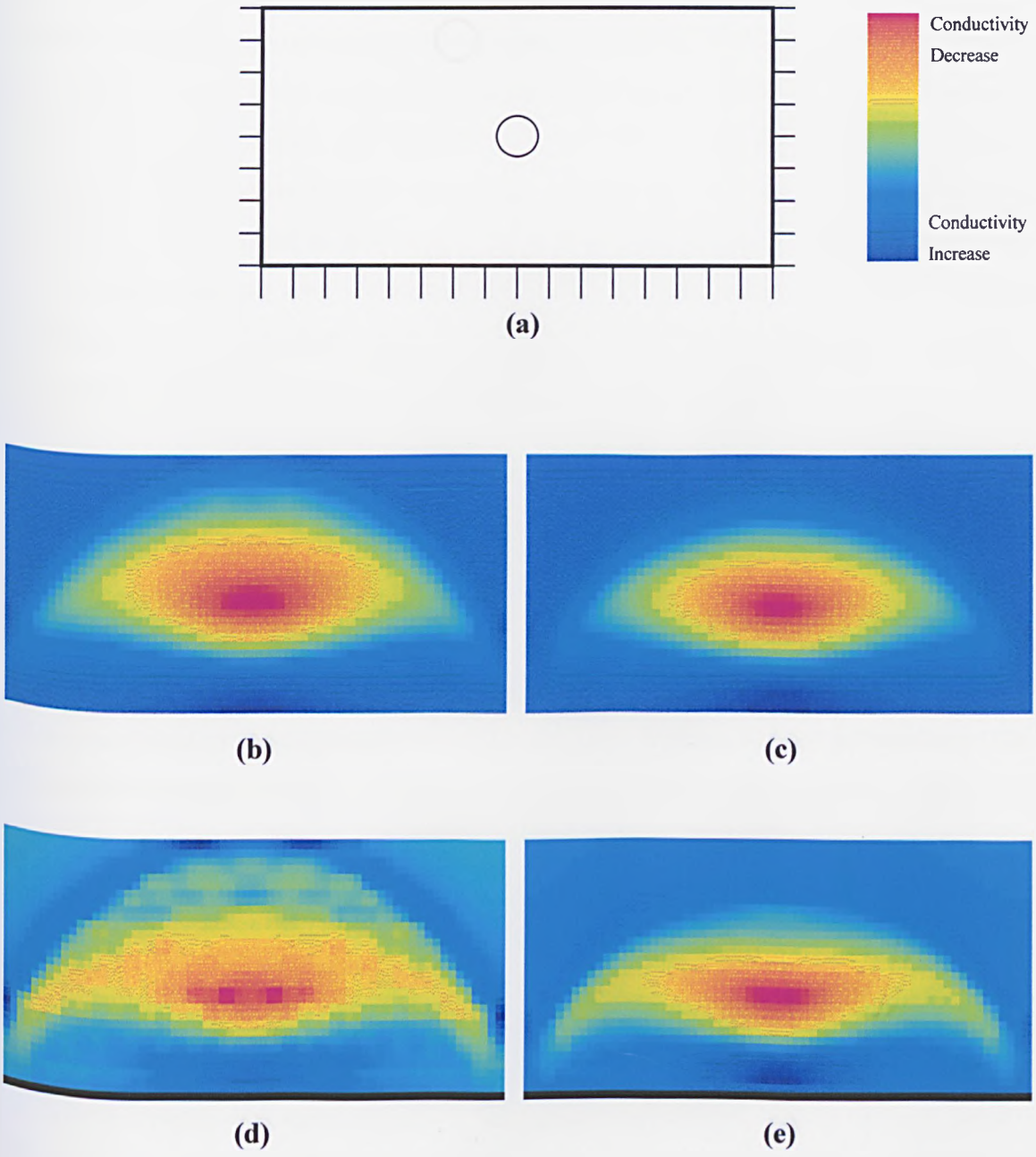

Figure 6.15 : Images formed from a simulated conductivity distribution.

- **(a)** The conductivity distribution with an object of $\sigma=0$ of radius 0.633 units centred at position (8,4) in a background of $\sigma=0.2Sm^{-1}$.
- **(b)** The image formed by WBP1.
- **(c)** The image formed by WBP2.
- **(d)** A ramp filtered version of image (b).
- **(e)** A ramp filtered version of image (c).

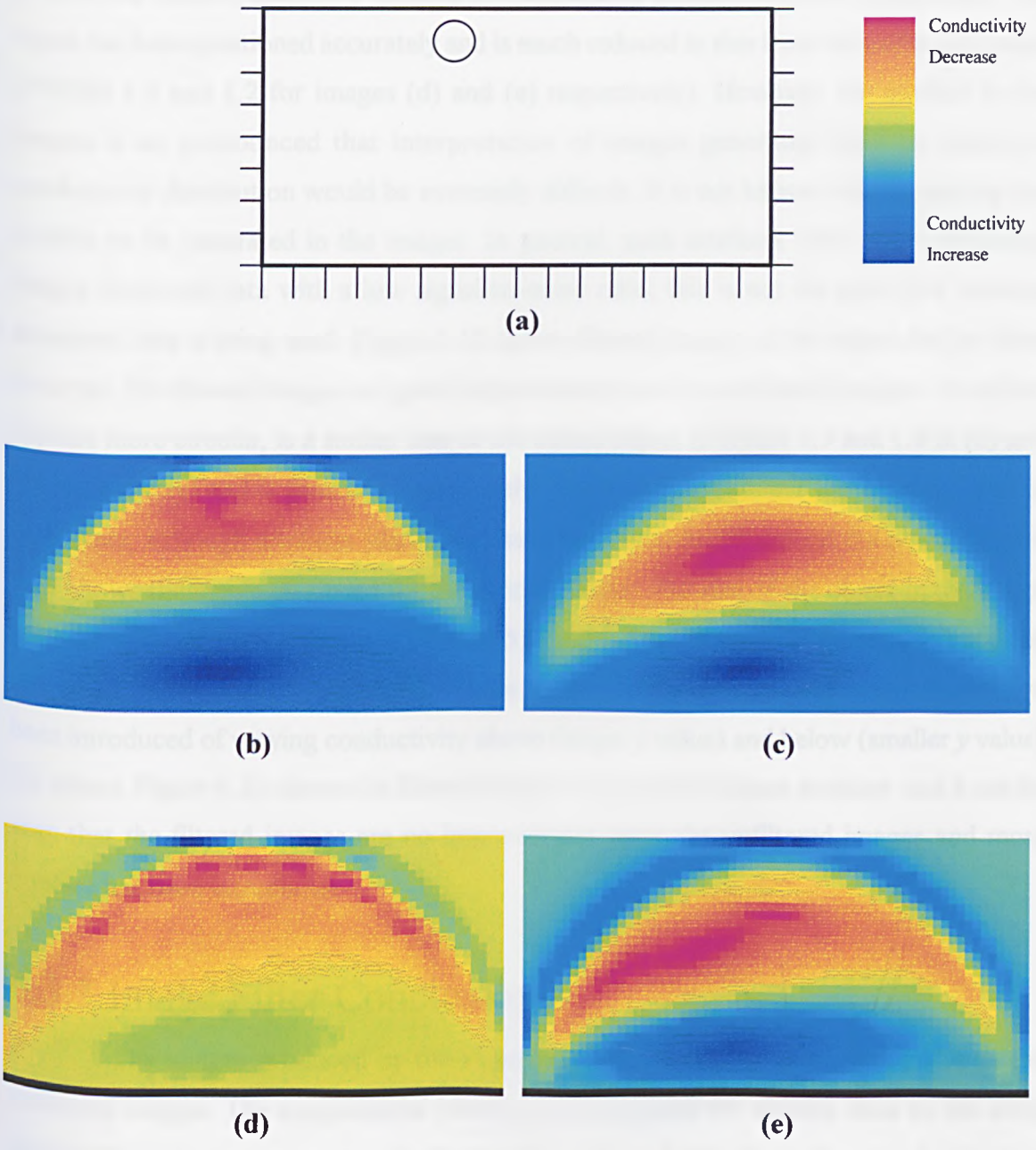

Figure 6.16 : Images formed from a simulated conductivity distribution.

- **(a)** The conductivity distribution with an object of $\sigma=0$ of radius 0.633 units centred at position (6,7) in a background of $\sigma=0.2Sm^{-1}$.
- **(b)** The image formed by WBP1.
- **(c)** The image formed by WBP2.
- **(d)** A ramp filtered version of image (b).
- **(e)** A ramp filtered version of image (c).

images formed using this matrix are shown in Figures 6.17 to 6.20.

Figure 6.17 shows filtered backprojected images for an object close to the array. In both the filtered images of (d) and (e), significant artefact has been introduced. The object has been positioned accurately and is much reduced in size from the unfiltered image (FWHM 1.3 and 1.2 for images (d) and (e) respectively). However, the artefact in the images is so pronounced that interpretation of images generated from an unknown conductivity distribution would be extremely difficult. It is not known what is causing the artefact to be generated in the images. In general, such artefacts arise when producing images from real data with a low signal-to-noise ratio; this is not the case here because simulated data is being used. Figure 6.18 shows filtered images of the object further from the array. The filtered images are great improvement upon the unfiltered images - the object appears more circular, is a similar size to the actual object (FWHM 1.9 and 1.8 in (d) and (e) respectively) and is positioned accurately. The equipotential 'tail' has been reduced in both cases, although artefacts (dark blue) have been introduced around the object. Figure 6.19 shows the image produced for the central object. The size of the object in the image has been reduced by the filtering (FWHM 5.0 and 4.7 in (d) and (e) respectively) and the centres of the object are in the same place as in the unfiltered image. Various artefacts have been introduced of varying conductivity above (larger y value) and below (smaller y value) the object. Figure 6.20 shows the filtered images of the fourth object position and it can be seen that the filtered images are no improvement upon the unfiltered images and more artefact has been introduced.

6.3.3 Image Filter Conclusions

The images produced by the Gaussian filter showed no improvement upon the unfiltered images. The equipotential blurring was enhanced for objects close to the array and the filtered images were severely distorted for objects further from the array. Application of this filter by using mapped gaussian distributions is perhaps ill-conceived since the unfiltered images produced from objects placed in different positions are not comparable with the circular conformally mapped gaussian distribution.

The ramp filter reduced the blurring of the images and enhanced the edges of the objects for objects placed close to the array ($y \leq 2$), especially for the WBP2 case. However, the filter did not improve the blurred images generated for objects placed at a distance from the array ($y \geq 4$).

The filtered backprojected images were an improvement upon the unfiltered images

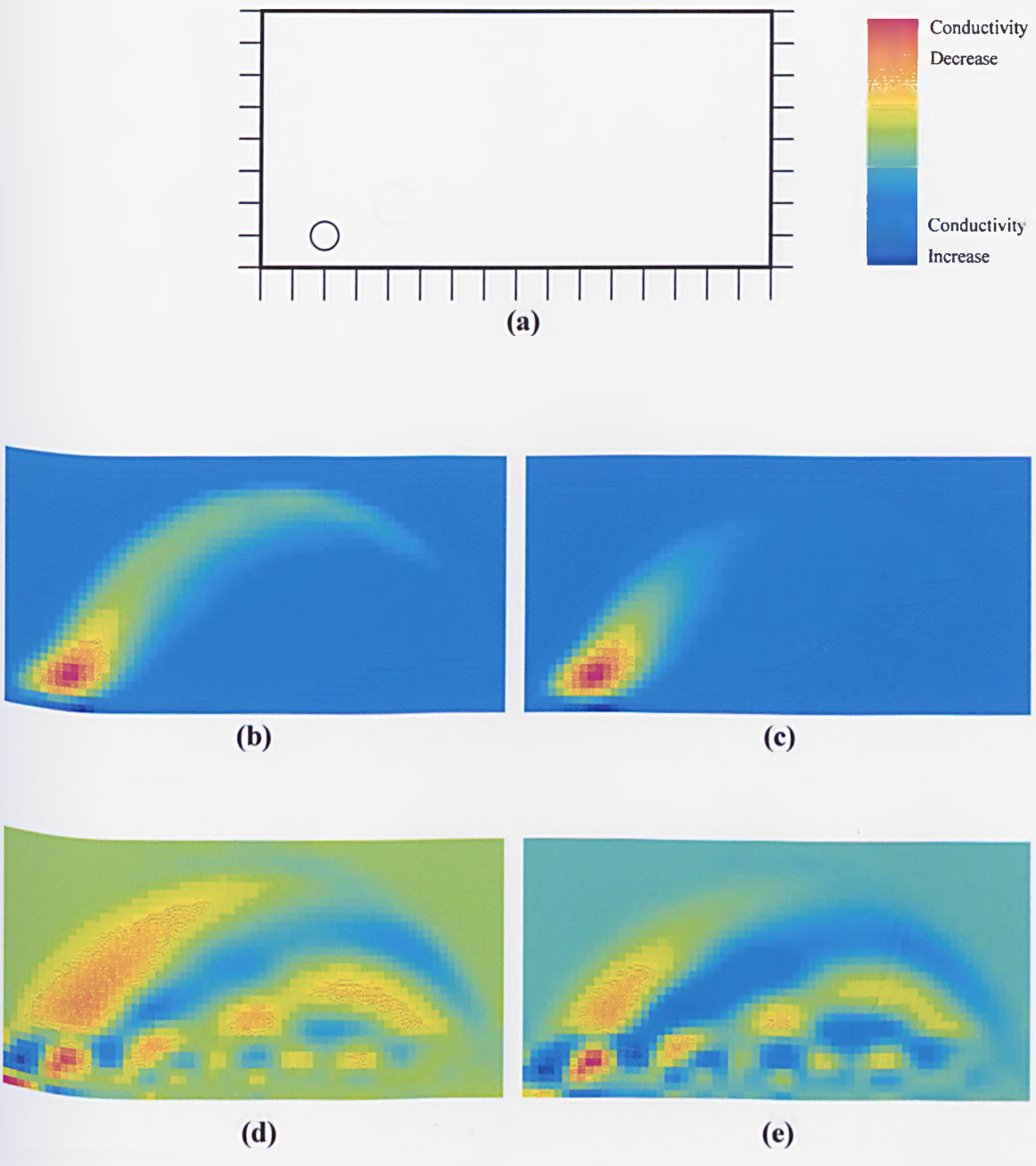

Figure 6.17 : Images formed from a simulated conductivity distribution.

- **(a)** The conductivity distribution with an object of $\sigma=0$ of radius 0.433 units centred at position (2,1) in a background of $\sigma=0.2Sm^{-1}$.
- **(b)** The image formed by WBP1.
- **(c)** The image formed by WBP2 .
- **(d)** An image produced by filtered backprojection of WBP1.
- **(e)** An image produced by filtered backprojection of WBP2.

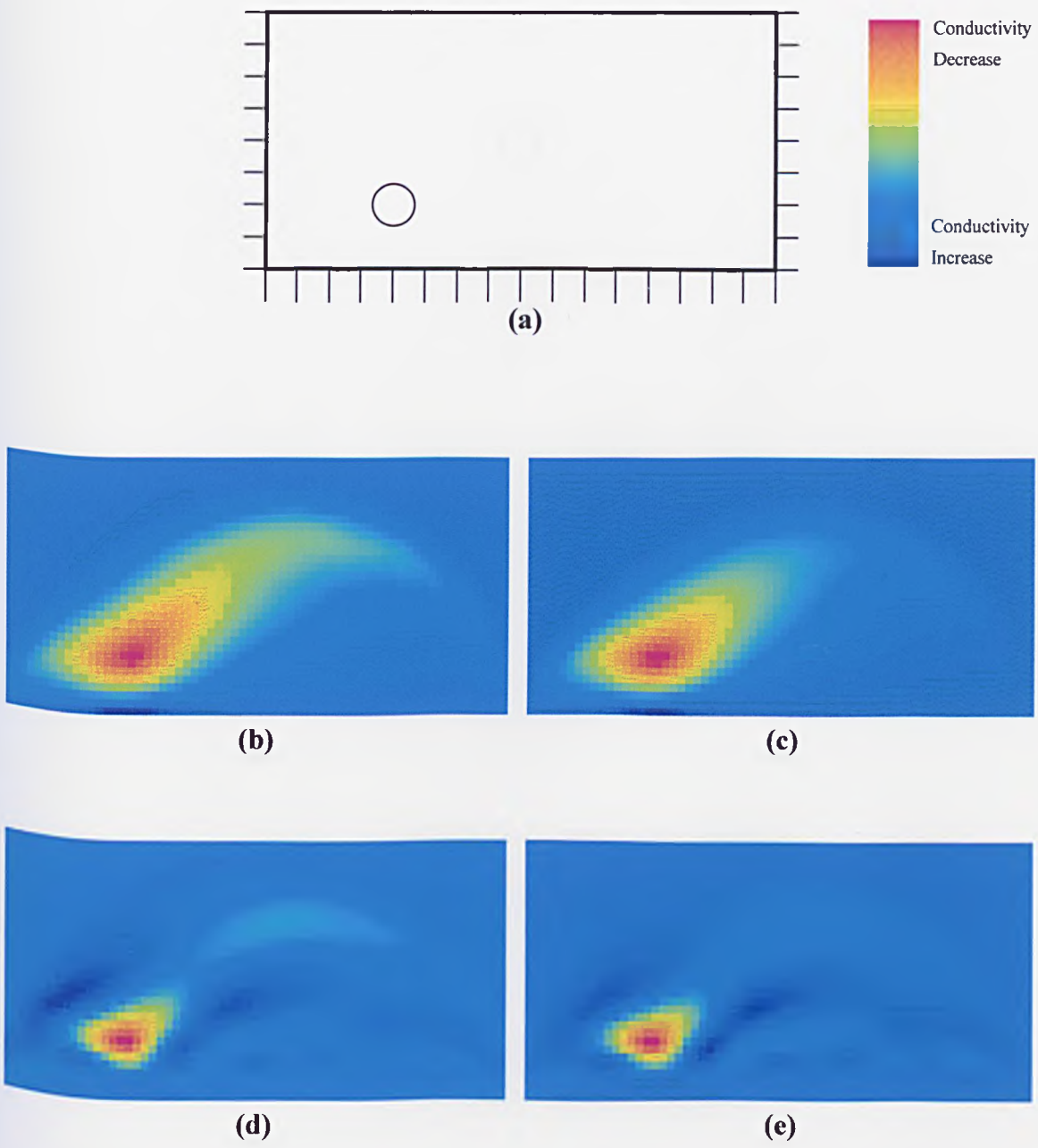

Figure 6.18 : Images formed from a simulated conductivity distribution.

- **(a)** The conductivity distribution with an object of $\sigma=0$ of radius 0.633 units centred at position (4,2) in a background of $\sigma=0.2Sm^{-1}$.
- **(b)** The image formed by WBP1.
- **(c)** The image formed by WBP2 .
- **(d)** An image produced by filtered backprojection of WBP1.
- **(e)** An image produced by filtered backprojection of WBP2.

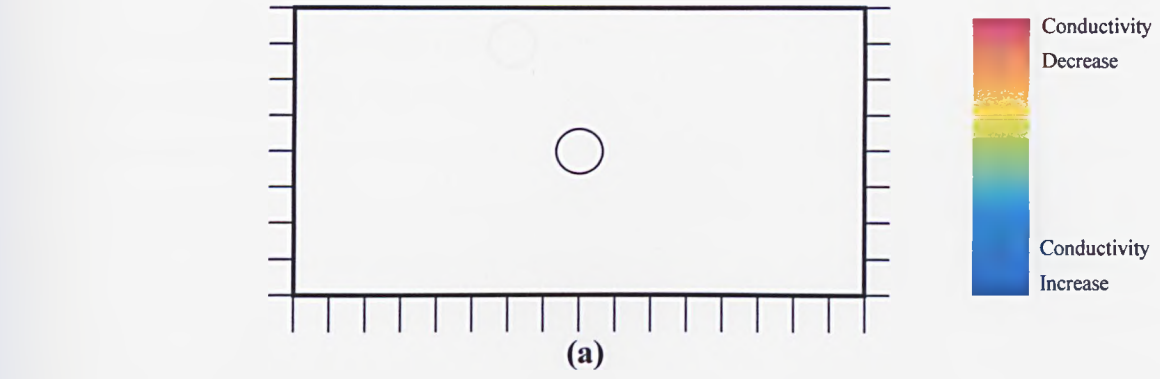

(a)

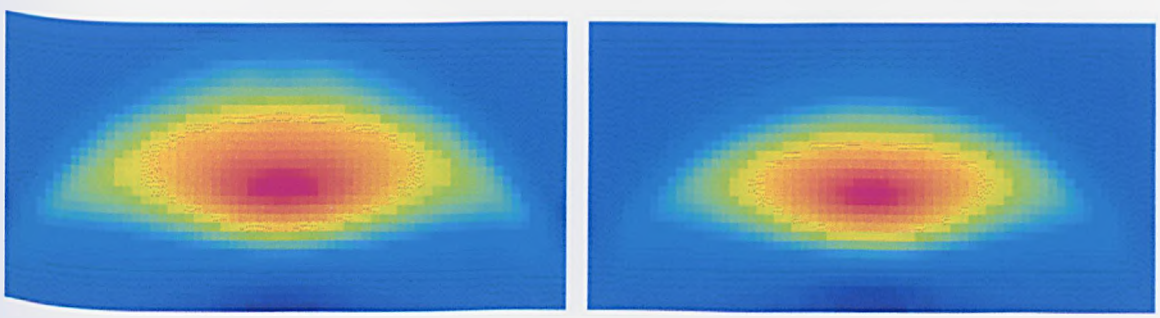

(b) (c)

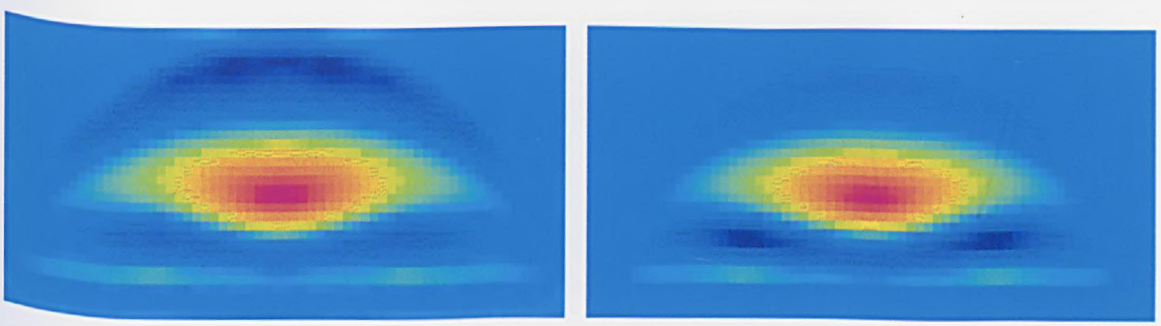

(d) (e)

Figure 6.19 : Images formed from a simulated conductivity distribution.

- **(a)** The conductivity distribution with an object of $\sigma=0$ of radius 0.633 units centred at position (8,4) in a background of $\sigma=0.2Sm^{-1}$.
- **(b)** The image formed by WBP1.
- **(c)** The image formed by WBP2 .
- **(d)** An image produced by filtered backprojection of WBP1.
- **(e)** An image produced by filtered backprojection of WBP2.

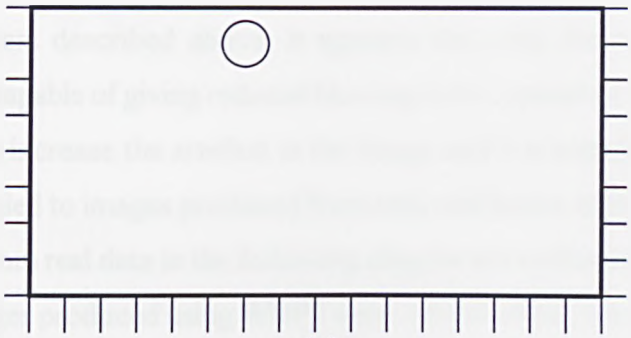

(a)

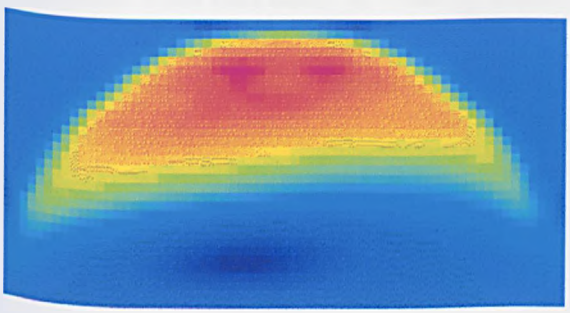

(b)

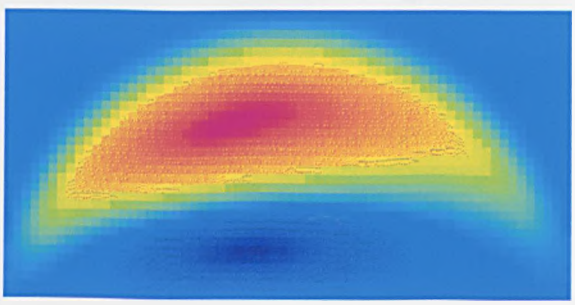

(c)

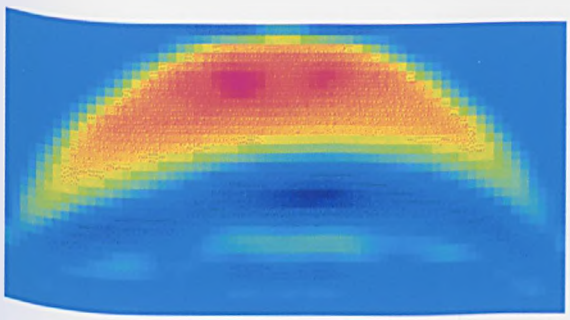

(d)

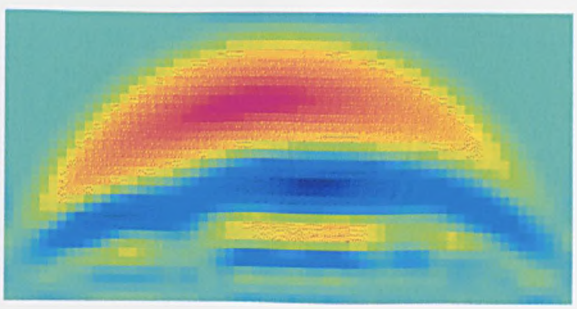

(e)

Figure 6.20 : Images formed from a simulated conductivity distribution.

(a) The conductivity distribution with an object of $\sigma=0$ of radius 0.633 units centred at position (6,7) in a background of $\sigma=0.2Sm^{-1}$.

(b) The image formed by WBP1.

(c) The image formed by WBP2 .

(d) An image produced by filtered backprojection of WBP1.

(e) An image produced by filtered backprojection of WBP2.

for y=2 to y=4 with much reduced blurring. However, in all the filtered backprojected cases artefact was introduced.

Of the filters described above, it appears that only the ramp filter and filtered backprojection are capable of giving reduced blurring in the context of a linear array. However both these methods increase the artefact in the image and it is expected that this will cause problems when applied to images produced from real, and hence noisy, data. For this reason, images produced from real data in the following chapter are unfiltered images, unless stated otherwise. The images produced using WBP2 were, on the whole, less prone to equipotential blurring than the images produced using WBP1. However, both methods are used in the generation of images from measured data in the next chapter and a thresholding technique (different from that used in WBP2) is used in the formation of images using WBP1.

Chapter 7 Measurements and Images

7.1 Introduction

This chapter describes measurements made on various conductivity distributions set up in the phantom and presents the images produced from some of those measurements.

To assess whether or not the system was performing as designed, the buffered electrode potentials measured at the surface of the medium are investigated and compared with the predicted electrode potential amplitudes. The effects of the common-mode feedback circuitry and the finite dimensions of the phantom on these potentials are discussed. The potential differences between adjacent electrodes measured for a homogeneous region are compared with those calculated theoretically, since any difference between these two will limit the likelihood of forming a static image. Possible reasons for any discrepancies are suggested. Simulated and measured voltage differences for specific object distributions are compared.

Reconstructed images of a number of conductivity distributions using data collected by the system are presented. The conductivity distributions imaged were chosen to evaluate the overall performance of the system. Images reconstructed from a distribution containing a single 2D object are compared with images produced from data generated analytically for the same object distribution. Images produced from distributions containing two objects (of the same and different conductivities) are then presented followed by sequences of images produced from data gathered from moving objects. Finally, images produced from data taken from a 3D medium are presented.

7.2 Measured Surface Electrode Potentials

By using Equations {1.1} and {1.3} it is possible to calculate the potential generated at any point in a semi-infinite homogeneous 3D and pseudo-2D medium by a single drive pair. A comparison of the predicted potentials at the receive electrode positions with the measured buffered electrode potentials will demonstrate the validity of the application of the equations to the phantom using the system described. Figure 7.1(a) shows a short section of the array comprising five drive electrodes, and the four drive currents associated

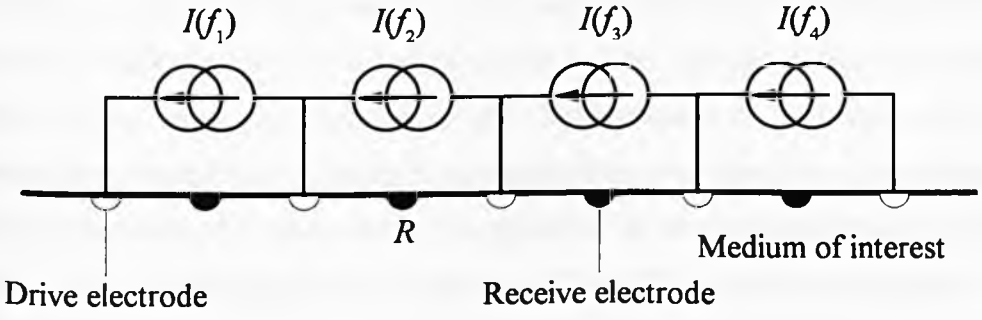

(a)

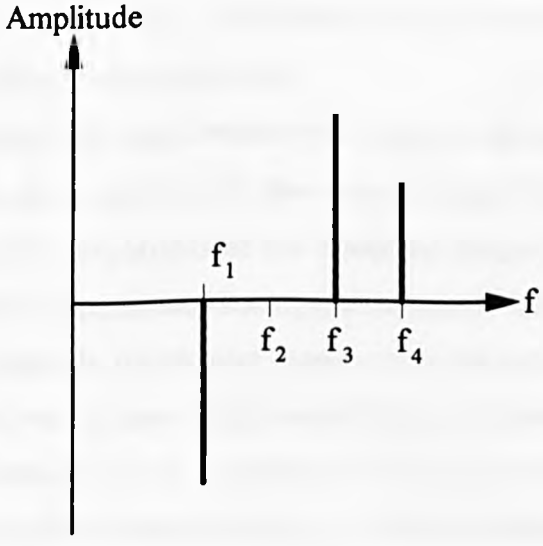

(b)

Figure 7.1 : Potentials at a receive electrode.

(a) Diagram showing four drive pairs injecting current into the medium of interest.

(b) The expected potentials at receive electrode, *R*.

with them, on the surface of a semi-infinite homogeneous medium. If the four drive currents were the only sources of current to be injected into the semi-infinite homogeneous medium, then the potential at receive electrode R would have four frequency components as shown in Figure 7.1(b). Assuming that the current sources are floating and that the current sources and contact impedances are matched, the potentials at two drive electrodes at the frequency of the source that drives them, will be in antiphase ie. they will be of the same amplitude, but 180° out of phase. The potential at the midpoint between two drive electrodes at the frequency of the source that drives them will be zero. All potentials are measured with respect to zero. Those potentials that are 180° out of phase with the drive current generating them will be referred to as negative. Potentials in phase with the drive current that generates them will be referred to as positive. The potential at receive electrode R at frequency f_1 would be negative, the potential at a frequency f_2 would be zero (assuming perfect matching of the current sources and contact impedances), the potential at frequency f_3 would be positive and equal in amplitude to the potential at f_1 and the potential at frequency f_4 would be positive but smaller in amplitude than at f_3. If this model is extended to the case where there are 16 drive frequencies, each receive electrode (except for the end electrodes) will have two large frequency components which are equal in amplitude and occur at the frequencies corresponding to the drives on either side of the receive electrode (similar to the frequencies f_1 and f_3 in Figure 7.1). These frequencies are henceforth referred to as the 'dominant' frequencies for a receive electrode.

Assuming perfect matching between the sources and assuming a semi-infinite homogeneous medium, the amplitudes of the two dominant frequencies at one receive electrode should equal the amplitudes of the dominant frequencies at another receive electrode. However, for the experimental homogeneous pseudo-2D medium of depth 20mm, the receive electrode potentials, which were monitored at the output of the buffers using a spectrum analyser, were found to have unequal amplitudes at the two 'dominant' frequencies. This error will not necessarily cause a problem if it is due to the addition of the same potential at a frequency at all the electrodes, since it is the potential differences between the receive electrodes which are important and not the potentials themselves. If, however, the effect was one of linear scaling (multiplication by a constant), then the voltage differences would be affected by the same constant. Consequently, since the potentials were not as expected, it was necessary to identify the source of these errors so that a better understanding of the system could be gained.

It was observed that if the common-mode feedback was connected between the

two corners furthest from the array as shown in Figure 7.2, the amplitudes of the dominant frequencies were higher on the side which was being driven ie on the right in the figure. This effect was due to the application of the common-mode feedback to the particular geometry of the tank and the mechanism giving rise to it is as follows. It was explained in section 3.6 that at any point within the medium of interest, a common mode voltage will be generated which will be dependent upon the position of the point relative to the drive electrodes. Figure 7.3 represents the potential distribution generated by the central drive pair in a homogeneous region and shows that the potentials at point A and B are of different sign (the colour scale is non-linear). By connecting the common mode feedback circuitry between A and B as shown in Figure 7.2, where the signal at A is detected, inverted and used to drive point B, the potential at A is reduced to almost zero (the purpose of common mode feedback). However, in order to achieve this, B has been driven more negative. This reasoning can be applied to all the drives and will increase the amplitude of the dominant potentials closest to the driven point, B. This is one of the reasons why common mode feedback is usually applied out of the plane of interest [10], an option not possible for a pseudo-2D case.

One method of removing the electrode potential mismatches caused by this effect would be to use a separate common mode feedback for each drive. However, this is not practical and instead, two identical common mode feedback circuits were used which were connected to the phantom as shown in Figure 7.4. The measured buffered electrode 'dominant' potentials for this arrangement are shown in Figure 7.5. For each receive electrode on the x-axis, two values are plotted (except for the two end electrodes). The left hand bar corresponds to the 'dominant' frequency amplitude at the lower drive frequency (this drive will be situated to the left of the receive electrode) and the bar on the right corresponds to the dominant frequency amplitude at the higher drive frequency (this drive will be situated to the right of the receive electrode). The mismatch in potentials of the same frequency can be readily observed. There is a reduction in amplitude of the 'dominant' potentials at the centre of the array. Two reasons for this are proposed : The effects of the phantom boundaries and the variation in gain across the frequency range of interest in the common mode feedback circuitry.

Figure 7.6 shows the distortion in current paths and equipotential loci that would occur if a drive pair injecting current into the medium of interest was close to a boundary. This would give rise to an increased potential gradient on the opposite side of the drive pair to the boundary and hence reduce the potential (at the frequency of the drive) on that side.

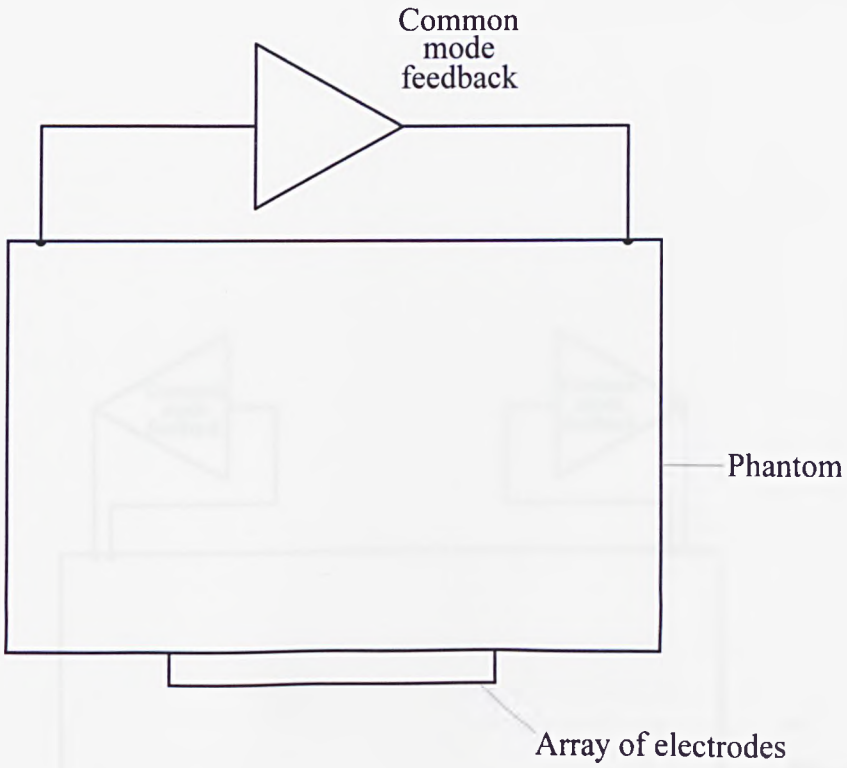

Figure 7.2 : Position of the single common mode feedback circuitry.

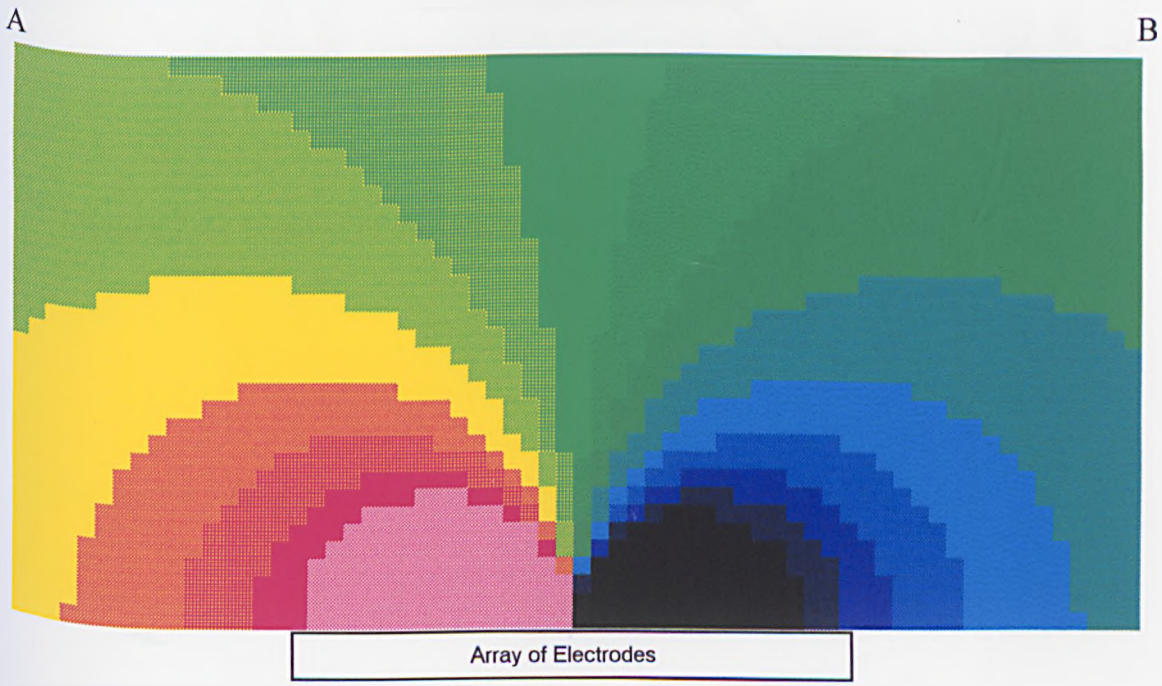

Figure 7.3 : A diagram showing the homogeneous potential distribution in the phantom caused by a central drive pair.

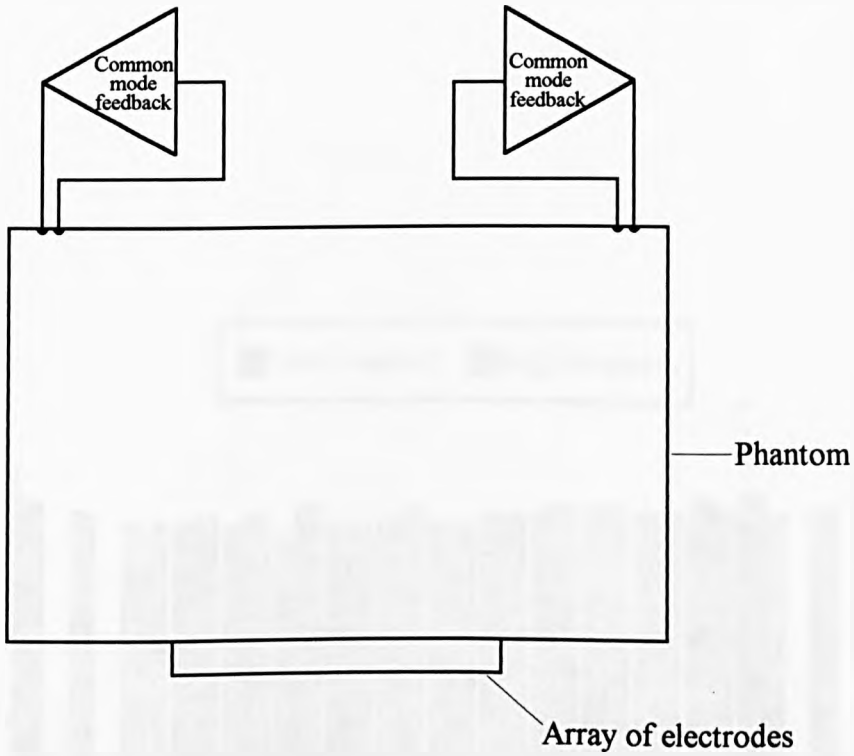

Figure 7.4 : Position of the dual common mode feedback circuits.

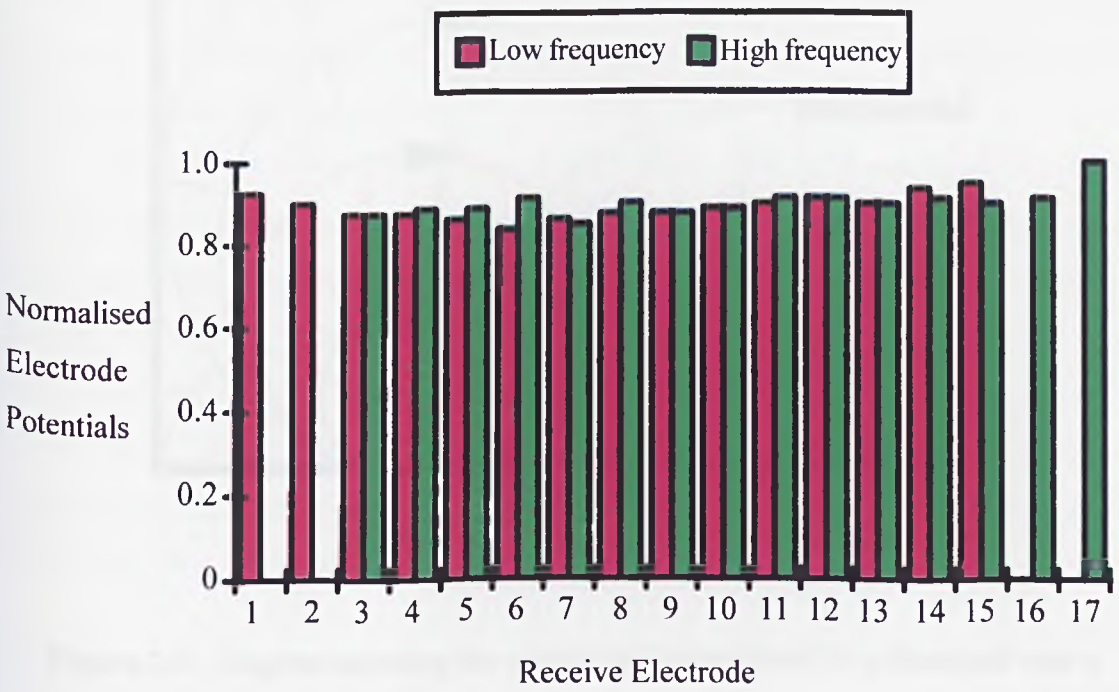

Figure 7.5 : Graph of the measured 'dominant' potentials at the receive electrodes.

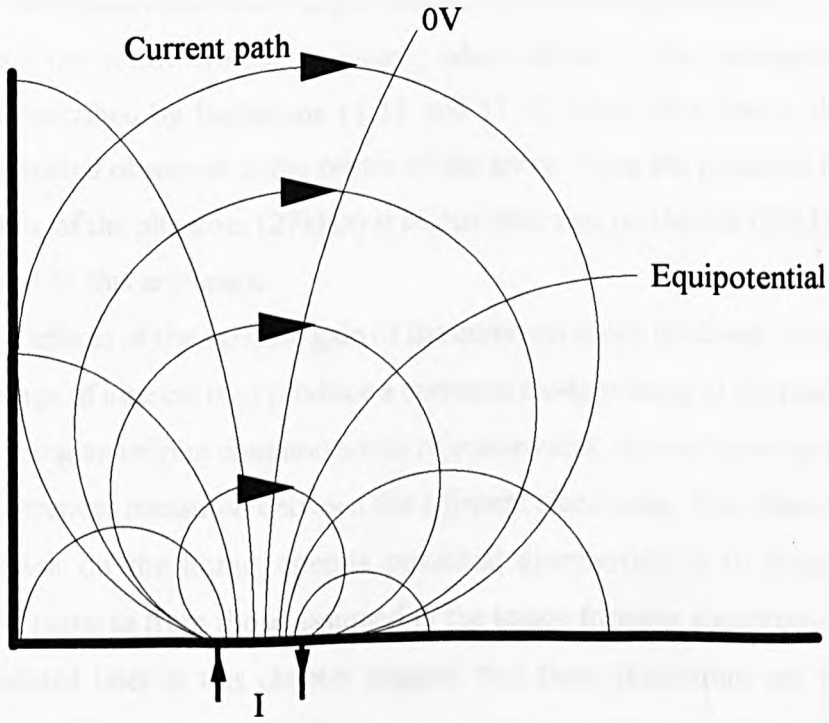

Figure 7.6 : Diagram showing the current path distortions for a drive pair near a boundary.

The solution to the boundary problem is shown in Appendix C, but calculations indicate that the potentials in the centre of the array would be reduced by less than 0.02%, and not by as much as measured.

The circuitry used for the common mode feedback was a bandpass filter which had a gain of 10 at the centre frequency of 22.6kHz. However, the gain at 20kHz is 9.5 and at a frequency of 27kHz the gain is only 8.4. This means that instead of reducing the common mode voltage at all frequencies by 1/11 (from Equation {3.17}) the common mode voltage at 20kHz will only be reduced by a factor of 1/(1+9.5) and at 27kHz by 1/(1+8.4). This would mean that a larger common mode voltage would occur at frequencies furthest from the centre frequency which, when added to the homogeneous potential distribution described by Equations {1.1} and {1.3} could give rise to the reduction in measured potential observed at the centre of the array. Since the potential detected on the right hand side of the phantom (27kHz) is higher than that on the left (20kHz) this appears to give weight to this argument.

The effects of the variable gain of the common mode feedback circuitry across the frequency range of interest is to produce a common mode voltage at the receive electrodes, and so, assuming an infinite common mode rejection ratio, this will have no effect upon the potential differences measured between the adjacent electrodes. The effect of the common mode feedback on the homogeneous potential distribution is to distort slightly the equipotential patterns from those assumed in the image forming algorithms. However, the images presented later in this chapter suggest that these distortions are to such a small degree that their effects are negligible.

7.3 Uniform Reference Set

Images produced from EIT systems are usually images of a difference in conductivity which occurs between two sets of measurements [14]. This difference can be due either to a temporal change in conductivity in a dynamic imaging application, or to a change in conductivity due to the drive frequency being altered if tissue characterisation is being performed [48]. One set of measurements is called the reference set and this is usually subtracted from the second set of measurements, called the data set. In some procedures the ratio of the data set to the reference set is used. These voltage differences are then used in the image forming algorithm. In order to test the performance of an EIT system it is useful to take a set of measurements on a region of homogeneous conductivity (called the uniform reference set) and then to change the conductivity distribution (eg by placing an

object) before taking the second set of measurements (the data set). The normalised magnitude of the uniform reference set for a semi-infinite homogeneous 3D and pseudo-2D region can be calculated using Equations {1.1} and {1.3}. The table in Figure 7.7 shows the values of normalised voltage differences calculated for pseudo-2D and 3D regions using these equations and also, for comparison, the measured normalised voltage differences for the leftmost drive pair on the pseudo-2D phantom of depth 20mm, and on the 3D phantom. The same data is shown graphically in Figure 7.8. It can be seen that the measured pseudo-2D values lie between the predicted pseudo-2D and 3D values. It appears that in predicting the measured pseudo-2D potential differences the uniformity of current paths in the z-direction cannot be assumed, and that the actual behaviour is somewhere between the ideal 2D and 3D cases. The differences between the predicted values and the measured values are up to 23% for the pseudo-2D case and are up to 8.5% for the 3D case for distances of less than half the array length from the drive. As explained in section 2.5.1, measurements at further distances from the array have a low signal-to-noise ratio and so have not been considered here.

The variations in the measured potential differences occur at all the drives as can be seen in Figure 7.9 which shows a plot of the potential difference against receive pair. Each plot represents one drive pair (and therefore frequency) and the position of the drive pair is indicated on each graph by small vertical lines on the x-axis. The peak value corresponds to the maximum potential difference measured at any frequency at any receive pair and is given in units of 0.032mV at the receive electrodes. 'Max' and 'min' are the maximum and minimum potential differences which occur in each plot, in units of 0.032mV.

The mismatch in amplitude of the potential differences on either side of the drive pairs occurs repeatably on most of the plots in Figure 7.9, implying that the error is systematic. The largest mismatch is 38mV (in an average amplitude of 260mV) which occurs on the last drive.

A possible cause of these errors is mismatches between the contact impedances at the drive electrodes. If the two drive electrodes which constitute a drive pair have unequal areas of contact with the medium of interest, the current density at each electrode would be unequal. This would give rise to an electric field that was asymmetric about the midpoint between the drive electrodes and hence an asymmetric potential gradient. This could produce unequal potential differences on either side of the drive pair.

On close inspection it was found that the electrodes in the array penetrated the wall of the phantom by varying depths (between 0.3mm and 0.7mm) rather than the 0.5mm

Receive Pair	Predicted Normalised Potential Differences for 2D	Measured Normalised Potential Differences for 2D	Predicted Normalised Potential Differences for 3D	Measured Normalised Potential Differences for 3D
1	-1.0000	-0.9942	-1.0000	-0.9790
2	-1.0000	-1.0000	-1.0000	-1.0000
3	0.5350	0.5695	0.8000	0.8679
4	0.1587	0.1421	0.1143	0.01141
5	0.0775	0.0672	0.0381	0.0380
6	0.0461	0.0405	0.0173	0.0182
7	0.0306	0.0261	0.0093	0.0090
8	0.0218	0.0175	0.0056	0.0059
9	0.0163	0.0136	0.0036	0.0037
10	0.0127	0.0098	0.0025	0.0021
11	0.0101	0.0078	0.0018	0.0014
12	0.0083	0.0064	0.0013	0.0012
13	0.0069	0.0058	0.0010	0.0014
14	0.0058	0.0046	0.0007	0.0011
15	0.0050	0.0037	0.0006	0.0011
16	0.0043	0.0036	0.0005	0.0008

Figure 7.7 : Table showing the calculated and measured voltage differences for pseudo-2D and 3D homogeneous regions for a drive current between drive electrodes 1 and 2.

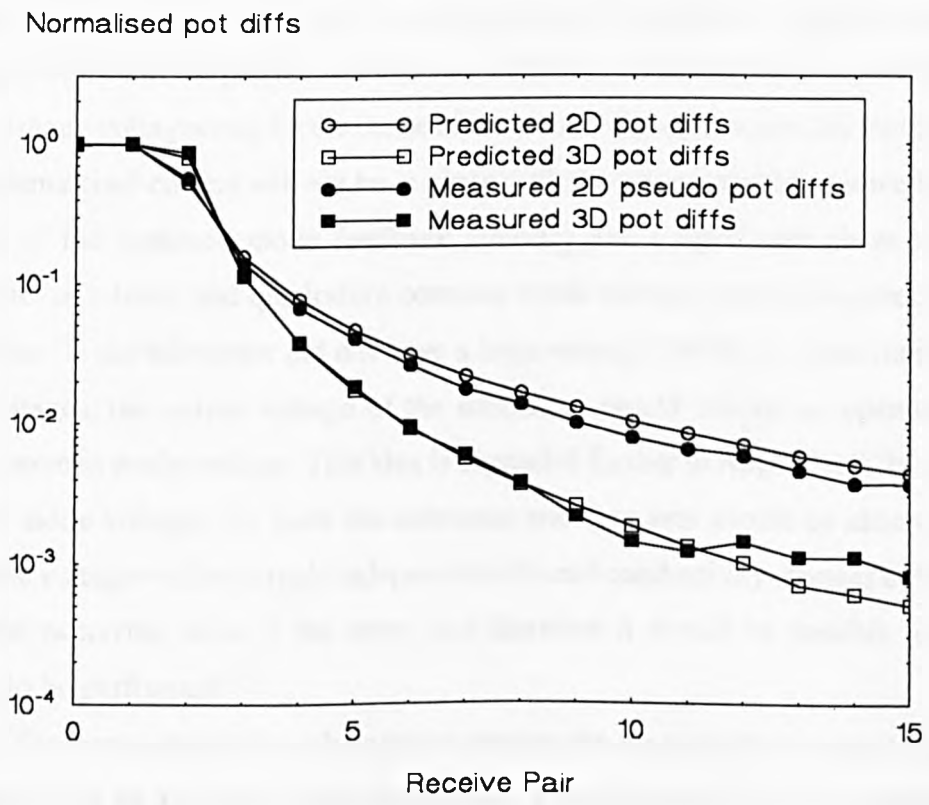

Figure 7.8 : A graph showing the measured and predicted normalised potential differences on a homogeneous phantom for 2D and 3D for a drive between drive electrodes 1 and 2.

specified. Despite these variations, no correlation could be found between the depth of penetration and the potential difference mismatches and so it is likely that there is another effect giving rise to the mismatches in the potential differences in the uniform reference set.

The potential differences plotted in Figure 7.9 represent the amplitude of the signal at a receive pair. When the phase shift through the system had been accounted for (eg the phase shift through the anti-alias filters), it was found that the signals still had a significant phase shift between them and the drive waveforms. Phase shifts of approximately 0° or 180° were expected. No pattern to the phase shifts was observed, but it is possible that the common mode voltages may be the cause of the errors. The common mode voltages caused by the mismatched current will not be in phase with the drive waveforms since the transfer function of the common mode feedback circuitry has a significant phase shift at the frequencies of interest and quadrature common mode voltages were also generated by the mismatches. If the subtractor did not have a large enough CMRR to reject these common mode voltages, the output voltage of the subtractor would contain an attenuated phase shifted common mode voltage. This idea is expanded further in Appendix L. However, the common mode voltages for both the reference and data sets should be almost identical, since these voltages will be largely independent of small conductivity changes in the medium of interest occurring close to the array, and therefore it should be possible for dynamic imaging to be performed.

The errors are sufficiently large to prevent the production of a static image using a measured data set and calculated reference set. If the electrode array were machined to a closer tolerance and the common mode voltages compensated for, static imaging may be possible using a linear array, although it is also possible that other systematic problems would exist.

7.4 Profiles of Measured Voltage Differences

As stated in section 6.2.3, the data used in the image forming algorithm is the fractional potential difference, $(V_{data} - V_{ref})/ V_{ref}$, where V_{data} are the measured potential differences (between adjacent receive electrodes) in the data set and V_{ref} are the measured potential differences (between adjacent receive electrodes) in the reference set. $(V_{data} - V_{ref})$ contains all the information about the change in conductivity between the two sets of measurements and as such can be used to make inferences about the conductivity distribution. Plots of $(V_{data} - V_{ref})$ against receive electrode pair, for a given drive pair, are referred to subsequently as profiles. There are 15 such profiles in a measurement set, one for each of

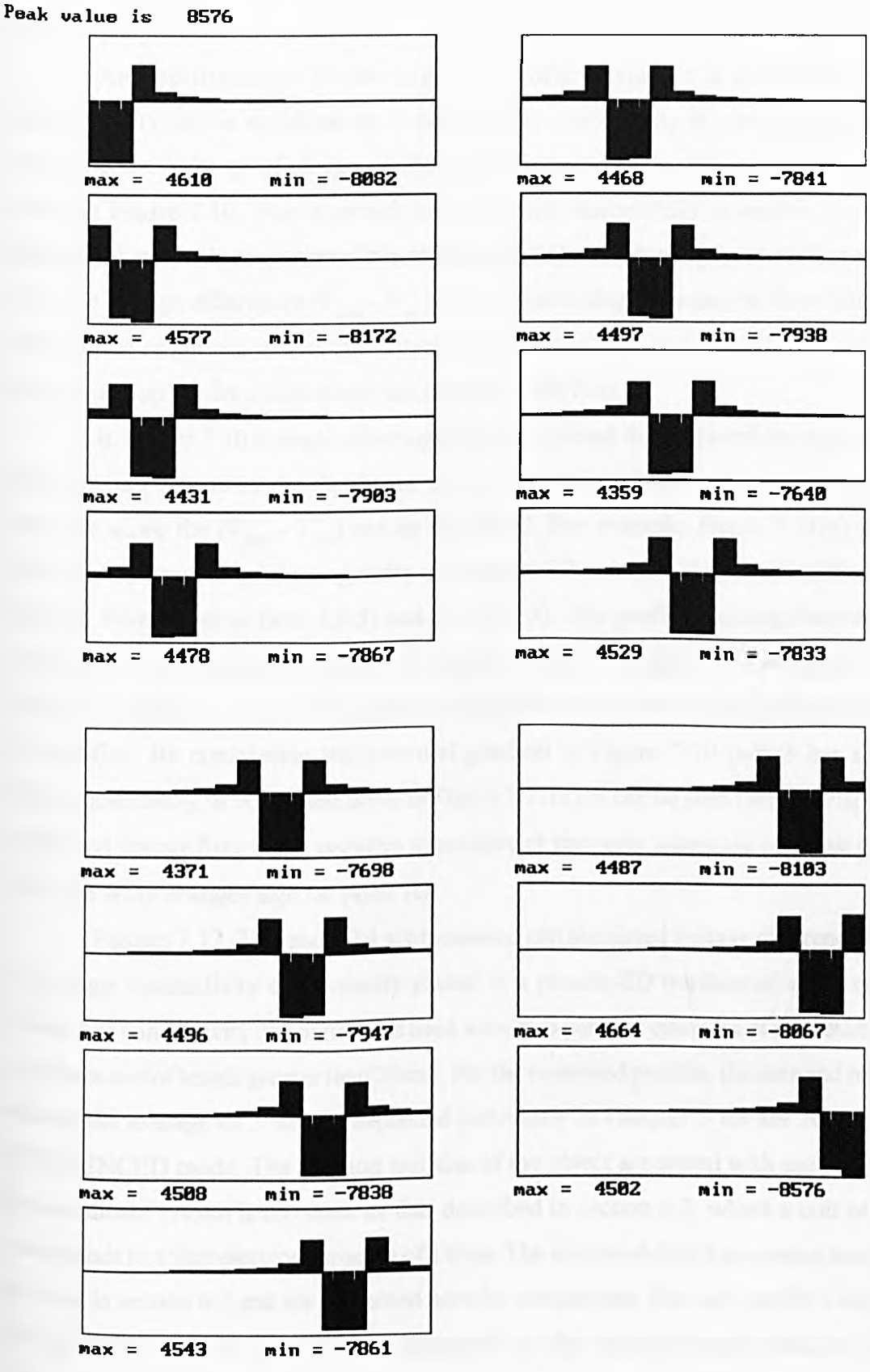

Figure 7.9 : Measured potential differences for a homogeneous region of saline solution of σ=0.2Sm^{-1} and depth 20mm. The 'peak value' is the maximum potential difference in any plot and 'max' and 'min' are the maximum and minimum value in each plot. One unit corresponds to a potential difference at the receive electrodes of 0.032mV.

the drive frequencies.

An approximation to the expected profile shape for a single conductivity inhomogeneity can be explained by thinking of the conductivity discontinuity as a dipole caused by the build up of charge on the interface between the saline and the object, as shown in Figure 7.10. This approach has been used successfully to explain the profiles obtained for small inhomogeneities in both injected [84] and induced [2] current EIT systems. Since the voltage differences (V_{data} - V_{ref}) are not due to any extra current flow (there is no extra source of current within the system) the voltage differences must be caused by the charge build up on the conductivity discontinuity interface.

In Figure 7.10 a single inhomogeneity is depicted in a semi-infinite medium. The equipotentials caused by the dipole are shown, and by considering the potential gradient along the array, the (V_{data} - V_{ref}) can be calculated. For example, Figure 7.11(a) shows a single circular insulating inhomogeneity of diameter 1.3 units and shows two of the profiles resulting from drives at (x=5.5,6.5) and (x=7.5,8.5). The profile resulting from the drive whose midpoint has the same x value as the object is always the largest [84] and approximately symmetrical (Figure 7.11(c)). Thus, from the profiles, the x position of the object can easily be identified. By considering the potential gradient in Figure 7.10 (which has a similar relative positioning of object and drive as Figure 7.11(a), it can be seen that the shape of the profile will change from being negative to positive at the point where the potential gradient along the array changes sign (at point A).

Figures 7.12, 7.13 and 7.14 are measured and simulated voltage difference profiles for a single conductivity discontinuity placed in a pseudo-2D medium of saline of depth 20mm. The conductivity discontinuities used were two perspex cylinders of diameters 13mm and 19mm and of length greater than 20mm. For the measured profiles, the data and reference sets are the average of 3 sets as explained previously in Chapter 5 for the AVERAGED REFERENCED mode. The position and size of the object are stated with each figure and the coordinate system is the same as that described in section 6.3, where a unit of length corresponds to a 'like' electrode spacing of 15mm. The simulated data is generated analytically as stated in section 6.3 and are presented here for comparison. For each profile a maximum and minimum value is given. This corresponds to the maximum and minimum voltage difference between adjacent electrodes in that profile. All the numerical figures given are normalised to the maximum potential difference in the reference set.

The measured profiles in Figure 7.12 and 7.13 closely resemble the simulated profiles, but the measured normalised potential differences are smaller than the simulated

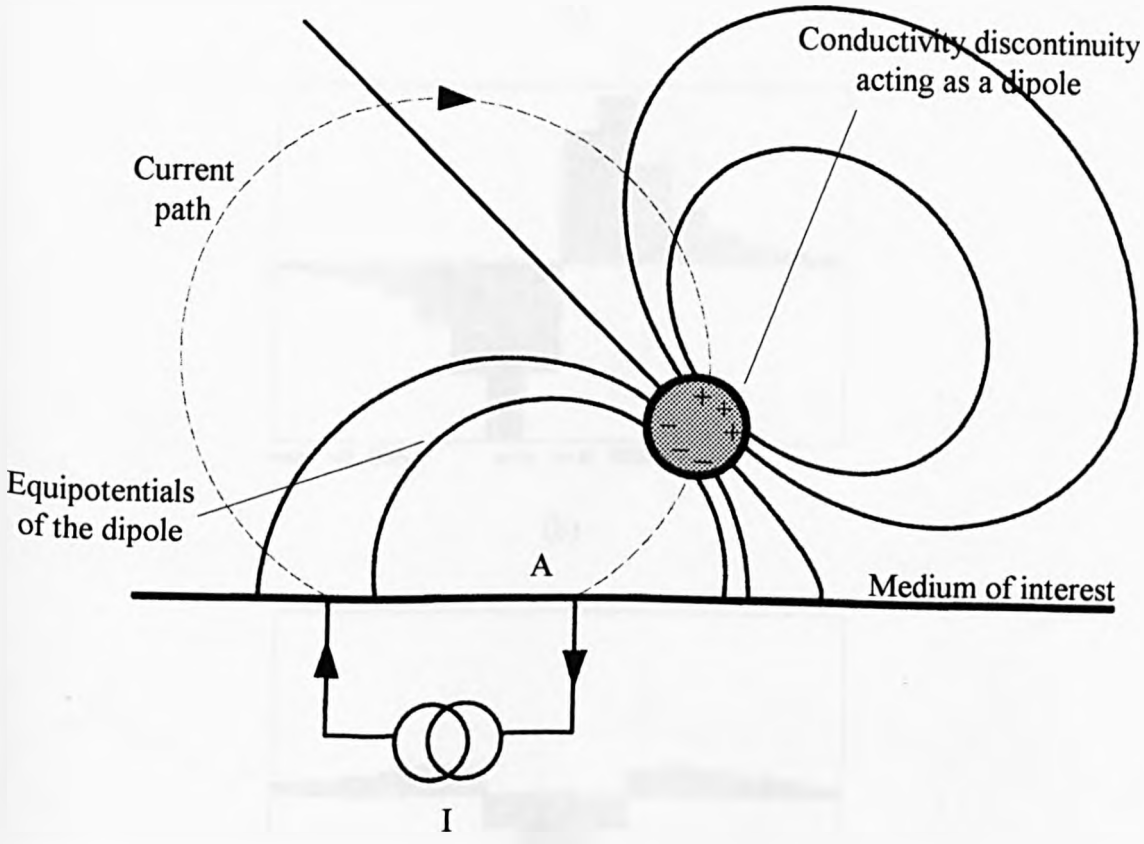

Figure 7.10 : Diagram showing the dipole associated with a conductivity discontinuity for a single drive pair and the resultant potentials.

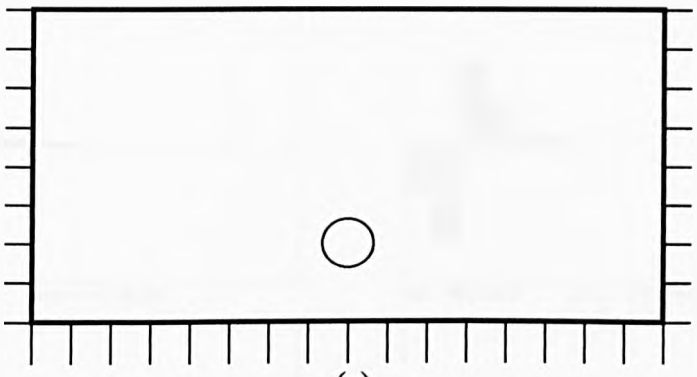

(a)

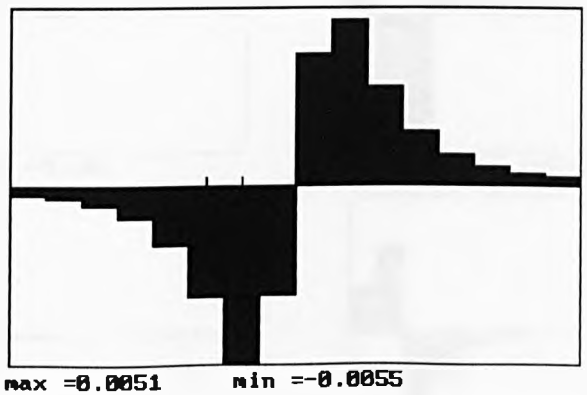

(b)

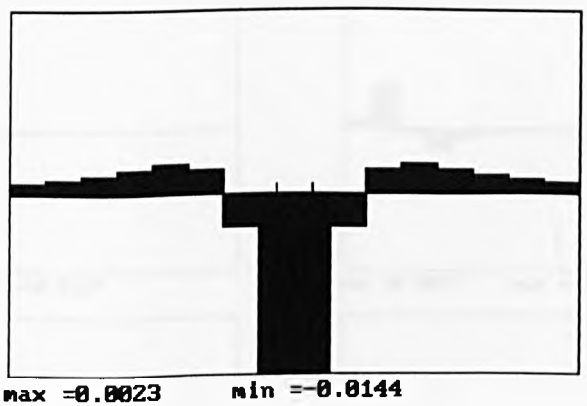

(c)

Figure 7.11 : Two potential difference profiles for a single conductivity inhomogeneity.

(a) The object distribution

(b) The profile of the calculated voltage differences caused by a drive between (x=5.5, 6.5)

(c) The profile of the calculated voltage differences caused by a drive between (x=7.5, 8.5)

The values are normalised to the maximum potential difference in the uniform reference set.

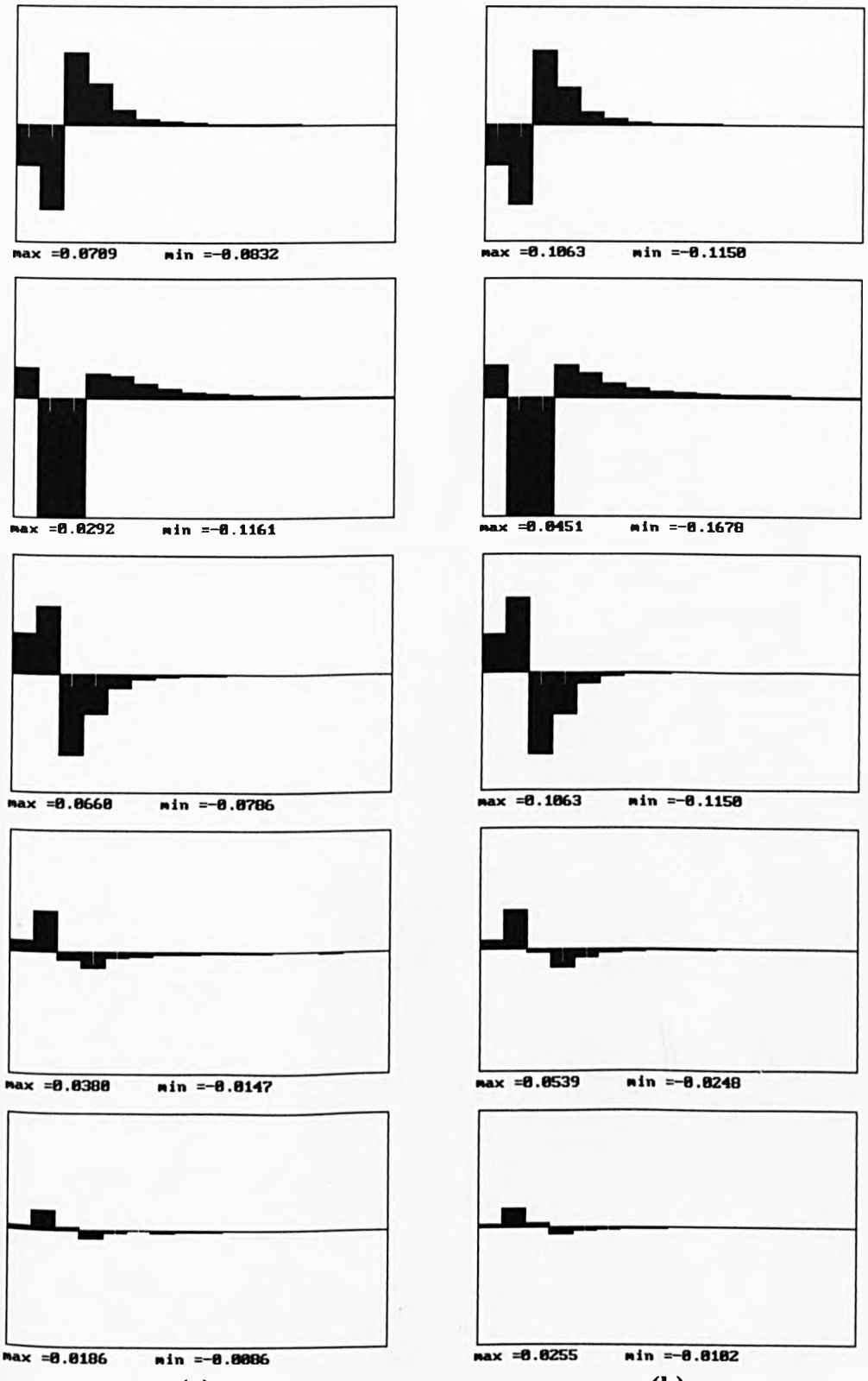

Figure 7.12 : Profiles of Voltage Differences for a circular object.

(a) Profiles of measured data. (Max $\Delta V = 29.9$mV at the receive electrodes).

(b) Profiles of simulated data.

The object is a perspex cylinder (σ=0) of radius 0.433 units ('like' electrode spacings) at (2,1) in a background saline solution of σ=0.2Sm^{-1} and depth 20mm. The values 'max' and 'min' indicate the maximum and minimum potential difference in each profile normalised to the maximum potential difference in the uniform reference set. **(Figure continued on next two pages)**

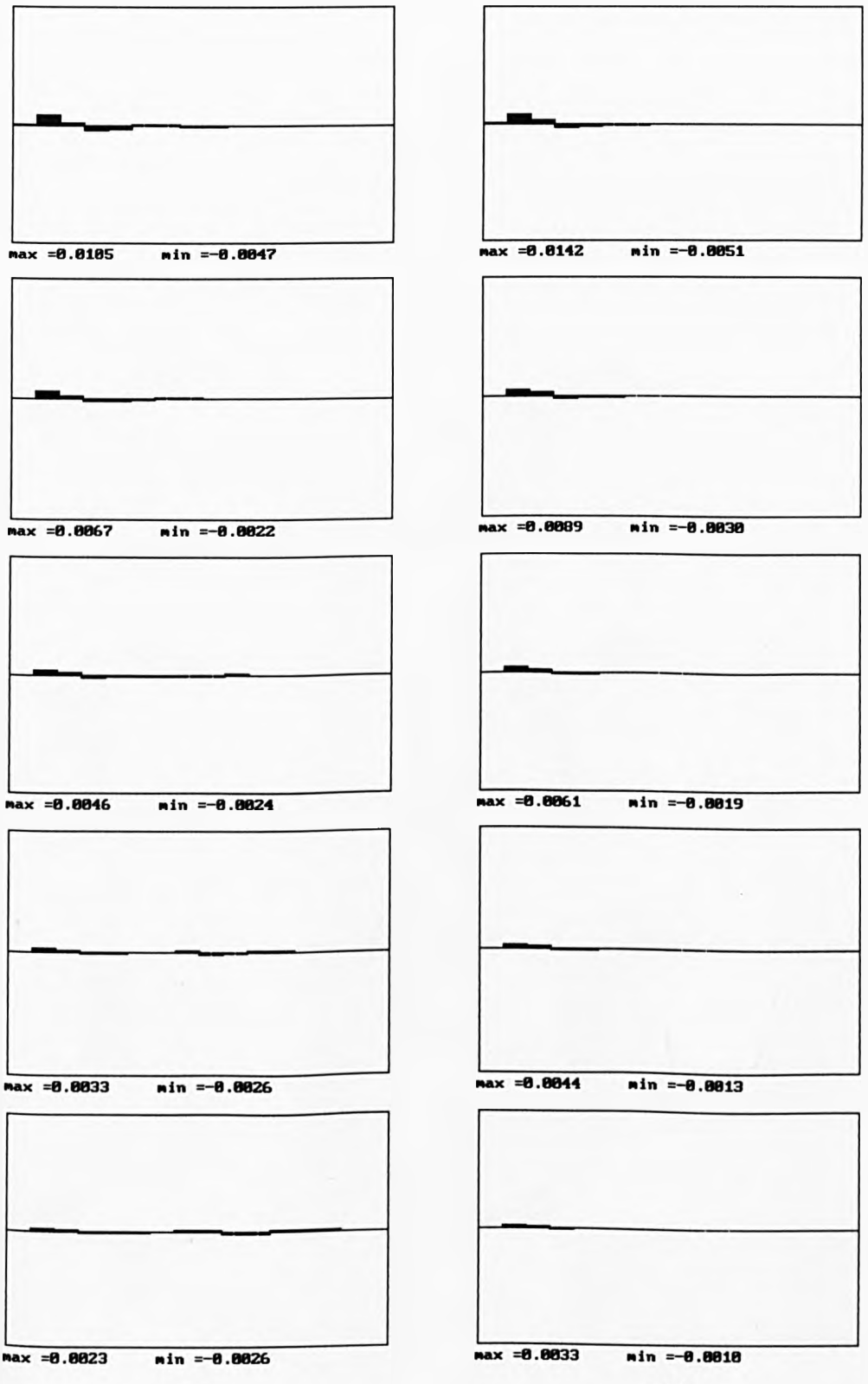

Figure 7.12 continued

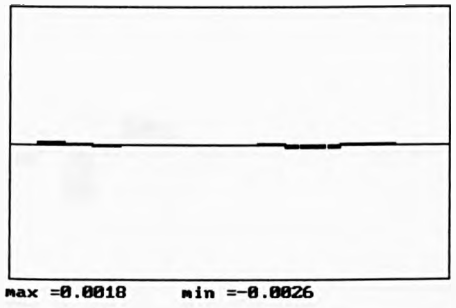

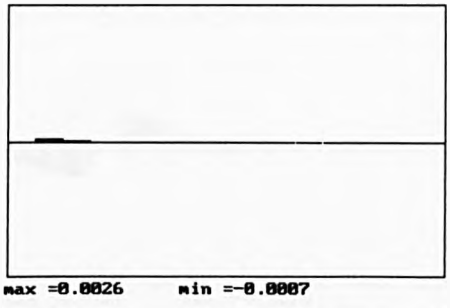

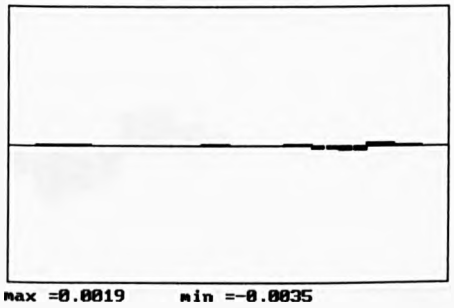

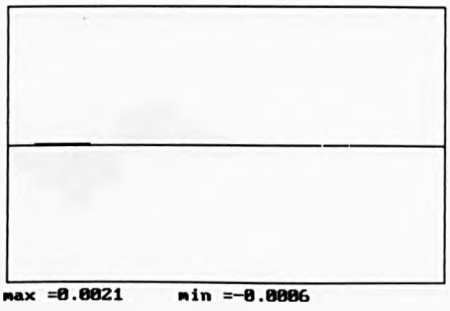

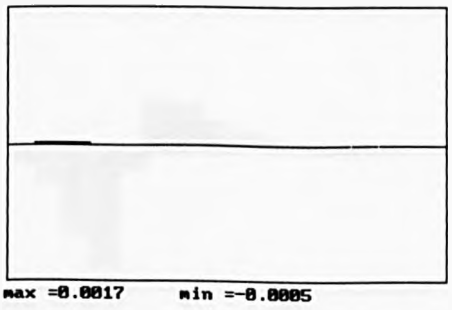

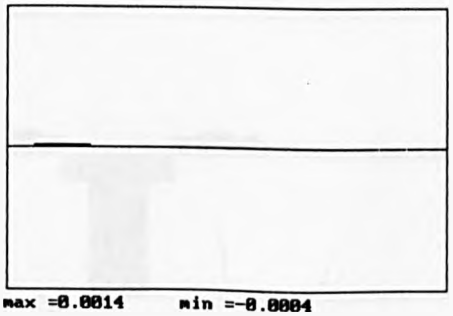

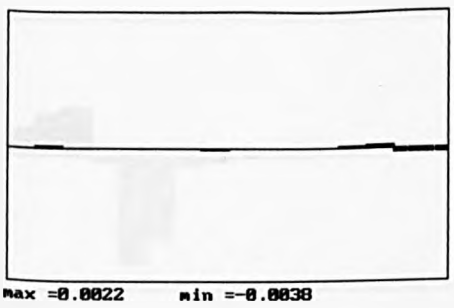

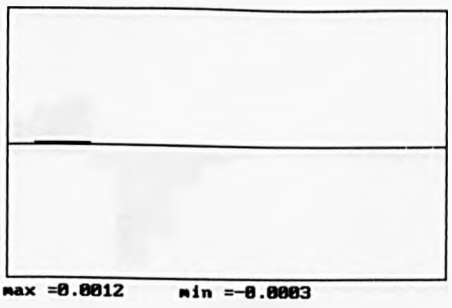

(a) **(b)**

Figure 7.12 continued

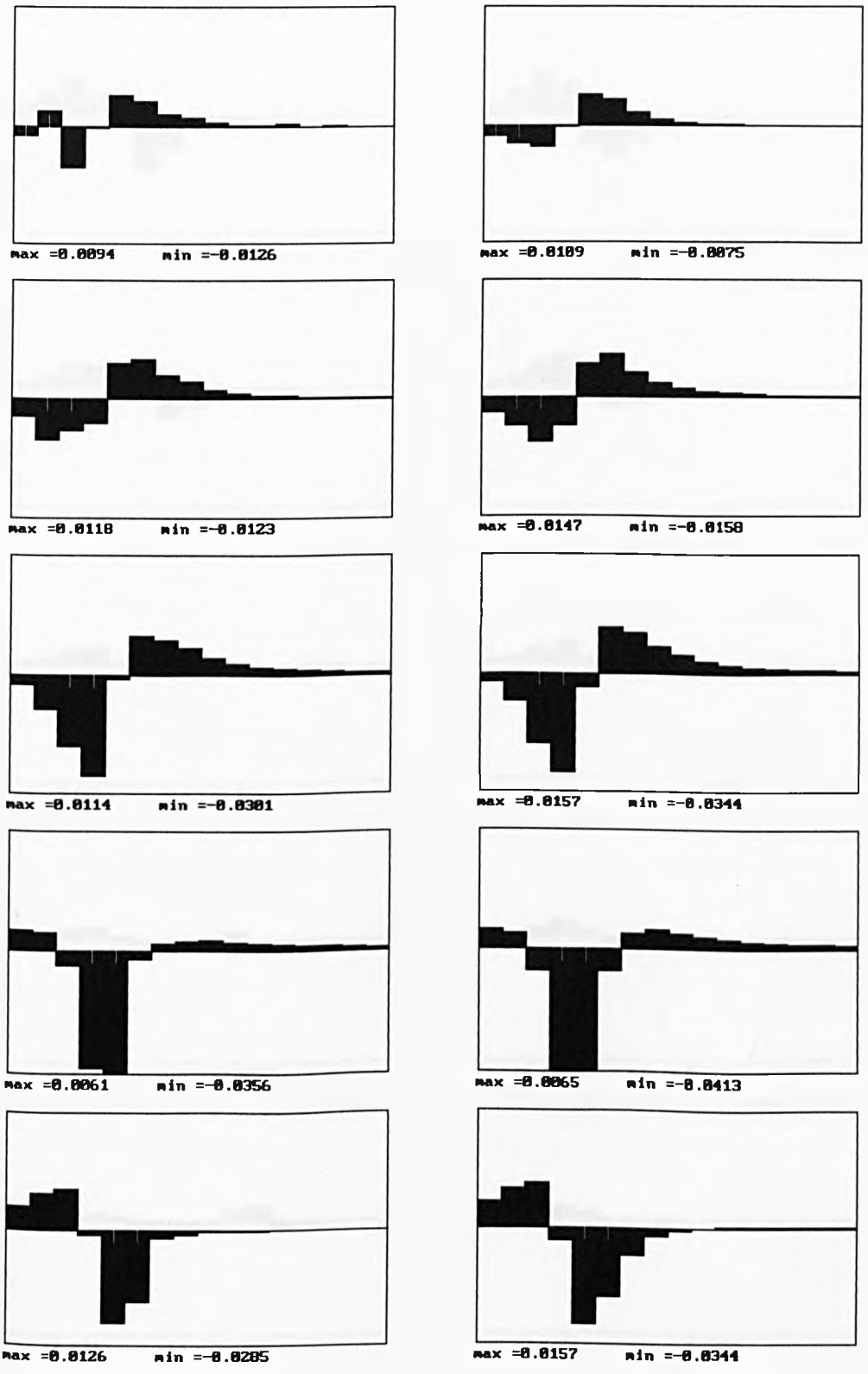

(a) **(b)**

Figure 7.13 : Profiles of Voltage Differences for a circular object.

(a) Profiles of measured data. (Max $\Delta V = 9.3$mV at the receive electrodes).

(b) Profiles of simulated data.

The object is a perspex cylinder (σ=0) of radius 0.633 units ('like' electrode spacings) at (4,2) in a background saline solution of σ=0.2Sm^{-1} and depth 20mm. The values 'max' and 'min' indicate the maximum and minimum potential difference in each profile normalised to the maximum potential difference in the uniform reference set. **(Figure continued on next two pages)**

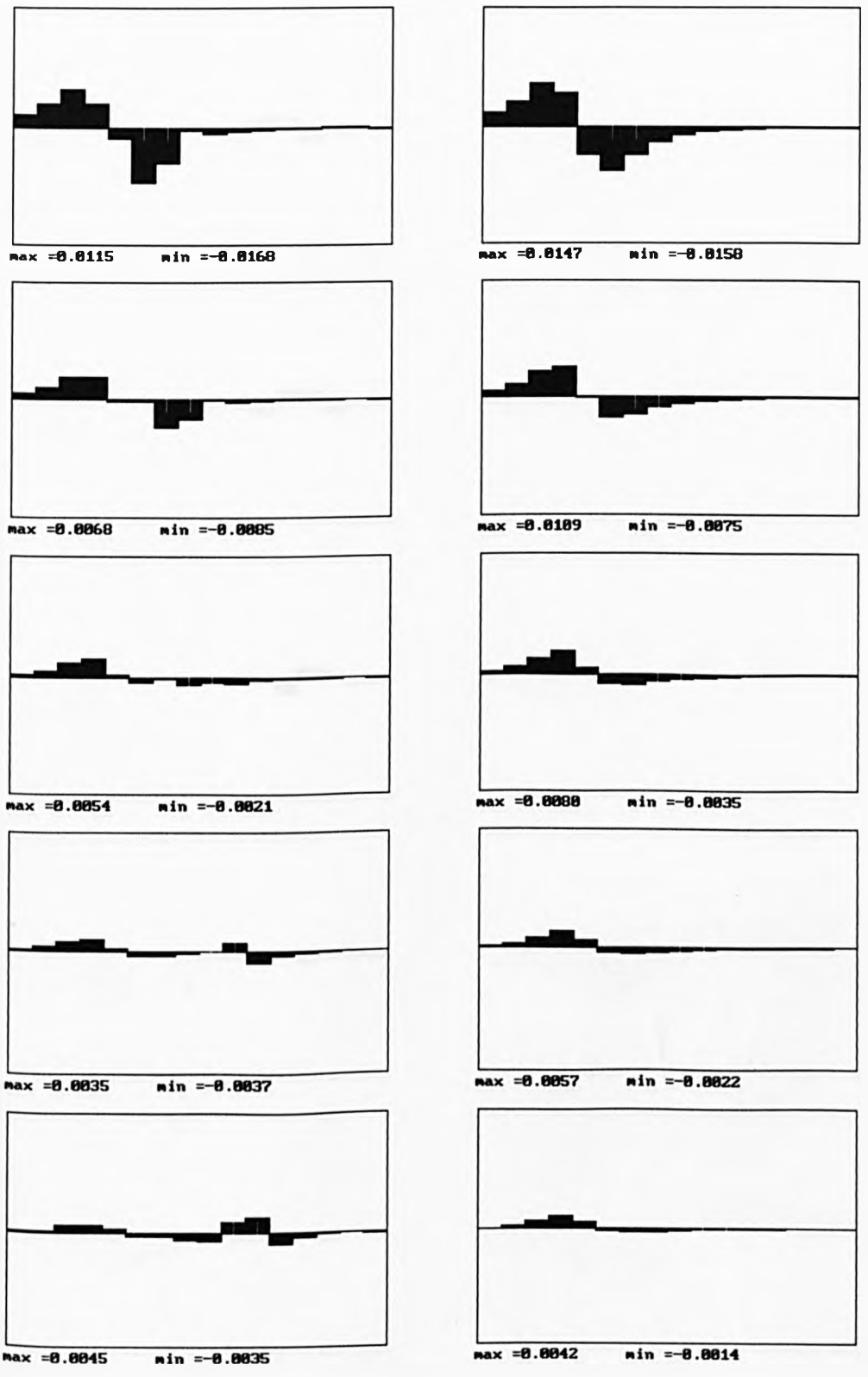

Figure 7.13 continued

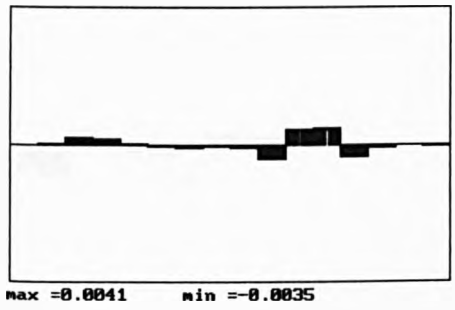

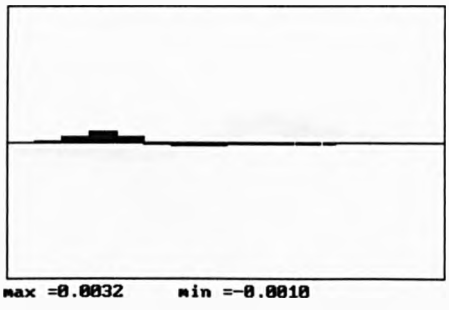

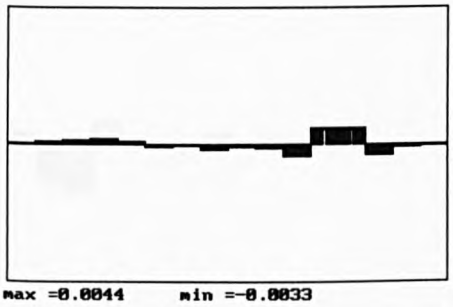

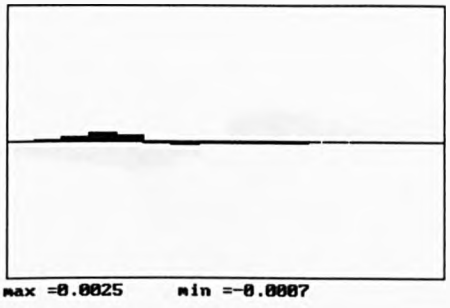

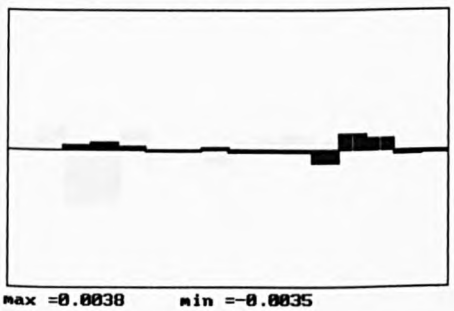

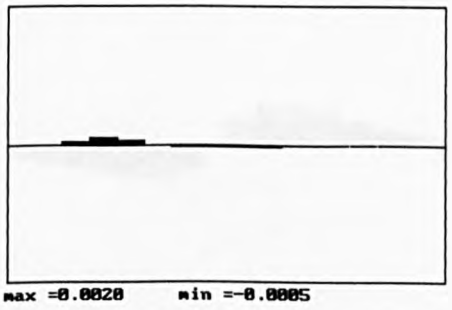

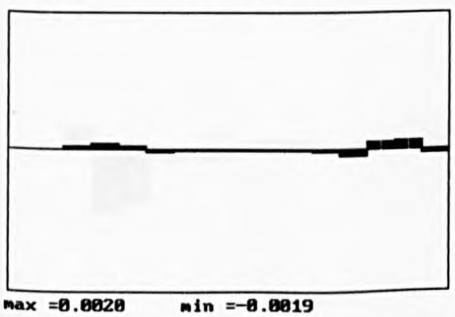

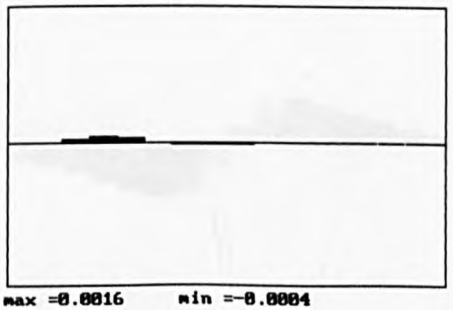

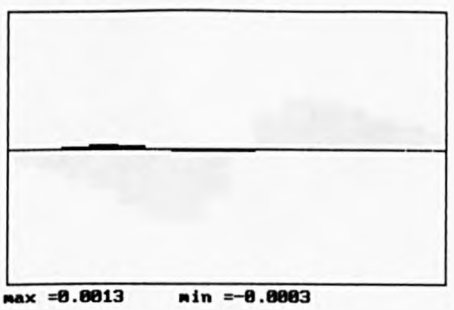

(a) **(b)**

Figure 7.13 continued

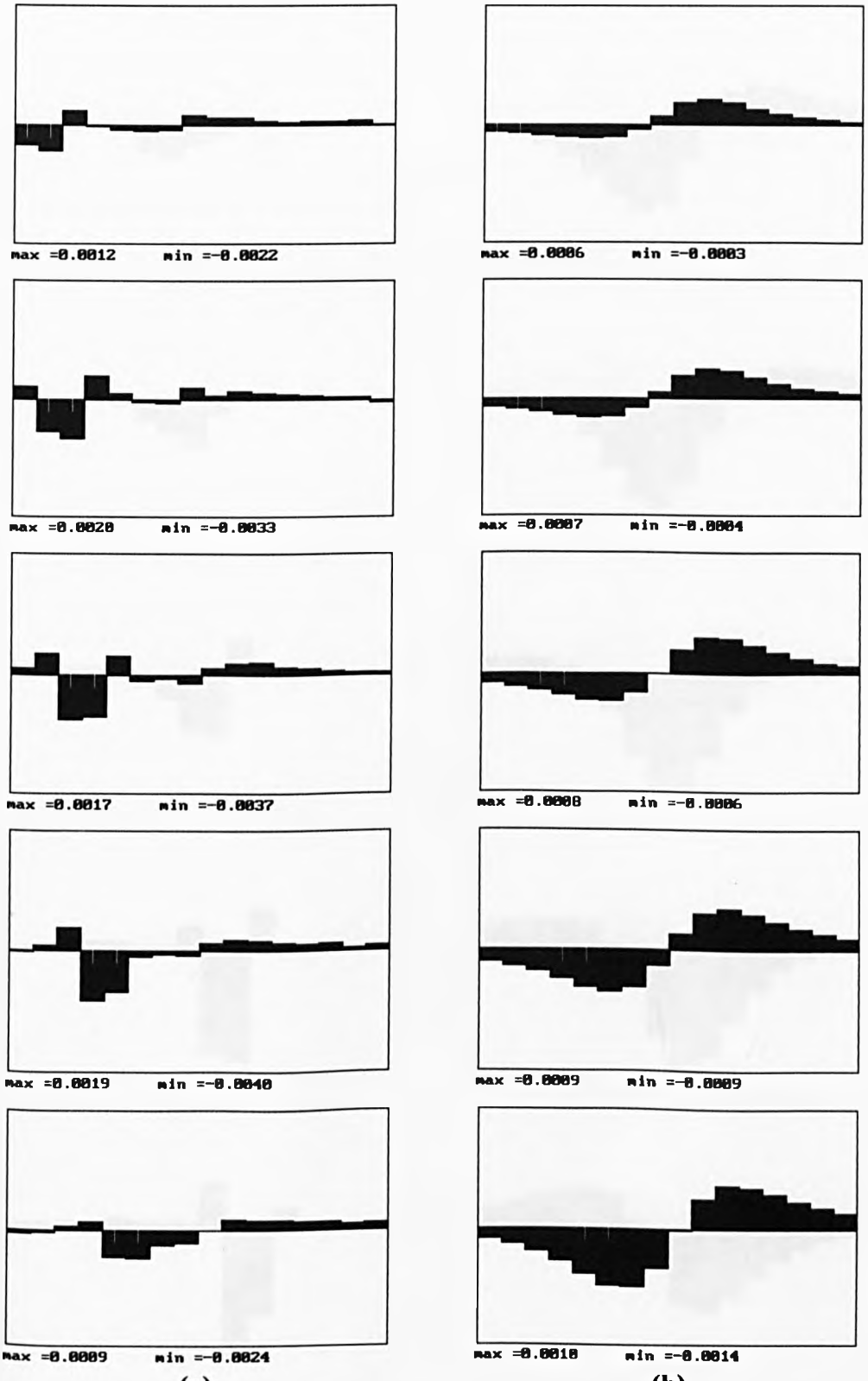

Figure 7.14 : Profiles of Voltage Differences for a circular object.

(a) Profiles of measured data. (Max $\Delta V = 2.6$mV at the receive electrodes).

(b) Profiles of simulated data.

The object is a perspex cylinder (σ=0) of radius 0.633 units ('like' electrode spacings) at (8,4) in a background saline solution of σ=0.2Sm^{-1} and depth 20mm. The values 'max' and 'min' indicate the maximum and minimum potential difference in each profile normalised to the maximum potential difference in the uniform reference set. **(Figure continued on next two pages)**

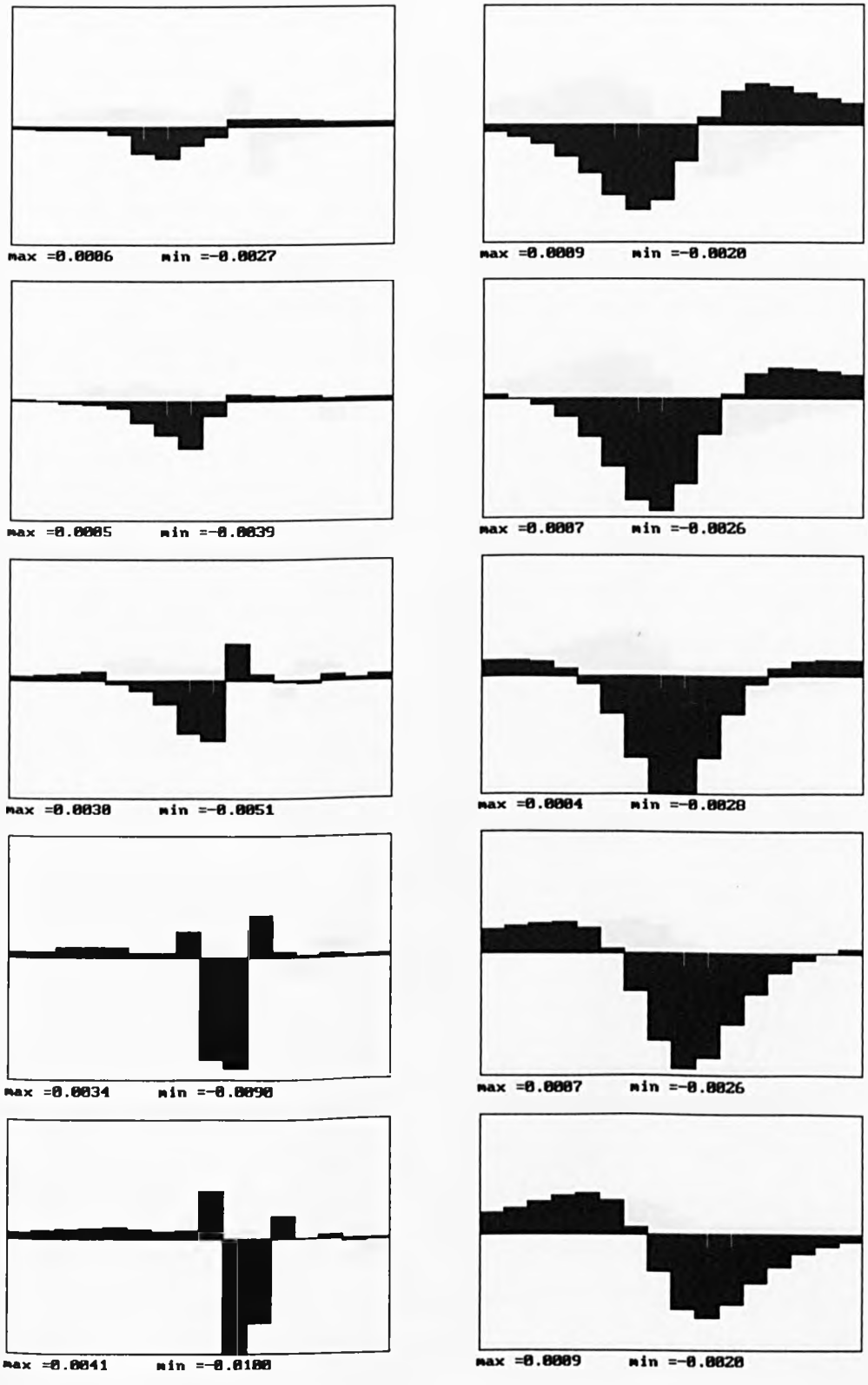

(a) **(b)**

Figure 7.14 continued

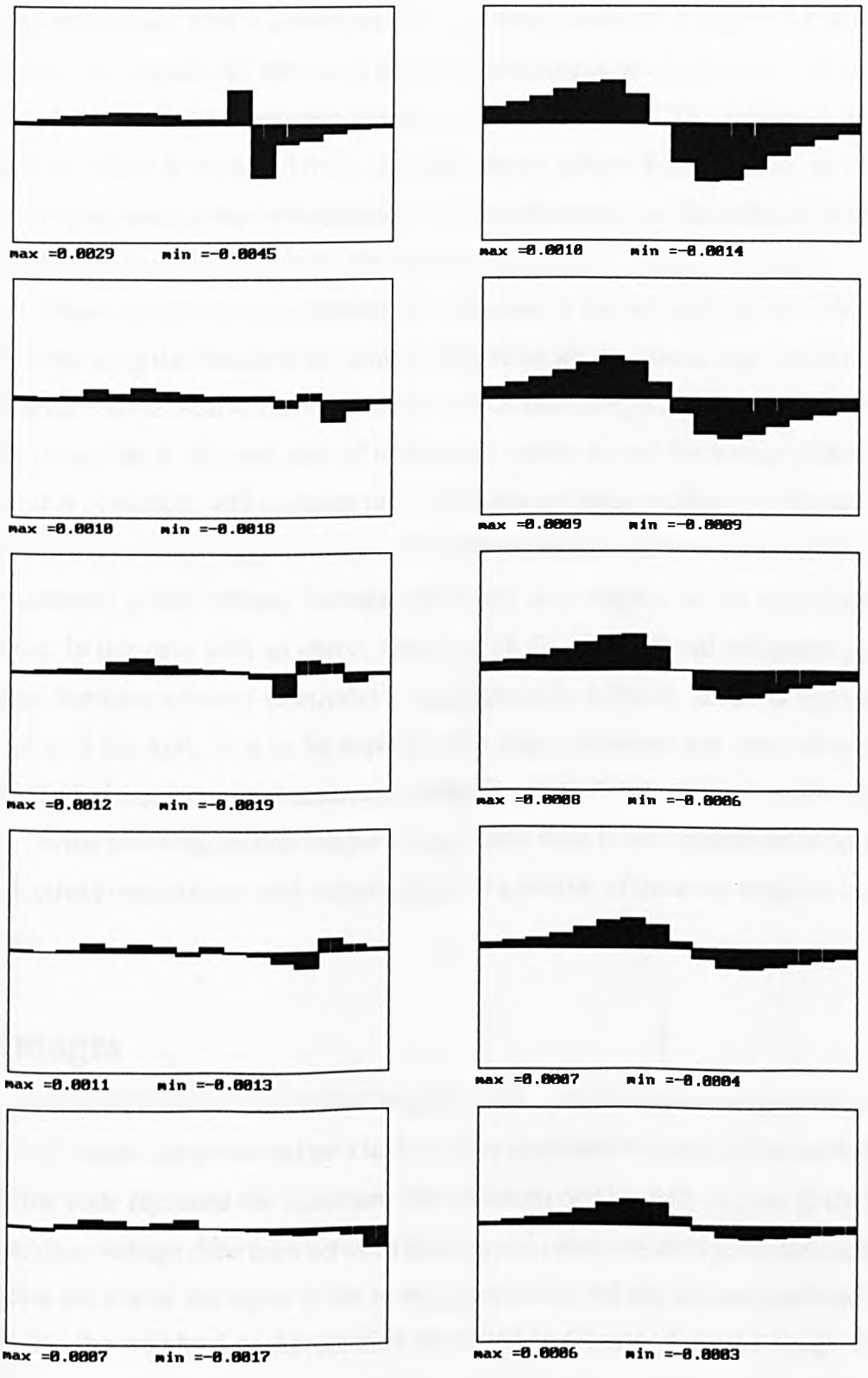

Figure 7.14 continued

potential differences. This is consistent with the data presented in Figure 7.8 where it is shown that the pseudo-2D measured potential differences are lower than 2D predicted values and lie somewhere between the ideal 2D and 3D case. The measured profile in Figure 7.14, which is produced from an object placed further from the array than for the other two cases, bears a small resemblance to the simulated profile. Apart from the potential differences near the drive electrode, the profiles are similar to those predicted.

There appears to be a coherent error at some of the drive electrodes. This can be seen by comparing the measured and simulated profiles for the second and third drive pairs. The potentials at the receive electrodes either side of the drive pair are larger than predicted and the potentials at the next pair of receive electrodes are of the wrong polarity. This behaviour is consistent with common mode voltages not being sufficiently rejected by the subtraction stage, which suggests that common mode voltages will limit the depth of imaging as the common mode voltages become significant with respect to the expected profile amplitude. In this case with an object located at (8,4), the predicted maximum potential difference between adjacent electrodes is approximately 0.26mV, which is equivalent to 1LSB of a 13 bit ADC. It is to be expected that noise (coherent and non-coherent) will become the limiting factor in measurement integrity at this level of signal amplitude.

In the following section images are generated from measurements made on a range of conductivity distributions with objects placed at a quarter of the array length or less from the array.

7.5 Images

Images produced from measurements made on the phantom are presented in this section. All images are presented on a linear colour scale which is normalised such that the ends of the scale represent the maximum and minimum conductivity regions in the image. The maximum voltage difference between the data and reference set is given for each figure to indicate the size of the signal at the receive electrodes. All the images produced in this chapter use the weighted backprojection described in Chapter 6 as the image forming algorithm. Images are formed both by WBP1 and WBP2. It was explained in section 6.2.3 that noise on a small signal could cause problems in image formation since it would cause a relatively large change in fractional voltage difference $(V_{data}-V_{ref})/V_{ref}$ and hence would be associated with a similarly large percentage change in conductivity of the image. To overcome this problem a threshold has been applied to the data used to generate the WBP1 images before image forming so that voltage differences below the threshold value are ignored in

the formation of the image. This is only necessary in the WBP1 method since the WBP2 method is biassed towards discontinuities close to the array which cause easily detectable voltage differences between the data and reference sets. The threshold value used with WBP1 is given for each figure.

Unless otherwise stated, all single, ie non sequenced, images are produced using measurements made in AVERAGED REFERENCED mode, where the average of 3 reference and data sets are used as described in Chapter 5 .

The conductivity distributions to be imaged were chosen to demonstrate the performance of the system and the images presented here are not evaluated by a strict criterion but are judged subjectively.

7.5.1 Single Object Images

Figures 7.15 to 7.19 show unfiltered images produced from analytic and measured data for different object positions in a pseudo-2D medium of depth 20mm. The information relating to the conductivity distributions is given in the captions of the figures. Figures 7.15 to 7.17 show three of the cases used in the previous chapter for evaluation of the filters. These object positions were chosen to demonstrate images produced for non central objects close to the array (Figure 7.15), objects centrally placed in the area of detection (Figure 7.17) and objects in an intermediate position (Figure 7.16).

The images produced from measured data in Figure 7.15(d) and (e) are almost indistinguishable from those images produced from the analytically generated data in (b) and (c). The only discernible difference is the slight reduction in equipotential blurring in (d) in comparison with (b). The 'tail' of the object is created by backprojection along an equipotential from one end of the array to the other, ie when the drive pair and receive pair are at opposite ends of the array. The potential difference measured for this situation is very small and so is likely to be below the threshold value applied to the data and consequently is excluded from the image (d). Figure 7.16 is a similar case where the equipotential 'tail' in the measured WBP1 case is reduced due to the thresholding, and the WBP2 is almost exactly the same as the analytic case.

Figure 7.17 shows the case where the object has been placed at the centre of the area of detection. The profiles for the measured and analytically generated data are shown in Figure 7.14. It can be seen that the positions of the large voltage differences in the measured profile and simulated profile occur at the same receive electrode positions, but the measured profile does not have the smooth shape that is characteristic of the simulated

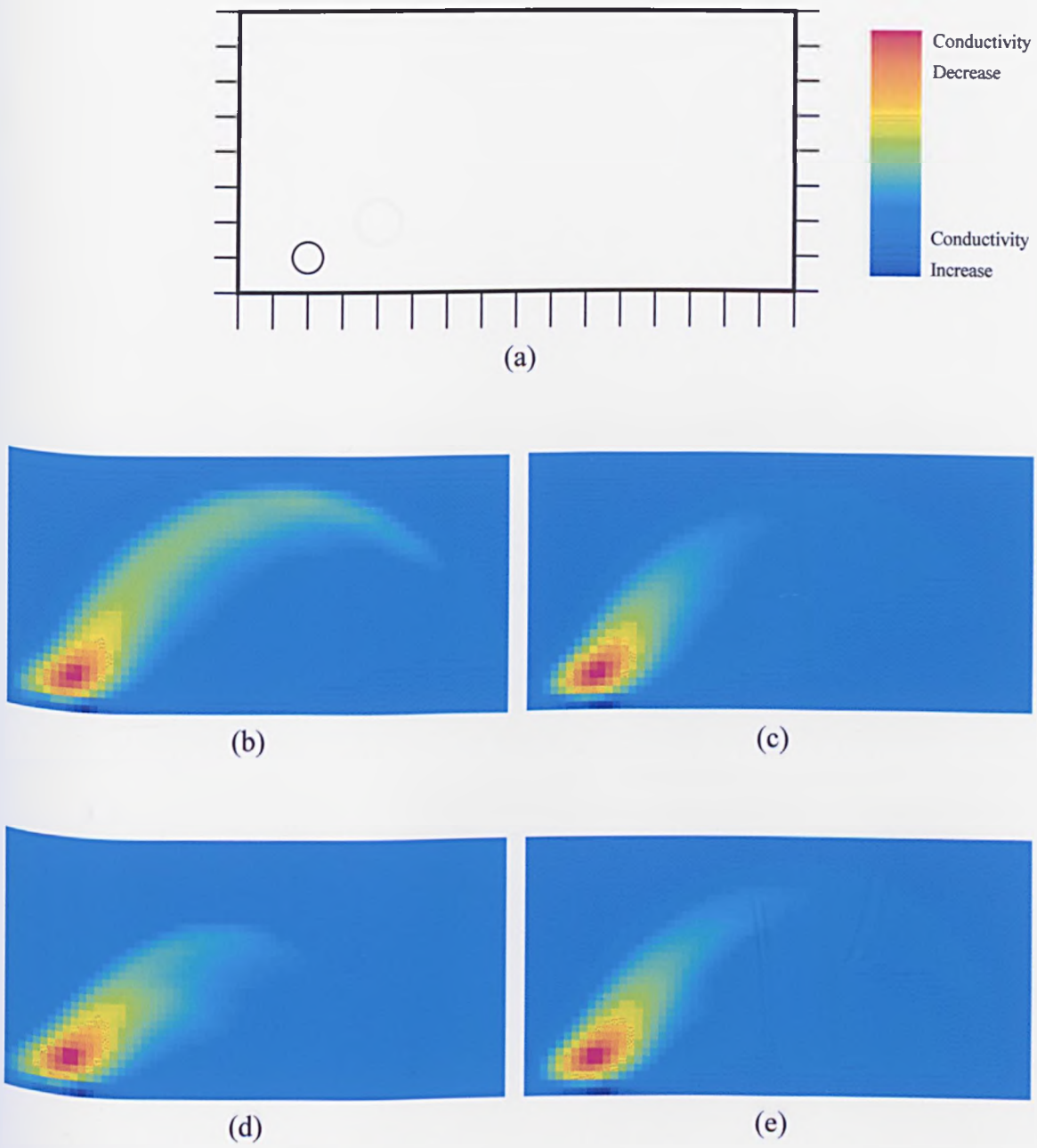

Figure 7.15 : Images produced for a single object located at (2,1) in a pseudo-2D phantom.

(a) The conductivity distribution. The object is a perspex cylinder of radius 0.433units and $\sigma=0$ in a background saline of $\sigma=0.2Sm^{-1}$.

(b) Images produced by WBP1 from analytically calculated data.

(c) Images produced by WBP2 from analytically calculated data.

(d) Images produced by WBP1(threshold=0.33mV) from measured data.

(e) Images produced by WBP2 from measured data.

(Max ΔV at electrodes = 29.9mV).

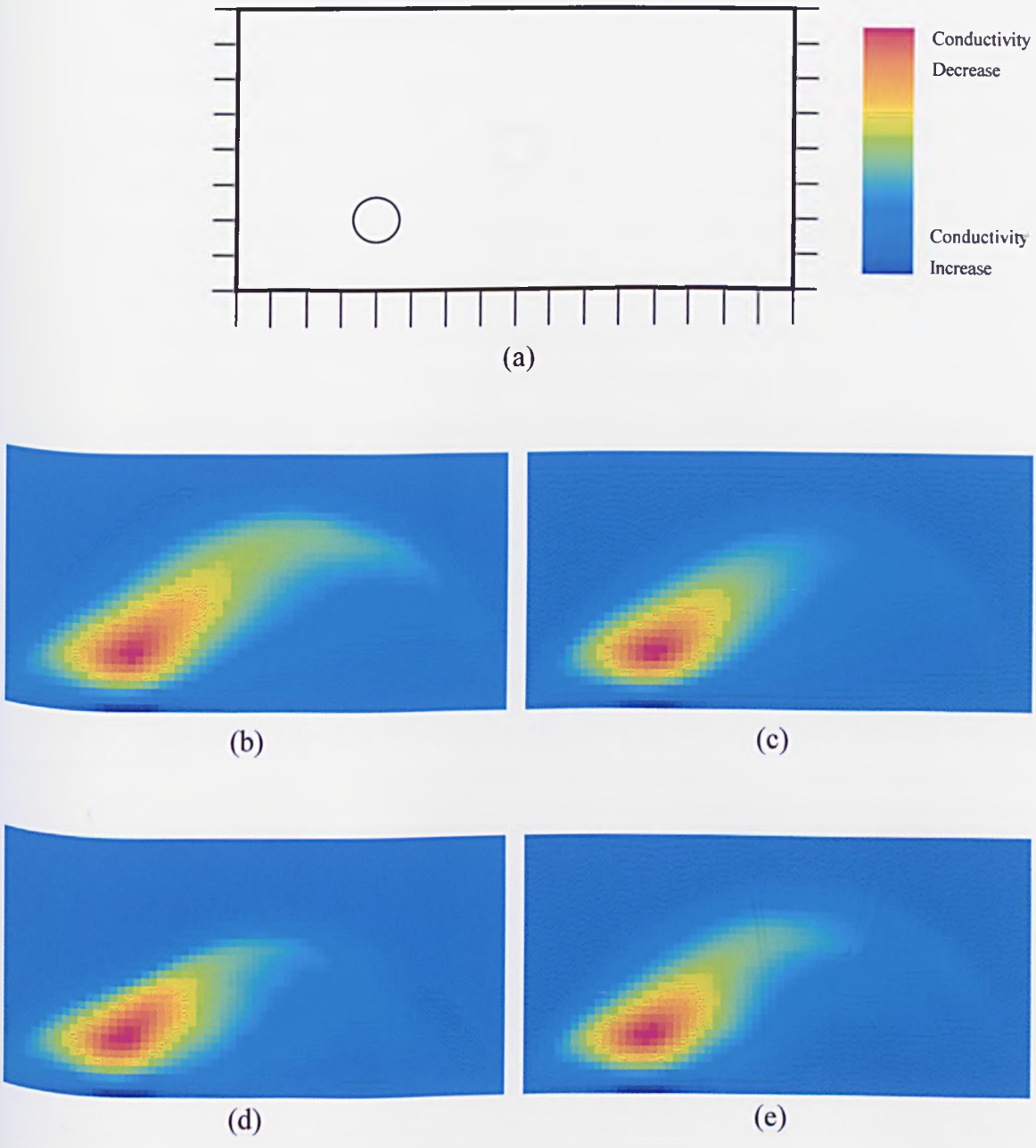

Figure 7.16 : Images produced for a single object located at (4,2) in a pseudo-2D phantom.

(a) The conductivity distribution. The object is a perspex cylinder of radius 0.633units and $\sigma=0$ in a background saline of $\sigma=0.2Sm^{-1}$.

(b) Images produced by WBP1 from analytically calculated data.

(c) Images produced by WBP2 from analytically calculated data.

(d) Images produced by WBP1(threshold=0.33mV) from measured data.

(e) Images produced by WBP2 from measured data.

(Max ΔV at electrodes = 9.3mV).

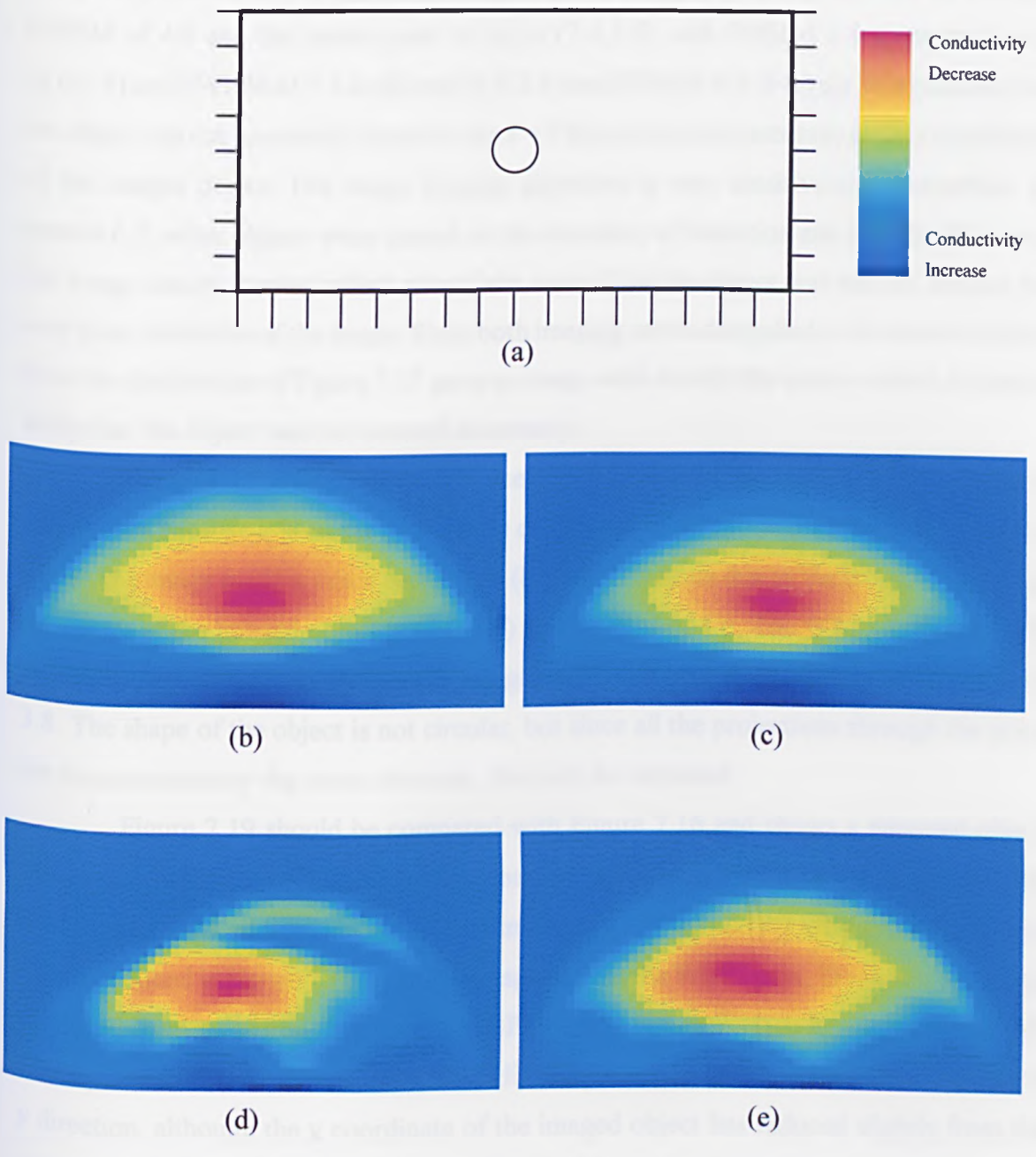

Figure 7.17 : Images produced for a single object located at (8,4) in a pseudo-2D phantom.

(a) The conductivity distribution. The object is a perspex cylinder of radius 0.633units and $\sigma=0$ in a background saline of $\sigma=0.2Sm^{-1}$.

(b) Images produced by WBP1 from analytically calculated data.

(c) Images produced by WBP2 from analytically calculated data.

(d) Images produced by WBP1(threshold=0.16mV) from measured data.

(e) Images produced by WBP2 from measured data.

(Max ΔV at electrodes = 2.6mV).

profile. Figure 7.17(d) and (e) are images produced from the measured data which clearly show the presence of the object. The centre point of (d) is (7.4,3.2) and has an average FWHM of 4.6 and the centre point of (e) is (7.4,3.6) with FWHM 6.4 (compared with (8.0,3.6) and FWHM of 7.1 in (b) and (8.0,3.4) and FWHM of 5.9 in (c)). It is possible that the object was not accurately placed on the $x = 8$ line giving the inaccuracy in the x coordinate of the imaged object. The image forming algorithm is very sensitive to asymmetries. In section 6.3, when objects were placed on the boundary of detection and slightly off centre, the image clearly showed which side of the central line the object was placed, despite the very poor resolution of the image. Since both imaging methods applied to the measurements from the distribution of Figure 7.17 gave an image with exactly the same x centre, it is most likely that the object was not centred accurately.

Figure 7.18 shows images produced from an object placed at (3,3). This position was chosen because it is closer to the edge of the area of detection than the three previous cases. The image in (d) is much better than (b), which is again due to the thresholding, with the centre of the imaged object at (3.0,2.8) and FWHM of 3.6. The WBP2 image in (e) is slightly more blurred than the analytic image in (c) with centre at (3.2,2.6) and FWHM of 3.8. The shape of the object is not circular, but since all the projections through the point are in approximately the same direction, this is to be expected.

Figure 7.19 should be compared with Figure 7.16 and shows a mirrored object placement with the y value of the object position increased from 2 to 3. It can be seen that the images produced from simulated data in Figures 7.19(b) and (c) are more blurred than those produced in Figure 7.16(b) and (c), especially in the WBP1 case. However, the image produced from measured data for the WBP1 case in Figure 7.19(d) is much less blurred. This again shows the effect of the thresholding and has reduced the size of the image in the y direction, although the y coordinate of the imaged object has reduced slightly from the simulated case (FWHM is 3.7 with centre at (11.8,2.6)). The image produced from WBP2 is slightly more blurred than the simulated image with a FWHM of 4.2 and centre at (11.8,2.6).

In general, when the object is close to the array of electrodes as in Figures 7.15 and 7.16, the image formed from the measurements is very similar to the image produced from the data which has been generated analytically. As the object moves further from the array, the images become more varied as in Figure 7.17. The effect of the thresholding in the WBP1 method can be seen in Figure 7.18 and 7.19 by comparing (b) and (d) where only the larger voltage differences have been used in producing the image giving a much less blurred image. This indicates that further work on the effects of thresholding in images

(a)

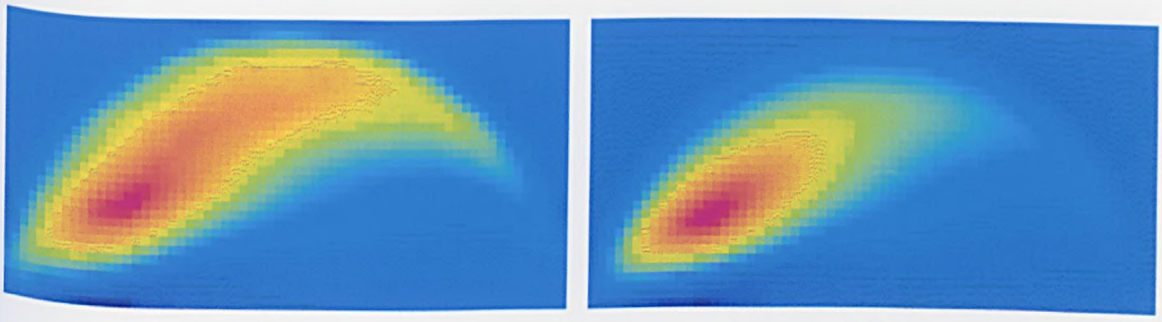

(b) (c)

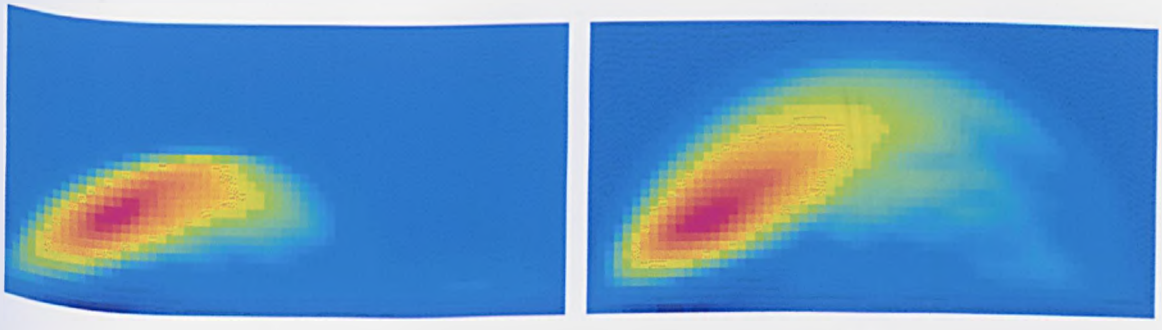

(d) (e)

Figure 7.18 : Images produced for a single object located at (3,3) in a pseudo-2D phantom.

(a) The conductivity distribution. The object is a perspex cylinder of radius 0.633units and $\sigma=0$ in a background saline of $\sigma=0.2Sm^{-1}$.

(b) Images produced by WBP1 from analytically calculated data.

(c) Images produced by WBP2 from analytically calculated data.

(d) Images produced by WBP1(threshold=0.20mV) from measured data.

(e) Images produced by WBP2 from measured data.

(Max ΔV at electrodes = 2.9mV).

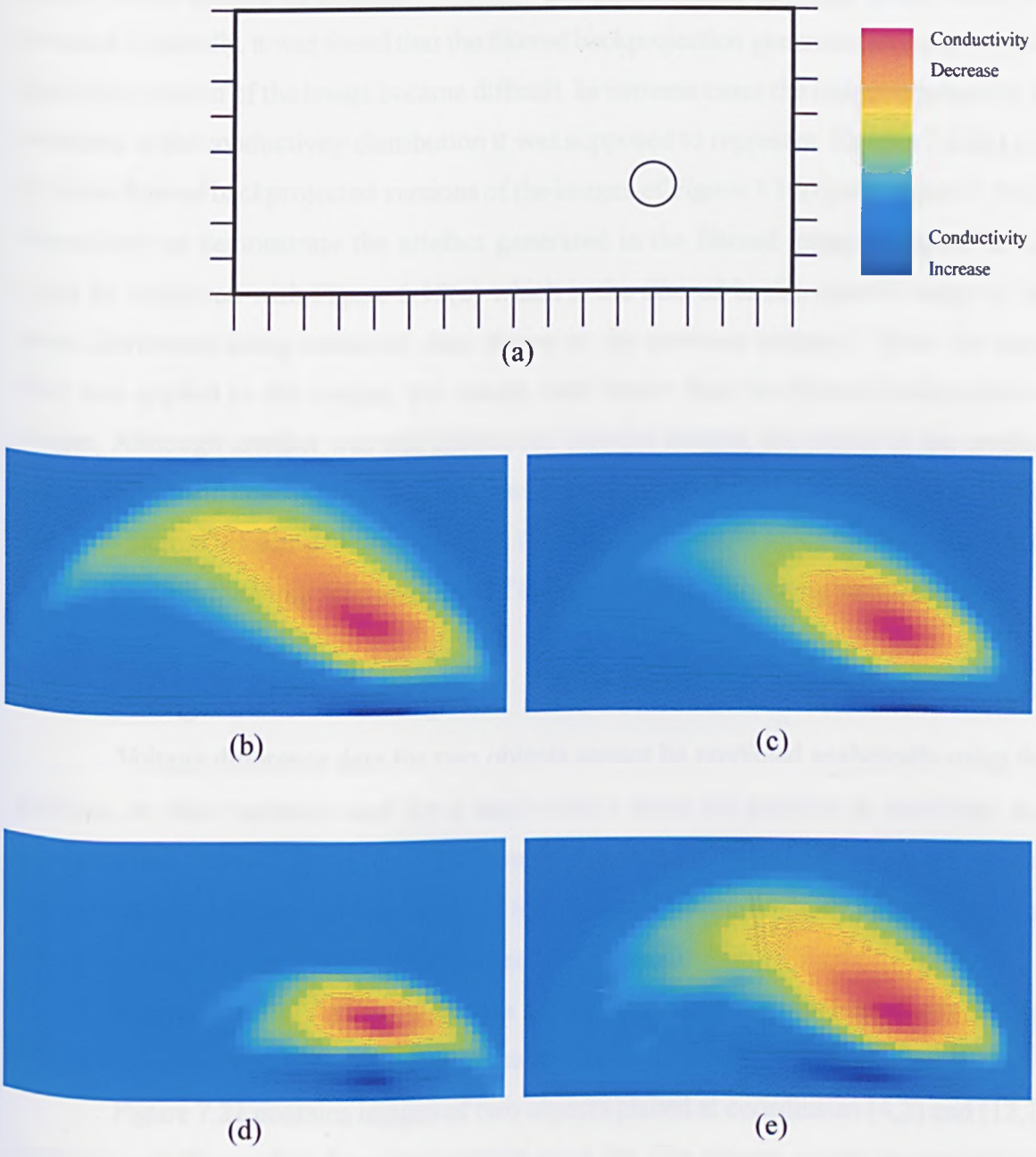

Figure 7.19 : Images produced for a single object located at (12,3) in a pseudo-2D phantom.

(a) The conductivity distribution. The object is a perspex cylinder of radius 0.633units and $\sigma=0$ in a background saline of $\sigma=0.2Sm^{-1}$.

(b) Images produced by WBP1 from analytically calculated data.

(c) Images produced by WBP2 from analytically calculated data.

(d) Images produced by WBP1(threshold=0.33mV) from measured data.

(e) Images produced by WBP2 from measured data.

(Max ΔV at electrodes = 1.9mV).

produced from data gathered by a linear array may be useful.

The filtered backprojection and ramp filter described in the previous chapter were applied to the images to determine whether any improvement in image quality could be obtained. Generally, it was found that the filtered backprojection generated so much artefact that interpretation of the image became difficult. In extreme cases the image appeared to be unrelated to the conductivity distribution it was supposed to represent. Figures 7.20(a) and (b) show filtered backprojected versions of the images of Figure 7.16(e) and Figure 7.19(d) respectively to demonstrate the artefact generated in the filtered images. (Figure7.20(a) could be compared with Figure 6.18(e) which is the filtered backprojected image of the same distribution using simulated data shown in the previous chapter). When the ramp filter was applied to the images, the results were better than the filtered backprojection images. Although artefact was still introduced into the images, the extent of the artefact was much less and hence the images were easier to interpret. As an example, Figure 7.20(c) is a ramp filtered version of Figure 7.15(e). (Figure7.20(c) could be compared with Figure 6.13(e) which is the ramp filtered image of the same distribution using simulated data).

7.5.2 Images of Two Objects

Voltage difference data for two objects cannot be predicted analytically using the previous or other methods used for a single object since the problem is non-linear and superposition cannot be applied (although the forward problem could be solved computationally, by finite element methods for example). Therefore, only images produced from measured data are presented in this section.

Figures 7.21 to 7.23 show images of two objects of the same conductivity. The data pertaining to each image is given in the caption.

Figure 7.21 contains images of two objects placed at coordinates (4,2) and (12,2) (compare with Figure 7.16 for a single object at (4,2)). The objects, which are spaced by 8 'like' electrode spacings (receive-receive/drive-drive electrode spacings), have been detected in both (b) and (c). The equipotential blurring which links the two objects is much reduced in the WBP1 case (b) in comparison with the WBP2 case (c). This is another example of thresholding making images easier to interpret by discarding the small signal information which is likely to be corrupted by noise in the formation of the images. The shapes of the objects are similar to those obtained in Figure 7.16 and their centres are at (4.0,2.0) and (11.8,2.0) in (b) and (4.0,2.0) and (12.0,2.0) in (c). The average FWHM of the imaged objects in the x and y directions were 2.7 in (b) and 3.2 in (c).

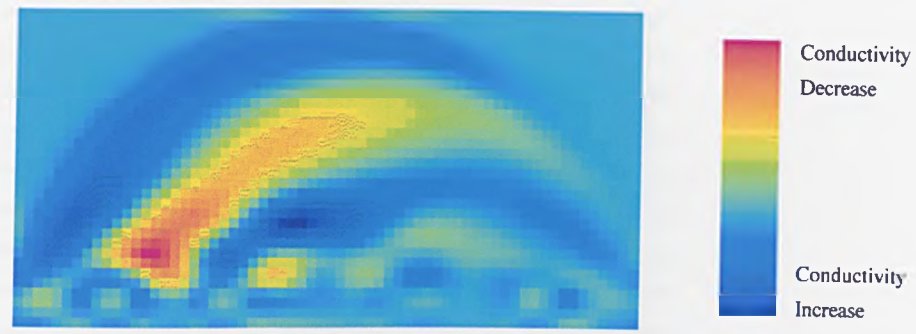

(a)

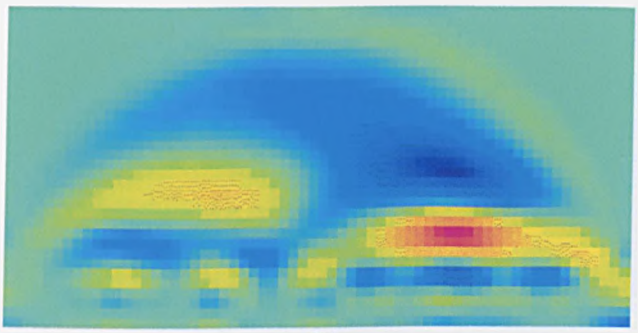

(b)

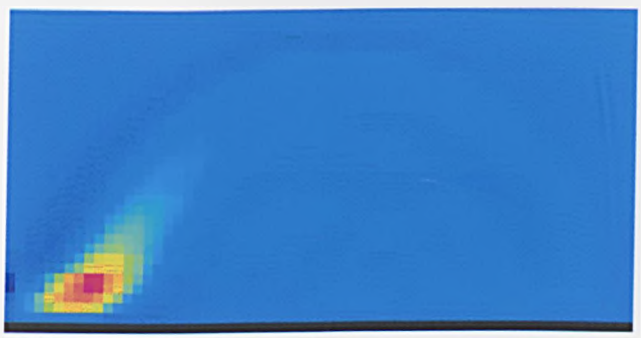

(c)

Figure 7.20 : Filtered images of single objects in a pseudo-2D phantom.

(a) A filtered backprojected version of Figure 7.16(e).

(b) A filtered backprojected version of Figure 7.19(d).

(c) A ramp filtered version of Figure 7.15(e).

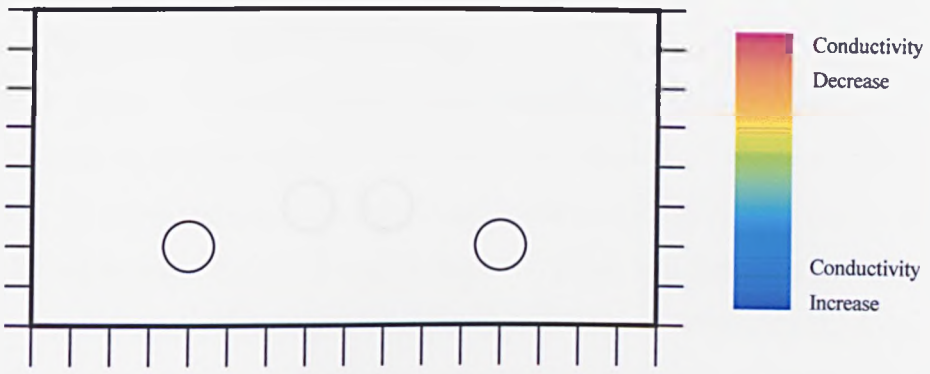

(a)

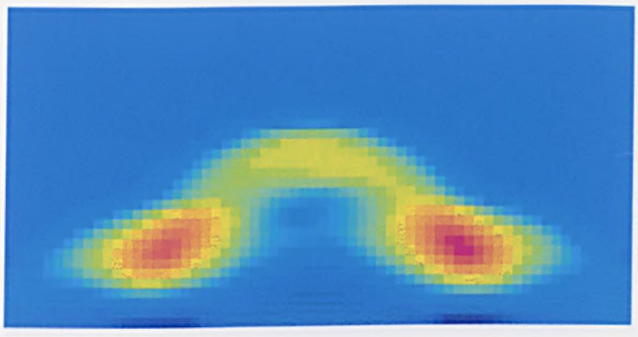

(b)

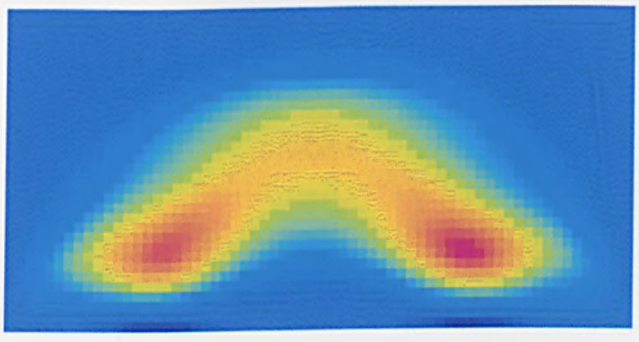

(c)

Figure 7.21 : Images produced for two objects in a pseudo-2D phantom of depth 20mm.

(a) The conductivity distribution. The objects are perspex cylinders of radii 0.633units and σ=0 in a background saline solution of σ=0.2Sm^{-1}.

(b) Images produced by WBP1(threshold=0.65mV) from measured data.

(c) Images produced by WBP2 from measured data.

(Max ΔV at electrodes = 5.4mV).

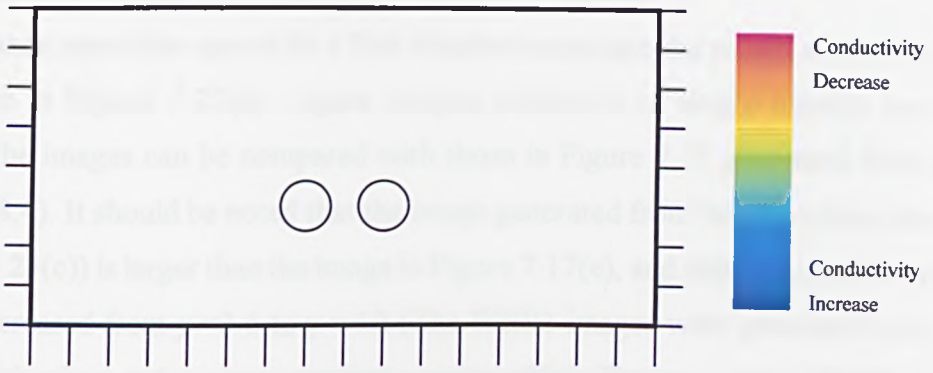

(a)

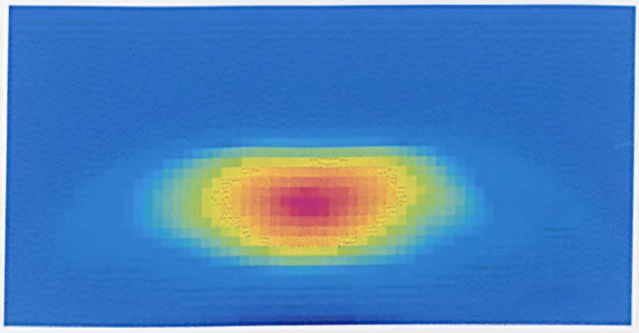

(b)

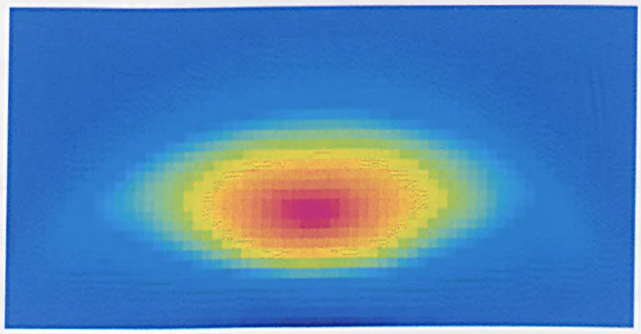

(c)

Figure 7.22 : Images produced for two objects in a pseudo-2D phantom of depth 20mm.

(a) The conductivity distribution. The objects are perspex cylinders of radii 0.633units and σ=0 in a background saline solution of σ=0.2Sm^{-1}.

(b) Images produced by WBP1(threshold=0.33mV) from measured data.

(c) Images produced by WBP2 from measured data.

(Max ΔV at electrodes = 2.6mV).

The objects were placed farther from the array and close together in Figure 7.22 at coordinates (7,3) and (9,3). The images produced using WBP1 and WBP2 both appeared to be of a single object at (8,3) of FWHM 3.8 in (b) and 4.5 in (c).

The objects were then spaced by 4 'like' electrode spacings and placed at (6,4) and (10,4) as shown in Figure 7.23(a). Again images indicative of single objects were reconstructed. The images can be compared with those in Figure 7.17 generated from a single object at (8,4). It should be noted that the image generated from the two object data by WBP2 (Fig. 7.23(c)) is larger than the image in Figure 7.17(e), and that the y position of the object has increased from y =3.6 to y =4.2 (The WBP1 images were generated using different threshold values and so are not strictly comparable). The ratio of the FWHM in the x direction to the FWHM in the y direction is larger for the two object case than the single object case, which could be used to infer that the object was either elongated in the x direction, or that more than one object was present.

These images in Figures 7.21 to 7.23 show that the resolution of the system between imaged objects is very positionally dependent and improves as the objects approach the array. This is to be expected since the resolution of single imaged objects is positionally dependent as demonstrated by Figures 7.15 to 7.19. It is also the case in systems using encircling arrays, that the resolution between objects placed furthest from the electrodes (ie in the centre of the region to be imaged) is poor.

Figures 7.24 to 7.27 show unfiltered images of two objects of different sizes and conductivities. These experiments were performed to investigate whether or not objects of different sizes and conductivities could be imaged.

The objects in Figure 7.24 were a small cylinder of hollow bone (5mm radius which is 0.33 units) and a perspex rod (13mm radius which is 0.633 units). The objects were well spaced and close to the array so that the resolution between the objects was as good as possible. The FWHMs of the objects in (b) are 2.1 and 2.8 and in (c) are 2.1 and 2.9. The positioning of the imaged objects in (b) and (c) is the same except for a marginal reduction in y position (0.2unit) of the centre of the image of the large object in (b). The peak of the image value occurs on the larger object which is as expected since this object is larger in size and has a lower conductivity than the other.

Figure 7.25 shows two objects of different sizes, one object less conductive than the background medium (radius 6.5mm which is 0.433units), and one more conductive (15.5mm radius which is 1.03 units). The images in (b) and (c) are very similar and both show the two objects. The approximate FWHM is calculated for these imaged objects

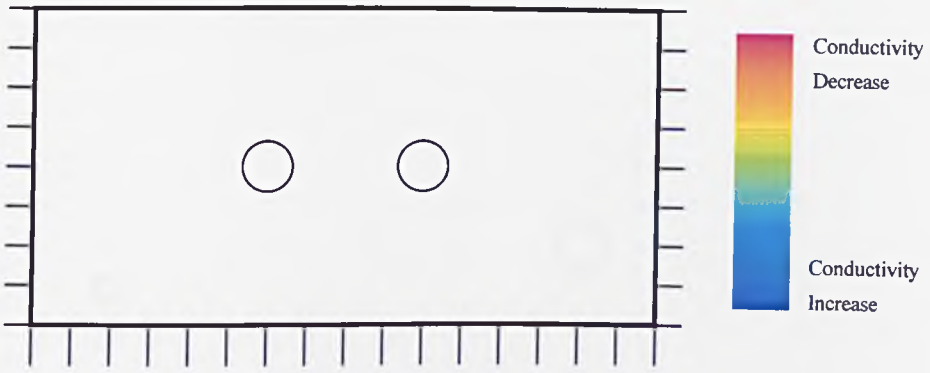

(a)

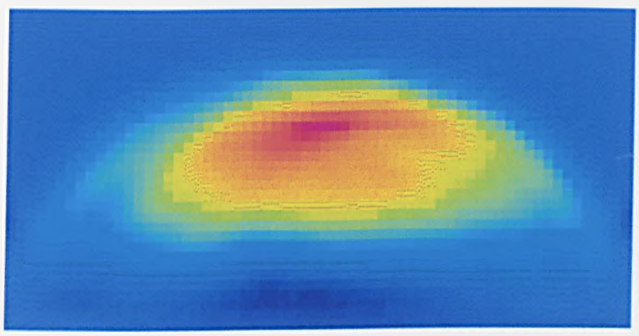

(b)

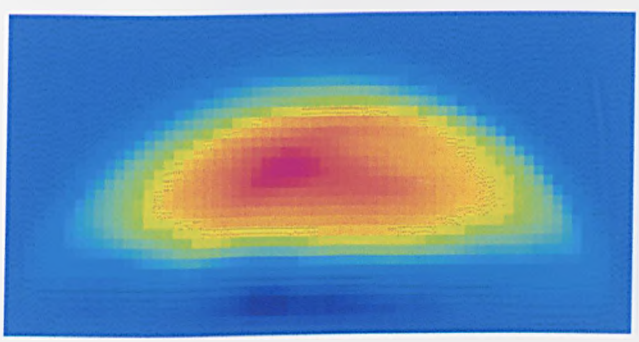

(c)

Figure 7.23 : Images produced for two objects in a pseudo-2D phantom of depth 20mm.

(a) The conductivity distribution. The objects are perspex cylinders of radii 0.633units and $\sigma=0$ in a background saline solution of $\sigma=0.2Sm^{-1}$.

(b) Images produced by WBP1(threshold=0.10mV) from measured data.

(c) Images produced by WBP2 from measured data.

(Max ΔV at electrodes = 3.4mV).

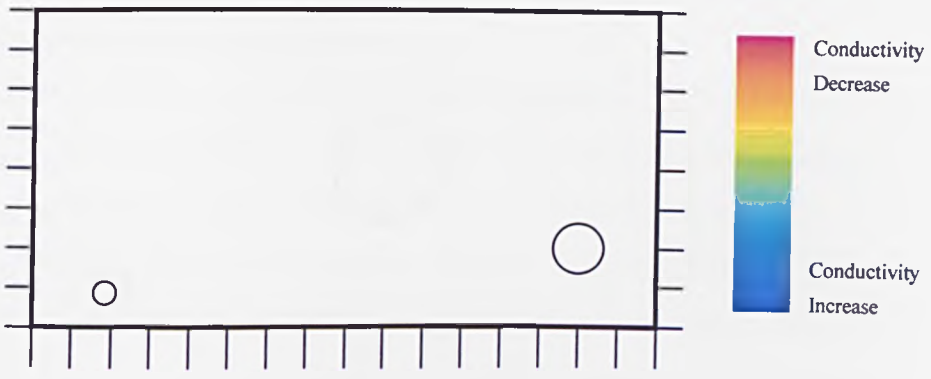

(a)

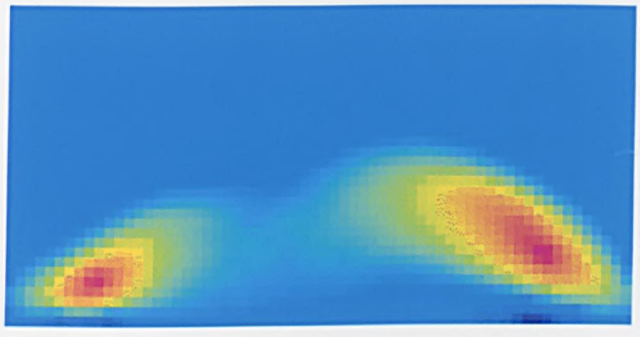

(b)

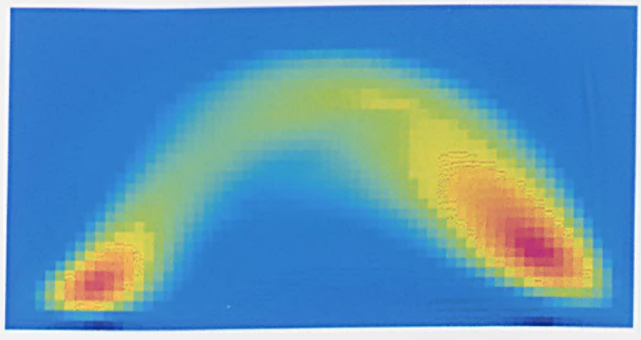

(c)

Figure 7.24 : Images produced for two objects in a pseudo-2D phantom of depth 20mm.

(a) The conductivity distribution. The smaller object is a hollow bone of σ=0.006Sm^{-1} and the larger object is a perspex rod of σ=0. The background solution is a saline solution of σ=0.2Sm^{-1}.

(b) Images produced by WBP1(threshold=0.49mV) from measured data.

(c) Images produced by WBP2 from measured data.

(Max ΔV at electrodes = 18.6mV).

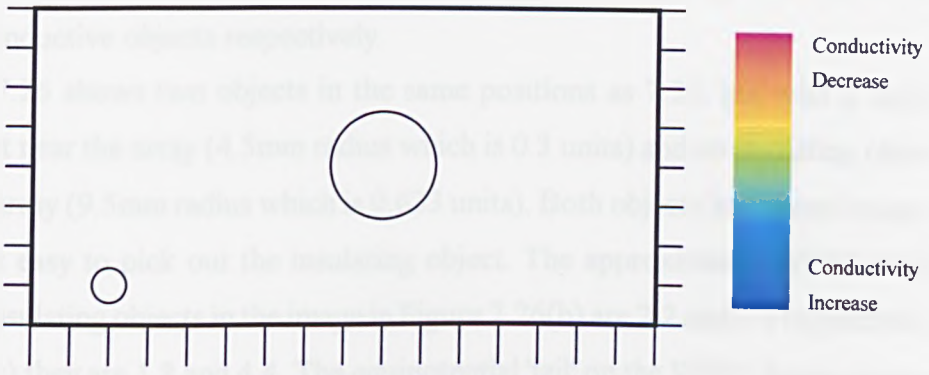

(a)

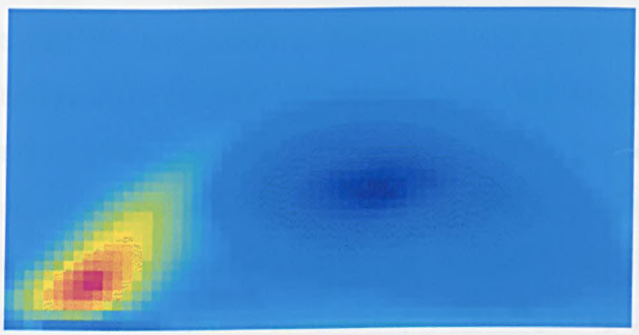

(b)

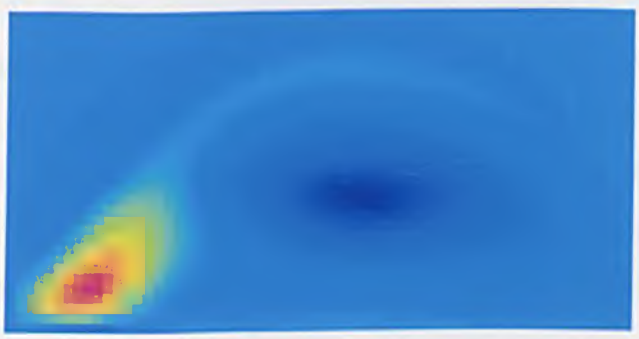

(c)

Figure 7.25 : Images produced for two objects in a pseudo-2D phantom of depth 20mm.

(a) The conductivity distribution. The smaller object is a perspex rod of $\sigma=0$ and the larger object is a cylinder of steel of $\sigma\rightarrow\infty$. The background solution is a saline solution of $\sigma=0.2Sm^{-1}$.

(b) Images produced by WBP1(threshold=0.26mV) from measured data.

(c) Images produced by WBP2 from measured data.

(Max ΔV at electrodes = 39.1mV).

where the 'Half Maximum' is defined as being halfway between the peak and the background. In Figure 7.25(b) the FWHM of the insulating object is approximately 2.6 and the conductive object is approximately 4.2. For (c) the FWHMs are approximately 2.5 and 4.2 for the insulating and conductive objects respectively.

Figure 7.26 shows two objects in the same positions as 7.25, but with a highly conductive object near the array (4.5mm radius which is 0.3 units) and an insulating object further from the array (9.5mm radius which is 0.633 units). Both objects have been imaged, although it is not easy to pick out the insulating object. The approximate FWHM of the conducting and insulating objects in the image in Figure 7.26(b) are 2.2 and 3.8 respectively. For Figure 7.26(c) they are 1.8 and 4.4. The equipotential 'tail' on the WBP1 image is more pronounced than in the WBP2 image, which is different from usual. The threshold level on the WBP1 image had to be kept low (0.13mV) in order to be able to detect the perspex object. This means that the equipotential blurring, which is normally suppressed is still present. As stated earlier in the chapter, the colour scale of the images is normalised to span the full range of conductivities in the image. By considering the position of the colour of the background medium on the colour scale for Figures 7.25, it can be seen that the steel is being imaged as only slightly more conductive than the background saline. This is because the signal associated with the object placed further from the array is very weak. Similarly for Figure 7.26, the signal associated with the perspex is very small in comparison with the signal associated with the steel (if the forward problem is solved for each object separately, the maximum voltage difference expected for the perspex in the position shown in Figure 7.26(a) is a factor of 23 larger than the maximum potential difference for the steel object).

Figure 7.27 shows two objects in the positions (4,2) and (12,2), one conducting and one insulating. The images can be compared with Figure 7.21 which shows two objects in the same position, but of the same conductivity. Both the objects have been imaged clearly with good resolution between the two. The centre positions of the two objects are identical in (b) and (c) with FWHMs of 2.8 (insulating) and 2.7 (conducting) in (b) and 2.8 and 2.7 in (c) also.

It has been shown that multiple objects can be imaged successfully using the linear array. The objects can either both be higher or lower in conductivity than the background, or one can be higher and one lower. Objects close to the array and separated from each other by a few electrode spacings are resolved effectively (Figures 7.25 and 7.27) but the masking effect of blurring along the equipotentials can be significant in situations where one object is placed further from the array than the other. If the position of the object

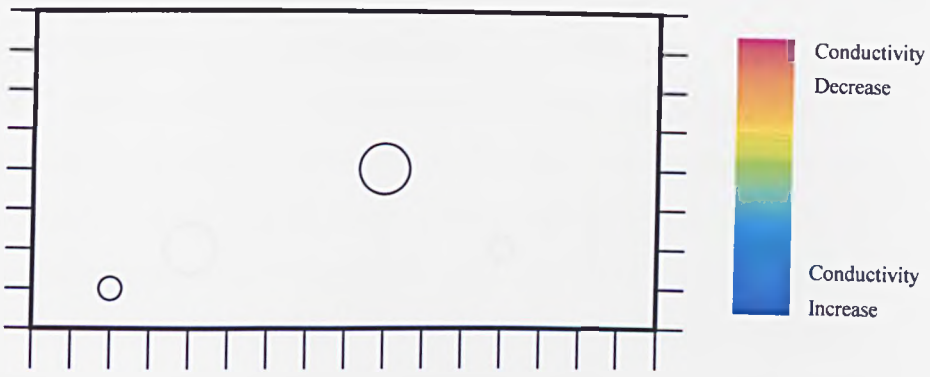

(a)

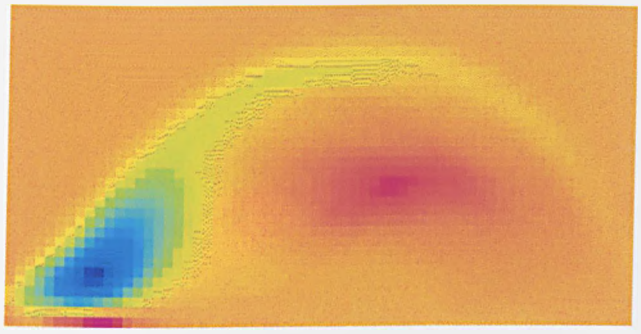

(b)

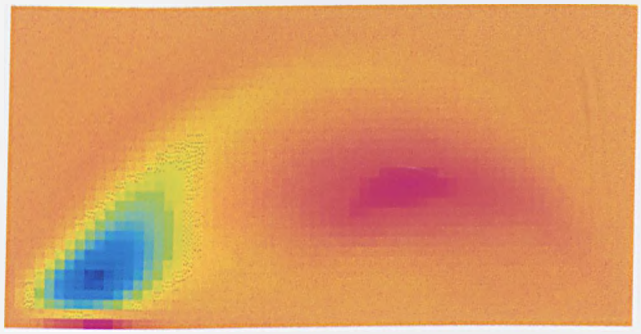

(c)

Figure 7.26 : Images produced for two objects in a pseudo-2D phantom of depth 20mm.

(a) The conductivity distribution. The smaller object is a small steel cylinder of $\sigma \rightarrow \infty$ and the larger object is a perspex rod of $\sigma=0$. The background solution is a saline solution of $\sigma=0.2 Sm^{-1}$.

(b) Images produced by WBP1(threshold=0.13mV) from measured data.

(c) Images produced by WBP2 from measured data.

(Max ΔV at electrodes = 19.3mV).

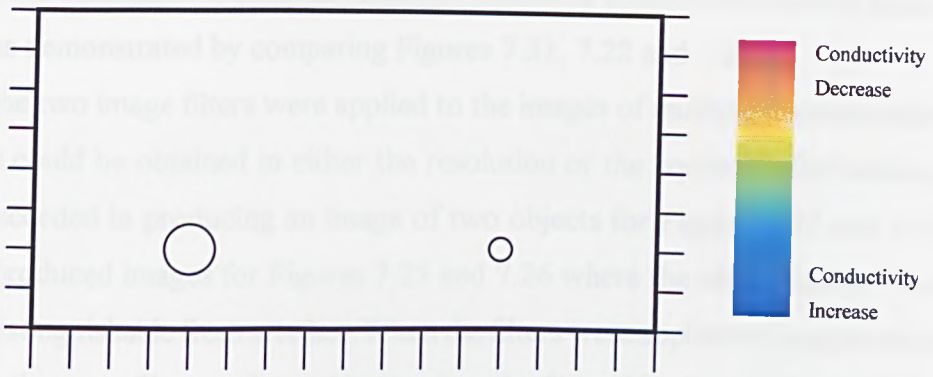

(a)

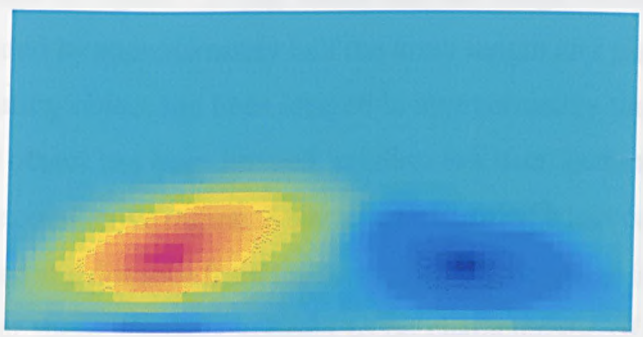

(b)

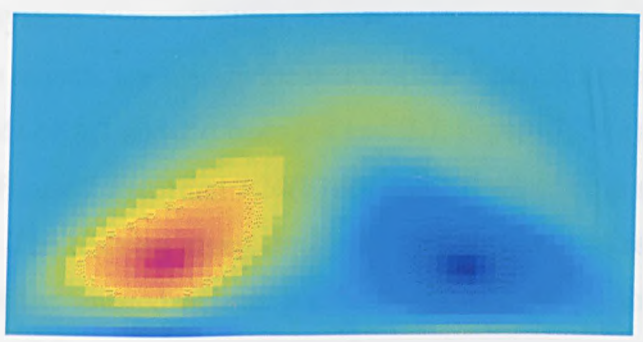

(c)

Figure 7.27 : Images produced for two objects in a pseudo-2D phantom of depth 20mm.

(a) The conductivity distribution. The smaller object is a small steel cylinder of $\sigma \rightarrow \infty$ and the larger object is a perspex rod of $\sigma=0$. The background solution is a saline solution of $\sigma=0.2 Sm^{-1}$.

(b) Images produced by WBP1(threshold=0.49mV) from measured data.

(c) Images produced by WBP2 from measured data.

(Max ΔV at electrodes = 6.6mV).

further from the array coincides with the typical equipotential blurring of the image of the object placed close to the array, the masking is much worse, as demonstrated by Figures 7.25 and 7.26. Poor resolution is obtained between objects of similar conductivity placed close together, as demonstrated by comparing Figures 7.21, 7.22 and 7.23.

When the two image filters were applied to the images of multiple discontinuities no improvement could be obtained in either the resolution or the equipotential masking. Neither filter succeeded in producing an image of two objects for Figures 7.22 and 7.23 and both filters produced images for Figures 7.25 and 7.26 where the object further from the array was indistinguishable from artefact. When the filters were applied to images which were reasonable, the ramp filter performed better than the filtered backprojection as it did with the single object distributions of Figures 7.15 to 7.19. Figure 7.28(a) shows a filtered backprojected image of Figure 7.27(b), which was the image formed from a perspex and steel object separated by approximately half the array length and placed close to the array. The perspex insulating object has been imaged in approximately the correct position, but, although the steel object has been imaged, artefact has been generated which implies the presence of a more conductive region. An artefact indicating a low conductivity region has also been introduced at a distance from the array, making the image impossible to interpret. The introduction of these artefacts appears to be characteristic of the behaviour of this particular filter in the presence of noise and so it is of limited use in improving images produced by this system. Figure 7.28(b), however, shows a ramp filtered version of Figure 7.27(c) where the objects are clearly located and the blurring around the object has been reduced to FWHMs of 2.3 and 2.6 from 2.8 and 2.7. Figure 7.29(a) and (b) shows a ramp filtered version of Figure 7.21(c) and 7.24(b) respectively which both show two well resolved insulating objects. The blurring along the equipotentials has been reduced in both (a) and (b) and the size of the imaged objects has been reduced. In (a) the FWHMs have been reduced to 2.6 from 3.2 and in (b) the FWHMs have been reduced to 1.5 and 1.9 from 2.1 and 2.8. These last two figures show that the ramp filter is quite good at defining the edges of the imaged objects and reducing the equipotential blurring, which is particularly pronounced in the linear array. Similar blurring occurs in images produced from data gathered on an encircling array, but this blurring tends to be radial. The ramp filter is used in the following section on images of moving objects, since, unlike the images presented in this section so far which have been produced from data gathered in the AVERAGED REFERENCED mode, the measurements made for a moving object are not averaged and it is expected that the noise will be too high for the filtered backprojection process to produce sensible images.

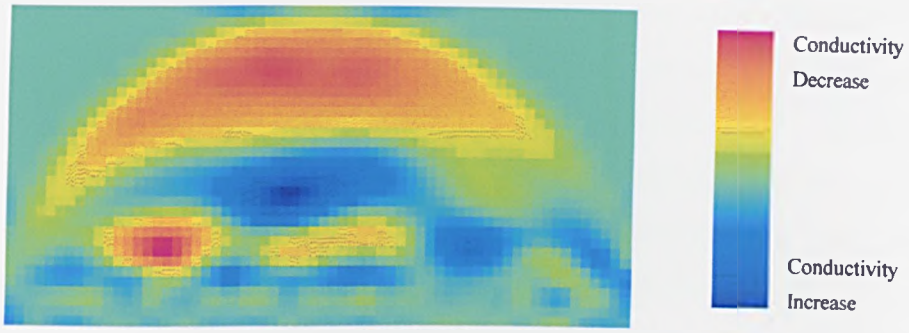

(a)

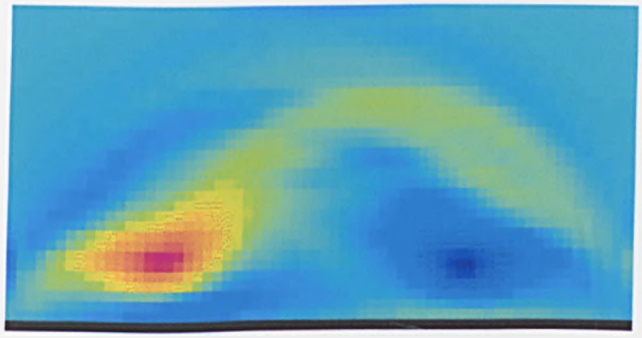

(b)

Figure 7.28 : Filtered images of two objects in a pseudo-2D phantom.

(a) is a filtered backprojected version of Figure 7.27(b).

(b) is a ramp filtered version of Figure 7.27(c).

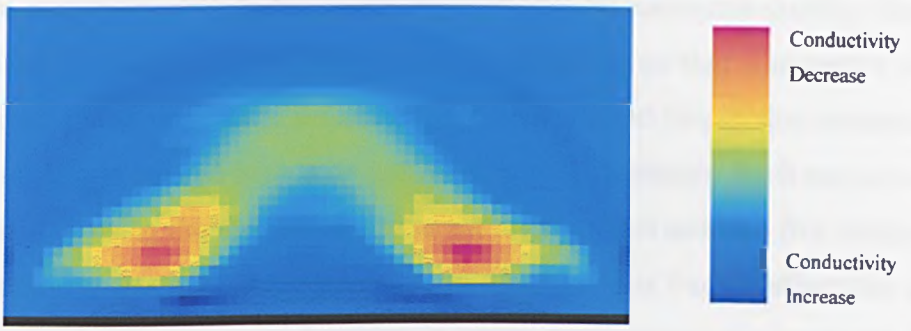

(a)

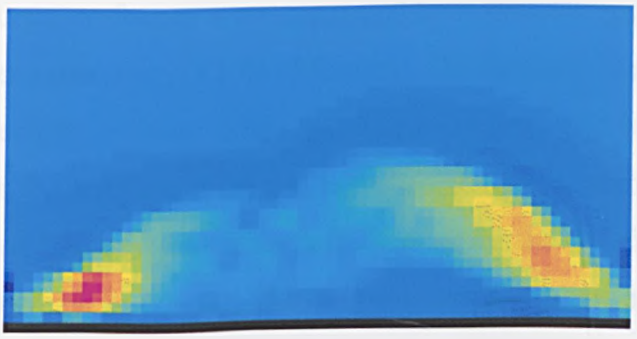

(b)

Figure 7.29 : Filtered Images of Two Objects.

(a) is a ramp filtered version of Figure 7.21(c).

(b) is a ramp filtered version of Figure 7.24(b).

7.5.3 Moving Objects

In this section the performance of the system at imaging a number of moving targets travelling at speeds of between 0.15 and 15ms^{-1} is investigated.

One of the major reasons for investigating the simultaneous drive multiple frequency narrowband system, was to investigate the possibility of taking measurements quickly, thus enabling moving targets to be imaged. This system was designed so that a sequence of continuous or delayed measurements of 6 frames could be made and this section presents images of moving objects produced from data collected by these methods. Each sequence of images is generated by using the previous frame as the reference set and thus five images are produced from the six sets of measurements made. The previous frame, rather than a homogeneous reference set, was used because in many applications (eg medical) a homogeneous reference is not available.

Figure 7.30 is a sequence of images produced from data collected while a perspex cylinder of radius 0.663 units ('like' electrode spacings) was moved by hand from one end of the electrode array to the other. The cylinder was moved parallel to the array at a distance of approximately 1.5 'like' electrode spacings from it ie approximately along the line $y=1.5$. The measurement frames were separated by a time interval of 200ms and so the data was taken over a time span of 1.0s (6 frames). The decrease in conductivity shows the position of the perspex cylinder when the frame of data was taken. The increase in conductivity shows the position of the perspex when the previous frame of data was taken because the previous frame is used as the reference set for the next frame. The positions of the increase and decrease in conductivity between frames do not exactly coincide due to the difficulty of imaging two objects of opposite polarity in such proximity. The position of the perspex rod can be seen clearly in all the images. Figure 7.31 is a ramp filtered version of Figure 7.30 and it can be seen that the object is imaged as being more circular than in the unfiltered image. As expected, filtered backprojection did not produce any sensible images for moving targets and so no images filtered by this method are presented in this section.

Figure 7.32 is a sequence of images produced from data collected while a plane wave was moving across the surface of the saline in the phantom. The wave was generated by the sudden sideways motion of an object with a vertical dimension greater than the depth of the saline which was placed along the full length of the left hand wall of the phantom ($x<0$). The amplitude of the wave was approximately 5mm and the measurements were separated by a time interval of 100ms. The peak of the wave appears as an increase in conductivity due to the increase in depth. The combined effects of the following trough and

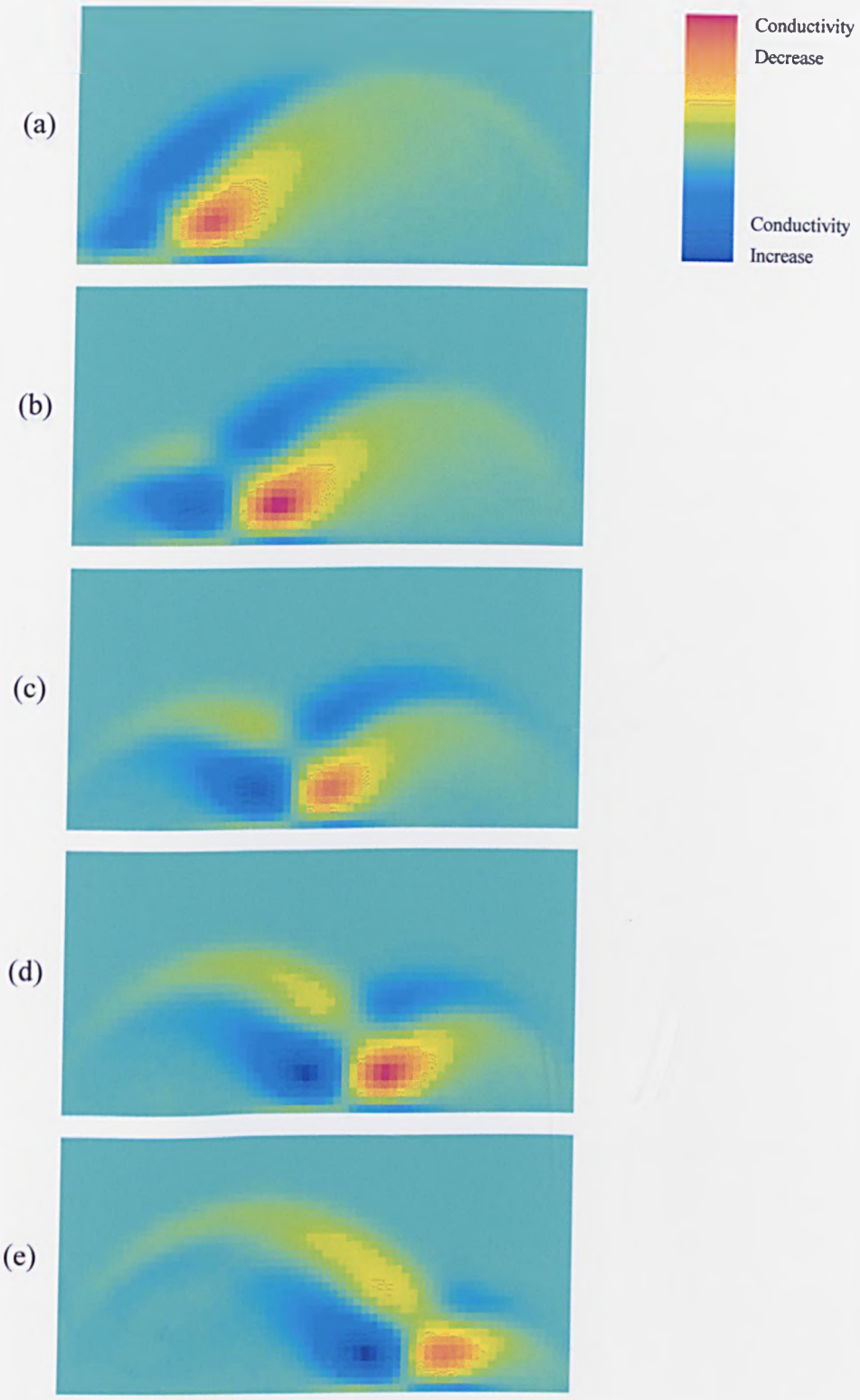

Figure 7.30 : Images of a moving object in a pseudo-2D phantom of depth 20mm.

(a)-(e) A sequence of images produced by the WBP1 method (threshold=0.49mV) of a perspex rod (σ=0) of radius 0.633 units being moved by hand along the approximate line y=1 in pseudo-2D saline of σ=0.2Sm^{-1} and depth 20mm. The time between frames is 200ms. (Max ΔV=41.6mV).

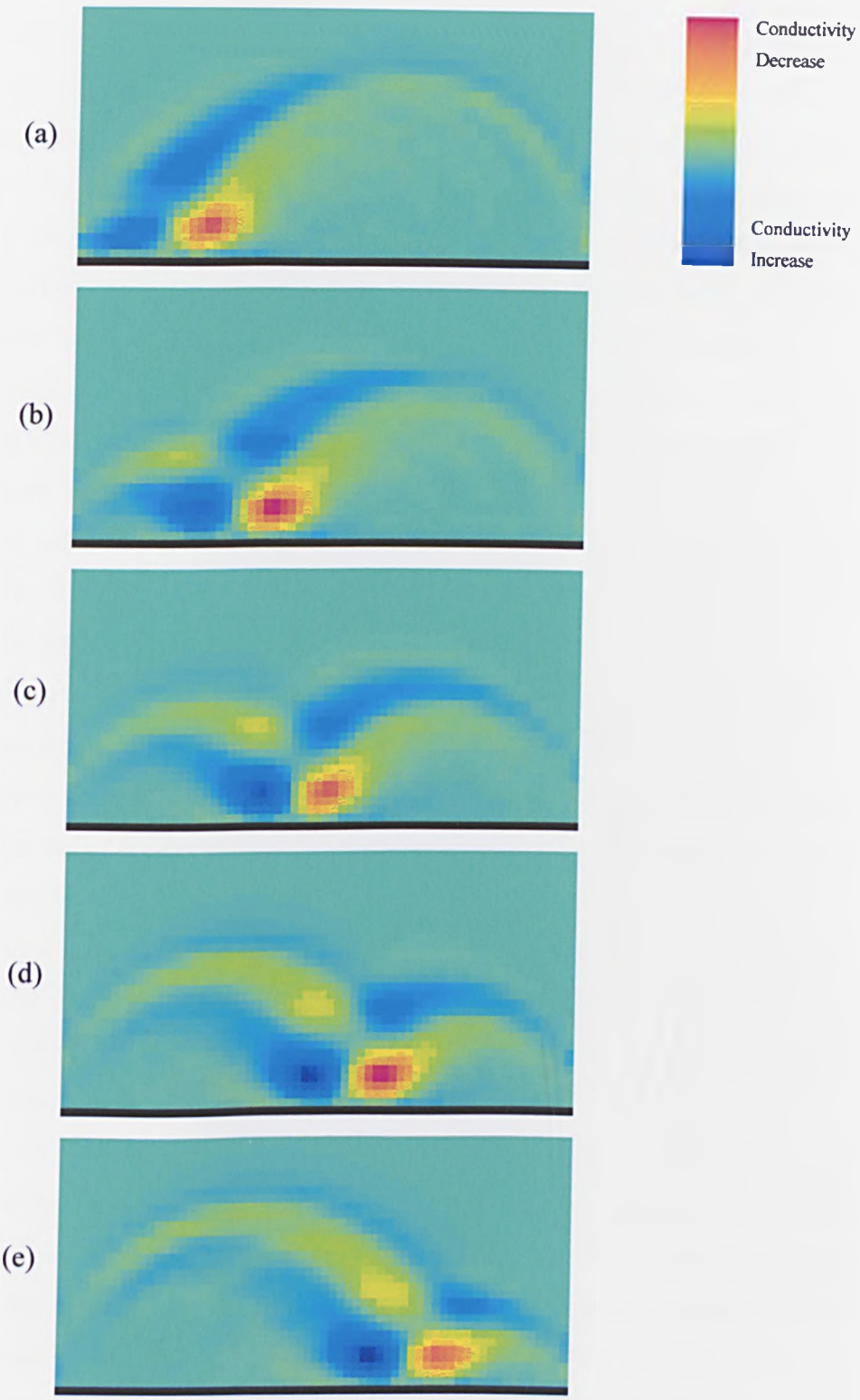

Figure 7.31 : A ramp filtered version of Figure 7.30.

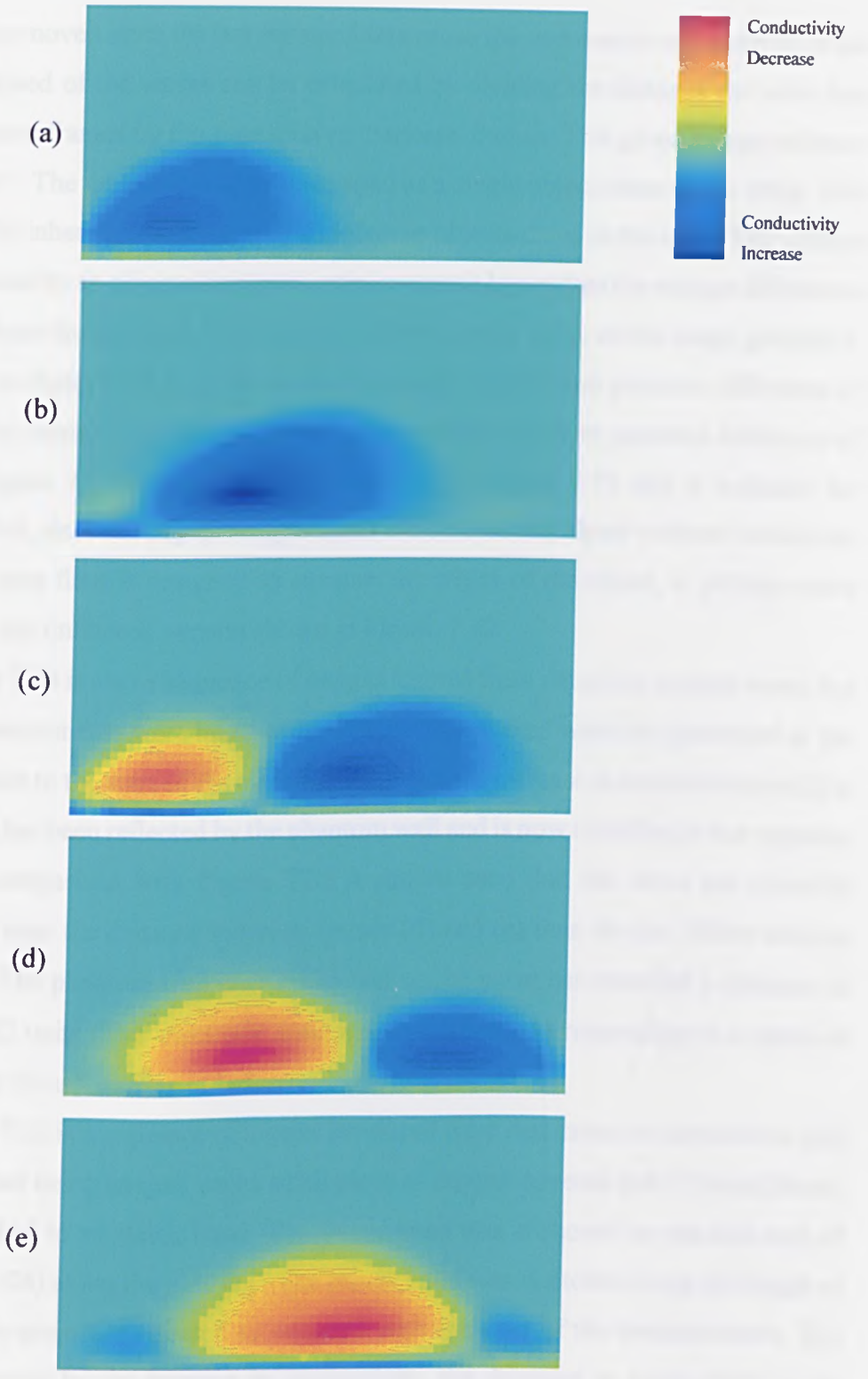

Figure 7.32 : Images of a plane wave in a pseudo-2D phantom of depth 20mm.

(a)-(e) A sequence of images produced by the WBP1 method (threshold=0.65mV) of a plane wave in pseudo-2D saline of conductivity σ=0.2Sm^{-1} and depth 20mm. The wave was approximately 5mm in amplitude and the time interval between frames is 100ms. (Max ΔV=37.1mV).

the peak having moved since the last frame of data cause the decrease in conductivity in the images. The speed of the waves can be calculated by dividing the distance the wave has travelled between frames by the time interval between frames. This gives an approximate value of $0.5ms^{-1}$. The waves appear to be imaged as a single object close to the array. This is because of the inherent sensitivity of the system to objects close to the array. The voltage differences caused by an object close to the array are much larger than the voltage differences caused by an object further from the array and so have a larger effect on the image generated. For example, an object at (8,1) gives rise to a normalised maximum potential difference of 0.160, whilst the same object at (8,4) gives a normalised maximum potential difference of only 0.001. Figure 7.33 is a ramp filtered version of Figure 7.32 and is included for completeness but, since the object being imaged is a continuous object without boundaries and since the ramp filter is designed to enhance the edges of the object, is perhaps more sensible to use the unfiltered version shown in Figure 7.32.

Figure 7.34 is also a sequence of images formed from data from a plane wave, but in this case measurements were taken every 200ms. The waves were not generated at the same time relative to the start of the measurements and the increase in conductivity in (d) is the wave which has been reflected by the phantom wall and is now travelling in the opposite direction. By comparison with Figure 7.32 it can be seen that the wave has travelled approximately twice the distance between frames (d) and (e) than for the 100ms delayed measurements. The phantom wall is at y =24 and so the wave has travelled a distance of approximately 22 units ('like' electrode spacings) in 3 frames corresponding to a speed of approximately $0.55ms^{-1}$, similar to before.

Figure 7.35 is a sequence of images produced from data taken in consecutive 2ms frames. The object being imaged was a small piece of copper covered pcb (15mmx28mm) which was attached to an elastic band. The elastic band was anchored on one side wall of the phantom (x =24) along the y =1 line. The elastic band was stretched along the length of the array and the projectile released to coincide with the start of the measurements. The object is represented by the increase in conductivity, the decrease in conductivity is the approximate position of the object in the previous frame. Any waves generated by the object will not appear in the images since their speed of travel is much slower than that of the projectile. For objects travelling at similar speeds to that imaged in Figure 7.35, the object will travel a significant distance in the measurement time - this will increase the blurring of the reconstructed image. In an attempt to reduce the blurring, the ramp filter was applied to the images of Figure 7.35 and the results can be seen in Figure 7.36 where

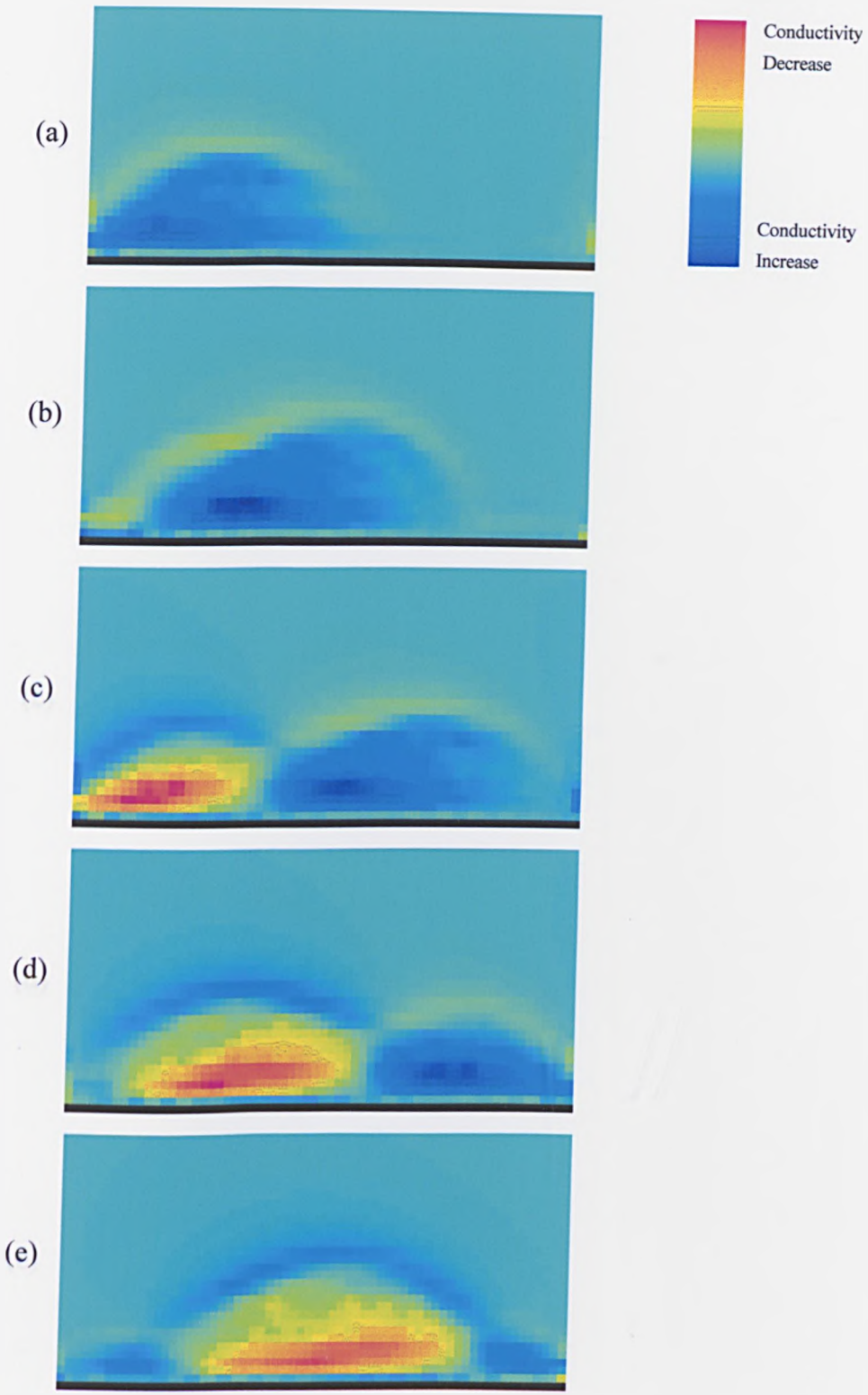

Figure 7.33 : A ramp filtered version of Figure 7.32.

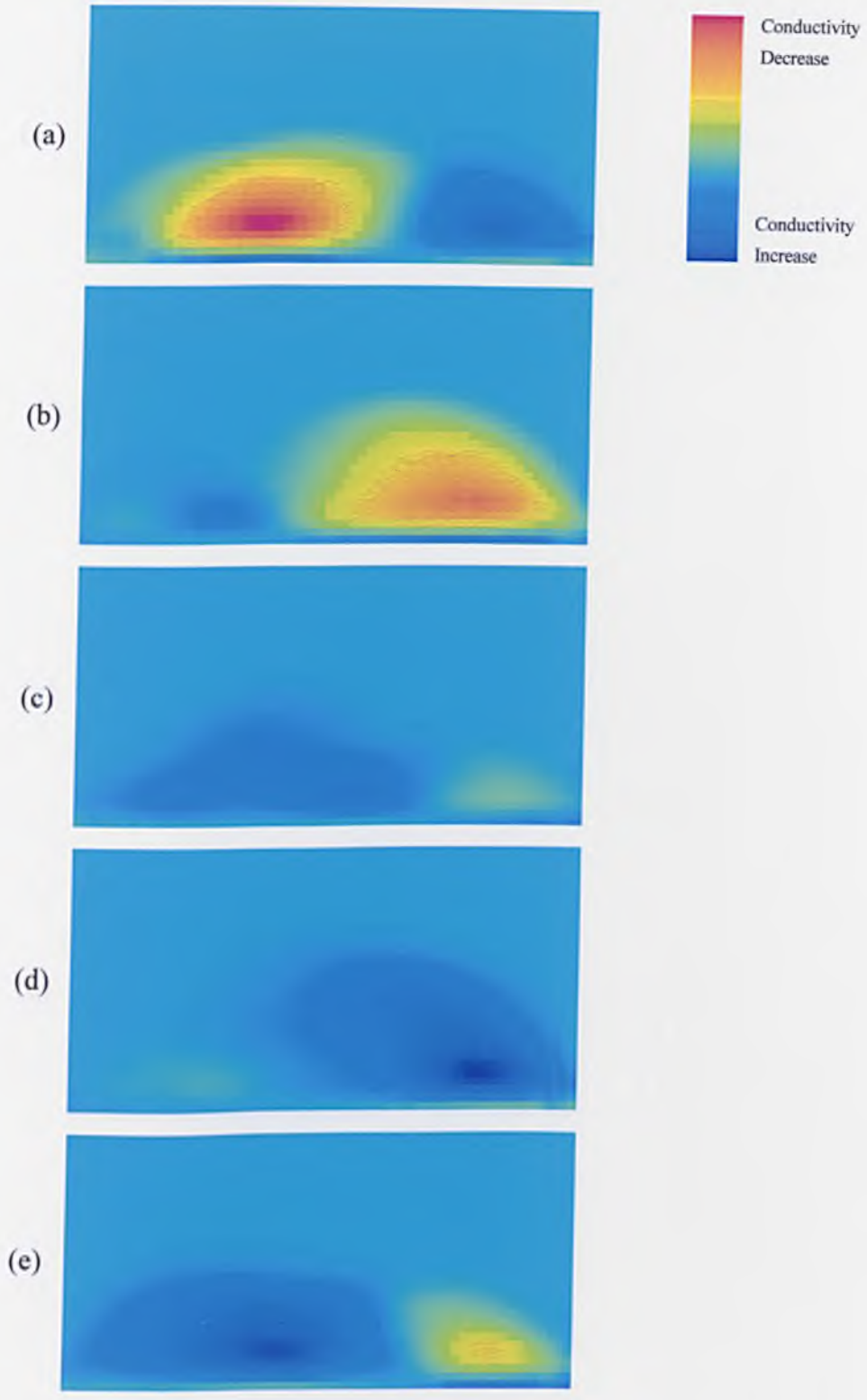

Figure 7.34 : Images of a plane wave in a pseudo-2D phantom of depth 20mm.

(a)-(e) A sequence of images produced by the WBP1 method (threshold=0.65mV) of a plane wave in pseudo-2D saline of conductivity σ=0.2Sm^{-1} and depth 20mm. The wave was approximately 5mm in amplitude and the time interval between frames is 200ms. (Max ΔV=70.6mV).

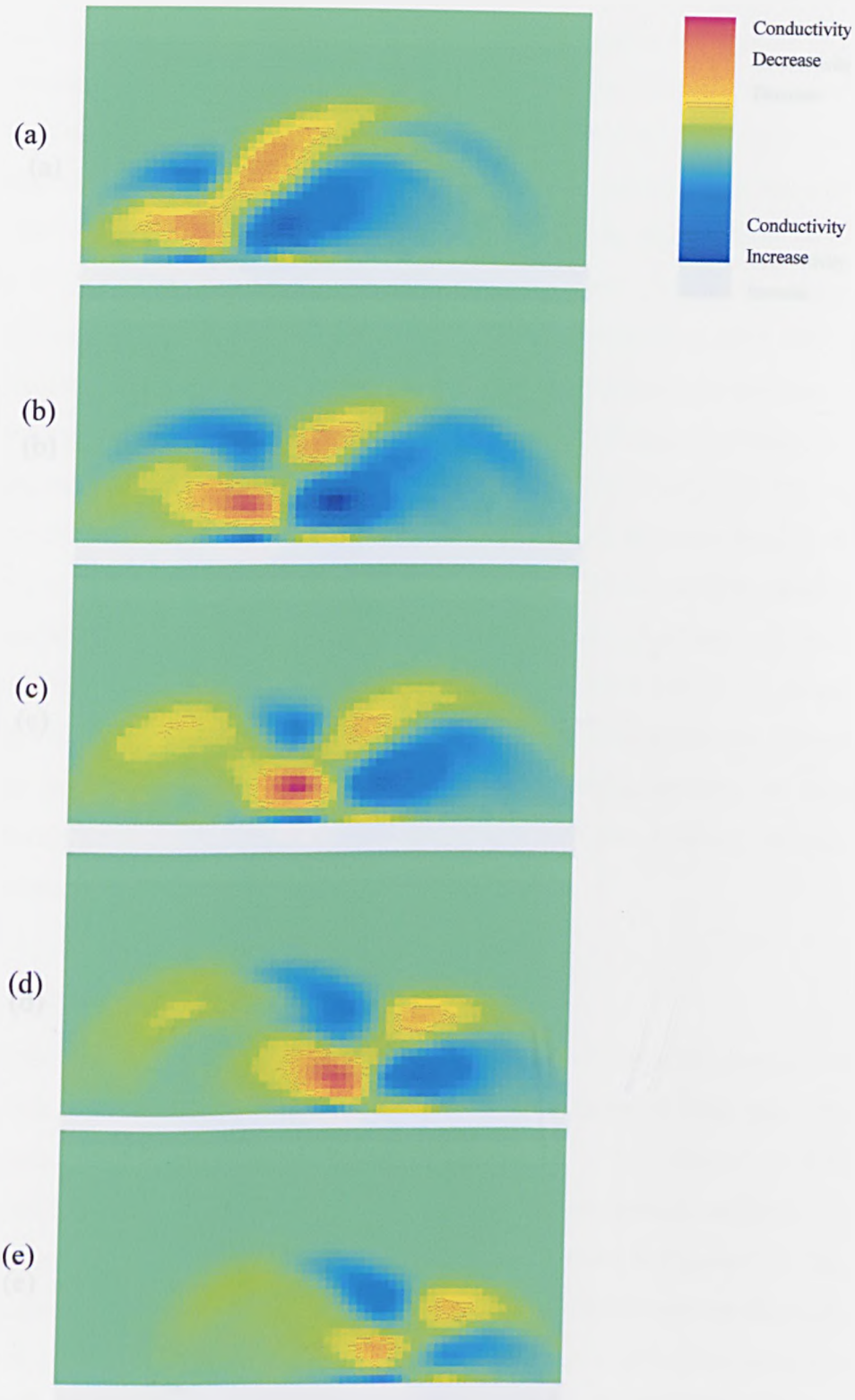

Figure 7.35 : Images of a projectile in a pseudo-2D phantom of depth 20mm.

(a)-(e) A sequence of images produced by the WBP1 method (threshold=0.49mV) of a copper covered projectile ($\sigma \rightarrow \infty$) of area 15x28mm in pseudo-2D saline of σ=0.2Sm^{-1} and depth 20mm. The frames were taken continuously and so represent 2ms intervals. (Max ΔV=18.4mV).

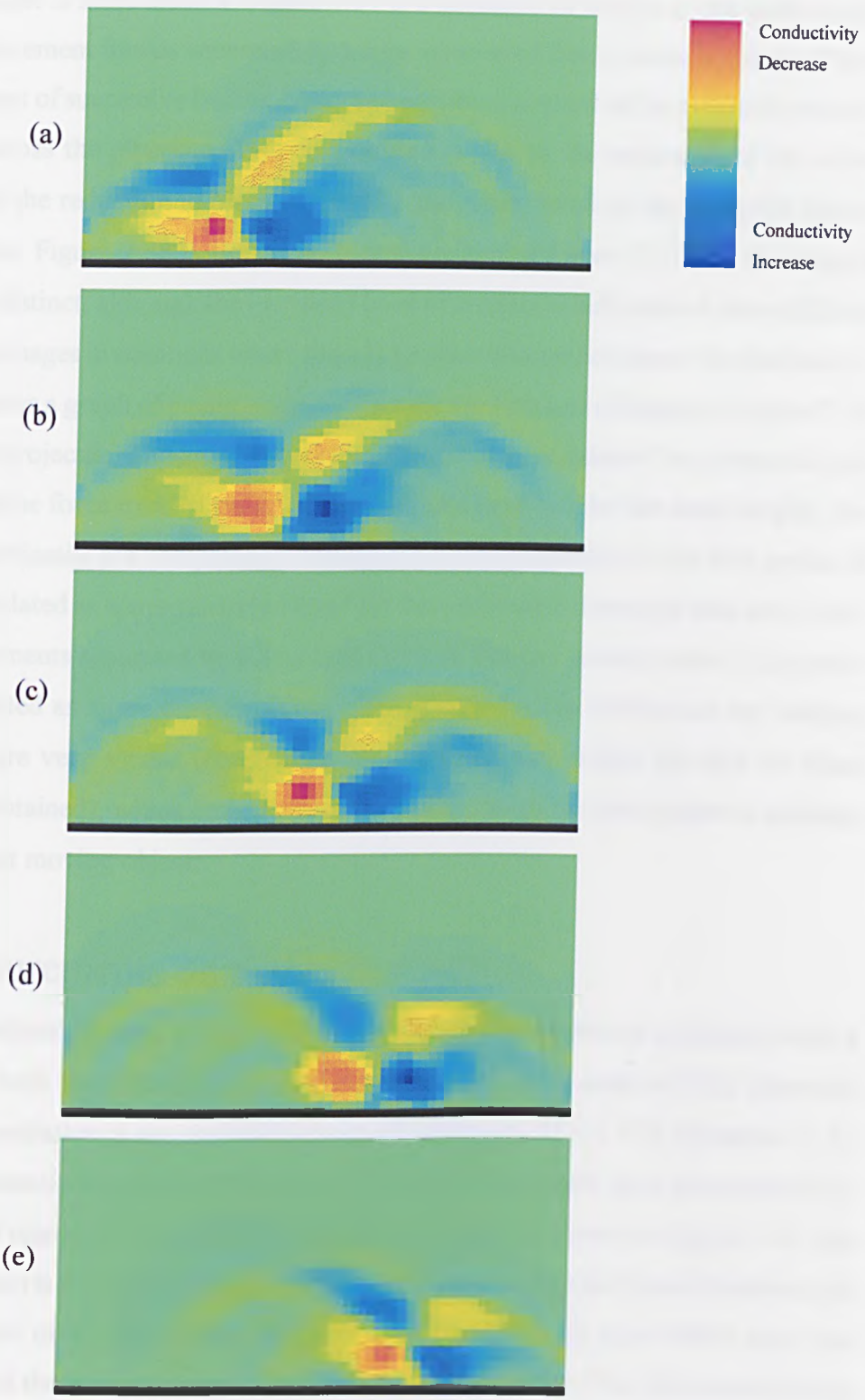

Figure 7.36 : A ramp filtered version of Figure 7.35.

the imaged object is more distinct. Figure 7.37 is a sequence of images of the same target but with measurement frames separated by a time interval of 2ms ie there is a time of 4ms between the start of successive frames. It can be seen that the speed of the projectile reduces as it moves across the phantom. This deceleration is due to the resistance of the saline combined with the reduction in force exerted by the elastic band as the projectile moves across the array. Figure 7.38 is the ramp filtered version of Figure 7.37 and the imaged object is more distinct, although the increased level of artefact would make it more difficult to interpret the images in situations where there is no prior information about the distribution. Figure 7.39 shows a graph of position against time for the two sets of images in Figure 7.35 and 7.37 of the projectile. The graph shows that, for the same position of the projectile (and therefore the same force exerted on it, since the elastic band will be the same length), the speeds of the projectile are comparable. The speeds of the projectile for the first period of motion are calculated as approximately $14ms^{-1}$ for the continuous measured data and $15ms^{-1}$ for the measurements separated by a 2ms time interval. For the second period, the speeds are both calculated as approximately $10ms^{-1}$. The speeds for the continuous and delayed measurements are very similar (considering the accuracy with which the data for these calculations is obtained), which demonstrates a possible use of this this system to estimate the speeds of fast moving objects.

7.5.4 Measurements on a 3D Phantom

This section presents images produced from measurements on a phantom with a depth of 21cm with the electrode array at the mid-depth (ie in units of 'like' electrode spacings, the boundaries of the phantom in the z-direction are $-7 < z < 7$). Equation {1.1} shows that the potential created in the medium of interest is dependent upon the conductivity of the whole 3D region. If the region is homogeneous then as shown in Figure 7.40, the current distribution is the same in all the planes which pass through the line of the electrode array, independent of θ. This means that each such plane has an equal effect upon the measurements and there is no distinguishability between the planes. This will cause blurring in the images of objects which are constant in the z-direction and perpendicular to the array of electrodes. In order to try to assess the significance of this blurring effect, some images were formed using the objects depicted in Figure 7.41 which were chosen to have the same cross sectional area. These are

a) A 15mm long square cross section perspex rod (17mm square) which is used to produce an inhomogeneity in one plane only.

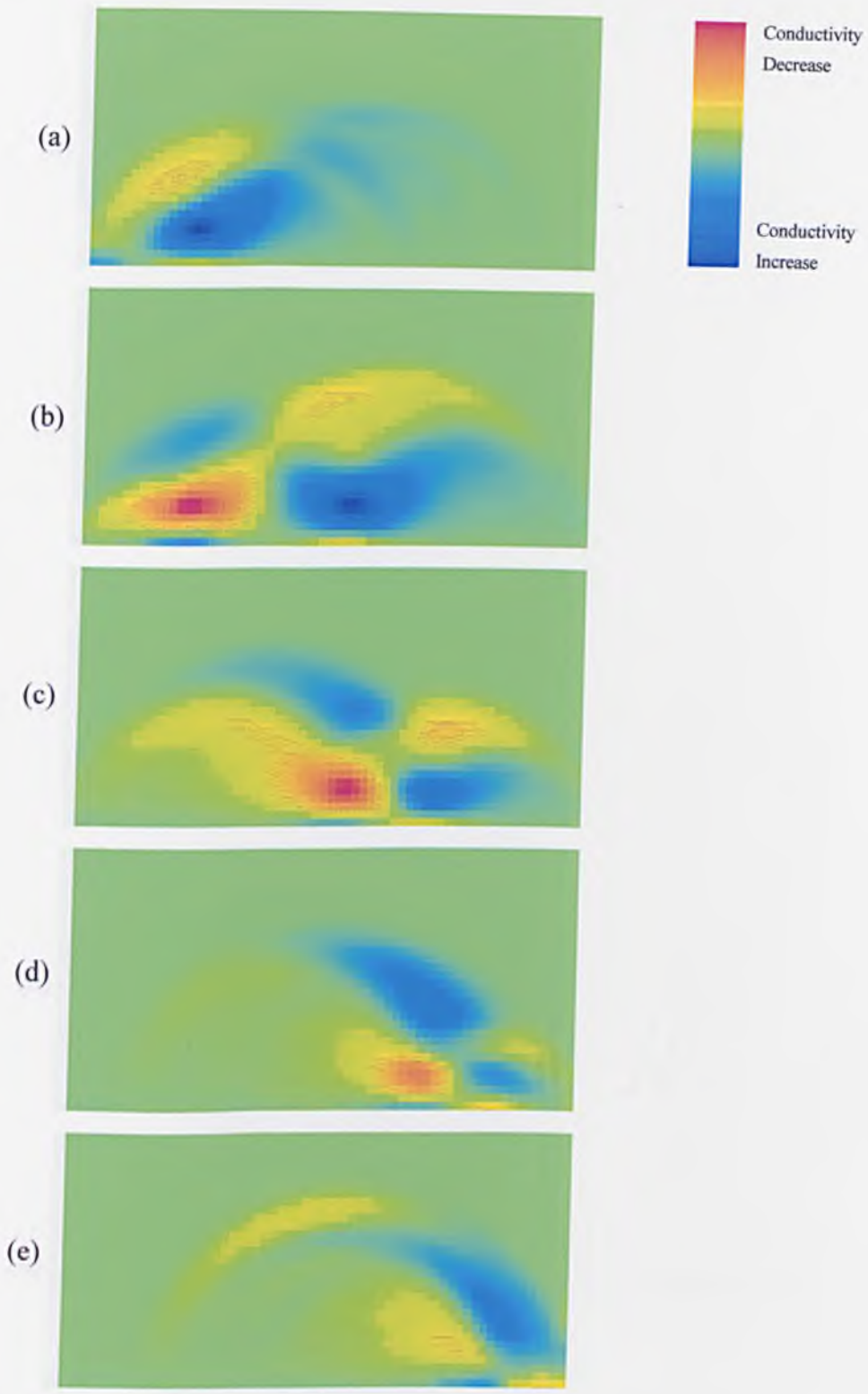

Figure 7.37 : Images of a projectile in a pseudo-2D phantom of depth 20mm.

(a)-(e) A sequence of images produced by the WBP1 method (threshold=0.49mV) of a copper covered projectile ($\sigma \rightarrow \infty$) of area 15x28mm in pseudo-2D saline of σ=0.2Sm^{-1} and depth 20mm. The frames were taken with a 2ms interval between them and so represent 4ms intervals.
(Max ΔV=24.6mV).

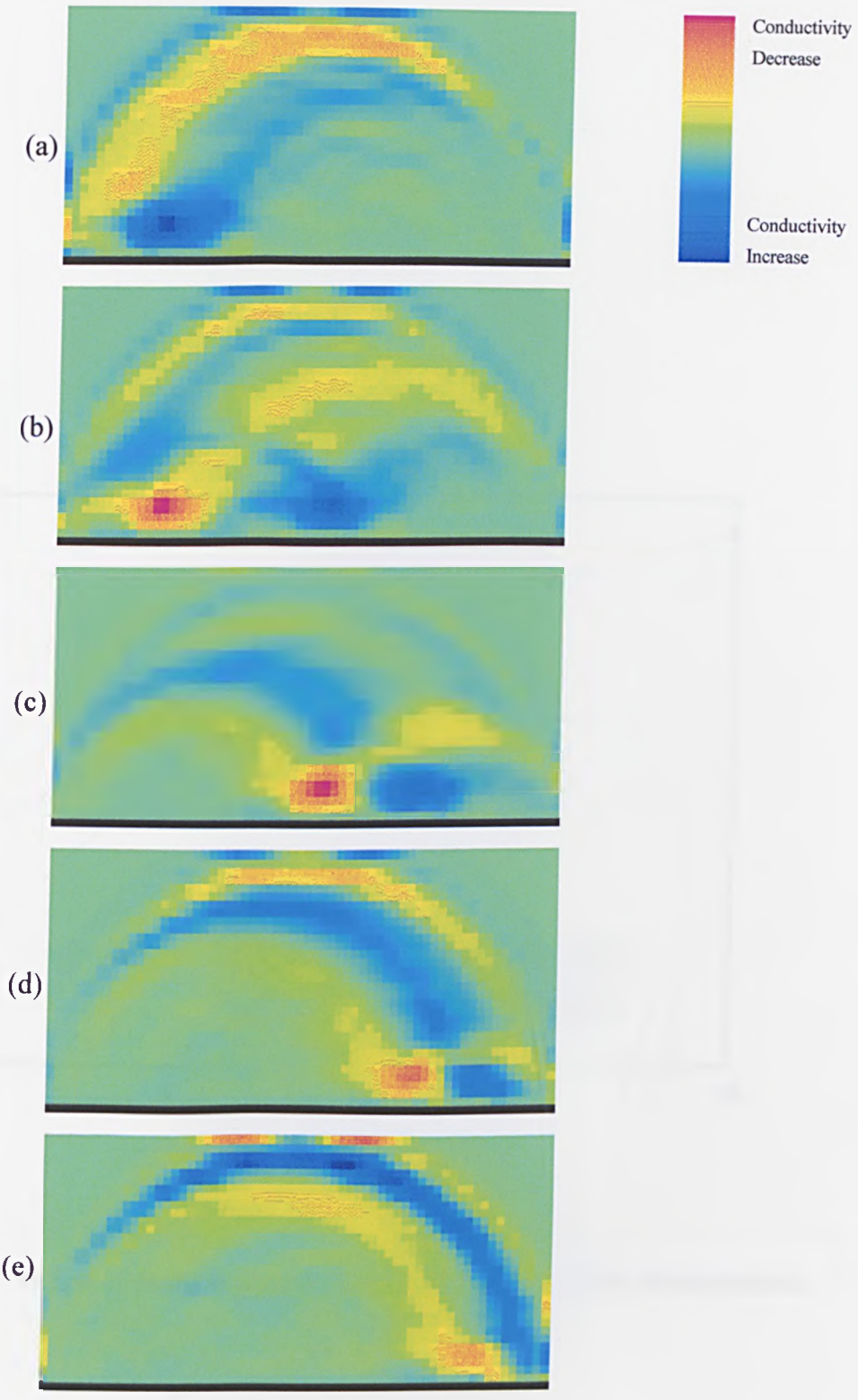

Figure 7.38 : A ramp filtered version of Figure 7.37.

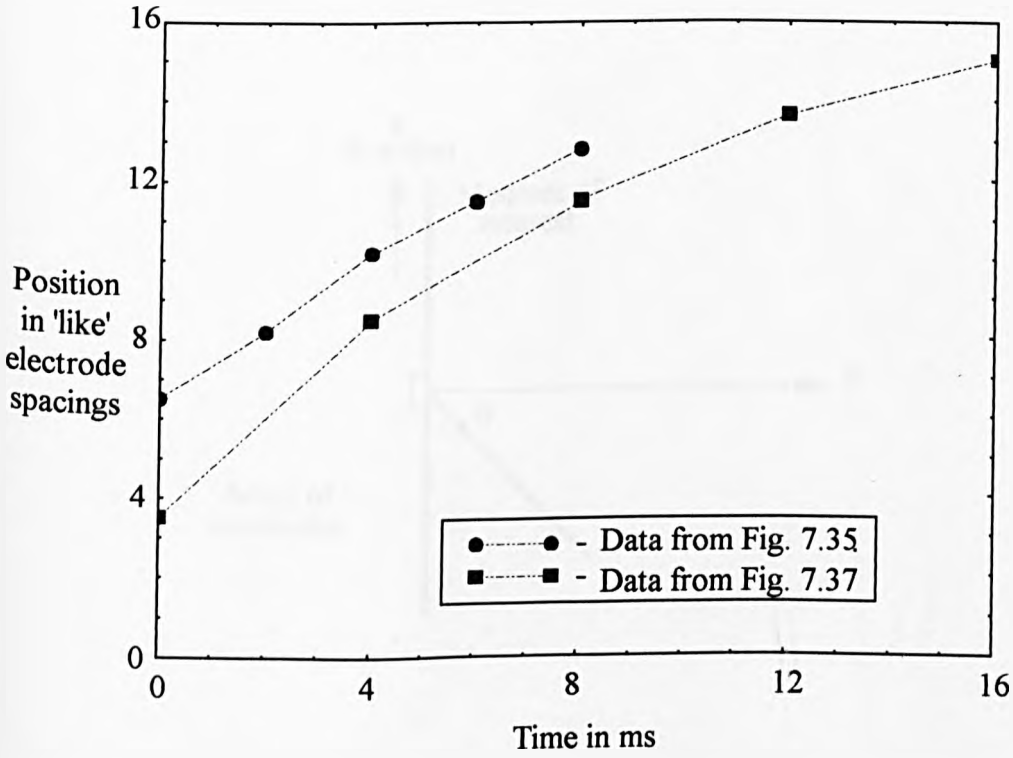

Figure 7.39 : Graph of position against time for the two projectile measurements.

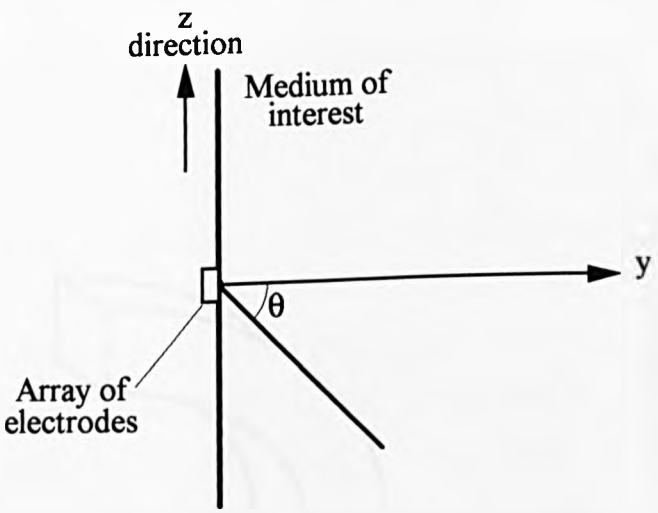

Figure 7.40 : Diagram showing the electrode array and the planes in which the current flows (all planes for $-90° \leq \theta \leq 90°$). The *x*-axis is along the array of electrodes.

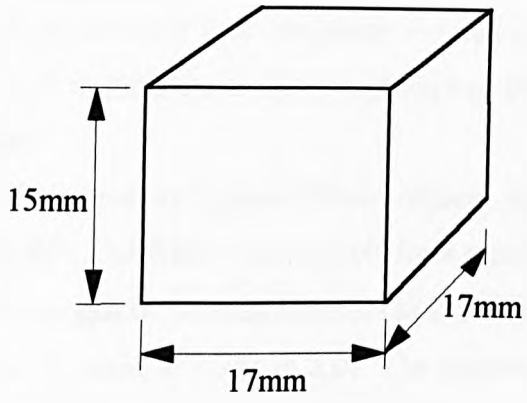

(a)

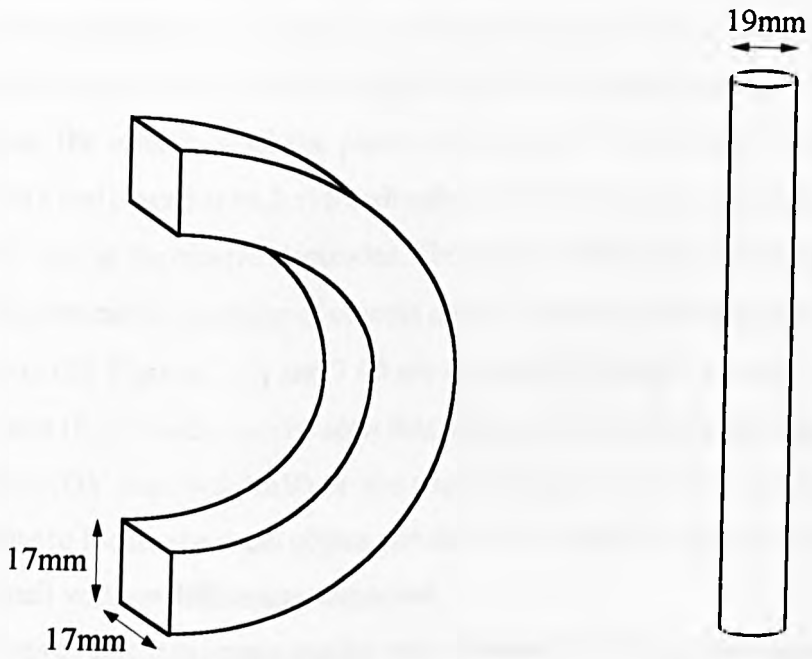

(b) (c)

Figure 7.41 : Perspex objects used in the 3D phantom.

(a) A square cross section block.

(b) A half annulus of square cross section (the point O is the centre of the semicircles from which the annulus is formed and on the plane which would bisect the half annulus to form two further half annuli).

(c) A cylinder of circular cross section with diameter 19mm and length 490mm.

b) A perspex half annulus of square cross section (17mm square) to be placed with its geometric centre, *O* in the figure, coincident with y=0 to generate an inhomogeneity at equal distances from the array in all the planes rotated about the array.

c) A 19mm diameter rod to generate an inhomogeneity at varying distances from the array in all the planes.

Figures 7.42 to 7.45 compare images of these objects. Figure 7.42(a) and 7.43(a) are images produced by WBP1 and WBP2 respectively from measurements made while the small square cross-section length of perspex (object (a) listed above) was suspended so that its centre lay in the z =0 plane at point (4,2,0). The maximum voltage difference is 1.0mV at the receive electrodes. Figure 7.42(b) and 7.43(b) are images produced from data collected while a half annulus of square cross-section piece of perspex was suspended in the phantom. The half annulus of radius 2 units was placed so that its origin (point *O* in Figure 7.41(b)) was on the point (4,0,0) hence producing a conductivity inhomogeneity at equal distances from the array for all the planes through the array. The imaged object is larger in size than that shown in figure (a) and the maximum voltage difference is 7.8mV at the receive electrodes which is much larger than for an inhomogeneity in a single plane. This is because the effects of all the planes add. Figure 7.42(c) and 7.43(c) are images produced from a rod placed at (4,2,z) for all values of z which produced a maximum voltage difference of 2.1mV at the receive electrodes. The position of the rod is found quite accurately because of the preferential imaging of objects close to the array although the image is more distorted than in (b). Figures 7.44 and 7.45 are similar to Figures 7.42 and 7.43 except that the objects are at (8,4,z) and it can be seen that although the half annulus is imaged, neither the small object (DV max = 0.4mV) or the rod (DV max = 0.4mV) can be found in this case. The failure to locate the small object and the rod is probably due to the effects of noise on the very small voltage differences expected.

No improvement in image quality was obtained by filtering the images, which is as expected, since the limiting factor in imaging 3D objects in this system is measurement noise and not image formation inaccuracies.

7.6 Conclusions

The profiles presented earlier in this chapter show the similarity between measured and simulated data for objects placed close to the array. However, as the objects move further from the array, noise on the measurements becomes significant which will limit the depth at which objects can be imaged. The random noise will be reduced by averaging the

(a)

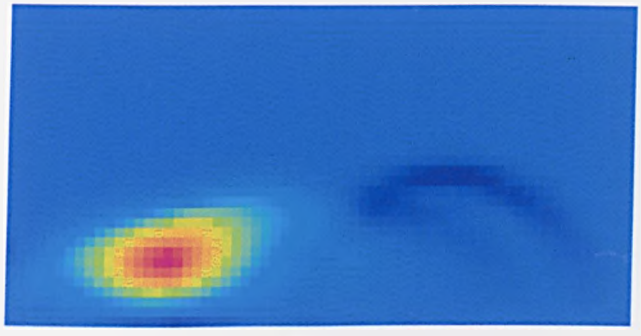

(b)

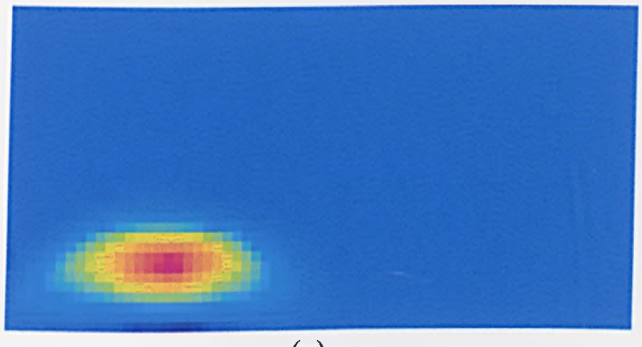

(c)

Figure 7.42 : Images of test objects in a 3D phantom.

(a) The image produced for a 1.1unit square cross section perspex block of length 20mm suspended at (4,2,0) to lie equally above and below the z=0 plane by WBP1(threshold=0.36mV). (Max ΔV=1.0mV).

(b) The image produced for a half perspex annulus of square cross section of 1.1 unit and radius 2 units suspended such that its origin is coincident with the point (4,0,0) by WBP1(threshold=0.29mV). (Max ΔV=7.9mV).

(c) The image produced for a perspex rod of diameter 1.2 units placed at the point (4,2,z) for all z by WBP1(threshold=0.29mV). (Max ΔV=2.1mV).

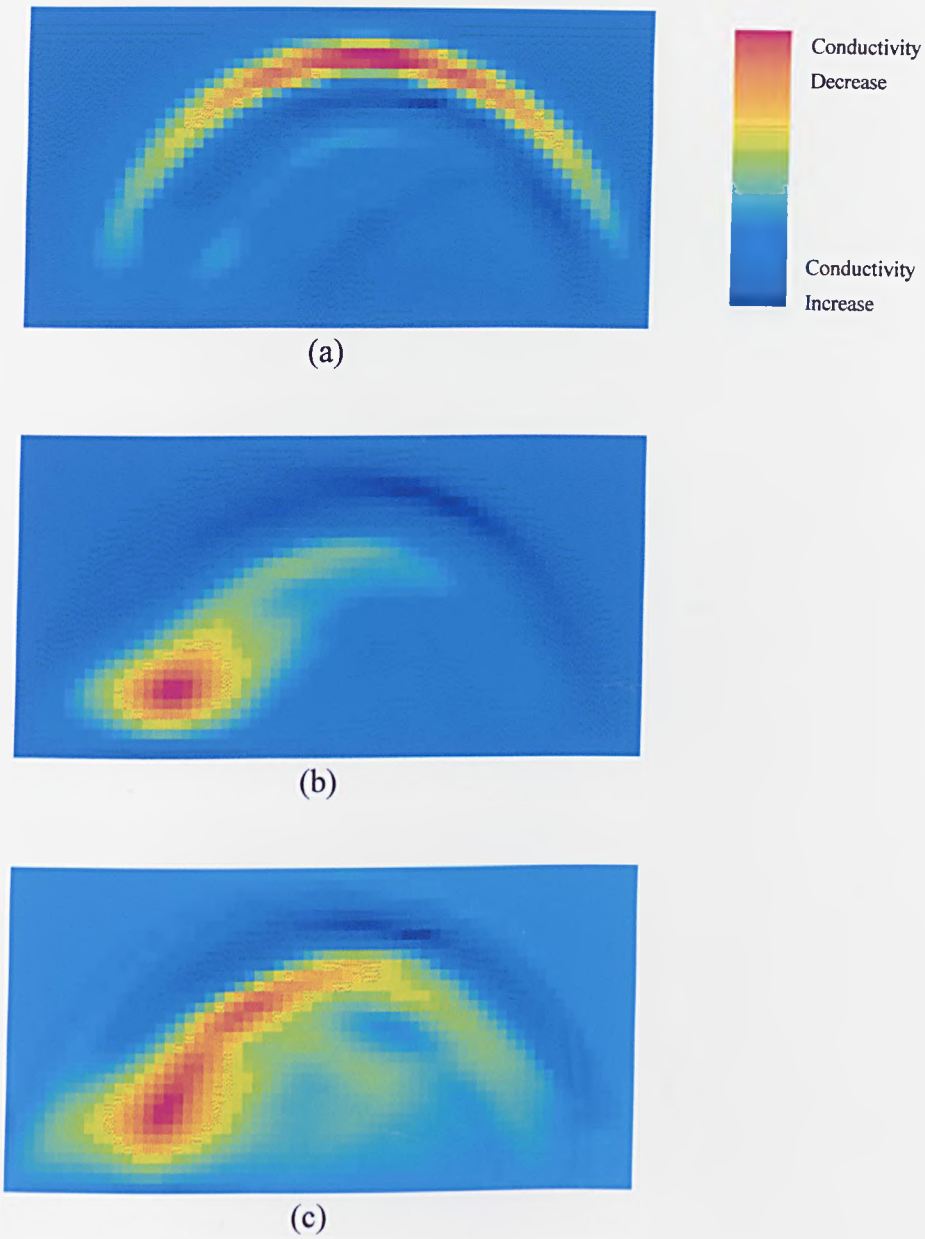

Figure 7.43 : Images of test objects in a 3D phantom.

(a) The image produced for a 1.1unit square cross section perspex block of length 20mm suspended at (4,2,0) to lie equally above and below the z=0 plane by WBP2. (Max ΔV=1.0mV).

(b) The image produced for a half perspex annulus of square cross section of 1.1 unit and radius 2 units suspended such that its origin is coincident with the point (4,0,0) by WBP2. (Max ΔV=7.9mV).

(c) The image produced for a perspex rod of diameter 1.2 units placed at the point (4,2,z) for all z by WBP2. (Max ΔV=2.1mV).

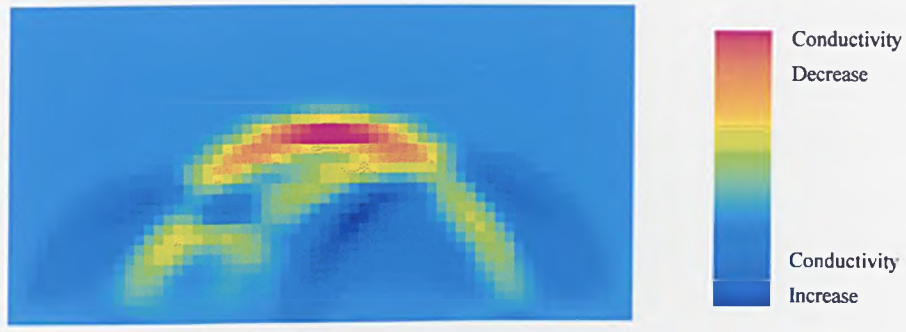

(a)

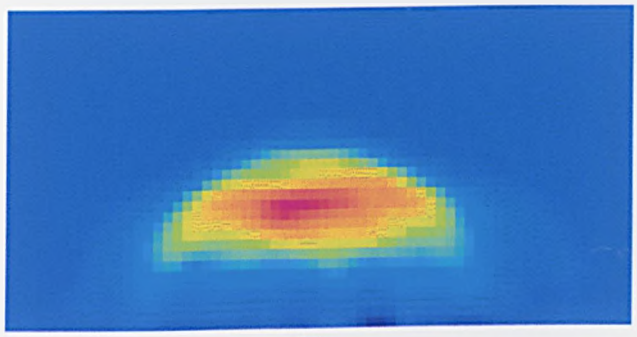

(b)

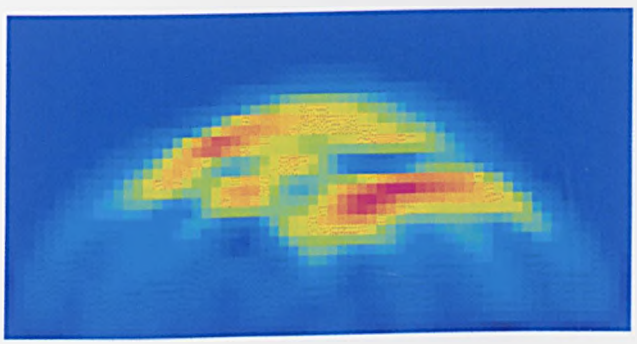

(c)

Figure 7.44 : Images of test objects in a 3D phantom.

(a) The image produced for a 1.1unit square cross section perspex block of length 20mm suspended at (8,4,0) to lie equally above and below the z=0 plane by WBP1(threshold=0.10mV). (Max ΔV=0.4mV).

(b) The image produced for a half perspex annulus of square cross section of 1.1 unit and radius 4 units suspended such that its origin is coincident with the point (8,0,0) by WBP1(threshold=0.10mV). (Max ΔV=5.9mV).

(c) The image produced for a perspex rod of diameter 1.2 units placed at the point (8,4,z) for all z by WBP1(threshold=0.07mV). (Max ΔV=0.4mV).

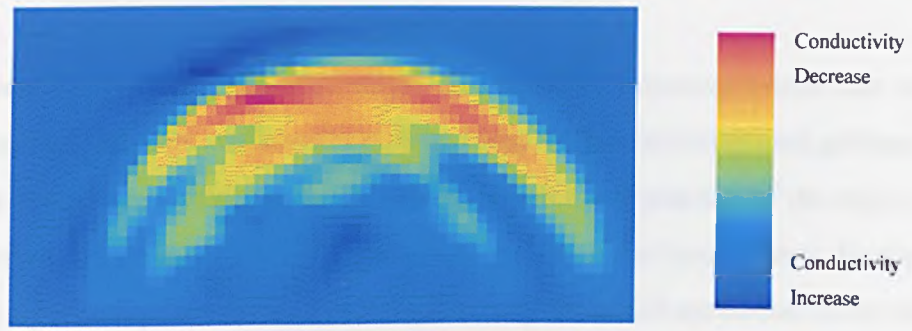

(a)

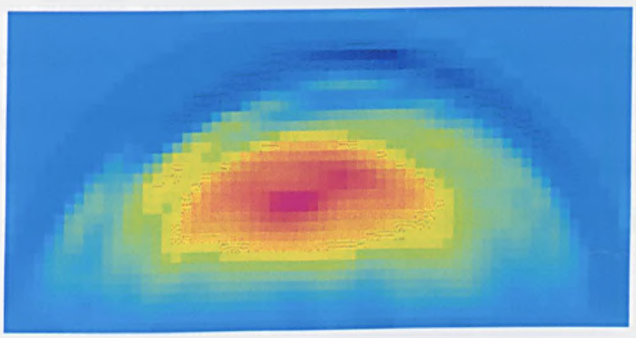

(b)

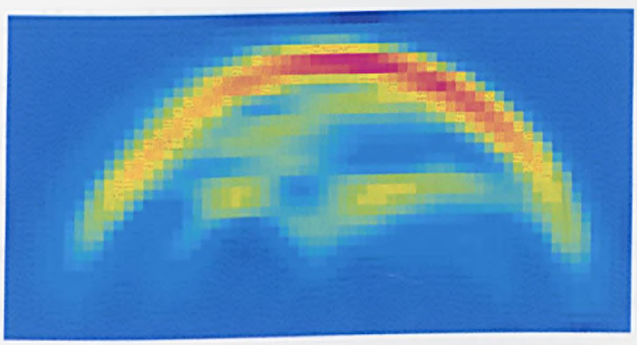

(c)

Figure 7.45 : Images of test objects in a 3D phantom.

(a) The image produced for a 1.1unit square cross section perspex block of length 20mm suspended at (8,4,0) to lie equally above and below the z=0 plane by WBP2. (Max ΔV=0.4mV).

(b) The image produced for a half perspex annulus of square cross section of 1.1 unit and radius 4 units suspended such that its origin is coincident with the point (8,0,0) by WBP2. (Max ΔV=5.9mV).

(c) The image produced for a perspex rod of diameter 1.2 units placed at the point (8,4,z) for all z by WBP2. (Max ΔV=0.4mV).

profiles, but any coherent noise, such as common mode voltages, will not be reduced by averaging and these would have to be reduced to increase the depth of detection of the system.

It has been shown that images of single and multiple inhomogeneities can be generated from the measurements made by the system. Images generated from data gathered from objects close to the array reflect more accurately the size and position of the objects than images generated from objects further from the array. This is for two reasons. Firstly, the image forming algorithm produces blurred images of objects which are further from the array, even when using noise free analytically generated data. Secondly, objects further from the array cause smaller voltage differences which are harder to detect in the presence of noise. For objects further than approximately 4 'like' electrode spacings from the array, the expected voltage differences are of a similar amplitude to the noise and so the blurring is exacerbated in these cases. This behaviour is consistent with that of circular EIT systems where the image forming at the centre of the region to be imaged (furthest from the array) is poor.

For two objects the resolution was positionally dependent : the resolution close to the array was better than the resolution further from the array. This effect is observed in other injected [21] and induced [62] EIT systems which use an encircling array. For particular object distributions masking along equipotentials occurred and this could not be reduced by applying any of the image filters available.

Moving targets were successfully detected at speeds of approximately $0.15ms^{-1}$ and $15ms^{-1}$ in a pseudo 2D medium, although at speeds of $15ms^{-1}$, the projectile will travel approximately two units ('like' electrode spacings) during the 2ms measurement time which will give rise to considerable blurring in the reconstructed image.

Some images of objects in a 3D medium were produced, but because the voltage differences resulting from the presence of a object were much smaller than in the pseudo-2D case, detection and imaging were more difficult. A number of objects were imaged and the largest voltage differences and best images were produced from objects which produced an inhomogeneity at the same point in each of the planes in which current flowed.

The filtered backprojection method and ramp filter were applied to some of the images and, in general, the filters appear to produce an improvement in the image quality when the signal to noise of the measurements is good, but introduce considerable artefact when the signal-to-noise ratio is poor. This is not surprising since the filters are enhancing the existing images and if these contain small artefacts caused by the presence of noise,

these artefacts will also be enhanced, along with the imaged object. When applied to the images, the filtered backprojection introduced too much artefact to be useful (this filter appears to be especially sensitive to noise) and sensible images could not be produced from data which had not been averaged to reduce noise. In some cases the ramp filter produced a better definition in the edges of the object and reduced the blurring along the equipotentials, making the object in the image more circular than in the unfiltered image.

Chapter 8 Conclusions and Suggestions for Further Work

8.1 Summary

The feasibility of using a narrowband multiple frequency simultaneous drive EIT system with a fast measurement time has been demonstrated in the context of a linear array. It has been shown that images similar in quality to those constructed from simulated data can be produced from data measured in 2ms using a simultaneous drive methodology. Image sequences of moving targets with measurement frame rates of up to 500Hz have been presented.

The rest of this chapter will be concerned with the conclusions that can be drawn from the work presented and with some suggestions for applications and further work

8.2 Conclusions

There are a number of important factors which should be considered in the design of a simultaneous drive system. These include the detection process, the dynamic range requirements, the common mode voltages generated and the measurement time.

The ability of the detector to distinguish between the signals generated by each drive is fundamental to a simultaneous drive technique. It has been demonstrated that by using different frequency sinewaves as the drive waveforms, together with a digital detection process based on an FFT the signal generated by each drive can be successfully detected. The crosstalk between the digital filters was lower than -72dB.

The performance of the narrowband multiple frequency simultaneous drive EIT system was limited by the large dynamic range required of the receiver circuitry and the large common mode voltages inherent in the system operation. The linear array is a particularly demanding electrode arrangement in terms of the receiver dynamic range requirements in comparison with the more usual encircling array. It was shown in Chapter 2 that the ratio of the largest instantaneous potential difference between two adjacent receive

electrodes to the amplitude of the smallest frequency component in the potential difference was 72dB for a 3D and 53dB for a 2D medium. Furthermore, if a change of 25% in the smallest component of potential difference caused by a change in conductivity was to be detected, the receiver requirement for dynamic range increased to 86dB for a 3D and 67dB for a 2D medium. This 3D dynamic range requirement is very large, and a more realistic dynamic range of 67dB was used, which allowed the full 2D dynamic range of measurements to be made. The receiver dynamic range was increased by a factor of 16 by using a digital filtering technique.

If the system were to be applied to an encircling array, the performance should be better than for a linear array. The encircling array requires a much lower dynamic range in the receiver circuitry (48dB for 2D and 61dB for 3D in comparison with 67dB and 86dB for a linear array), and so for a receiver with the same resolution, the voltage differences can be measured with greater precision.

The dynamic range problem can be eased in single frequency systems, by using programmable gain amplification to amplify small signals by a predetermined amount so that the signal at the input of the ADC is approximately the full scale of the input range, and so resolution is not lost. Such an approach is not feasible in the simultaneous drive system because the small signals at one frequency are one component of a multifrequency signal which also contains large components at other frequencies.

The common mode voltage present in a simultaneous drive EIT system consists of two components, one inherent to the injected current EIT process, and one caused by mismatches in the drive and receive channels. Common mode feedback was used to reduce the common mode voltage caused by mismatches between channels and succeeded in reducing the common mode voltage by a factor of 10, but also introduced phase shifts in the residual common mode voltage. These phase shifts, in conjunction with the finite CMRR of the subtractor and buffer matching, caused some corruption of the smallest signals.

The measurement time of 2ms was a compromise between speed of measurement and the range of frequencies used. It would be possible, for example, to reduce the measurement time to 1ms at the expense of doubling the frequency interval between drive signals to 1kHz, giving a range of 20kHz to 35kHz for the drive frequencies. However, there are a number of issues that would have to be considered before this or other reductions in measurement time were to be employed. The conductivity of many biological tissues and

chemicals vary with frequency and so for a large range of drive frequencies, the assumption that the conductivity remains constant across the drive frequency range becomes more approximate. However, it is quite possible that for particular materials, the conductivity variation over a larger range of frequencies is small and in these cases, this limitation will not apply. If the base frequency were doubled to maintain the same proportional bandwidth, the sampling rate would also need to be doubled, and this would both increase the cost of the components and complicate the control of the system. A reduction in measurement time would also increase the bandwidth of the detection filters which would decrease the signal-to-noise ratio of the detected signal.

The image forming algorithm used to produce the images for the linear array was weighted backprojection. No attempt was made to generate a new image forming algorithm, but for conductivity distributions where the object was placed close to the array (within 4 'like' electrode spacings) this image forming algorithm proved to be a limiting factor, which is demonstrated by the fact that some of the images presented in Chapter 7 produced from measured data are indistinguishable from images produced from analytically generated data. In these cases it would be necessary to improve the image forming algorithm before the effects on the image of the noise in the measured data could be detected. Filters were applied to the image in an attempt to improve the image quality and although the ramp filter improved the definition of the edges of objects, the other filters, in general, produced poor results on the images produced from analytically generated data and so, not surprisingly, did not improve images produced from measured data.

Thresholding was applied to the images to prevent small data values, ie those most likely to be affected by noise, having a disproportionate effect on the image quality. Although thresholding of the image reduced the maximum depth at which objects could be imaged, the thresholded images produced from objects close to the array were, in some cases, better than images produced using non-thresholded simulated data.

It has been shown that images of single and multiple inhomogeneities of conductivities less than and greater than the background conductivity can be produced. The distance from the array at which objects could be imaged was less than the expected value of half the array length. However, images formed from analytically generated data for objects at a distance greater than a quarter of the array length from the array were very poor and so some of the depth limitations are due to the reconstruction algorithm. However,

when the predicted profile of an object placed at greater than a quarter of the array length was compared with the profile of the measured data, no similarity could be seen. This is not surprising since objects placed towards the boundary of the area of detection are predicted to cause voltage differences smaller than 1 least significant bit of the A/D converter.

Images of moving targets, produced from measurements made in 2ms with a specified time interval between the frames or continuous measurements made in 2ms intervals, were shown in Chapter 7. It has been shown that it is possible to measure rapidly changing conductivity distributions (objects travelling at speeds of approximately $15ms^{-1}$ have been imaged) using a simultaneous drive methodology.

Images of 3D conductivity distributions were formed, despite the measured voltage differences being much smaller than for the pseudo-2D case. However, the depth of detection was reduced, which was expected since the dynamic range required to obtain the maximum depth of detection was too large. The inability of the system to distinguish between the planes passing through the electrode array for the 3D case was evident, in the form of blurring of objects with a large z dimension. This 3D problem is common to injected and induced systems which use an encircling array and it is not possible to compensate for the blurring using a single stationary array of electrodes. For multiple arrays or a mobile array, a set of measurements could be made for each array or position and an image generated of a plane of the conductivity distribution at a particular depth (planes of constant y value for the coordinate system used here). A similar process to this has been attempted by Kotre using orthogonal multiple arrays with promising results [87].

8.3 Applications

The most likely application for a narrowband multiple frequency simultaneous drive EIT system is industrial. The increase in measurement speed to be gained from using simultaneous drives could be useful for imaging fast industrial processes, whereas it is unlikely that biological or geological phenomena occur fast enough to make it advantageous to use a system optimised for speed. Many man-made containers have flat surfaces where the linear array could be used, for example in the wall of a tank, or where the array could be swept across the surface of a conducting liquid. The system could also be applied to a circular geometry such as pipes and mixing vessels.

If the narrowband multiple frequency simultaneous drive EIT system, were to be used medically, a reduction in injected current amplitude would be necessary to comply with BS5724. Although a frame rate of 500Hz would not be required for medical imaging,

it would be possible to configure the system such that, for example, 10 consecutive frames were taken in 2ms intervals and then another 10 frames taken after the desired time interval had elapsed. This would allow averaging of the consecutive frames to give an increase in signal-to-noise ratio (by a factor of approximately 3 for 10 averages), which would go some way towards offsetting the reduction in signal amplitude levels. However, the programmable gain amplification which can be used with single frequency multiplexed systems gives a much better signal-to-noise ratio without averaging and so the use of such a system may be more appropriate if signal-to-noise ratio is of paramount importance. Encircling arrays are usually used in medical applications, although a linear array could be used for particular applications. Few areas of the body are perfectly flat, but spring loaded electrodes designed to apply equal pressure to the electrode, but allow small variations in surface shape, could be used.

In certain applications, eg geology where accuracy and resolution are much more important parameters than the speed of image generation, the simultaneous drive method would be inappropriate. The required signal-to-noise ratio would be more readily achieved by a single multiplexed drive system.

8.4 Further Work

Further work or development on the existing system or one similar should concentrate on the following areas.

The application of common mode feedback to the medium of interest needs to be investigated further since it is an essential component of a system using a simultaneous drive strategy. Two common mode feedback circuits were used in this system to ensure symmetry, but this arrangement is not necessarily the optimum configuration. Furthermore, the common mode feedback circuitry used produced significant phase shifts at the frequencies of the drive signals. A wideband low pass filter would be an ideal common mode feedback circuit, but generally has stability problems [44][58] in this application and so future work should investigate other circuits which could be used for common mode feedback.

The memory ICs which are mounted on the backplane and used to store the measurement data should be replaced by either a larger memory, so that more frames of data can be stored, or by a fast processor to perform the FFT and the weighted backprojection algorithm before passing the image data to the PC for storage or immediate display. At present, the second option would only be feasible for delayed measurements since processors available would not be able to perform the processing required in 2ms. However, it is quite

possible that in the future ICs will become available which will work at the required speed. It should be possible to perform the required processing in 20-50ms and so if a time interval of this order was used between frame measurements it would be possible to view the images in real time. For continuous measurements or measurements delayed by less than 20ms there would be little point in producing the images in real time since it would be too fast for the human observer. In this case it would be useful to have a large quantity of memory available for storage so that data for a reasonable period of time could be stored and the subsequent images viewed at a lower speed. One frame of data requires 8192 bytes for storage before processing which reduces to 1920 bytes after the FFT has been performed. The data acquired in successive 2ms frames during 1 second of continuous measurements would therefore require a memory space of 4Mbytes.

The image forming algorithm used in this system produced images from measured data which were, in some cases, indistinguishable from images produced from simulated data. The development of a new image forming algorithm was not undertaken in the course of this project, but in order to take full advantage of the system capabilities, this should be considered.

One of the objectives of looking at a fast linear system was in the interests of mobility of the array and so it would be useful to place the front-end hardware - the current sources and the receive electrode buffers - in a box with the electrodes in a fixed position protruding from the box. This would make the probe mobile and allow it to be swept across the surface of a region of interest. The circuitry presently mounted at the phantom could be reduced to a hybrid or surface mount version in the interest of size reduction of the probe. Buffers of this type have already been constructed [88], although the cables will limit the mobility somewhat. If the surface is not even, contact impedance may cause a problem since it will not necessarily be the same for each measurement set, but if the surface is a liquid, the contact resistance will be similar and it should be possible to produce images.

It is possible that the method of narrowband multiple frequency simultaneous drive could be applied by groups using wideband multiple frequencies for tissue characterisation if a decrease in measurement time is required. At present, such groups drive a single electrode pair at any one time with a swept frequency signal and take measurements at other electrode pairs. The drive is multiplexed to the next drive pair and the measurements repeated. It would be possible to drive each drive pair simultaneously with a frequency similar to the other drive frequencies (Eg for a nominal frequency of 10kHz, the drives could be at 10.0kHz,10.5kHz, 11.0kHz etc.), and then the next wideband

frequency could be applied. In this way the wideband frequencies would still have to be applied serially to the medium of interest, but all the drive pairs could be simultaneously injecting current of slightly different narrowband frequencies thus removing the need for multiplexing the drives. Problems with this method would include the high sampling frequency required (it may be necessary to down convert the signal before sampling) and the difficulties in matching the channels across the wideband frequency range.

A multiple drive strategy could also be applied to an induced current EIT system. Usually 3 coils are excited serially to induce current in the circular medium of interest (although more coils have been proposed). The coils could, in principle, be excited at the same time with different frequencies if a reduction in measurement time was required. The common mode problem would be significantly reduced (the current is induced and so no mismatches in drive current occur), but it would be necessary to consider the mutual coupling of the coils and the effect of this on the induced currents.

List of References

[1] Barber D.C. and Brown B.H., "Applied potential tomography", J. Phys. E. : Sci. Instrum., Vol. 17, 1984, 723-732.

[2] Purvis W.R., Tozer R.C., Anderson D.K. and Freeston I.L., "Induced current impedance imaging", IEE Proc. A, 1993, Vol. 140, No. 2, 135-141.

[3] Schlumberger C., "Etude sur la prospection electrique du sous-sol", Gauthier-Villars et Cie, Paris, 1920.

[4] Sharma P.V., "Geophysical methods in geology", Elsevier, 1986.

[5] Henderson R.P. and Webster J.G., "An impedance camera for spatially specific measurements of the thorax", IEEE Trans. Biomed. Eng., 1978, Vol. BME-25, 250-254.

[6] Barber D.C., Brown B.H. and Freeston I.L., "Imaging spatial distributions of resistivity using applied potential tomography", Electron. Lett., October 1983, Vol. 19, No. 22, 933-935.

[7] Brown B.H. and Seagar A.D., "The Sheffield data collection system", Clin. Phys. Physiol. Meas., 1987, Vol. 9, Suppl. A, 91-97.

[8] Kim Y. and Woo H.W., "A prototype system and reconstruction algorithm for electrical impedance techniques in medical body imaging", Clin. Phys. Physiol. Meas., 1987, Vol. 8, Suppl. A, 63-70.

[9] Zhu Q. *et al*, "An adaptive current tomograph using voltage sources", IEEE Trans. on Biomed. Eng., 1993, Vol. 40, No. 2, 163-168.

[10] Smith R.W.M., Freeston I.L. and Brown B.H., "A real-time electrical impedance tomography system for clinical use - design and preliminary results", IEEE Trans. Biomed. Eng., 1995, Vol. 42, No. 2, 133-140.

[11] Zhu Q.S. *et al*, "Development of a real-time adaptive current tomograph", Physiol. Meas., 1994, Vol. 15, Suppl 2A, 37-43.

[12] Dickin F.J., "Resistive electrical impedance tomography - design reports and indication of industrial applications", Proc ECAPT, 1993 (Karlsrhue), 7-10.

[13] Barber D.C., "Quantification in impedance imaging", Clin. Phys. Physiol. Meas., 1990, Vol. 11, Suppl. A, 45-56.

[14] Griffiths H. and Zhang Z., "A dual frequency electrical impedance tomography system", Phys. Med. Biol., 1989, Vol. 34, No. 10, 1465-1476.

[15] Griffiths H. and Ahmed A., "A dual frequency applied potential tomography technique : Computer simulations", Clin. Phys. Physiol. Meas., 1987, Vol. 8, Suppl. A, 103-107.

[16] McArdle F.J., Sugget A.J., Brown B.H. and Barber D.C. "An assessment of dynamic images by applied potential tomography for monitoring pulmonary perfusion", Clin. Phys. Physiol. Meas., 1988, Vol. 9, Suppl. A, 87-91.

[17] Harris N.D., Sugget A.J., Brown B.H. and Barber D.C. "Application of applied potential tomography (APT) in respiratory medicine", Clin. Phys. Physiol. Meas., 1987, Vol. 8, Suppl. A, 155-165.

[18] Smallwood R.H., Mangnall Y.F. and Leathard A.D., "Transport of gastric contents", Physiol. Meas., 1994, Vol. 15, Suppl. 2A, 175-188.

[19] Brown B.H., Lindley E., Knowles R. and Wilson A.J., "A body worn APT system for space use", Proc CAEIT EC Workshop, 1990 (Copenhagen), 162-167.

[20] Amasha H.M., Anderson A.P., Conway J. and Barber D.C., "Quantitative assessment of impedance tomography for temperature measurements in microwave hyperthermia", Clin. Phys. Physiol. Meas., 1988, Vol. 9, Suppl. A, 49-53.

[21] Seagar A.D., Barber D.C. and Brown B.H., "Theoretical limits to sensitivity and resolution in impedance imaging", Clin. Phys. Physiol. Meas., 1987, Vol. 8, Suppl. A, 13-31.

[22] Healey T.J., Tozer R.C. and Freeston I.L. "Impedance imaging of 3D objects using magnetically induced currents", Proc. 14th Int. Conf. IEEE Engineering in Medicine and Biology Society, 1992 (Paris) 1719-1720.

[23] Ilyas O.M. *et al*, "Investigation of batch mixing using multiple-plane impedance tomography", Proc. ECAPT, 1993 (Karlsrhue), 268-271.

[24] Morucci J.P. *et al*, "Direct sensitivity matrix approach for fast 3D reconstruction in EIT", Proc CAIT, 1994 (Ankara).

[25] Brown B.H., Barber D.C. and Seagar A.D., "Applied potential tomography : Possible clinical applications", Clin. Phys. Physiol. Meas., 1985, Vol. 6, No. 2, 109-121.

[26] Webster J.G. (Ed), "Electrical impedance tomography", Adam Hilger, 1990.

[27] Flack F.C., "Recent advances in medical functional imaging", IEE Eng. Sci. Ed. J, Oct 1994, Vol. 3, No. 5, 213-222.

[28] Dickin F.J. *et al*, "Tomographic imaging of industrial process equipment : Techniques and applications", IEE Proc. G, 1992, Vol. 139, No. 1, 72-82.

[29] Xie C.G., "Electrical capacitance tomography (ECT)", Proc. ECAPT, 1993 (Karlsrhue), 11-13.

[30] He R. *et al*, "Electrical impedance techniques to study combustion processes", Proc. ECAPT, 1995 (Bergen), 102-109.

[31] Binley A.M. *et al*, "Observation of tracer migration in soils using resistive electrical impedance tomography", Proc. ECAPT, 1993 (Karlsrhue), 275-278.

[32] Gutierrez J.A., Etuke E.O., Dyakowski T. and Beck M.S., "The use of electrical impedance tomography for multiphase flow imaging in hydrocyclones", Proc. ECAPT, 1995 (Bergen), 29-40.

[33] Gorvin A.C. *et al,* "The use of applied current tomography to measure the resistivity distribution of semiconductor wafers", Proc. ECAPT, 1995 (Bergen), 150-158.

[34] Bolomey J. Ch., Joachimowicz N. and Pichot Ch., "Microwave imaging techniques for non-destructive testing of industrial materials : From projections to tomography", Proc. ECAPT, 1993 (Karlsrhue), 233-235.

[35] Parker D.J., Dijkstra A.E. and McNeil P.A., "Positron emission particle tracking studies of granular flow in a rotating drum", Proc. ECAPT, 1995 (Bergen), 352-360.

[36] Brown G.J., Reilly D. and Mills D., "Ultrasonic transmission-mode tomography applied to gas/solids flow", Proc. ECAPT, 1995 (Bergen), 176-186.

[37] Hubbert M.K., "Results of earth resistivity survey on various geologic structures in Illinois", Am. Inst. Min. Metall. Engnrs., 1932, Tech. Publ., No. 463.

[38] Van Dam J.C. and Meulenkamp J.J., "Some results of the geoelectrical resistivity method in ground water investigations in the Netherlands", Geophys. Prospect., 1967, Vol. 15, 92-115.

[39] Milsom J., "Field Geophysics", Open University Press, 1989.

[40] Keller G.V. and Frischknecht F.C., "Electrical methods in geophysical prospecting", Pergamon Press, 1966.

[41] Noel M. and Xu B., "Archaeological investigation by electrical resistivity tomography : A preliminary study", Geophys. J. Int., 1991, Vol. 107, 95-102.

[42] Powell H.M., "Impedance Imaging using linear arrays of electrodes", PhD thesis, University of Sheffield, March 1988.

[43] Edic P.M. *et al*, "Implementation of a real-time electric impedance tomograph", Proc. 15th Int. Conf. IEEE Engineering in Medicine and Biology Society, 1993 (San Diego), 84-85.

[44] Smith R.W.M., "Design of a real-time impedance imaging system for medical applications", PhD thesis, University of Sheffield, October 1990.

[45] Murphy D., "Developments of the electrical impedance method with application to plethysmography and tomography", PhD thesis, University of Oxford, 1987.

[46] Rosell J., Murphy D., Pallas R. and Rolfe P., "Analysis and assessment of errors in a parallel data acquisition system for electrical impedance tomography", Clin. Phys. Physiol. Meas., 1988, Vol. 9, Suppl. A, 93-99.

[47] Hasekioglu O. and Kimymik K., "Multiple simultaneous excitation electrical impedance tomography using low cross correlated signals", Proc. of SPIE, 1992, Vol. 1818, 1256-1263.

[48] Jossinet J. and Trillaud C., "Imaging the complex impedance in electrical impedance tomography", Clin. Phys. Physiol. Meas., 1992, Vol. 13, Suppl. A, 47-50.

[49] Etuke E.O., Waterfall R.C., Dickin F.J. and Beck M.S., "Applications of multi-frequency excitation for electrical impedance tomography", Proc. ECAPT, 1995 (Bergen), 241-246.

[50] Cole K.S. and Cole R.H., "Dispersion and absorption in dielectrics", J. Chem. Phys., 1941, Vol. 9, 341-351.

[51] Powell H.M., Barber D.C. and Freeston I.L., "Impedance imaging using linear electrode arrays", Clin. Phys. Physiol. Meas., 1987, Vol. 8, Suppl. A, 109-118.

[52] Griffiths D.H. and Turnbull J., "A multi-electrode array for resistivity surveying", First Break, July 1985, Vol. 3, No. 7, 16-20.

[53] Lyon G.M. and Oakley J.P., "EIT for stirred vessels : Back-projected image enhancement using central electrode measurement", Proc. ECAPT, 1993 (Karlsrhue), 271-274.

[54] "Design-in reference manual", Analog Devices, 1994.

[55] Leung H.T.L., Williams R.J. and Griffiths H., "A wideband current source for electrical impedance tomography", Proc CAEIT EC Workshop, 1990 (Copenhagen), 206-211.

[56] Gisser D.G., Isaacson D. and Newell J.C., "Current topics in impedance imaging", Clin. Phys. Physiol. Meas., 1987, Vol. 8, Suppl. A, 39-46.

[57] Denyer C.W., Lidgey F.J., Zhu Q.S. and McLeod C.N., "A high output impedance current source", Physiol. Meas., 1994, Vol. 15, Suppl. 2A, 79-82.

[58] Rosell J. and Riu P., "Common-mode feedback in electrical impedance tomography", Clin. Phys. Physiol. Meas., 1992, Vol. 13, Suppl. A, 11-14.

[59] Carpenter E.W. and Habberjam G.M., "A tripotential method of resistivity prospecting", Geophysics, 1956, Vol. 21, No. 2, 455-469.

[60] Riu P.J., Lozano A. and Rosell J., "Errors in tomography systems caused by reactive electrode impedances", Proc CAEIT EC Workshop, 1990 (Copenhagen), 198-205.

[61] Duck F.A., "Physical properties of tissue", Academic Press, 1990.

[62] Scaife J.M., Tozer R.C. and Freeston I.L., "Conductivity and Permittivity images from an induced current electrical impedance tomography system", IEE Proc. A, Vol. 141, No. 5, 1994, 356-362.

[63] Grant P.M., Cowan C.F.N., Mulgrew B. and Dripps J.H., "Analogue and digital signal processing and coding", Chartwell-Bratt, 1989, 186.

[64] Lidgey J., Vere-Hunt M. and Toumazou C., "Developments in current driver circuitry", Proc CAEIT EC Workshop, 1990 (Copenhagen), 183-190.

[65] Blad B., *et al*, "A current injecting device for electrical impedance tomography", Physiol. Meas., 1994, Vol. 15, Suppl. 2A, 69-78.

[66] Toumazou C. and Lidgey F.J., "A novel bipolar differential input output current-controlled current source", Electron. Lett., 1985, Vol. 21, No. 5, 199-200.

[67] Fabre A., "Translinear current conveyors implementation", Int. J. Electronics, 1985, Vol. 59, No. 5, 619-623.

[68] Fabre A. and Longeumard J., "A translinear floating current source with current control", Int. J. Electronics, 1988, Vol. 65, No. 6, 1137-1142.

[69] Bragos R., Rosell J. and Riu P., "A wideband AC-coupled current source for electrical impedance tomography", Physiol. Meas., 1994, Vol. 15, Suppl. 2A, 91-100.

[70] Special purpose linear devices databook, National Semiconductors, 1989, 5/33-5/50.

[71] Tektronix Catalogue 1989, 541.

[72] Seagar A.D. and Brown B.H., "Limitations in hardware design in impedance imaging", Clin. Phys. Physiol. Meas., 1987, Vol. 8, Suppl. A, 85-90.

[73] Murphy D. and Rolfe P., "Aspects of instrumentation design for impedance imaging", Clin. Phys. Physiol. Meas., 1988, Vol. 9, Suppl. A, 5-14.

[74] Van Valkenburg M.E., "Analog filter design", Holt Saunders International Editions, 1982, p203 and p182.

[75] Record P., Gadd R. and Rolfe P., "A signal conditioning electrode for use in electrical impedance tomography", Proc CAEIT EC Workshop, 1990 (Copenhagen), 168-174.

[76] Tozer R.C., "A low input capacitance sense amplifier for impedance imaging applications", Meas. Sci. Technol., 1992, Vol. 3, 508-514.

[77] Pallas-Areny R. and Casas O., "Analog front end for bio-impedance measurements based on the floating capacitor technique", Innovation et Technologie en Biologie et Medicine, 1994, Vol. 15, No. special 1, 110-115.

[78] Elantec Data Book, 1994.

[79] Trillaud C. and Jossinet J., "An improved design of voltmeter for semi-parallel data acquisition", Clin. Phys. Physiol. Meas., 1992, Vol. 13, Suppl. A, 5-10.

[80] Bracewell R.N., "The fourier transform and its applications", McGraw-Hill, 2nd Ed., 1978, 358.

[81] Smith R.W.M., Freeston I.L., Brown B.H. and Sinton A.M., "Design of a phase-sensitive detector to maximise signal-to-noise ratio in the presence of gaussian wideband noise", Meas. Sci. Technol., 1992, Vol. 3, 1054-1062.

[82] Barber D.C. and Seagar A.D., "Fast reconstruction of resistance images", Clin. Phys. Physiol. Meas., 1987, Vol. 8, Suppl. A, 47-54.

[83] Anderson D.K., Tozer R.C. and Freeston I.L., "Back-projection in an induced current impedance imaging system", Proc. 15th Int. Conf. IEEE Engineering in Medicine and Biology Society, 1992 (San Diego), 80-81.

[84] Barber D.C. and Brown B.H., "Recent developments in applied potential tomography (APT)", Proc. 9th Conf. on Information in Medical Imaging, 1986, Bacharach S.L. (Ed), Martinus Nijhoff publishers, 106-121.

[85] Barber D.C, Brown B.H. and Avis N.J., "Image reconstruction in electrical impedance tomography using filtered backprojection", Proc. 14th Int. Conf. IEEE Engineering in Medicine and Biology Society, 1992 (Paris), 1691-1692.

[86] Pratt W.K., "Digital image processing", Wiley, 1978, 323.

[87] Kotre C.J., "Sub-surface electrical impedance imaging using orthogonal linear electrode arrays", IEE Colloquium on "Innovations in Instrumentation for Electrical Tomography", 11th May 1995, 12/1-12/4.

[88] Simpson J.C. *et al*, "Unreferenced non-contacting impedance imaging using an induced current system" Proc. 15th Int. Conf. IEEE Engineering in Medicine and Biology Society, 1992 (San Diego), 90-91.

[89] Davies E.R., "Electronics, noise and signal recovery", Academic Press, 1993, 49-54.

[90] Ramo S., Whinnery J.R. and Van Duzer T., "Fields and waves in communication electronics", Wiley, 2nd Ed., 1984, p36 and pp346-349.

Appendix A
Quantised Sinewave Frequency Spectrum

The waveform generators described in section 3.3 produce quantised waveforms which are converted to currents. It is necessary to calculate the frequency spectrum of the quantised waveform to determine the quantisation noise level for different DAC resolutions and clock frequencies in order to make design decisions. This Appendix describes the process used to calculate the information given in the graphs shown in Figures 3.6 to 3.8.

The frequency spectrum of the quantised waveform is calculated by summing the effects of time shifted rectangular pulses. A rectangular pulse of amplitude A and width τ centred around the time t_o has the Fourier transform,

$$F(\omega) = \frac{A}{\pi f} \sin \pi f \tau \cdot \left[\cos 2\pi f t_0 - j \sin 2\pi f t_0\right] \qquad \{A.1\}$$

For a quantised sinewave of unit amplitude and frequency f_1, quantised by a converter with a least significant bit (LSB) of size *bit*, the amplitude of the pulse A is given by

$$A = round\left[\frac{\sin 2\pi f_1 t_0}{bit}\right].bit \qquad \{A.2\}$$

where *round*[] signifies the quantisation effect. If the quantised sinewave consists of N samples generated at a sampling frequency of f_s, then the frequency resolution Δf can be defined as $\Delta f = f_s/N = 1/\tau$. The real part of the Fourier Transform is given by

$$\mathrm{Re}\left[F(m)\right] = \sum_{n=0}^{N-1} round\left[\frac{\sin 2\pi f_1 nT}{bit}\right] \cdot bit \cdot \frac{\sin \pi m}{\pi m \Delta f} \cdot \cos 2\pi m(n+0.5) \qquad \{A.3\}$$

where n=sample number, m=frequency number (ie $m\Delta f$=frequency), T is the sampling period ($=1/f_s$), *round*[] signifies the quantisation effect and *bit* is the effective size of the LSB of the DAC.

Similarly the imaginary component of the Fourier Transform is given by

$$\mathrm{Im}\left[F(m)\right] = \sum_{n=0}^{N-1} round\left[\frac{\sin 2\pi f_1 nT}{bit}\right] \cdot bit \cdot \frac{\sin \pi m}{\pi m \Delta f} \cdot \sin 2\pi m(n+0.5) \qquad \{A.4\}$$

By calculating the summations of equations {A.3} and {A.4} numerically, the frequency spectra (magnitude against frequency) can be calculated. Figures 3.6 to 3.8 show graphically data calculated in this manner.

Appendix B
Current Mirrors

Current mirrors are often used as a basis for current sources [55][68]. There are a number of current mirror configurations, the simplest being shown in Figure B.1. i_1 is the generated signal current which is to be mirrored to produce the output current i_o. Assuming that the two transistors are identical, the output current is related to the input current by the relationship

$$\frac{i_o}{i_1} = \frac{\beta}{\beta+2} \qquad \{B.1\}$$

where β is the current gain of both of the transistors. Ideally, the current gain from i_1 / i_o would be unity, but this is not the case because the current i_1 must provide both the base currents for the transistors T_1 and T_2. Thus the current which is mirrored to i_o is i_1-$2i_b$. If absolute amplitude matching of the output current to the input current is required there are a number of three and four transistor circuits with current gains closer to unity [89] which can be used. Emitter resistors are often included in the current mirror as shown in Figure B.2 to compensate for transistor parameter mismatches and increase the output impedance of the circuit.

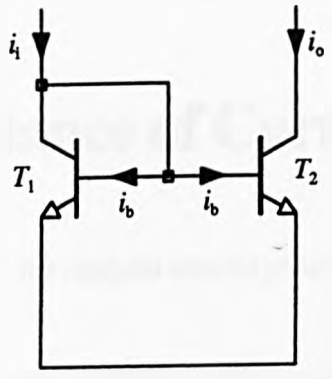

Figure B.1 : A basic current mirror circuit.

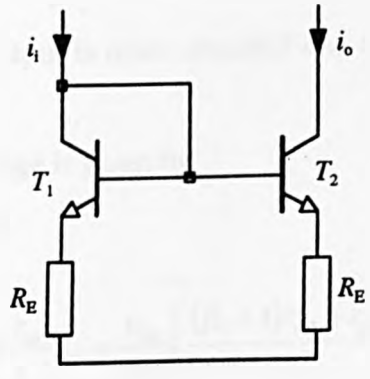

Figure B.2 : A basic current mirror with emitter resistors.

Appendix C
Output Resistance of Current Source

This Appendix details the analysis used to produce the figures for output impedance quoted in section 3.4.6.

The analysis is based on a simplified hybrid π small signal model of a transistor and aims to calculate the output resistance of the circuit shown in Figure C.1. The reactive circuit elements are not considered in this analysis. The approach used is to take each stage (transistor) separately and to represent the output of each stage as a Thevenin equivalent source which provides the input for the next stage. By using this approach the factors critical to the performance at each stage may be identified.

(a) First Stage

The equivalent circuit of the first stage is shown in Figure C.2. The output resistance of this stage is given by

$$r_{out1} = \frac{v_{p\,o/c}}{i_{p\,s/c}} \qquad \{C.1\}$$

where $v_{p\,o/c} = v_p$ when the output is open circuited and $i_{p\,s/c} = i_p$ when the output is short circuited.

The open circuit output voltage is given by

$$v_{p\,o/c} = v_{be1} + i_{in1}R \qquad \{C.2\}$$

where $$i_{in1} = (\beta_1 + 1)i_{b1} + \frac{r_{be1}}{r_{ce1}}i_{b1} = \frac{v_{be1}}{r_{be1}}\left[\frac{(\beta_1 + 1)r_{ce1} + r_{be1}}{r_{ce1}}\right] \qquad \{C.3\}$$

Substituting for i_{in1} in {C.2} gives

$$v_{p\,o/c} = v_{be1}\left[\frac{r_{be1}r_{ce1} + (\beta_1 + 1)r_{ce1}R + r_{be1}R}{r_{be1}r_{ce1}}\right] \qquad \{C.4\}$$

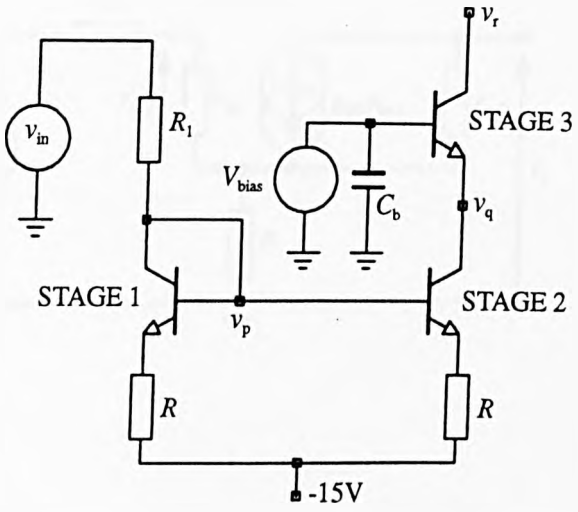

Figure C.1 : The transistor stages of the current mirror circuit. The small signal voltages v_p, v_q and v_r are measured with respect to ground.

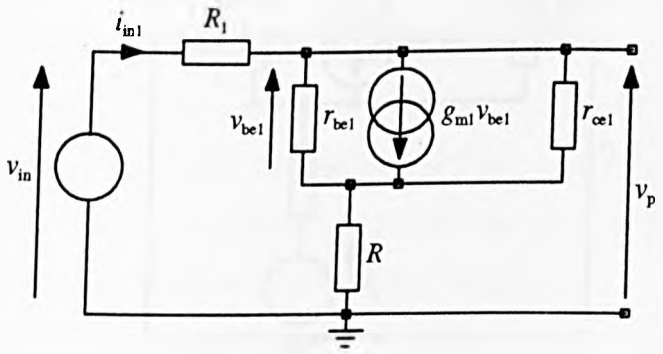

Figure C.2 : The small signal equivalent circuit of stage 1.

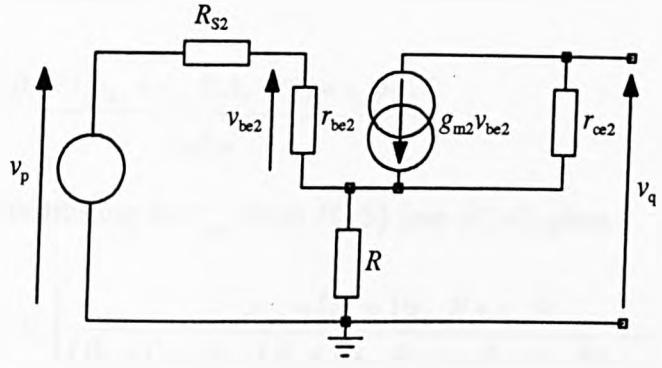

Figure C.3 : The small signal equivalent circuit of stage 2.

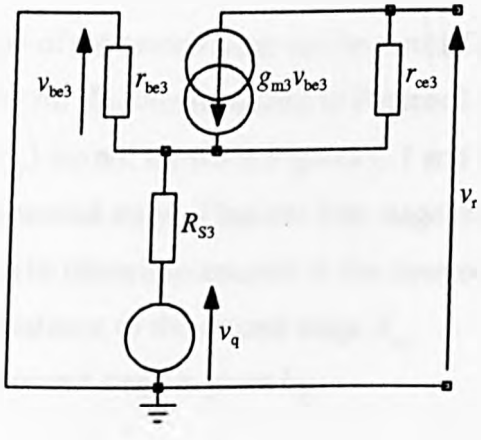

Figure C.4 : The small signal equivalent circuit of stage 3.

Now

$$v_{in} = i_{in}(R_1 + R) + v_{be1}$$

$$= v_{be1}\left[\frac{((\beta_1 + 1)r_{ce1} + r_{be1})(R_1 + R) + r_{be1}r_{ce1}}{r_{be1}r_{ce1}}\right] \quad \{C.5\}$$

and therefore substituting for v_{be1} from {C.5} into {C.4} gives

$$v_{p\,o/c} = v_{in}\left[\frac{r_{be1}r_{ce1} + (\beta_1 + 1)r_{ce1}R + r_{be1}R}{(\beta_1 + 1)r_{ce1}R_1 + (\beta_1 + 1)r_{ce1}R + r_{be1}R_1 + r_{be1}R + r_{be1}r_{ce1}}\right] \quad \{C.6\}$$

The short circuit output current is given by

$$i_{p\,s/c} = \frac{v_{in}}{R_1} \quad \{C.7\}$$

which gives $$r_{out1} = \frac{R_1[(\beta+1)Rr_{ce1} + Rr_{be1} + r_{be1}r_{ce1}]}{(\beta+1)R_1r_{ce1} + (\beta+1)Rr_{ce1} + R_1r_{be1} + Rr_{be1} + r_{be1}r_{ce1}} \quad \{C.8\}$$

Substituting the values used in the circuit of R=100Ω, R_1=2kΩ, and typical transistor values of β=250, r_{be1}=920Ω, r_{ce1}=36kΩ gives r_{out1} = 99Ω.

(b) Second Stage

The equivalent circuit of the second stage can be seen in Figure C.3. The transistors used to create the ac feedback for the circuits shown in Figures 3.13 and 3.14 (those in the section driving the resistor R_{ref}) are not shown in Figures C.1 and C.3, but are connected in parallel with the input to the second stage. Thus the first stage is driving the bases of two transistors in parallel. This can be taken into account at the input of stage 2 by using a value of (2 x r_{out1}) as the source resistance to the second stage R_{s2} .

The output resistance of the second stage is given by

$$r_{out2} = \frac{v_{q\,o/c}}{i_{q\,s/c}} \quad \{C.9\}$$

But

$$v_{q\,o/c} = \frac{v_{be2}}{r_{be2}}[R - \beta r_{ce2}] \quad \{C.10\}$$

where $v_{be2} = v_p\left[\frac{r_{be2}}{R_{s2}+r_{be2}+R}\right]$ {C.11}

Substituting {C.11} into {C.10} gives

$$v_{q\,o/c} = v_p\left[\frac{R-\beta r_{ce2}}{r_{be2}}\right]\left[\frac{r_{be2}}{R_{s2}+r_{be2}+R}\right] \quad \{C.12\}$$

The equation for the short circuit output current is

$$i_{q\,s/c} = \frac{R}{R+r_{ce2}}(\beta+1)\frac{v'_{be2}}{r_{be2}} - \beta\frac{v'_{be2}}{r_{be2}} \quad \{C.13\}$$

where v'_{be2} is the small signal base-emitter voltage across T_2 (v_{be2}) for the output short-circuited. This can be simplified to

$$i_{q\,s/c} = v'_{be2}\left[\frac{R-\beta r_{ce2}}{r_{be2}(R+r_{ce2})}\right] \quad \{C.14\}$$

The relationship between v'_{be2} and v_p is

$$\begin{aligned} v_p &= \frac{v'_{be2}}{r_{be2}}(R_{s2}+r_{be2}) + \frac{v'_{be2}}{r_{be2}}(\beta+1)\frac{Rr_{ce2}}{R+r_{ce2}} \\ &= v'_{be2}\left[\frac{(R_{s2}+r_{be2})(R+r_{ce2})+(\beta+1)Rr_{ce2}}{r_{be2}(R+r_{ce2})}\right] \end{aligned} \quad \{C.15\}$$

Substituting for v'_{be2} in {C.14} gives

$$i_{q\,s/c} = v_p\left[\frac{(R-\beta r_{ce2})}{(R_{s2}+r_{be2})(R+r_{ce2})+(\beta+1)Rr_{ce2}}\right] \quad \{C.16\}$$

and using {C.9}, {C.12} and {C.16}

$$r_{out2} = \frac{v_{q\,o/c}}{i_{q\,s/c}} = \frac{(R_{s2}+r_{be2})(r_{ce2}+R)+(\beta+1)r_{ce2}R}{R_{s2}+r_{be2}+R} \quad \{C.17\}$$

Substituting the same values as in the previous stage for R, β, r_{ce2}, r_{be2}, and $R_{s2} = (r_{out1}$ x 2) gives $r_{out2} = 775\text{k}\Omega$. This is the output impedance of the second stage due to

the lower part (npn transistor part) of the circuit. The circuit of Figure 3.13 consists of two stages only, and so the output impedance of the lower part of the circuit of Figure 3.13 (ie that part containing npn transistors) is given by Equation {C.17}. The total output impedance of the circuit of Figure 3.13 will be the output impedance of the upper half of the circuit (that part containing the pnp transistors) in parallel with the output impedance of the lower half of the circuit.

By substituting the typical values for pnp transistors of $r_{be2} = 920\Omega$ and $r_{ce2} = 8k\Omega$, the output impedances of the upper half of the circuit of Figure 3.13 are $r_{out1\,pnp} = 99\Omega$ for the first stage and $r_{out2\,pnp} = 173k\Omega$ for the second stage. Thus the total output impedance of the circuit of Figure 3.13 is $r_{out2Total} = r_{out2\,npn} \| r_{out2\,pnp} = 141k\Omega$

(c) Third Stage

By placing a common base connected transistor at the output of stage 2 as shown in Figure C.1, the output impedance of the circuit is increased. The small signal equivalent circuit of the stage is shown in Figure C.4 where v_q is the voltage source with source resistance R_{s3}, given by r_{out2} calculated for the previous stage using Equation {C.17}, at the input.

The output resistance of the circuit is given by

$$r_{out3} = \frac{v_{r\,o/c}}{i_{r\,s/c}} \qquad \{C.18\}$$

$$v_{r\,o/c} = -\beta \frac{v_{be3}}{r_{be3}} r_{ce3} + v_q + \frac{v_{be3}}{r_{be3}} R_{s3} \qquad \{C.19\}$$

where $$v_{be3} = -v_q \left[\frac{r_{be3}}{r_{be3} + R_{s3}} \right] \qquad \{C.20\}$$

Substituting {C.20} into {C.19} gives

$$v_{r\,o/c} = v_q \left[\frac{\beta r_{ce3} + r_{be3}}{r_{be3} + R_{s3}} \right] \qquad \{C.21\}$$

The output short circuit current is given by

$$i_{r\,s/c} = -v'_{be3}\left[\frac{\beta r_{ce3} + r_{be3}}{r_{ce3} r_{be3}}\right] \qquad \{C.22\}$$

where v'_{be3} is the v_{be3} for the output short circuit.
This can be expressed as

$$-v'_{be3}\left[1 + \frac{\beta R_{s3}}{r_{be3}} + \frac{R_{s3}}{r_{ce3}} + \frac{R_{s3}}{r_{be3}}\right] = v_q \qquad \{C.23\}$$

Therefore $$v'_{be3} = v_q\left[\frac{-r_{ce3} r_{be3}}{r_{ce3} r_{be3} + \beta r_{ce3} R_{s3} + r_{be3} R_{s3} + r_{ce3} R_{s3}}\right] \qquad \{C.24\}$$

So from {C.22} $$i_{r\,s/c} = v_q\left[\frac{\beta r_{ce3} + r_{be3}}{r_{ce3} r_{be3} + R_{s3}\left[(\beta+1) r_{ce3} + r_{be3}\right]}\right] \qquad \{C.25\}$$

Thus $$r_{out3} = \frac{v_{r\,o/c}}{i_{r\,s/c}} = \frac{r_{ce3} r_{be3} + R_{s3}\left[(\beta+1) r_{ce3} + r_{be3}\right]}{r_{be3} + R_{s3}} \qquad \{C.26\}$$

Substituting r_{ce3}=36kΩ, r_{be3}=920Ω, β=250, R_{s3}=775kΩ for the npn transistors gives an output impedance for the bottom half of the circuit of $r_{out3\,npn}$ = 9.0MΩ. Substituting r_{ce3}=14kΩ, r_{be3}=920Ω, β=250, R_{s3}=173kΩ for the pnp transistors gives an output impedance of the top half of the circuit of $r_{out3\,pnp}$ = 3.5MΩ. Since the total output impedance is the parallel combination of the two output impedances, $r_{out3} = r_{out3\,npn} \parallel r_{out3\,pnp}$ = 2.5MΩ.

Appendix D
Calculation of the Voltage Differences if the Anti-Alias Filters precede the Subtractor

In Figure D.1 the Anti-Alias Filters (AAFs) precede the subtraction and have a transfer function which produces a phase shift of ϕ and a gain of α at the frequency ω. Thus the measured voltage difference, ΔV_m will be given by

$$\Delta V_m = V_1\alpha_1 \sin(\omega t + \phi_1) - V_2\alpha_2 \sin(\omega t + \phi_2) \qquad \{D.1\}$$

Where V_1 and V_2 are the amplitudes of the input voltages at the electrodes. The required voltage difference ΔV is given by

$$\Delta V = (V_1 - V_2)\sin \omega t \qquad \{D.2\}$$

Since α_1, α_2, ϕ_1, ϕ_2 are known (they can be determined by calibration with the Network Analyser) it is necessary to find ΔV in terms of ΔV_m

Expanding Equation {D.1}

$$\begin{aligned}\Delta V_m &= V_1\alpha_1(\sin \omega t \cos\phi_1 + \sin \phi_1 \cos\omega t) - V_2\alpha_2(\sin \omega t \cos\phi_2 + \sin \phi_2 \cos\omega t) \\ &= \sin \omega t(V_1\alpha_1 \cos\phi_1 - V_2\alpha_2 \cos\phi_2) + \cos\omega t(V_1\alpha_1 \sin \phi_1 - V_2\alpha_2 \sin \phi_2)\end{aligned} \qquad \{D.3\}$$

The in-phase voltage V_p and the out-of-phase voltage V_q can then be written as

$$V_p = V_1\alpha_1 \cos\phi_1 - V_2\alpha_2 \cos\phi_2 \qquad \{D.4\}$$

$$V_q = V_1\alpha_1 \sin \phi_1 - V_2\alpha_2 \sin \phi_2 \qquad \{D.5\}$$

Substituting {D.5} in {D.4} for V_2 gives

$$V_1 = \frac{V_p \sin \phi_2 - V_q \cos\phi_2}{\alpha_1(\cos\phi_1 \sin \phi_2 - \sin \phi_1 \cos\phi_2)} \qquad \{D.6\}$$

From Equation {D.5} $\quad V_1 - V_2 = V_1 - \left(\dfrac{V_1\alpha_1 \sin \phi_1 - V_q}{\alpha_2 \sin \phi_2}\right)$ $\qquad \{D.7\}$

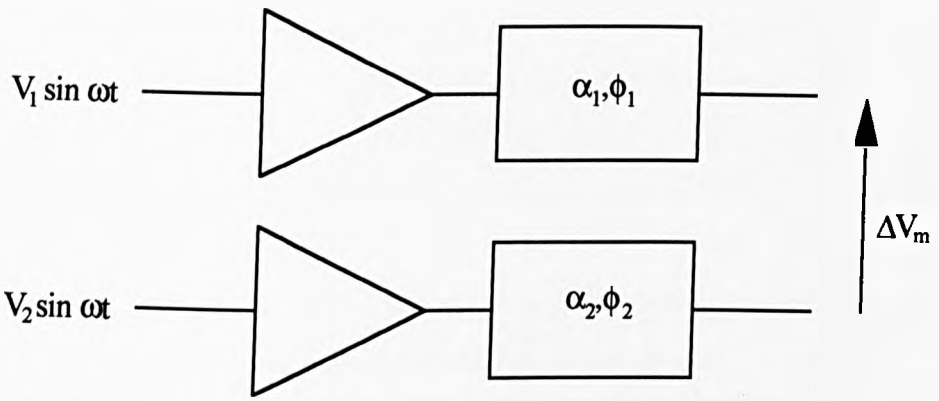

Figure D.1 : Diagram showing two receive channels prior to subtraction.

And substituting for V_1 from Equation {D.6}

$$V_1 - V_2 = \frac{V_p(\alpha_2 \sin\phi_2 - \alpha_1 \sin\phi_1) + V_q(\alpha_1 \cos\phi_1 - \alpha_2 \cos\phi_2)}{\alpha_1\alpha_2 \sin(\phi_2 - \phi_1)} \qquad \{D.8\}$$

Thus the amplitude of the required voltage difference V_1-V_2 can be calculated by using the values of α_1, α_2, ϕ_1, ϕ_2 and the measured in phase and quadrature voltage differences.

Appendix E
Subtractor Calculations

E.1 Gain of the Subtractor

Figure 4.11 shows the circuit being investigated. It consists of the input resistances r_o, the decoupling capacitors C, the base bias resistors R_b, the differential input transistors T_1 and T_2, the collector resistors R_c, the emitter resistors R_e and the op-amp with gain resistors R. The small signal equivalent circuit of the transistor stages is shown in Figure E.1 followed by an ideal op-amp. It has been assumed that the current source loading the emitters of the transistors has an infinite output impedance. The resistors R, R_c and R_e are matched to 0.1% and so will be assumed to be perfectly matched in both the channels in this analysis.

The input voltages are v_1 and v_2 and the desired transfer function is given by the ratio $v_o/(v_1-v_2)$ where v_o is the voltage at the output of the op-amp.

The voltage at the non-inverting input of the op-amp, A_1, is given by

$$v^+ = -g_{m2} v_{be2} \left[\frac{R_c R}{R_c + 2R} \right] \qquad \{E1.1\}$$

where $$v_{be2} = v_2 - v_e - (\beta_2 + 1) R_e \frac{v_{be2}}{r_{be2}} - \left(r_{o2} + \frac{1}{sC_2} \right) \left(\frac{v_{be2}}{r_{be2}} + i_{x2} \right) \qquad \{E1.2\}$$

And $$i_{x2} = \left[v_e + (\beta_2 + 1) R_e \frac{v_{be2}}{r_{be2}} + v_{be2} \right] \frac{1}{R_{b2}} \qquad \{E1.3\}$$

Eliminating i_{x2} and v_{be2} gives

$$v^+ = -\frac{R_c R}{R_c + 2R} \left[\frac{g_{m2} r_{be2} \left(v_2 R_{b2} - v_e \left(R_{b2} + r_{o2} + \frac{1}{sC_2} \right) \right)}{r_{be2} R_{b2} + (\beta_2 + 1) R_e R_{b2} + \left(r_{o2} + \frac{1}{sC_2} \right) \left(R_{b2} + (\beta_2 + 1) R_e + r_{be2} \right)} \right] \qquad \{E1.4\}$$

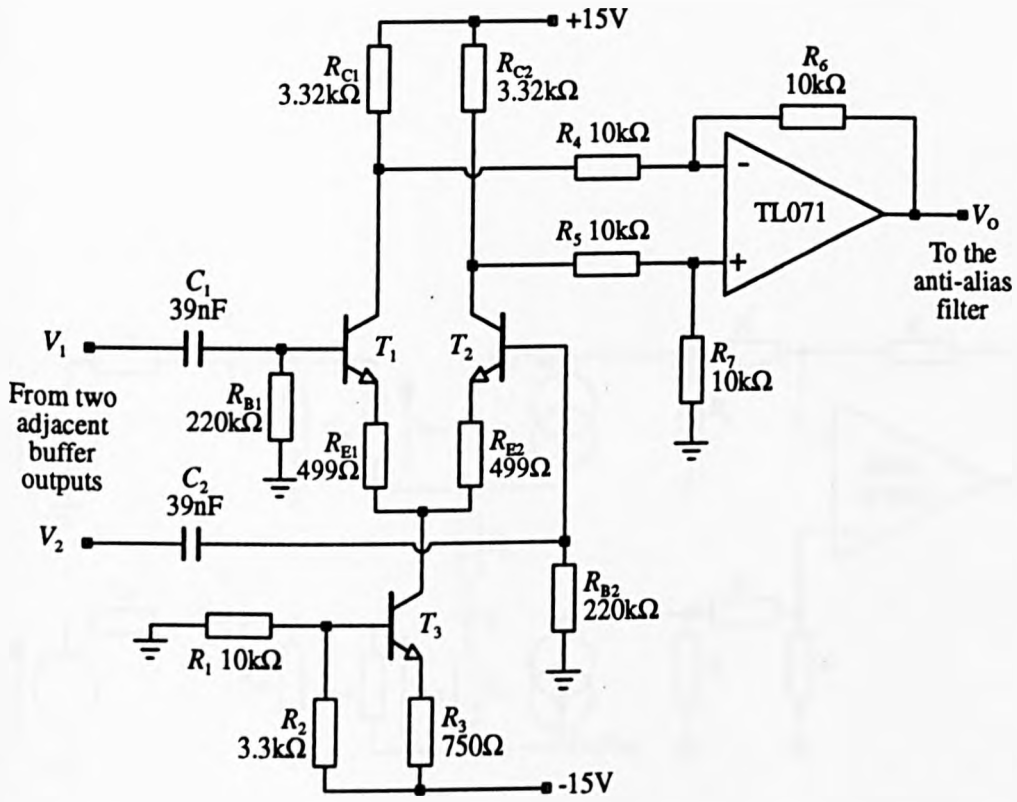

Figure 4.11 : The subtractor circuit.
Transistors T_1, T_2 and T_3 are BC184LC.
Resistors R_{E1}, R_{E2}, R_{C1}, R_{C2}, R_4, R_5, R_6 and R_7 are 0.1%.

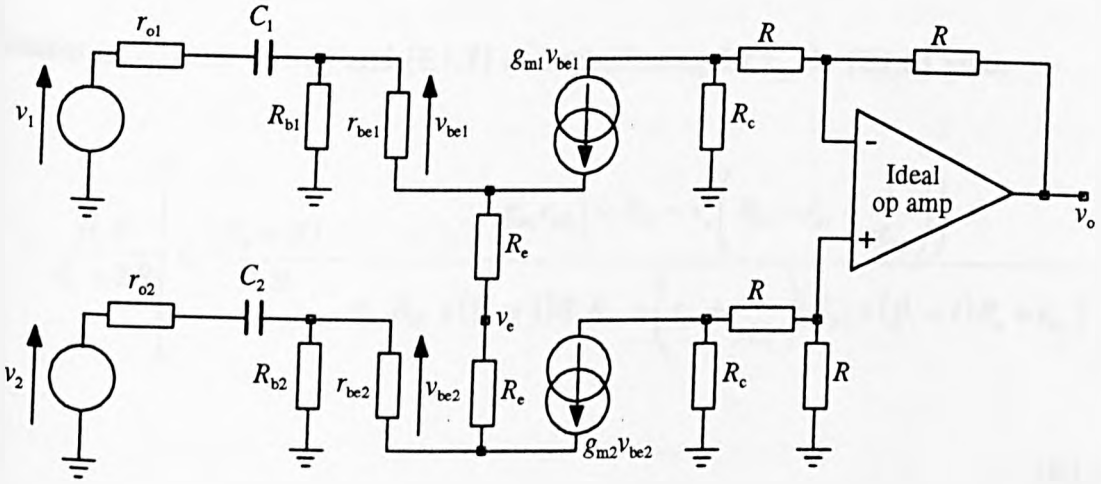

Figure E.1 : The small signal equivalent circuit of the subtractor shown in figure 4.11. The long tailed pair transistor stage is assumed to be followed by an ideal op amp subtractor circuit.

Summing the currents at the collector of T_1 to get an expression including v^- gives

$$g_{m1}v_{be1} = \frac{v^- - (2v^- - v_o)}{R} - \frac{(2v^- - v_o)}{R_c} \qquad \{E1.5\}$$

where

$$v_{be1} = v_1 - v_e - (\beta_1 + 1)R_e\frac{v_{be1}}{r_{be1}} - \left(r_{o1} + \frac{1}{sC_1}\right)\left(\frac{v_{be1}}{r_{be1}} + i_{x1}\right) \qquad \{E1.6\}$$

and

$$i_{x1} = \left[v_e + (\beta_1 + 1)R_e\frac{v_{be1}}{r_{be1}} + v_{be1}\right]\frac{1}{R_{b1}} \qquad \{E1.7\}$$

Eliminating i_{x1} from {E1.6} and {E1.7} and substituting for v_{be1} in {E1.6} gives

$$v^- = \frac{R_c R}{R_c + 2R}\left[v_o\frac{(R_c + R)}{R_c R} - \frac{g_{m1}r_{be1}\left(v_1 R_{b1} - v_e\left(R_{b1} + r_{o1} + \frac{1}{sC_1}\right)\right)}{r_{be1}R_{b1} + (\beta_1 + 1)R_e R_{b1} + \left(r_{o1} + \frac{1}{sC_1}\right)\left(R_{b1} + (\beta_1 + 1)R_e + r_{be1}\right)}\right]$$

{E1.8}

{E1.9}

Assuming an ideal op-amp, $v^+ = v^-$

Assuming identical matching in the channels for all parameters (g_m, r_{be}, β, R_b, C, r_o) then by combining equations {E1.4}, {E1.8} and {E1.9} gives

$$v_o = \frac{R_c R}{R_c + R}\left[\frac{g_m r_{be}R_b(v_1 - v_2)}{r_{be}R_b + (\beta+1)R_e R_b + \left(r_o + \frac{1}{sC}\right)\left(R_b + (\beta+1)R_e + r_{be}\right)}\right] \qquad \{E1.10\}$$

This can be rearranged into the form

$$\frac{v_o}{v_2 - v_1} = k.\frac{s\tau}{1 + s\tau} \qquad \{E1.11\}$$

Where $$k = \frac{R_c R}{R_c + R}\cdot\frac{\beta R_b}{(\beta+1)R_e R_b + (\beta+1)R_e r_o + R_b r_{be} + R_b r_o + r_o r_{be}} \qquad \{E1.12\}$$

and $$\tau = \frac{C\left[(\beta+1)R_b R_e + (\beta+1)R_e r_o + R_b r_{be} + R_b r_o + r_{be} r_o\right]}{(\beta+1)R_e + R_b + r_{be}} \qquad \{E1.13\}$$

Making the approximation that β is large so $(\beta+1)\approx\beta$ and assuming that $r_o << R_b$, R_e and r_{be} then the gain k simplifies to

$$k \approx \frac{R_c R}{(R_c + R)(r_e + R_e)} \qquad \{E1.14\}$$

where $r_e = 1/g_m$. This is the value of gain quoted in section 4.3.3.

E.2 Common Mode Voltage Range of the Subtractor

If the maximum voltage difference, ΔV, at the inputs of the subtractor is 0.75V (section 4.3.1), then the maximum common mode voltage that the circuit can work under can be calculated using large signal considerations as follows. Figure 4.10 shows the differential part of the circuit. If $V_1 = V_{cm} + \Delta V/2$ and $V_2 = V_{cm} - \Delta V/2$ then summing the currents at the collector of the current source

$$\frac{1}{R_e}\left(V_b + V_{cm} + \frac{\Delta V}{2} - 0.7 - V_{c3}\right) + \frac{1}{R_e}\left(V_b + V_{cm} - \frac{\Delta V}{2} - 0.7 - V_{c3}\right) = I \qquad \{E2.1\}$$

where V_b is the bias voltage at the bases of the transistors given by

$$V_b = I_{bias} R_b = 10\times10^{-6}\times220\times10^{3} = -2.2V \qquad \{E2.2\}$$

The minimum common mode voltage must not allow V_{c3} to be more negative than V_{b3}. So substituting the value V_b=-2.2V from {E2.2}, ΔV=0.75V, I=4mA, R_e=499Ω and $V_{c3}=V_{b3}$ gives a minimum limit of the common mode voltage of -7.4V. The maximum common mode voltage must not allow V_{b2} to exceed V_{c2} (or V_{b1} to exceed V_{c1}). The emitter current, I_{e2}, through transistor T_2 is given by

$$I_{e2} = \frac{\Delta V}{2R_e} + \frac{I}{2} \qquad \{E2.3\}$$

The collector current, I_{c2}, through transistor T_2 is given by

$$I_{c2} = \frac{V_s}{R_c} - \left(\frac{2R + R_c}{2RR_c}\right)V_{c2} \qquad \{E2.4\}$$

For transistors with reasonable current gain, the collector current equals the emitter current. Thus equating Equations {E2.3} and {E2.4} for I_{e2} and I_{c2} gives

$$V_{c2} = \left(\frac{V_s}{R_c} - \frac{\Delta V}{2R_e} - \frac{I}{2} \right) \frac{2RR_c}{2R + R_c} \qquad \{E2.5\}$$

Using V_s=15V, I=4mA, R_e=499Ω, ΔV=0.75V, R_c=3.32kΩ, R=10kΩ gives V_{c2}=5.0V. Thus

$$5.0 > V_b + V_{cm} + \frac{\Delta V}{2} \qquad \{E2.6\}$$

Giving $V_{cm}^{+} < 6.8$V for V_b=-2.2V and ΔV=0.75V.

Thus the common mode range that can be accommodated for a maximum differential voltage of 0.7V is -7.4V < V_{cm} < 6.8V.

E.3 The effects of input channel mismatch on the CMRR of a subtractor

The matching of the channels preceding the subtraction stage in the receivers has a significant effect upon the maximum Common Mode Rejection Ratio (CMRR) that can be achieved.

Figure 4.10 shows the subtractor circuit. The voltage at the base of the two input transistors T_1 and T_2 are high pass filtered versions of the input voltages v_1 and v_2.

$$\text{ie} \quad v_{b1} = \frac{j\frac{\omega}{\omega_0}}{1 + j\frac{\omega}{\omega_0}} \cdot v_1 \text{ and } \quad v_{b2} = \frac{j\frac{\omega}{\omega_1}}{1 + j\frac{\omega}{\omega_1}} \cdot v_2 \qquad \{E3.1\}$$

For a common mode signal $v_1 = v_2 = v$, the output of the subtractor (ignoring all other effects - including the common mode gain) is given by

$$v_0 = v \cdot \left(\frac{j\frac{\omega}{\omega_0}}{1+j\frac{\omega}{\omega_0}} - \frac{j\frac{\omega}{\omega_1}}{1+j\frac{\omega}{\omega_1}} \right)$$

$$= v \cdot \frac{(\omega_1 - \omega_0)}{(\omega_1 + \omega_0)} \cdot \frac{j\omega\left(\frac{\omega_0 + \omega_1}{\omega_0\omega_1}\right)}{\left(1 + j\omega\left(\frac{\omega_0 + \omega_1}{\omega_0\omega_1}\right) + \frac{(j\omega)^2}{\omega_0\omega_1}\right)} \qquad \{E3.2\}$$

This is a standard form of frequency response for a bandpass filter with centre frequency $\sqrt{\omega_0\omega_1}$ and peak gain of $\left[\frac{\omega_1 - \omega_0}{\omega_1 + \omega_0}\right]$. For a differential gain of 1, the CMRR due to mismatch in the input decoupling is given by

$$20\log_{10}\left[\frac{\omega(\omega_1 - \omega_0)}{\sqrt{\left(\omega^2 + \omega_0^{\,2}\right)\left(\omega^2 + \omega_1^{\,2}\right)}}\right] \qquad \{E3.3\}$$

Using 1% capacitors and 1% resistors of nominal value 39nF and 220kΩ respectively, ω_1 and ω_2 could be mismatched to ω_1=114.25rads^{-1} and ω_2=118.92rads^{-1}. At 20 kHz this gives a CMRR of -88.6dB which is acceptable. The high pass function will cause a gain error of 4.5 x 10^{-5} and a phase error of 0.05° at 20kHz, both of which are acceptable.

Appendix F
Drawings of Phantom and Electrode Array

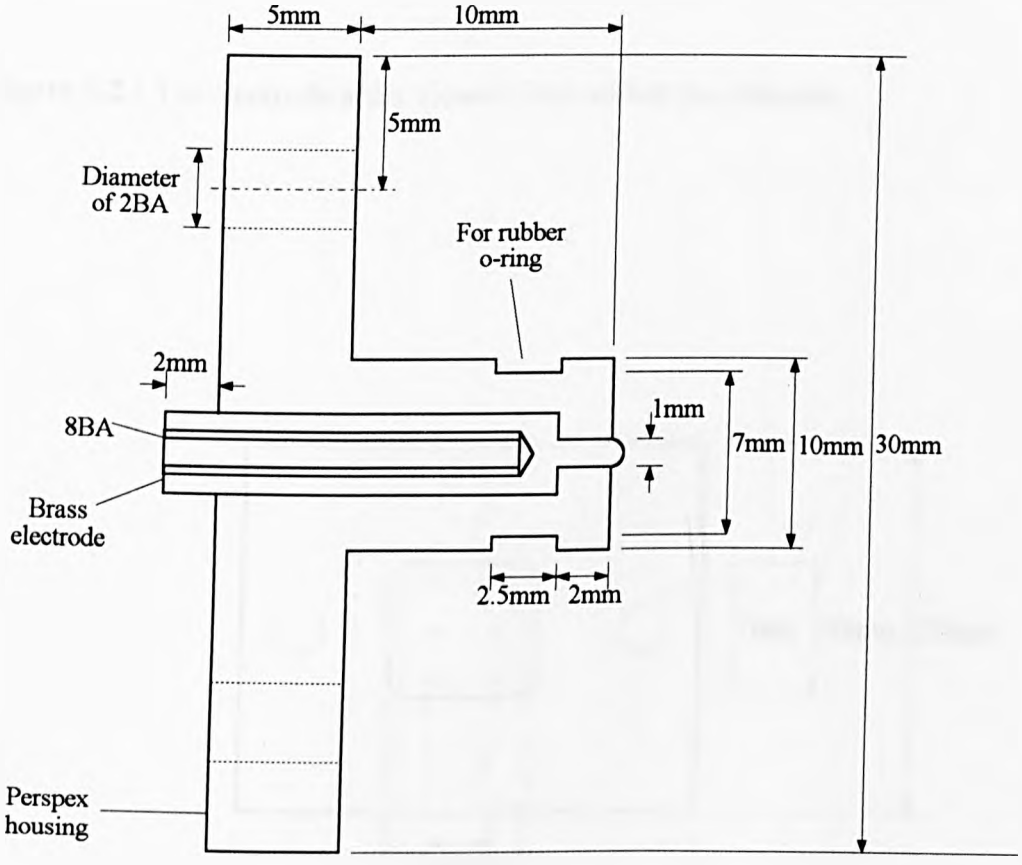

Figure F.1 : Cross section of the electrode array.

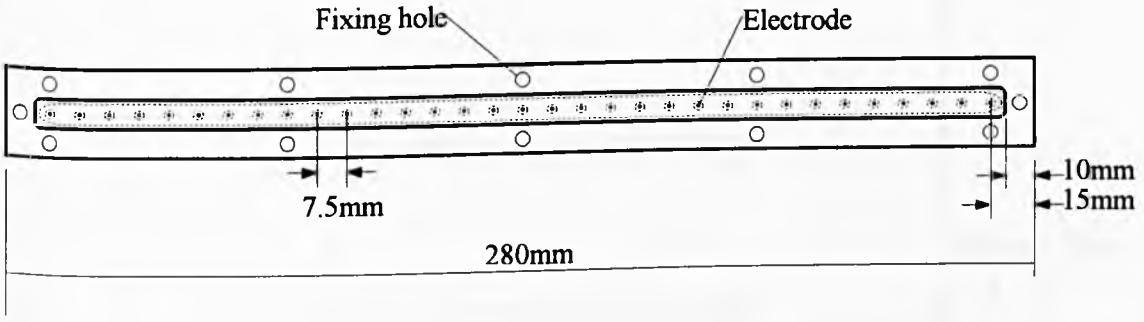

Figure F.2 : The electrode array viewed from within the phantom.

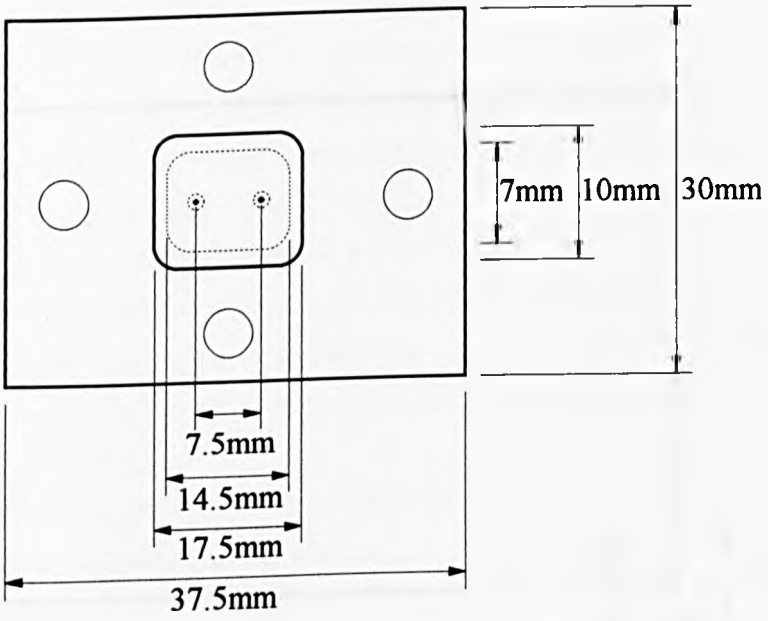

Figure F.3 : The common mode feedback electrode array.

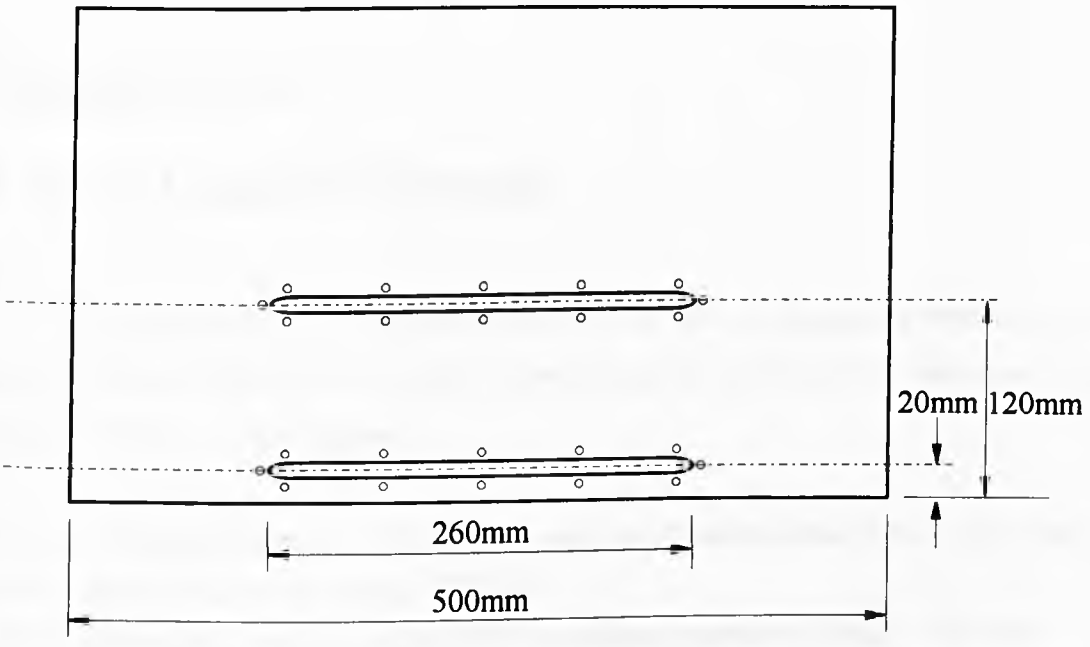

Figure F.4 : The phantom viewed from the front showing the pseudo-2D and 3D position of the electrode array.

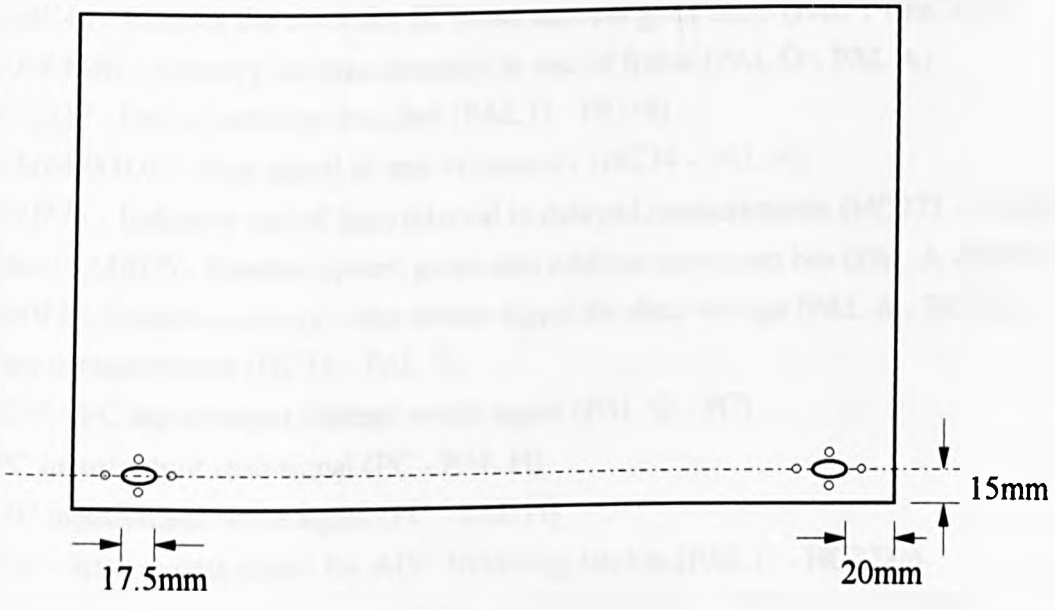

Figure F.5 : The phantom viewed from the back showing the common mode feedback application points.

Appendix G
List of Control Signals

This Appendix lists the signals used in the control of the system referred to in Chapter 5. The name and brief description of the signal is given, followed by the source and destination of the signal in brackets.

ADDVALID - Enables the memory address bus onto the PC address bus (PAL F - ACT244)
AEN - PC address enable signal (PC - PAL H)
CLKOUT - Generated clock signal for EPROM address generators (PAL 1 - HC125)
CLKRD - Sets direction of data flow through buffer to read/write ports (PAL H -AC245)
CLKREAD - Clocks data from read port to PC (PAL H - HC373)
CLKWR - Clocks data from PC into write port (PAL H - HC273)
CONTINUOUS - Set low for continuous measurements (HC273 - PAL A)
/CONVST - Conversion signal for ADCs in receivers (PAL C - ADCs)
COUNT - Enables both counters used in drive control (PAL 1 - HC163)
/DACCS - Chip select for DACs in waveform generators (PAL 1 - DACs)
/DACWR - Write enable for DACs in waveform generators (PAL 2 - DACs)
ENCLKMEAS - Enables the clock for EPROM address generators (PAL 1 - HC125)
ENDOFFRAME - Memory address decoded at end of frame (PAL D - PAL A)
ENDOFMEM - End of memory decoded (PAL D - HC74)
ENDOFMEMSTOP - Stop signal at end of memory (HC74 - PAL A)
ENDOFTIME - Indicates end of time interval in delayed measurements (HC273 - AC00)
/ENMEMADDABUS - Enables system generated address onto mem bus (PAL A -HC244)
/ENMEMWE - Enables memory write enable signal for data storage (PAL A - HC125)
GO - Start measurements (HC74 - PAL A)
I/OCHRDY - PC input/output channel ready signal (PAL G - PC)
/IOR - PC input/output read signal (PC - PAL H)
/IOW - PC input/output write signal (PC - PAL H)
LATCHEN - latch in data signal for ADC following latches (PAL C - HC373s)
LSBADDVALID - Enables memIC1 data bus onto PC data bus (PAL F - ACT244)
MEASURE - Starts the measurement process (HC273 - many)
MEASURECOUNT - Enables measurement control signal counters (PAL A - AC163)
/MEASCOUNTERCLR - Clears counter on reset & 128th count (PAL C - AC163)

MEMADDCOUNT - Enables memory address generator counters (PAL A - AC163)
MEMADDGEN - Measurement data addresses (AC163 - PAL D)
MEMADDGENCLK - Generated clock for memory address generators (PAL C - HC125)
MEMADDGENCLKOUT - Clocks memory address generators (HC125 - AC163)
/MEMCS12 - Chip select for both memory ICs (PAL A - memory)
/MEMOE1 - Output enable for memory LSBs (HC273 - memIC1)
/MEMOE2 - Output enable for memory MSBs (HC273 - memIC2)
/MEMR - PC memory read signal (PC - PAL G)
/MEMWE - System generated write enable signal for data write to mem (PAL C - HC125)
/MEMWEOUT - Memory write enable signal (HC125 - memory)
MSBADDVALID - Enables memIC2 data bus onto PC data bus (PAL F - ACT244)
NOTRESET - Used to enable OSC as clock for counters reset (PAL A - HC125)
/OC1-16 - Output enable for data latches onto memory data bus (PAL B/C - HC373s)
ONEWS - One wait state to be inserted in PC read cycle (PAL G - switch - *I/OCHRDY*)
OSC - 16.384MHz clock oscillator (many)
PCABUS - PC address bus (PC - many)
PCCLK - PC clock signal (PC - PALG)
PCDBUS - PC data bus (PC - many)
/PCREAD1 - Indicates lsbs of data to be read (HC373 - PAL A)
/PCREAD2 - Indicates MSBs of data to be read (HC373 - PAL A)
PROMADD - Address of EPROMs (HC163 - EPROMs)
PROMADDGENCLK - Clocks EPROM address generator counters (HC125 - HC163)
/PROMADDGENCLR - Clears counter on reset and 2048th count (PAL 1 - HC163)
/PROMCE - Chip enable signal for EPROMs (PAL 1 - EPROMs)
/PROMOE - Output enable signal for the EPROMs (PAL 1 - EPROMs)
/RESET - Resets counters etc after power up (HC273 - many)
RESETDRV - PC reset drive signal (PC - PAL G)
RESTART - Restarts measurements after time interval elapsed (HC74 - PAL A)
RDWREN - Enables buffer to read/write ports (PAL H - ACT254)
SINSYNC - Indicates first EPROM location for synchronisation (PAL 1 - many)
THREEWS - Three wait states to be inserted in PC read cycle (PAL G - switch - *I/OCHRDY*)
TRACKHOLD - Signal for deglitcher in waveform generators (PAL 2 - HA5330s)
TWOWS - Two wait states to be inserted in PC read cycle (PAL G - switch - *I/OCHRDY*)
WAITING - Signals end of frame and waiting to restart measurements (PAL A - AC00)
ZEROWS - No wait states to be inserted in PC read cycle (PAL G - switch - *I/OCHRDY*)

Appendix H

Program to control the measurements

```
#include "measure.h"

/*Subprogram to setup the system in the chosen configuration and take
the measurements
Possibilities of referenced, continuous, delayed and averaged referenced */

void initiatemeas(unsigned char mv,unsigned char wtv,unsigned char eot,
        unsigned char wait,int p1,int p2)
{  eot = mv + 1;
   outportb(p1,eot);
   wait = wtv;
   while (wait !=0)
   {  wait = inportb(p2);
   }
}

void framerun(unsigned char mv,unsigned char wtv,unsigned char wait,
      int p1,int p2)
{  outportb(p1,mv);      /*reset reg1=0*/
   wait = 0;
   while (wait != wtv)    /*waiting till endofframe*/
   {  wait = inportb(p2);
   }
}

void waitstart()
{  unsigned char readstart;

   readstart =0;
   while (readstart !=10)
   {  readstart = getchar();
   }
}


int meas(void)
{  int port1 = 0x0370;          /*port to write to*/
   int port2 = 0x0371;          /*port to read from*/
   int datatype;
   int choice,tempvalue,finaldelay,p,q,r,
   unsigned char readon,readchoice,readdelay;
   unsigned char reg2waiting;
   unsigned char resetvalue = 136;
   unsigned char idlevalue = 152;
   unsigned char delayedvalue = 216;
   unsigned char continuousvalue = 152;
   unsigned char measurevalue;
   unsigned char waitvalue = 8;
```

```
    unsigned char reg1endoftime;
     outportb(port1,resetvalue);
     printf("Ensure that the system is switched on. \n");
      printf("Press return to continue.");
      readon =0;
      while (readon !=10)    /*10 is ASCII for return*/
      {  readon = getchar();
      }
      outportb(port1,resetvalue);
      delay(100);
      outportb(port1,idlevalue);
      printf("Do you want to do take \n\n");
      printf("      1  One referenced measurement \n");
      printf("      2  A continuous set of six frames \n");
      printf("      3  A delayed set of six frames \n");
      printf("   or 4  An averaged referenced measurement. \n");
      choice = 0;
      readchoice = 0;
      while (readchoice !=10)
      {  readchoice = getchar();
       choice = readchoice + choice;}

 /*Choice : 49 ascii for 1, 50 ascii for 2 and 51 ascii for 3 etc. The */
 /*ascii code for return (10) has been added.*/

      if (choice == 59)          /*Single referenced measurement*/
      {  datatype = 1;
       outportb(port1,delayedvalue);
       measurevalue = delayedvalue + 32;
       framerun(measurevalue,waitvalue,reg2waiting,port1,port2);
       printf("Press return to take homogeneous measurements.\n");
       waitstart();
       initiatemeas(measurevalue,waitvalue,reg1endoftime,reg2waiting,
              port1,port2);
       framerun(measurevalue,waitvalue,reg2waiting,port1,port2);
       printf("Position object, then press return.\n");
       waitstart();
       initiatemeas(measurevalue,waitvalue,reg1endoftime,reg2waiting,
              port1,port2);
       framerun(measurevalue,waitvalue,reg2waiting,port1,port2);
       outportb(port1,idlevalue);
      } /* End of single referenced choice */

      if (choice == 60)          /*Continuous frames*/
      {  datatype = 2;
       outportb(port1,continuousvalue);
       printf("Press return to take measurements.\n");
       waitstart();
       measurevalue = continuousvalue + 32;
       framerun(measurevalue,waitvalue,reg2waiting,port1,port2);
 /*end of mem*/
       outportb(port1,idlevalue);
      } /* End of continuous choice */

      if (choice == 61)          /*Delayed set of frames*/
      {  datatype = 3;
       outportb(port1,delayedvalue);
       printf("Please type delay in ms between frames.\n");
```

```
/*This bit is to convert the ASCii read from the keyboard to decimal */
      tempvalue = 0;
      readdelay = 48;          /* 48 is decimal ASCII for '0' */
      while (readdelay != 10)   /* 10 is decimal ASCII for <LF>*/
      {  tempvalue = 10 * tempvalue + (readdelay-48);
        readdelay = getchar();
      }
      finaldelay = tempvalue;
      printf("Press return to begin taking measurements.\n");
      waitstart();
      measurevalue = delayedvalue + 32;
      for (p=1; p<=6; p++)
      {  framerun(measurevalue,waitvalue,reg2waiting,port1,port2);
        delay(finaldelay);          /*count*/
        initiatemeas(measurevalue,waitvalue,reg1endoftime,reg2waiting,
                    port1,port2);
      }
      framerun(measurevalue,waitvalue,reg2waiting,port1,port2);
/* 7th wait is end of mem*/
      outportb(port1,idlevalue);
     }    /*end of delayed choice*/

     if (choice ==62)          /*Averaged referenced measurement*/
     {  datatype=4;
      outportb(port1,delayedvalue);
      measurevalue = delayedvalue + 32;
      framerun(measurevalue,waitvalue,reg2waiting,port1,port2);
      printf("Press return to take homogeneous measurements.\n");
      waitstart();
      for (q=1; q<=3; q++)
      {  initiatemeas(measurevalue,waitvalue,reg1endoftime,reg2waiting,
                    port1,port2);
        framerun(measurevalue,waitvalue,reg2waiting,port1,port2);
      }
      printf("Position object, then press return.\n");
      waitstart();
      for (r=1; r<=3; r++)
      {  initiatemeas(measurevalue,waitvalue,reg1endoftime,reg2waiting,
                    port1,port2);
        framerun(measurevalue,waitvalue,reg2waiting,port1,port2);
      }
     }  /*end of averaged ref*/
     outportb(port1,idlevalue);
     outportb(port1,resetvalue);
     delay(100);
     outportb(port1,idlevalue);
     printf("Measurements complete. \n");

/* Readings taken. */
 return (datatype);
}
```

Appendix J
Calculation of the Weighting Factors

This appendix presents the derivation of the weighting factors used in the image forming algorithm described in Chapter 6.

The drive current between two adjacent drive electrodes can be modelled as a point dipole at the midpoint between the two drive electrodes. For a homogenous semi-infinite 2D medium, the drive current flows in circular current paths in the medium, hence generating circular equipotential loci as shown in Figure 1.2. The weighting factor is defined in section 6.2.3 as the rate of change of angle of current through a pixel with change in drive position. Figure J.1 shows the drive dipole, D, at point $(x_o,0)$ on the surface of a medium of interest A-B. Point $P\,(x_p, y_p)$ is a point within the medium and the equipotential passing through P is the arc C-D. The geometric centre of this arc (semicircle) is on the surface (line AB) and is shown as O. The current passing through the pixel P is in the direction OP, perpendicular to the tangent of CD at P. OP makes an angle θ with the axis AB. The required weighting factor is $\delta\theta/\delta x_0$.

Angle ψ is related to θ by

$$\psi = 90 - \frac{\theta}{2} \qquad \{J.1\}$$

Relating ψ to x_0

$$\tan\psi = \frac{y_p}{(x_0 - x_p)} \qquad \{J.2\}$$

Differentiating both sides of {J.2} with respect to ψ and rearranging gives

$$\frac{\delta\psi}{\delta x_0} = \frac{-y_p}{(x_0 - x_p)^2} \cdot \cos^2\psi \qquad \{J.3\}$$

Since

$$\cos\psi = \frac{(x_0 - x_p)}{\sqrt{(x_0 - x_p)^2 + y_p{}^2}} \qquad \{J.4\}$$

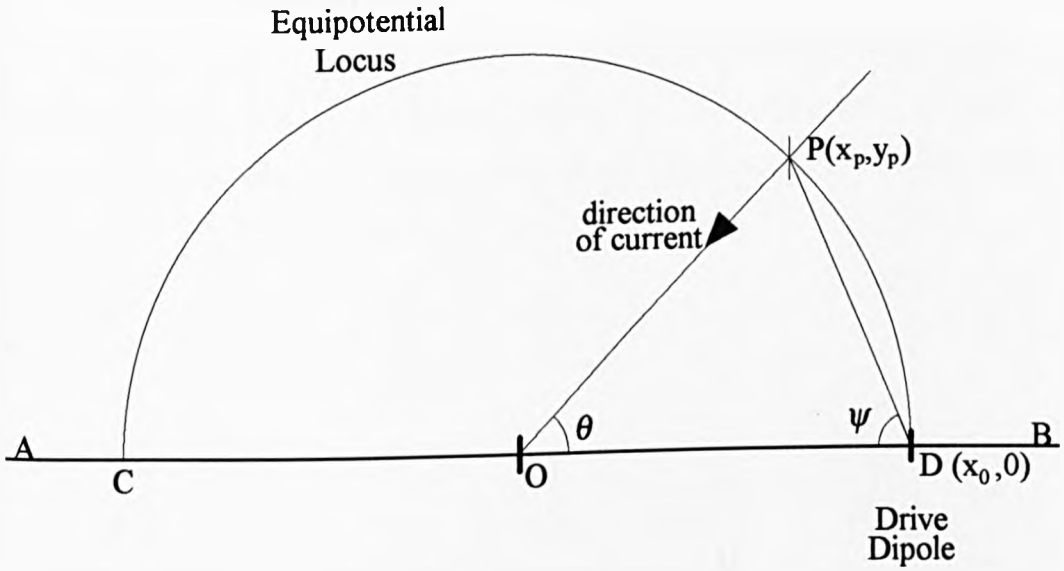

Figure J.1 : Diagram to show the derivation of the linear weightings for weighted backprojection

Then

$$\frac{\delta\psi}{\delta x_0} = \frac{y_p^{\,2}}{\left(x_0 - x_p\right)^2 + y_p^{\,2}} \qquad \{J.5\}$$

From Equation {J.1} it can be seen that $\frac{\delta\psi}{\delta x_0} = \frac{1}{2}\frac{\delta\theta}{\delta x_0}$. Therefore, the weighting factor $W(x_p, y_p)$ is given by

$$W\left(x_p, y_p\right) = \frac{2y_p^{\,2}}{\left(x_0 - x_p\right)^2 + y_p^{\,2}} \qquad \{J.6\}$$

Appendix K
Calculation of the Effect of the Phantom Boundaries on the Measured Potential.

This appendix presents the calculation of the effects of a bounded region (the phantom) on the potentials generated in the phantom, in comparison with a semi-infinite region.

Figure K.1 shows the phantom of dimensions a and b and a single drive current injected at x_1 and extracted at x_2. The walls of the phantom are boundaries across which no current passes except for the drive current (ignoring common mode feedback). Thus for a bounded region, the boundary conditions are

$$\left.\frac{\partial \Phi}{\partial x}\right|_{x=0} = 0 \qquad \{K.1\} \qquad \left.\frac{\partial \Phi}{\partial x}\right|_{x=b} = 0 \qquad \{K.2\}$$

$$\left.\frac{\partial \Phi}{\partial y}\right|_{y=a} = 0 \qquad \{K.3\} \qquad \left.\frac{\partial \Phi}{\partial y}\right|_{y=0} = \frac{I}{\pi \sigma d}\left[\delta(x_1) - \delta(x_2)\right] \qquad \{K.4\}$$

Since there is no current generated within the phantom, Lapiace's Equation {K.5} can be applied [90].

$$\nabla^2 \Phi = 0 \qquad \{K.5\}$$

By performing separation of variables and using the above boundary conditions Laplace's equation {K.5} for this situation can be solved using separation of variables [90] yields the solution to Laplace's equation of

$$\frac{X''}{X} = \frac{Y''}{Y} = k^2 \qquad \{K.6\}$$

where $\Phi(x,y) = X(x)Y(y)$ where

$$X(x) = A\cosh kx + B\sinh kx \quad \text{or} \quad X(x) = A'\cos kx + B'\sin kx \qquad \{K.7a\}$$

and $$Y(y) = C\cosh ky + D\sinh ky \quad \text{or} \quad Y(y) = C'\cos ky + D'\sin ky \qquad \{K.7b\}$$

Where A, B, C and D are real coefficients and A', B', C' and D' are imaginary coefficients.

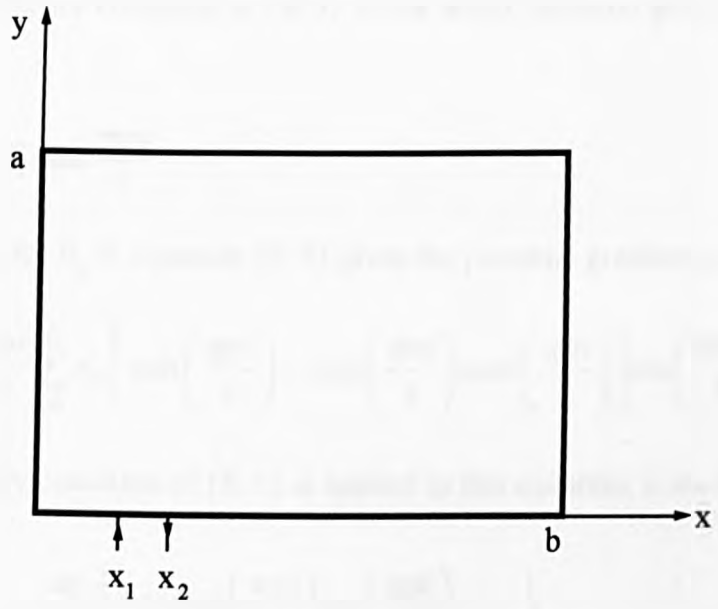

Figure K.1 : Diagram showing the phantom boundaries and position of current injection pair.

In order to satisfy the boundary conditions in {K.1} and {K.2} the solution must include a 'cos($\pi nx/b$)' term, where n is an integer. Thus the solution is of the form

$$\Phi(x,y)=\sum_{n=0}^{\infty}\left[A_n\cosh\left(\frac{\pi yn}{b}\right)+B_n\sinh\left(\frac{\pi yn}{b}\right)\right]\cos\left(\frac{\pi xn}{b}\right) \qquad \{K.8\}$$

where A_n and B_n are constant coefficients. Differentiating equation {K.8} with respect to y gives

$$\frac{\partial\Phi}{\partial y}=\sum_{n=0}^{\infty}\frac{\pi n}{b}\left[A_n\sinh\left(\frac{\pi yn}{b}\right)+B_n\cosh\left(\frac{\pi yn}{b}\right)\right]\cos\left(\frac{\pi xn}{b}\right) \qquad \{K.9\}$$

Applying the boundary condition in {K.3} to the above equation gives a solution for B_n which is

$$B_n=-A_n\tanh\frac{\pi an}{b} \qquad \{K.10\}$$

Thus substituting for B_n in equation {K.9} gives the potential gradient as

$$\frac{\partial\Phi}{\partial y}=\frac{\pi n}{b}\sum_{n=0}^{\infty}A_n\left[\sinh\left(\frac{\pi yn}{b}\right)-\tanh\left(\frac{\pi an}{b}\right)\cosh\left(\frac{\pi yn}{b}\right)\right]\cos\left(\frac{\pi xn}{b}\right) \qquad \{K.11\}$$

When the boundary condition of {K.4} is applied to this equation, it can be seen that

$$\left.\frac{\partial\Phi}{\partial y}\right|_{y=0}=-\frac{\pi n}{b}\sum_{n=0}^{\infty}A_n\tanh\left(\frac{\pi an}{b}\right)\cos\left(\frac{\pi xn}{b}\right) \qquad \{K.12\}$$

This expression can be written as a Fourier series ie

$$f(x)=\sum_{n=1}^{\infty}C_n\cos\frac{\pi xn}{b} \qquad \{K.13\}$$

where

$$\begin{aligned}C_n&=2\int_{-\infty}^{\infty}f(x)\cos\frac{\pi xn}{b}dx\\&=\frac{2}{2b}\int_{-\infty}^{\infty}\frac{I}{\pi\sigma d}\left[\delta(x_1)-\delta(x_2)\right]\cos\frac{\pi xn}{b}dx\\&=\frac{I}{b\pi\sigma d}\left[\cos\frac{\pi x_1 n}{b}-\cos\frac{\pi x_2 n}{b}\right]\end{aligned} \qquad \{K.14\}$$

From Equations {K.12} and {K.14} it can be seen that

$$A_n = \frac{I\left[\cos\left(\frac{\pi x_1 n}{b}\right) - \cos\left(\frac{\pi x_2 n}{b}\right)\right]}{\pi^2 n d\sigma \tanh\left(\frac{\pi a n}{b}\right)} \qquad \{K.15\}$$

Thus substituting for A_n and B_n in equation {K.8}, the potential distribution in the phantom is given by

$$\Phi(x,y) = \frac{I}{\pi^2 d\sigma}\sum_{n=1}^{\infty}\left[\cosh\frac{\pi y n}{b} - \tanh\frac{\pi a n}{b}\sinh\frac{\pi y n}{b}\right]\cos\left(\frac{\pi x n}{b}\right)\cdot\frac{\left[\cos\frac{\pi n x_1}{b} - \cos\frac{\pi n x_2}{b}\right]}{n\tanh\frac{\pi a n}{b}} \qquad \{K.16\}$$

This equation can be used to calculate the expected voltage differences between the receive electrodes by substituting y=0 and suitable values for x. By substituting y=0, Equation {K.16} reduces to

$$\Phi(x,y) = \frac{I}{\pi^2 d\sigma}\sum_{n=1}^{\infty}\cos\left(\frac{\pi x n}{b}\right)\cdot\frac{\left[\cos\frac{\pi n x_1}{b} - \cos\frac{\pi n x_2}{b}\right]}{n\tanh\frac{\pi a n}{b}} \qquad \{K.17\}$$

For adjacent drives, if the drive positions x_1 and x_2 were defined by $x_1 = x_d - l/2$ and $x_2 = x_d + l/2$ then equation {K.17} becomes

$$\Phi(x,y) = \frac{I}{\pi^2 d\sigma}\sum_{n=1}^{\infty}\cos\left(\frac{\pi x n}{b}\right)\cdot\frac{\left[2\sin\frac{\pi n x_d}{b}\sin\frac{\pi n l}{b}\right]}{n\tanh\frac{\pi a n}{b}} \qquad \{K.18\}$$

This solution was used in the computation of the potential differences measured at the receive electrodes in the presence of the phantom walls. The effect was to cause an error of less than 0.02%.

Appendix L
Common Mode Voltage Compensation

Section 3.5.4 describes the use of common mode feedback to reduce the common mode voltages generated by mismatches in the system parameters. The circuitry used to perform the common mode feedback introduced a phase shift between the differential signal and this common mode voltage. If the permittivity of the medium under investigation is small, no phase shift should be introduced by the medium of interest itself and the measured potential difference signals should either be 0° or 180° with respect to the drive waveforms (after fixed phase shifts through the system have been taken into account).

Figure L.1 shows a phasor representation of the output of the subtractor at one signal frequency. The desired measurement is the voltage v_d, the phase shifted common mode voltage is v_c and the measured voltage, v_m, is the resultant of the two. If the common mode rejection ratio of the subtractors were large enough, v_c would be small and $v_m = v_d$. This is approximately the case for large values of v_d.

The phase shift of the measured voltage, α, is known, the phase shift generated by the common mode feedback circuitry at the signal frequencies, β, is known and the magnitude of v_m is known. Since v_m is assumed to have no components which are phase shifted,

$$v_m \sin\alpha = v_c \sin\beta \qquad \{L.1\}$$

Since

$$\begin{aligned} v_d &= v_m \cos\alpha - v_c \cos\beta \\ &= v_m \cos\alpha - \frac{v_m \sin\alpha}{\sin\beta}\cos\beta \end{aligned} \qquad \{L.2\}$$

Thus by measuring v_m and α, and knowing β, v_d is calculable. This method has not been tried on real data due to lack of time, but it may prove to be useful in the compensation of common mode voltages. This method assumes that there is no phase shift of v_d, which is not true for permittivity discontinuities and it does not compensate for any common mode voltage which is in phase with the differential voltage.

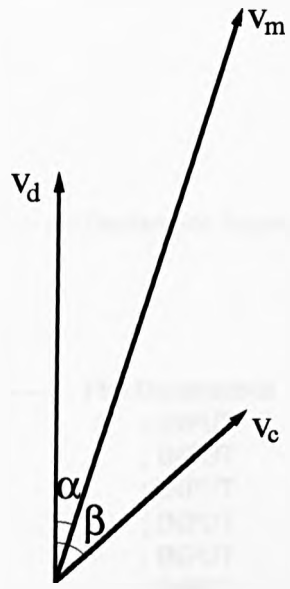

Figure L.1 : Phasor diagram showing the measured voltage differences

v_d is the required voltage difference

v_c is the output of the subtractor caused by a finite CMRR

v_m is the measured voltage.

Appendix M
Data for programming PALs

This Appendix lists the data used to program the PALs which are used in the control circuitry.

PAL 1

```
;PALASM Design Description

;---------------------------------- Declaration Segment ----------
PAL1

CHIP  _pal1  PAL22V10

;---------------------------------- PIN Declarations -------------
PIN  1      A0                    ; INPUT
PIN  2      A1                    ; INPUT
PIN  3      A2                    ; INPUT
PIN  4      A3                    ; INPUT
PIN  5      A4                    ; INPUT
PIN  6      A5                    ; INPUT
PIN  7      A6                    ; INPUT
PIN  8      A7                    ; INPUT
PIN  9      A8                    ; INPUT
PIN  10     A9                    ; INPUT
PIN  11     A10                   ; INPUT
PIN  12     GND                   ;
PIN  14     ENCLKMEAS             COMBINATORIAL ; OUTPUT
PIN  16     /PROMADDGENCLR        COMBINATORIAL ; OUTPUT
PIN  17     COUNT                 COMBINATORIAL ; OUTPUT
PIN  18     /PROMOE               COMBINATORIAL ; OUTPUT
PIN  19     /PROMCE               COMBINATORIAL ; OUTPUT
PIN  20     /DACCS                COMBINATORIAL ; OUTPUT
PIN  21     RESET                 ; INPUT
PIN  22     MEASURE               ; INPUT
PIN  23     SINSYNC               COMBINATORIAL ; OUTPUT
PIN  24     VCC                   ;

;---------------------------------- Boolean Equation Segment -----
EQUATIONS

PROMADDGENCLR = (MEASURE*A0*A1*A2*A3*A4*A5*A6*A7*A8*A9*A10) + /RESET

SINSYNC = MEASURE*A0*/A1*/A2*/A3*/A4*/A5*/A6*/A7*/A8*/A9*/A10

DACCS = RESET
```

```
PROMCE = MEASURE

PROMOE = MEASURE

COUNT = MEASURE
```

PAL 2

```
;PALASM Design Description

;———————————————— Declaration Segment ————————————
PAL2

CHIP _PAL2 PALCE16V8

;———————————————— PIN Declarations ————————————
PIN 5      QALSB                    ; INPUT
PIN 6      QB                       ; INPUT
PIN 7      QC                       ; INPUT
PIN 8      QDMSB                    ; INPUT
PIN 10     GND                      ;
PIN 13     CLKOUT                   COMBINATORIAL ; OUTPUT
PIN 14     /DACWR                   COMBINATORIAL ; OUTPUT
PIN 15     TRACKHOLD                COMBINATORIAL ; OUTPUT
PIN 20     VCC                      ;

;———————————————— Boolean Equation Segment ————————
EQUATIONS

CLKOUT = QALSB*/QB*/QC*/QDMSB

DACWR =  /QALSB*QB*QC*/QDMSB + QALSB*QB*QC*/QDMSB +
         /QALSB*/QB*/QC*QDMSB + QALSB*/QB*/QC*QDMSB +
         /QALSB*QB*/QC*QDMSB + QALSB*QB*QC*QDMSB +
         /QALSB*/QB*QC*QDMSB + QALSB*/QB*QC*QDMSB +
         /QALSB*QB*QC*QDMSB+ QALSB*QB*QC*QDMSB

TRACKHOLD = QALSB*/QB*QC*/QDMSB + /QALSB*QB*QC*/QDMSB +
            QALSB*QB*QC*/QDMSB + /QALSB*/QB*/QC*QDMSB +
            QALSB*/QB*/QC*QDMSB + /QALSB*QB*/QC*QDMSB +
            QALSB*QB*/QC*QDMSB
```

PAL A

```
;PALASM Design Description

;———————————————— Declaration Segment ————————————
PAL A

CHIP _pala PALCE16V8

;———————————————— PIN Declarations ————————————
PIN 1      ENDOFFRAME               ; INPUT
PIN 2      ENDOFMEMSTOP             ; INPUT
PIN 3      PCREAD2                  ; INPUT
```

```
PIN 4       PCREAD1                 ; INPUT
PIN 5       CONTINUOUS              ; INPUT
PIN 6       GO                      ; INPUT
PIN 7       MEASURE                 ; INPUT
PIN 8       RESTART                 ; INPUT
PIN 9       RESET                   ; INPUT
PIN 10      GND                     ;
PIN 12      WAITING                 COMBINATORIAL ; OUTPUT
PIN 13      /NOTRESET               COMBINATORIAL ; OUTPUT
PIN 14      /MEMCS12                COMBINATORIAL ; OUTPUT
PIN 15      /ENMEMADDABUS           COMBINATORIAL ; OUTPUT
PIN 16      MEMADDCOUNT             COMBINATORIAL ; OUTPUT
PIN 17      MEASURECOUNT            COMBINATORIAL ; OUTPUT
PIN 18      MEMADDGENCLR            COMBINATORIAL ; OUTPUT
PIN 19      /ENMEMWE                COMBINATORIAL ; OUTPUT
PIN 20      VCC                     ;

;————————————————————— Boolean Equation Segment ———
EQUATIONS

ENMEMWE = GO*(RESTART+/(ENDOFFRAME*CONTINUOUS))*PCREAD1*PCREAD2
          *MEASURE

MEASURECOUNT = GO*PCREAD1*PCREAD2*MEASURE

MEMADDCOUNT = GO*(RESTART+/(ENDOFFRAME*CONTINUOUS))*PCREAD1*PCREAD2
              *MEASURE

WAITING = (ENDOFFRAME*CONTINUOUS) + ENDOFMEMSTOP

ENMEMADDABUS = MEASURE*PCREAD1*PCREAD2

MEMCS12 = MEASURE+/PCREAD1+/PCREAD2

NOTRESET = RESET

MEMADDGENCLR = RESET
```

PAL B

```
;PALASM Design Description

;————————————————————— Declaration Segment ————————
PAL B

CHIP _palb  PALCE26V12

;————————————————————— PIN Declarations ————————————
PIN 1       Q1LSB                   ; INPUT
PIN 2       Q2                      ; INPUT
PIN 3       Q3                      ; INPUT
PIN 4       Q4                      ; INPUT
PIN 5       Q5                      ; INPUT
PIN 6       Q6                      ; INPUT
PIN 7       VCC                     ;
PIN 8       Q7MSB                   ; INPUT
```

```
PIN 15      /OC8                    ; OUTPUT
PIN 16      /OC10                   ; OUTPUT
PIN 17      /OC7                    ; OUTPUT
PIN 18      /OC6                    ; OUTPUT
PIN 19      /OC5                    ; OUTPUT
PIN 20      /OC4                    ; OUTPUT
PIN 21      GND                     ;
PIN 22      /OC13                   ; OUTPUT
PIN 23      /OC3                    ; OUTPUT
PIN 24      /OC16                   ; OUTPUT
PIN 25      /OC2                    ; OUTPUT
PIN 26      /OC15                   ; OUTPUT
PIN 27      /OC1                    ; OUTPUT

;————————————————————— Boolean Equation Segment ———
EQUATIONS


OC1 = Q1LSB*/Q2*/Q3*/Q4*/Q5*/Q6*/Q7MSB + /Q1LSB*Q2*/Q3*/Q4*/Q5*/Q6*/Q7MSB
      +Q1LSB*Q2*/Q3*/Q4*/Q5*/Q6*/Q7MSB +  /Q1LSB*/Q2*Q3*/Q4*/Q5*/Q6*/Q7MSB

OC2 = /Q1LSB*Q2*Q3*/Q4*/Q5*/Q6*/Q7MSB + Q1LSB*Q2*Q3*/Q4*/Q5*/Q6*/Q7MSB
      +/Q1LSB*/Q2*/Q3*Q4*/Q5*/Q6*/Q7MSB + Q1LSB*/Q2*/Q3*Q4*/Q5*/Q6*/Q7MSB

OC3 = Q1LSB*Q2*/Q3*Q4*/Q5*/Q6*/Q7MSB + /Q1LSB*/Q2*Q3*Q4*/Q5*/Q6*/Q7MSB
      +Q1LSB*/Q2*Q3*Q4*/Q5*/Q6*/Q7MSB + /Q1LSB*Q2*Q3*Q4*/Q5*/Q6*/Q7MSB

OC4 = /Q1LSB*/Q2*/Q3*/Q4*Q5*/Q6*/Q7MSB + Q1LSB*/Q2*/Q3*/Q4*Q5*/Q6*/Q7MSB
      +/Q1LSB*Q2*/Q3*/Q4*Q5*/Q6*/Q7MSB + Q1LSB*Q2*/Q3*/Q4*Q5*/Q6*/Q7MSB

OC5 = Q1LSB*/Q2*Q3*/Q4*Q5*/Q6*/Q7MSB + /Q1LSB*Q2*Q3*/Q4*Q5*/Q6*/Q7MSB
      +Q1LSB*Q2*Q3*/Q4*Q5*/Q6*/Q7MSB +/ Q1LSB*/Q2*/Q3*Q4*Q5*/Q6*/Q7MSB

OC6 = /Q1LSB*Q2*/Q3*Q4*Q5*/Q6*/Q7MSB + Q1LSB*Q2*/Q3*Q4*Q5*/Q6*/Q7MSB
      +/Q1LSB*/Q2*Q3*Q4*Q5*/Q6*/Q7MSB + Q1LSB*/Q2*Q3*Q4*Q5*/Q6*/Q7MSB

OC7 = Q1LSB*Q2*Q3*Q4*Q5*/Q6*/Q7MSB + /Q1LSB*/Q2*/Q3*/Q4*/Q5*Q6*/Q7MSB
      +Q1LSB*/Q2*/Q3*/Q4*/Q5*Q6*/Q7MSB + /Q1LSB*Q2*/Q3*/Q4*/Q5*Q6*/Q7MSB

OC8 = /Q1LSB*/Q2*Q3*/Q4*/Q5*Q6*/Q7MSB + Q1LSB*/Q2*Q3*/Q4*/Q5*Q6*/Q7MSB
      +/Q1LSB*Q2*Q3*/Q4*/Q5*Q6*/Q7MSB + Q1LSB*Q2*Q3*/Q4*/Q5*Q6*/Q7MSB

OC10 = /Q1LSB*Q2*Q3*Q4*/Q5*Q6*/Q7MSB + Q1LSB*Q2*Q3*Q4*/Q5*Q6*/Q7MSB
      +/Q1LSB*/Q2*/Q3*/Q4*Q5*Q6*/Q7MSB + Q1LSB*/Q2*/Q3*/Q4*Q5*Q6*/Q7MSB

OC13 = Q1LSB*/Q2*Q3*Q4*Q5*Q6*/Q7MSB + /Q1LSB*Q2*Q3*Q4*Q5*Q6*/Q7MSB
      +Q1LSB*Q2*Q3*Q4*Q5*Q6*/Q7MSB + /Q1LSB*/Q2*/Q3*/Q4*/Q5*/Q6*Q7MSB

OC15 = Q1LSB*Q2*Q3*/Q4*/Q5*/Q6*Q7MSB + /Q1LSB*/Q2*/Q3*Q4*/Q5*/Q6*Q7MSB
      +Q1LSB*/Q2*/Q3*Q4*/Q5*/Q6*Q7MSB + /Q1LSB*Q2*/Q3*Q4*/Q5*/Q6*Q7MSB

OC16 = /Q1LSB*/Q2*Q3*Q4*/Q5*/Q6*Q7MSB + Q1LSB*/Q2*Q3*Q4*/Q5*/Q6*Q7MSB
      +/Q1LSB*Q2*Q3*Q4*/Q5*/Q6*Q7MSB + Q1LSB*Q2*Q3*Q4*/Q5*/Q6*Q7MSB
```

PAL C

```
;PALASM Design Description

;———————————————— Declaration Segment ————————————
PAL C

CHIP _PALC PAL22V10

;———————————————— PIN Declarations ————————————
PIN 1     Q1LSB                 ; INPUT
PIN 2     Q2                    ; INPUT
PIN 3     Q3                    ; INPUT
PIN 4     Q4                    ; INPUT
PIN 5     Q5                    ; INPUT
PIN 6     Q6                    ; INPUT
PIN 7     Q7MSB                 ; INPUT
PIN 8     FEEDBACKIN            ; INPUT
PIN 9     RESET                 ; INPUT
PIN 12    GND                   ;
PIN 14    /OC9                  COMBINATORIAL ; OUTPUT
PIN 15    /OC12                 COMBINATORIAL ; OUTPUT
PIN 16    LATCHEN               COMBINATORIAL ; OUTPUT
PIN 17    /CONVST               COMBINATORIAL ; OUTPUT
PIN 18    /MEMWE                COMBINATORIAL ; OUTPUT
PIN 19    MEMADDGENCLK          COMBINATORIAL ; OUTPUT
PIN 20    /OC11                 COMBINATORIAL ; OUTPUT
PIN 21    /OC14                 COMBINATORIAL ; OUTPUT
PIN 22    FDBACKOUT             COMBINATORIAL ; OUTPUT
PIN 23    /MEASCOUNTERCLR       COMBINATORIAL ; OUTPUT
PIN 24    VCC                   ;

;———————————————— Boolean Equation Segment ————————
EQUATIONS

FDBACKOUT = (/Q2*Q3*/Q4*Q5*Q6*/Q7MSB)
          + (Q1LSB*/Q2*/Q3*Q4*Q5*Q6*/Q7MSB)
          + (/Q1LSB*Q2*/Q3*Q4*Q5*Q6*/Q7MSB)
          + (Q2*Q3*Q4*Q5*Q6*/Q7MSB)
          + (Q1LSB*Q2*/Q3*/Q4*/Q5*/Q6*Q7MSB)
          + (/Q1LSB*/Q2*Q3*/Q4*/Q5*/Q6*Q7MSB)
          + (/Q2*/Q3*Q4*/Q5*/Q6*Q7MSB)
          + (Q1LSB*/Q2*Q3*Q4*/Q5*/Q6*Q7MSB)
          + (/Q1LSB*Q2*Q3*Q4*/Q5*/Q6*Q7MSB)

LATCHEN = (Q1LSB*/Q2*Q3*Q4*Q5*Q6*Q7MSB) + (/Q1LSB*Q2*Q3*Q4*Q5*Q6*Q7MSB)

CONVST = Q1LSB*/Q2*/Q3*/Q4*/Q5*/Q6*/Q7MSB

MEMWE = (Q2*/Q3*/Q4*/Q5*/Q6*/Q7MSB) + (Q1LSB*Q2*Q3*/Q4*/Q5*/Q6*/Q7MSB)
      + (/Q1LSB*/Q2*/Q3*Q4*/Q5*/Q6*/Q7MSB) + (/Q2*Q3*Q4*/Q5*/Q6*/Q7MSB)
      + (Q1LSB*/Q2*/Q3*/Q4*Q5*/Q6*/Q7MSB) + (/Q1LSB*Q2*/Q3*/Q4*Q5*/Q6*/Q7MSB)
      + (Q2*Q3*/Q4*Q5*/Q6*/Q7MSB) + (Q1LSB*Q2*/Q3*Q4*Q5*/Q6*/Q7MSB)
      + (/Q1LSB*/Q2*Q3*Q4*Q5*/Q6*/Q7MSB) + (/Q2*/Q3*/Q4*/Q5*Q6*/Q7MSB)
      + (Q1LSB*/Q2*Q3*/Q4*/Q5*Q6*/Q7MSB) + (/Q1LSB*Q2*Q3*/Q4*/Q5*Q6*/Q7MSB)
      + (Q2*/Q3*Q4*/Q5*Q6*/Q7MSB) + (Q1LSB*Q2*Q3*Q4*/Q5*Q6*/Q7MSB)
      + (/Q1LSB*/Q2*/Q3*/Q4*Q5*Q6*/Q7MSB) + FDBACKOUT
```

```
MEMADDGENCLK = (Q1LSB*/Q2*/Q3*/Q4*/Q5*/Q6*/Q7MSB)
             + (/Q1LSB*Q2*Q3*/Q4*/Q5*/Q6*/Q7MSB)
             + (Q1LSB*Q2*/Q3*Q4*/Q5*/Q6*/Q7MSB)
             + (/Q1LSB*/Q2*/Q3*/Q4*Q5*/Q6*/Q7MSB)
             + (Q1LSB*/Q2*Q3*/Q4*Q5*/Q6*/Q7MSB)
             + (/Q1LSB*Q2*/Q3*Q4*Q5*/Q6*/Q7MSB)
             + (Q1LSB*Q2*Q3*Q4*Q5*/Q6*/Q7MSB)
             + (/Q1LSB*/Q2*Q3*/Q4*/Q5*Q6*/Q7MSB)
             + (Q1LSB*/Q2*/Q3*Q4*/Q5*Q6*/Q7MSB)
             + (/Q1LSB*Q2*Q3*Q4*/Q5*Q6*/Q7MSB)
             + (Q1LSB*Q2*/Q3*/Q4*Q5*Q6*/Q7MSB)
             + (/Q1LSB*/Q2*/Q3*Q4*Q5*Q6*/Q7MSB)
             + (Q1LSB*/Q2*Q3*Q4*Q5*Q6*/Q7MSB)
             + (/Q1LSB*Q2*/Q3*/Q4*/Q5*/Q6*Q7MSB)
             + (Q1LSB*Q2*Q3*/Q4*/Q5*/Q6*Q7MSB)
             + (/Q1LSB*/Q2*Q3*Q4*/Q5*/Q6*Q7MSB)

OC9 =    (Q1LSB*/Q2*/Q3*Q4*/Q5*Q6*/Q7MSB) + (/Q1LSB*Q2*/Q3*Q4*/Q5*Q6*/Q7MSB)
         + (Q1LSB*Q2*/Q3*Q4*/Q5*Q6*/Q7MSB) + (/Q1LSB*/Q2*Q3*Q4*/Q5*Q6*/Q7MSB)

OC11 =   (Q1LSB*Q2*/Q3*/Q4*Q5*Q6*/Q7MSB) + (/Q1LSB*/Q2*Q3*/Q4*Q5*Q6*/Q7MSB)
         + (Q1LSB*/Q2*Q3*/Q4*Q5*Q6*/Q7MSB) + (/Q1LSB*Q2*Q3*/Q4*Q5*Q6*/Q7MSB)

OC12 =   (/Q1LSB*/Q2*/Q3*Q4*Q5*Q6*/Q7MSB) + (Q1LSB*/Q2*/Q3*Q4*Q5*Q6*/Q7MSB)
         + (/Q1LSB*Q2*/Q3*Q4*Q5*Q6*/Q7MSB) + (Q1LSB*Q2*/Q3*Q4*Q5*Q6*/Q7MSB)

OC14 =   (/Q1LSB*Q2*/Q3*/Q4*/Q5*/Q6*Q7MSB) + (Q1LSB*Q2*/Q3*/Q4*/Q5*/Q6*Q7MSB)
         + (/Q1LSB*/Q2*Q3*/Q4*/Q5*/Q6*Q7MSB) + (Q1LSB*/Q2*Q3*/Q4*/Q5*/Q6*Q7MSB)

MEASCOUNTERCLR = /RESET + (Q1LSB*Q2*Q3*Q4*Q5*Q6*Q7MSB)
```

PAL D

```
;PALASM Design Description

;---------------------------------- Declaration Segment ------------
PAL D

CHIP _PALD  PAL22V10

;---------------------------------- PIN Declarations ---------------
PIN  5     A11                    ; INPUT
PIN  6     A10                    ; INPUT
PIN  7     A9                     ; INPUT
PIN  8     A8                     ; INPUT
PIN  9     A14MSB                 ; INPUT
PIN  10    A13                    ; INPUT
PIN  11    A12                    ; INPUT
PIN  12    GND                    ;
PIN  13    A4                     ; INPUT
PIN  14    A5                     ; INPUT
PIN  15    A6                     ; INPUT
PIN  16    A7                     ; INPUT
PIN  17    A0LSB                  ; INPUT
PIN  18    A1                     ; INPUT
PIN  19    A2                     ; INPUT
```

```
PIN 20      A3                          ; INPUT
PIN 22      ENDOFFRAME                  COMBINATORIAL ; OUTPUT
PIN 23      ENDOFMEM                    COMBINATORIAL ; OUTPUT
PIN 24      VCC                         ;

;------------------------------ Boolean Equation Segment ------
EQUATIONS

ENDOFMEM = (A14MSB*A13*A12*/A11*/A10*/A9*/A8*/A7*/A6*/A5*A4*/A3*A2*A1*A0LSB)

ENDOFFRAME = (/A14MSB*/A13*A12*/A11*/A10*/A9*/A8*/A7*/A6*/A5*A4*/A3*/A2*/A1
                                                                *A0LSB)
           + (/A14MSB*A13*/A12*/A11*/A10*/A9*/A8*/A7*/A6*/A5*A4*/A3*/A2*A1
                                                                */A0LSB)
           + (/A14MSB*A13*A12*/A11*/A10*/A9*/A8*/A7*/A6*/A5*A4*/A3*/A2*A1
                                                                *A0LSB)
           + (A14MSB*/A13*/A12*/A11*/A10*/A9*/A8*/A7*/A6*/A5*A4*/A3*A2*/A1
                                                                */A0LSB)
           + (A14MSB*/A13*A12*/A11*/A10*/A9*/A8*/A7*/A6*/A5*A4*/A3*A2*/A1
                                                                *A0LSB)
           + (A14MSB*A13*/A12*/A11*/A10*/A9*/A8*/A7*/A6*/A5*A4*/A3*A2*A1
                                                                */A0LSB)
           + (A14MSB*A13*A12*/A11*/A10*/A9*/A8*/A7*/A6*/A5*A4*/A3*A2*A1
                                                                *A0LSB)
```

PAL F

```
;PALASM Design Description

;------------------------------ Declaration Segment ------------
PAL F

CHIP _PALF  PALCE16V8

;------------------------------ PIN Declarations ---------------
PIN 3       PCREAD2                     ; INPUT
PIN 4       PCREAD1                     ; INPUT
PIN 5       A19                         ; INPUT
PIN 6       A18                         ; INPUT
PIN 7       A17                         ; INPUT
PIN 8       A16                         ; INPUT
PIN 9       A15                         ; INPUT
PIN 10      GND                         ;
PIN 12      /LSBADDVALID                COMBINATORIAL ; OUTPUT
PIN 14      /MSBADDVALID                COMBINATORIAL ; OUTPUT
PIN 17      /ADDVALID                   COMBINATORIAL ; OUTPUT
PIN 20      VCC                         ;

;------------------------------ Boolean Equation Segment ------
EQUATIONS

ADDVALID = /A15*/A16*A17*A18*A19

LSBADDVALID = /A15*/A16*A17*A18*A19*/PCREAD1

MSBADDVALID = /A15*/A16*A17*A18*A19*/PCREAD2
```

PAL G

```
;PALASM Design Description

;———————————————— Declaration Segment ————————————
PAL G

CHIP _PALG PAL22V10

;———————————————— PIN Declarations ————————————
PIN 1       PCCLK                   ; INPUT
PIN 2       ADDVALID                ; INPUT
PIN 3       MEMRSIG                 ; INPUT
PIN 4       RESETDRV                ; INPUT
PIN 5       DIN0                    ; INPUT
PIN 8       DIN1                    ; INPUT
PIN 9       DIN2                    ; INPUT
PIN 10      DIN3                    ; INPUT
PIN 11      OUTRESET                ; INPUT
PIN 12      GND                     ;
PIN 14      OUTOUTRESET             COMBINATORIAL ; OUTPUT
PIN 15      THREEWS                 REGISTERED ; OUTPUT
PIN 16      TWOWS                   REGISTERED ; OUTPUT
PIN 17      ONEWS                   REGISTERED ; OUTPUT
PIN 18      ZEROWS                  REGISTERED ; OUTPUT
PIN 24      VCC                     ;
NODE 1      GLOBAL

;———————————————— Boolean Equation Segment ————————
EQUATIONS

GLOBAL.RSTF = OUTRESET

OUTOUTRESET = RESETDRV + ADDVALID + MEMRSIG

ZEROWS.TRST = /RESETDRV*/ADDVALID*/MEMRSIG
ONEWS.TRST = /RESETDRV*/ADDVALID*/MEMRSIG
TWOWS.TRST = /RESETDRV*/ADDVALID*/MEMRSIG
THREEWS.TRST = /RESETDRV*/ADDVALID*/MEMRSIG

ZEROWS = DIN0

ONEWS = DIN1

TWOWS = DIN2

THREEWS = DIN3
```

PAL H

```
;PALASM Design Description

;———————————————— Declaration Segment ————————————
PAL H

CHIP _palh PAL22V10
```

```
;------------------------------ PIN Declarations ------------------------------
PIN 2     A8                    ; INPUT
PIN 3     A9                    ; INPUT
PIN 4     A7                    ; INPUT
PIN 5     A6                    ; INPUT
PIN 6     A5                    ; INPUT
PIN 7     A4                    ; INPUT
PIN 8     A3                    ; INPUT
PIN 9     A2                    ; INPUT
PIN 10    A1                    ; INPUT
PIN 11    A0                    ; INPUT
PIN 12    GND                   ;
PIN 14    CLKRD                 COMBINATORIAL ; OUTPUT
PIN 15    /RDWREN               COMBINATORIAL ; OUTPUT
PIN 16    /CLKREAD              COMBINATORIAL ; OUTPUT
PIN 17    /CLKWR                COMBINATORIAL ; OUTPUT
PIN 20    AENSIG                ; INPUT
PIN 21    IOWSIG                ; INPUT
PIN 22    IORSIG                ; INPUT
PIN 24    VCC                   ;

;---------------------------- Boolean Equation Segment ----------------------
EQUATIONS

CLKWR = /IOWSIG*/A0*/A1*/A2*/A3*A4*A5*A6*/A7*A8*A9*/AENSIG

CLKRD = (/IOWSIG*/A0*/A1*/A2*/A3*A4*A5*A6*/A7*A8*A9) + (IOWSIG*IORSIG)

RDWREN = /A1*/A2*/A3*A4*A5*A6*/A7*A8*A9*/AENSIG

CLKREAD = /IORSIG*A0*/A1*/A2*/A3*A4*A5*A6*/A7*A8*A9*/AENSIG
```